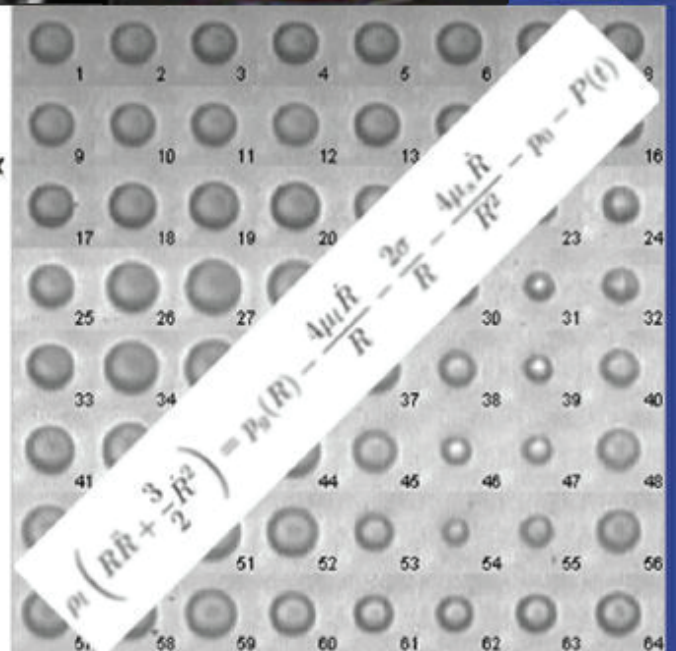
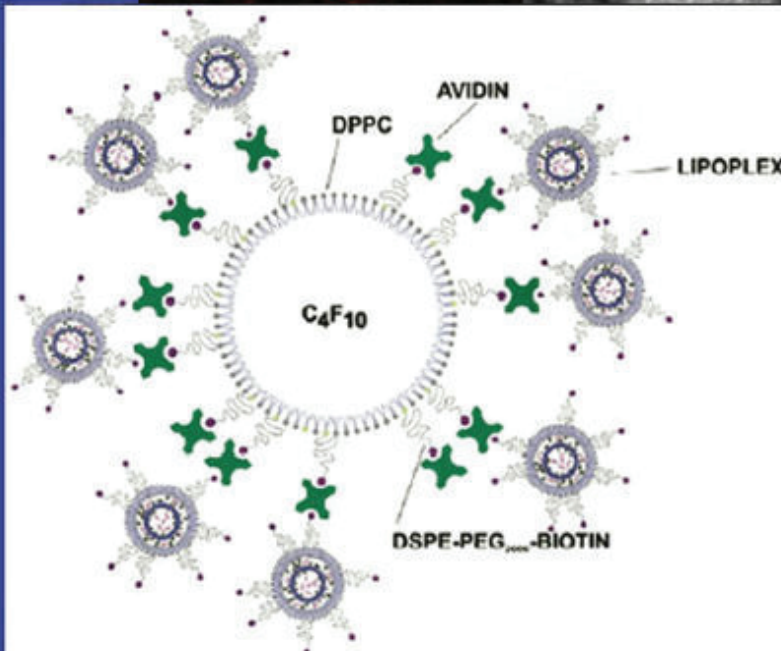
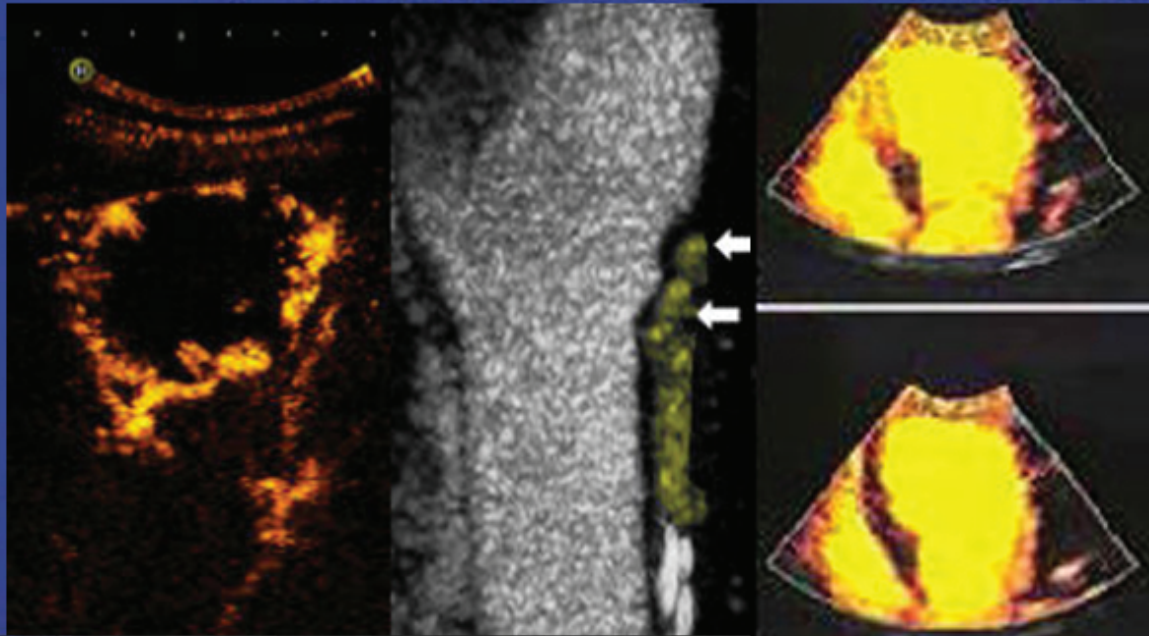


The 18th European Symposium on Ultrasound Contrast Imaging

- An ICUS Conference -



Abstract book

January, 17-18 2013, Rotterdam, The Netherlands

Organized by Folkert ten Cate, Nico de Jong, Arend Schinkel, Edward Leen
Erasmus MC Rotterdam - Imperial College London

18th EUROPEAN SYMPOSIUM ON ULTRASOUND CONTRAST IMAGING
17-18 JANUARY 2013, Rotterdam, The Netherlands

WEDNESDAY, 16 January 2013

18.00 – 20.00 **Registration - Welcome Drinks**

THURSDAY, 17 January 2013

Oral program

08.00 – 09.00	Registration	
09.00 – 09.05	Introduction and opening	<i>Ton van der Steen</i>
09.05 – 10.35	PERFUSION IMAGING	<i>Chairpersons: Stephen Meairs / Folkert ten Cate</i>
Paolo Colonna	The Phoenix trial, diagnosis of coronary artery disease using contrast perfusion imaging	1
Roxy Senior	Comparison of sulfur hexafluoride microbubble (SonoVue)-enhanced myocardial echocardiography to single photon emission computerized tomography at rest and vasodilator stress in the assessment of significant coronary artery disease: a large European multicentre study	3
Peter Burns	Fast contrast imaging	5
Chloé Arthuis	New insights into uteroplacental perfusion: Quantitative analysis using Doppler and contrast-enhanced ultrasound imaging	6
John Pacella	New rat hindlimb model of microvascular no-reflow to evaluate treatment of microvascular obstruction with long tone burst sonothrombolysis.....	8
10.35 – 11.05	Intermission	
11.05 – 12.30	RADIOLOGY	<i>Chairpersons: David Cosgrove / Hans-Peter Weskott</i>
Pavel Taimr	Diagnostic performance of contrast-enhanced ultrasound versus computed tomography in detection of liver metastases in patients suspected for pancreatic- or periampullary cancer.....	12
Edward Leen	Applications of CEUS for therapy	13
Hans Peter Weskott	Taking advantage of a high spatial resolution contrast mode in the detection of liver metastases: Impact of small liver metastases in different primary malignancies: First results	14
Mike Averkiou	Perfusion quantification: the known knowns, the known unknowns, and the unknown unknowns.....	16
Massimo Mischi	Prostate cancer imaging by DCE-US	17
12.30 – 14.00	LUNCH	
14.00 – 14.30	COEUR LECTURE	<i>Chairperson: Nico de Jong</i>
Tom Porter	The future of sonothrombolysis.....	20
14.30 – 16.15	THERAPY	<i>Chairpersons: Liza Villanueva / Klazina Kooiman</i>
Steve Feinstein	State-of-the-art: Pre-clinical and clinical diagnostic and therapeutic applications of contrast-enhanced ultrasound imaging: vasa vasorum	22
Stephen Meairs	Therapeutic ultrasound.....	23
Ine Lentacker	Targeted gene therapy using lipoplex loaded microbubbles: concept, mechanism and application	24
Fuminori Moriyasu	High Intensity Focused Untrasound (HIFU) for pancreas cancer treatment and efficacy evaluation using contrast ultrasound.....	25
Per Christian Sontum	Development concept and physicochemical characteristics of a phase shift formulation platform for ultrasound mediated drug delivery	28
Ayache Bouakaz	Sonoporation, endocytosis and pore formation.....	33
16.15 – 16.45	Intermission	
16.45 – 17.45	QUANTIFICATION AND NEW STRATEGIES	<i>Chairpersons: Steve Feinstein / Mike Averkiou</i>
Dan Adam	Semi-automated detection of neovascularization.....	39
Hans Bosch	Quantification of neovascularization in carotid artery plaques	41
Jacopo Viti	A systematic comparison of contrast imaging strategies.....	45
Matthew Bruce	Trade-offs in ultrafast imaging of microbubbles	47
18.30 – 22.30	SOCIAL EVENT (Incl. Dinner buffet)	

18th EUROPEAN SYMPOSIUM ON ULTRASOUND CONTRAST IMAGING
17-18 JANUARY 2013, Rotterdam, The Netherlands

FRIDAY, 18 January 2013

07.30 – 08.00 Registration

Poster sessions

07.30 – 09.00 MODERATED POSTER SESSION A: BIOLOGY *Moderator: Arend Schinkel*

A1)	Stijn van Oord/ Zeynettin Akkus	Automated quantification of carotid intraplaque neovascularization using contrast-enhanced ultrasound	52
A2)	Xucai Chen	Mechanistic insights of therapeutic potential of long ultrasound tone bursts in microbubble-ultrasound mediated therapies using high speed imaging	55
A3)	Damianos Christofides	Automatic respiratory motion gating for the quantification of liver therapy monitoring	58
A4)	Wing-Keung Cheung	Towards quantification of plaque neovascularisation in human carotid arteries – a preliminary study of attenuation correction and segmentation in CEUS images	62
A5)	Rick Kwekkeboom	Ultrasound and microbubble guided delivery of microRNA-based therapeutics in vitro and in vivo	65
A6)	Jason Castle	Studies on agent delivery via ultrasound and microbubbles	67
A7)	Maria-Louisa Izamis	Quantitative evaluation of ex vivo livers in machine perfusion with dynamic contrast-enhanced ultrasound	68
A8)	Harm Ebben	Feasibility of standard thrombolysis with the additional therapeutic application of contrast-enhanced ultrasound for acute peripheral arterial occlusions in a porcine model	72

07.30 – 09.00 MODERATED POSTER SESSION B: TECHNOLOGY *Moderator: Nico de Jong*

B1)	Elena Igualada	Numerical and experimental analyses of the translation of microbubbles under short acoustic pulses	75
B2)	Adam Dixon	Transiently stable microbubbles produced by a microfluidic device for therapeutic applications	78
B3)	Tim Segers	Acoustic bubble sorting of ultrasound contrast agents	81
B4)	Vera Daeichin	Sub-to-ultra harmonic imaging of contrast agent at high frequency: In vitro characterization	83
B5)	Tamerlan Saidov	Fractal dimension of tumor microvasculature by CEUS: preliminary study in mice	85
B6)	Charles Tremblay	Ultrafast Doppler imaging of microbubbles	90
B7)	Nikita Reznik	Investigation of acoustic properties of vaporized submicron perfluorocarbon droplets	93
B8)	Fumiko Ueki	Molecular dynamics study on inclination change of molecules forming the surface membrane of an insonified coated microbubble	97

Wednesday–Friday POSTER SESSION C: NEW DIRECTIONS *Election by the audience*

C1)	Radwa Abou-Saleh	Microfluidic production and nanomechanics of therapeutic microbubbles for targeted drug delivery	99
C2)	Guillaume Lajoie	New production method for a nanoscale phase change contrast microbubbles	100
C3)	Brahman Dharmarajah	Assessment of carotid plaque perfusion and ulceration with dynamic contrast enhanced ultrasound	102
C4)	Anna Bjällmark	Three modality contrast imaging using multi-functionalized microbubbles - Achievements so far in the FP7-NMP project 3MiCRON (245575)	105
C5)	Shashank Sirsi	Polyplex-microbubble hybrids for ultrasound-guided plasmid DNA delivery to solid tumors	108
C6)	Caroline Harfield	Investigating the potential of microbubble contrast agents as biosensors	110
C7)	Joshua Owen	Magnetic targeting of microbubbles at physiologically relevant flow rates	112
C8)	Yann Desailly	Ultrasound super-localization (USL)	114
C9)	Carmel Moran	The acoustic properties of different size-populations of microbubbles from 12 - 43 MHz	116
C10)	Nicola Ingram	Improving drug uptake by sonoporation using chirp excitation of polydispersed microbubbles	119
C11)	Ilya Skachkov	Ultrasound contrast agents mediated cell labeling for MRI tracking	121

18th EUROPEAN SYMPOSIUM ON ULTRASOUND CONTRAST IMAGING
17-18 JANUARY 2013, Rotterdam, The Netherlands

FRIDAY, 18 January 2013

Oral program

09.00 – 10.30	INDIVIDUAL BUBBLES <i>Chairpersons: Michel Versluis / Ayache Bouakaz</i>	
Kausik Sarkar	Modeling contrast microbubbles: From echocardiography to noninvasive blood pressure monitoring and targeted drug delivery.....	124
Michel Versluis	Brandaris 128 ultra-high-speed imaging facility: 10 years of operation, updates, and enhanced features.....	125
Guillaume Renaud	Sensing subharmonic volume variations of single contrast agent microbubbles in response to ultrasound with an "acoustical camera".....	126
Tom Kokhuis	Dynamics of StemBells in an ultrasound field.....	129
Brandon Helfield	The effect of boundary proximity on the frequency of maximum response and nonlinear emissions of individual microbubbles in the 4 to 13.5 MHz range.....	132
10.30 – 11.00	Intermission	
11.00 – 12.30	MOLECULAR IMAGING and THERAPY <i>Chairpersons: Stuart Foster / Fuminori Moriyasu</i>	
Stuart Foster	Ultrasound contrast and molecular imaging in small animals.....	134
Alexander Klibanov	Molecular imaging in humans: Ultrasound in comparison with other imaging modalities.....	136
Liza Villanueva	Ultrasound-targeted microbubble destruction to deliver siRNA cancer therapy.....	139
Richard Browning	DNA loaded albumin microbubbles for ultrasound & microbubble mediated gene transfection in vivo.....	140
Klazina Kooiman	The optimal lipid coating for therapeutic bubbles.....	144
12.30 – 14.00	LUNCH	
14.00 – 14.30	Dutch Heart Foundation lecture <i>Chairperson: Peter Burns</i>	
Sharon Mulvagh	Cardio perfusion imaging.....	148
14.30 – 16.00	COMPETITION: THERAPEUTIC USE OF MICROBUBBLES ... <i>Chairpersons: Nico de Jong / Tom Porter</i>	
Jean-Michel Escoffre	In-vivo irinotecan delivery using microbubble-mediated ultrasound into subcutaneous glioblastoma tumors.....	152
Ine de Cock	Real-time imaging of sonoporation in ultrasound mediated drug delivery.....	155
Noboru Sasaki	Contrast enhanced ultrasound image-guided cisplatin delivery -an in vivo feasibility study.....	158
Heleen Dewitte	The bubble breakthrough in cancer immunotherapy.....	160
Ying Luan	Time-resolved ultrasound-triggered release from a liposome-loaded microbubble.....	164
Oleksandr Shpak	Ultrafast dynamics of the acoustic vaporization of phase-change droplets.....	167
16.00 – 16.10	DISCUSSION AND CONCLUSIONS	
16.10	ADJOURN AND ANNOUNCEMENT OF THE WINNERS OF THE COMPETITION AND POSTER PRIZES	

SPONSORS

FIRST ANNOUNCEMENT 2014.....

The Phoenix trial, diagnosis of coronary artery disease using contrast perfusion imaging

Paolo Colonna¹, Roxy Senior², Jaroslaw Kasprzak³, Luciano Agati⁴, Klaus Tiemann⁵, Harald Becher⁶, Folker Ten Cate⁷ for the PHOENIX (A PHase III study Of Myocardial SonoVue[®] ENanced Echocardiography In Patients with Coronary Artery Disease, using X-Ray Coronary Angiography as Gold Standard) trial investigators

¹Hosp Policlinico of Bari, Bari, Italy

²Royal Brompton Hosp & Northwick Park Hosp, London, Harrow, United Kingdom

³Biegański Regional Specialty Hosp, Lodz, Poland

⁴Sapienza University of Rome, Rome, Italy

⁵University of Munster, Munster, Germany

⁶ABACUS Mazankowski Alberta Heart Inst, Alberta, AB, Canada

⁷Erasmus Medical Center, Rotterdam, the Netherlands

Background

Small-scale studies have shown that myocardial perfusion assessed by SonoVue (sulphur hexafluoride microbubbles)-enhanced myocardial contrast echocardiography (MCE) is a viable alternative technique to single-photon-emission tomography (SPECT) for assessment of coronary artery disease (CAD). The large multicentre study PHOENIX (A PHase III study Of Myocardial SonoVue[®] ENanced Echocardiography In Patients with Coronary Artery Disease, using X-Ray Coronary Angiography as Gold Standard) assessed the diagnostic value of these techniques for CAD detection compared to invasive coronary angiography (CA).

Methods

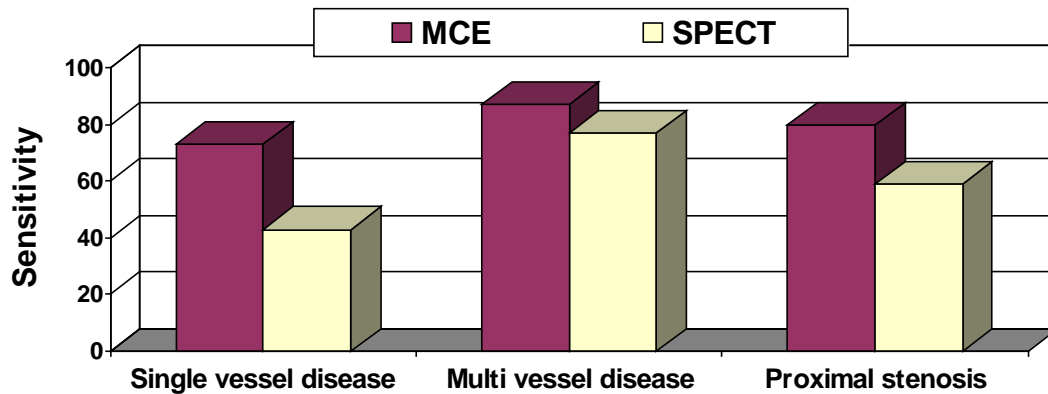
From 34 European centers 630 patients presenting with chest pain underwent rest/vasodilator stress SonoVue-enhanced MCE, 99mTc ECG-gated SPECT and CA within a one-month period. MCE was performed in real time and using end-systolic post-flash frames for ≥ 8 cardiac cycles. SPECT was acquired as standard. Three independent off-site blinded readers for MCE and 3 for SPECT graded myocardial perfusion by segment (17-segment model) based on the difference between corresponding rest and stress results. The results from the 3 readers were collapsed into one diagnosis per patient per technique. Quantitative CA was assessed at a centralized off-site laboratory.

Clinical characteristics

Males: 73%; mean age: 64 yrs; 75% hypertensive; 71% hyperlipedemic; 27% diabetic, 25% previous AMI, 31% previous PCI) enrolled 516 underwent all three examinations. Of these, 161 (31.2%) had $\geq 70\%$ stenosis at CA (131: single vessel disease; 30: multi-vessel disease).

Results

Significantly higher sensitivity was obtained on MCE vs SPECT (75.2% vs 52.4%; $P < 0.0001$) although specificity was lower (52.4% vs 80.6%; $P < 0.0001$), reflecting the high prevalence of co-existing cardiovascular morbidity. Similar sensitivity/specificity values for MCE and SPECT were obtained in patients with no history of AMI (66%/57.3% and 44.3%/83.2%, respectively). Sensitivity for the detection of single and multi-vessel disease was also higher for MCE (73% and 87%) vs SPECT (43% and 77%).



Conclusions

Sensitivity of MCE was superior to SPECT for detection of CAD. Lower specificity on MCE was likely due to the high prevalence of co-existing cardiovascular morbidity. Lack of radiation exposure, wider availability and superior sensitivity makes MCE a suitable first-line diagnostic procedure compared to SPECT in this patient group.

Comparison of sulfur hexafluoride microbubble(SonoVue)-enhanced myocardial echocardiography to single photon emission computerized tomography at rest and vasodilator stress in the assessment of significant coronary artery disease: A large European multicentre study

Roxy Senior, Jaroslaw Kasprzak, Antonella Moreo, Nicola Gaibazzi, Luciano Agati, Klaus Tiemann, Bharati Shivalkar, Stephan von Bardeleben, Leonarda Rosaria Galiuto, Herve Lardoux, Giuseppe Trocino, Ignasi Carrio, Dominique Le Guludec, Gianmario Sambuceti, Harald Becher, Paolo Colonna, Folker Ten Cate, Ezio Bramucci, Ariel Cohen, Gianpolo Bezante and Costantina Aggeli

Background

Single centre studies have shown that myocardial perfusion assessed by SonoVue (sulphur hexafluoride microbubbles)-enhanced myocardial contrast echocardiography (MCE) is an alternate technique to single-photon-emission tomography (SPECT) for assessment of coronary artery disease (CAD). Our large multicentre study assessed the diagnostic value of these techniques for CAD detection compared to invasive coronary angiography (CA).

Methods and results

Patients presenting with chest pain at 34 European centers underwent rest/vasodilator stress SonoVue-enhanced MCE, ^{99m}Tc ECG-gated SPECT and CA within a one-month period. MCE was performed in real time and using end-systolic post-flash frames for ≥ 8 cardiac cycles. SPECT was acquired as standard. Three independent off-site blinded readers for MCE and 3 for SPECT graded myocardial perfusion by segment (17-segment model) based on the difference between corresponding rest and stress results. The results from the 3 readers were collapsed into one diagnosis per patient per technique. Quantitative CA was assessed at a centralized off-site laboratory.

Of the 630 patients (males: 73%; mean age: 64 yrs; 75% hypertensive; 71% hyperlipedemic; 27% diabetic, 25% previous AMI, 31% previous PCI) enrolled 516 underwent all three examinations. Of these, 161 (31.2%) had $\geq 70\%$ stenosis at CA (131: single vessel disease; 30: multi-vessel disease). Significantly higher sensitivity was obtained on MCE vs SPECT (75.2% vs 52.4%; $P < 0.0001$) although specificity was lower (52.4% vs 80.6%; $P < 0.0001$), reflecting the high prevalence of co-existing cardiovascular morbidity. Similar sensitivity/specificity values for MCE and SPECT were obtained in patients with no history of AMI (66%/57.3% and 44.3%/83.2%, respectively). Sensitivity for the detection of single and multi-vessel disease was also higher for MCE (73% and 87%) vs SPECT (43% and 77%).

Conclusions

Sensitivity of MCE was superior to SPECT for detection of CAD. Lower specificity on MCE was likely due to the high prevalence of co-existing cardiovascular morbidity. Lack of radiation exposure, wider availability and superior sensitivity makes MCE a suitable first-line diagnostic procedure compared to SPECT in this patient group.

Fast contrast imaging

Peter N. Burns

University of Toronto and Sunnybrook Research Institute, Toronto, Canada



New insights into uteroplacental perfusion: Quantitative analysis using Doppler and contrast-enhanced ultrasound imaging

*Chloé Arthuis^{1,2}, Anthony Novell¹, Jean-Michel Escoffre¹, Frédéric Patat^{1,3},
Ayache Bouakaz¹, Franck Perrotin^{1,2}*

¹UMR Inserm U 930, University François-Rabelais Tours, 10 bd ter Tonnellé, 37032 Tours Cedex 1, France

²Department of Obstetrics and Gynecology CHRU Tours, 2 bd Tonnellé, 37044 Tours Cedex 9, France

³Inserm CIC-IT 806, CHRU Tours, 2 bd Tonnellé, 37044 Tours Cedex 9, France

Introduction

During pregnancy, several complications, such as intrauterine growth restriction, gestational hypertension and preeclampsia, are associated with such a reduction in uteroplacental blood flow and are major causes of maternal and fetal morbidity and mortality. The use of Doppler ultrasound to assess uteroplacental blood flow is currently the reference method for the clinical management of high-risk pregnancies. Unfortunately, both uterine and umbilical artery Doppler measurements are only indirect parameters of placental vascular development, and their application as screening tools for intrauterine growth restriction, preeclampsia and perinatal death remains controversial. In obstetrics, contrast-enhanced ultrasound (CEUS) offers a new opportunity to monitor the uteroplacental circulation and quantify the intervillous space flow velocity.

Objective

To monitor and quantify uteroplacental perfusion in rat pregnancies by Doppler ultrasound and CEUS.

Methods

Fourteen rats were randomized in two groups (the CEUS group and the control group). On days 8, 11, 14, 17, 19 and 20 of gestation, we used DUS to measure the resistance index (RI), pulsatility index and blood velocity in the uterine, arcuate and umbilical arteries in both groups. On days 14, 17 and 20, one group was also examined by CEUS. Quantitative perfusion parameters were calculated in 4 compartments (mesometrial triangle, placenta, umbilical cord and fetus) and compared.

Results and discussion

The Doppler ultrasound measurement showed that the RI of the uterine and arcuate arteries decreased ($p < 0.01$) from day 14 to day 17, while velocity increased each of these arteries ($p < 0.01$ and $p < 0.05$, respectively). Quantification of uteroplacental perfusion by CEUS in bolus mode revealed that blood volume and local blood flow increased from day 14 to day 20 in the mesometrial triangle ($p < 0.01$) and

the placenta ($p < 0.05$). In the CEUS destruction-replenishment mode, the perfusion parameters showed trends similar to those observed in bolus mode. No microbubbles were detected in the umbilical vein or fetal compartments. The weights of pups in the two groups did not differ significantly. These results showed that MM1[®] for contrast ultrasound imaging is a noninvasive and safe method in rats.

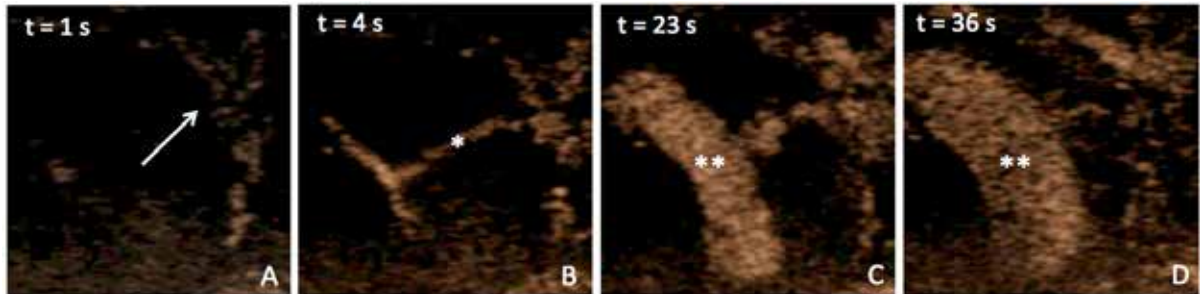


Figure 1: Monitoring of contrast agents in the uteroplacental unit by CEUS on the 17th gestational day.

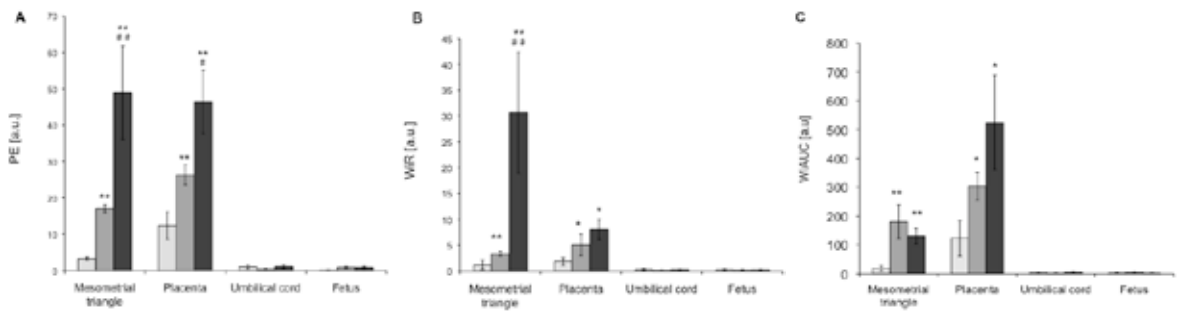


Figure 2: Quantitative analysis of uteroplacental perfusion by CEUS in bolus mode on the 14th, 17th and 20th gestational day.

Conclusions

CEUS estimates of placental perfusion complement the data provided by Doppler ultrasound. Noninvasive quantification of low-velocity placental microcirculation by CEUS could be helpful in managing placental insufficiency in human pregnancies.

New rat hindlimb model of microvascular no-reflow to evaluate treatment of microvascular obstruction with long tone burst sonothrombolysis

John Pacella, Judith Brands, Xucai Chen, Frederick Schnatz, Jianjun Wang, Linda Lavery, and Flordeliza Villanueva

*Center for Ultrasound Molecular Imaging and Therapeutics
University of Pittsburgh, Pittsburgh, PA*

Background

Despite successful reperfusion by percutaneous coronary intervention (PCI) during acute myocardial infarction (AMI), microembolization of thrombotic debris distally into the microcirculation contributes to the no-reflow phenomenon and limits myocardial salvage. Current therapies, which target platelets and microvascular tone are ineffective, as up to 40% of patients exhibit poor microvascular perfusion even after patency of the infarct artery has been established (1). Ultrasound (US)-microbubble (MB)-induced thrombolysis, or sonothrombolysis, is a potentially attractive approach to treating no-reflow because it can be used to not only identify the defective areas of perfusion but also to induce microbubble oscillations in the vicinity of the microvascular thrombus to restore perfusion.

To date, evidence that sonothrombolysis mitigates microvascular no-reflow has been limited. While it was shown in porcine models of AMI that US + MB recanalized the infarct artery 53% of the time, even when the infarct artery remained occluded after treatment, microvascular perfusion still improved in many cases (2), suggesting a separate effect of US + MB on the microcirculation itself. These data suggest that the independent effects of sonothrombolytic regimens on the microcirculation in the setting of AMI warrant further study, necessitating experimental models that isolate the interactions between MB, US, and the microcirculation. To this end, we previously developed an *in vitro* model of microvascular thromboembolism and demonstrated the efficacy of long tone burst sonothrombolysis (3). The purpose of the present study was twofold: (1) To develop an *in vivo* experimental model of microvascular thromboembolism to allow evaluation of sonothrombolytic regimens specifically on the microcirculation; and (2) to use this new *in vivo* model to demonstrate primary efficacy of sonothrombolysis for treating microvascular no-reflow caused by microembolism.

Methods

A rat hindlimb model of microvascular embolization was developed. Anesthetized rats underwent degloving of the left hindlimb. The experimental preparation is shown in **Figure 1**. The rat was placed in the right lateral position and an US imaging probe (15L8, Sequoia 512, Siemens) was positioned just anterior to the left hindlimb to horizontally scan the long axis plane of the left hind limb muscle.

A single element treatment transducer was positioned vertically just above the hindlimb, orthogonal to and centered within the beam of the imaging probe. Microclots were prepared from porcine blood by successively forcing blood clots through smaller needle bores down to 30 g, and then passing the clots through a 200 μm pore filter. The filtered microclots (range 15-100 μm , mean of 30 μm) were drawn into a syringe for later injection.

Baseline destruction-replenishment US contrast imaging (7 MHz, CPS, Sequoia) of the hindlimb was performed during a continuous infusion of lipid MB via the right internal jugular vein. For microclot administration into the left hindlimb, a catheter was advanced into the right iliac artery via the contralateral (right) femoral artery. Microclots were administered through this catheter in 0.5 cc increments to cause a persistent reduction of at least 50% in left hindlimb muscle perfusion, as

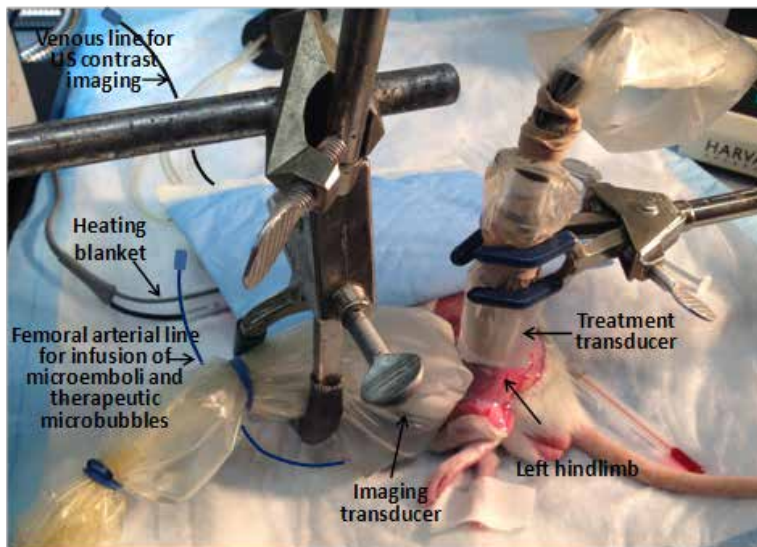


Figure 1. Experimental model for microembolization of left rat hindlimb and image-guided sonothrombolysis

measured by contrast US performed immediately and 10 minutes after clot injection.

After confirmation of stable hypoperfusion of the hindlimb muscle by contrast ultrasound perfusion imaging performed 10 minutes after microembolization, US treatment was applied for 10-30 minutes with the single element transducer (1.5 MPa, 5000 cycles per tone burst, 3

seconds pulsing interval) during a continuous infusion of lipid MB via the femoral artery catheter (n=5 rats). In 2 control rats, microembolization was performed, but no treatment US and MB were given. Contrast enhanced US imaging of the hindlimb muscle was performed every ten minutes until the conclusion of the experiment.

US perfusion images were analyzed off line. Regions of interest were drawn to encompass the hindlimb muscle microcirculation, and videointensity (dB) time data were fit to the exponential function $y=A(1-e^{-\beta t})$ where y = videointensity, A =plateau videointensity (proportional to blood volume), β =slope (proportional to velocity), and the product of $A \times \beta$ = perfusion rate.

Results

Injection of a range of 0.5 to 3.0 cc of thrombotic material successfully produced stable hindlimb muscle hypoperfusion. Contrast enhanced US imaging of the muscle demonstrated a 65% reduction in perfusion ($A \times \beta$ from 6.73 ± 1.78 to 1.97 ± 0.92 dB/sec, $p=0.057$) after embolization of clot material into the hindlimb microcirculation. In the 5 rats receiving treatment US + MB, perfusion increased three-fold and was restored to baseline ($A \times \beta$ from 1.97 ± 0.92 to 6.82 ± 0.62 dB/sec, $p<0.001$). In the 2 control rats receiving microembolization only, there was no significant improvement in hindlimb perfusion during contrast US imaging performed up to 30 minutes after injection of the clots. The upper panels in **Figure 2** demonstrate images from a rat at baseline, 10 minutes after microembolization, and 10 minutes after treatment US + MB. The lower panels are from a microembolized but untreated control rat at the same time points: baseline and 10 and 20 minutes after microembolization.

Conclusions

We have developed an *in vivo* model to simulate the phenomenon of distal microembolization such as occurs after primary PCI in AMI. This model allows isolated evaluation of the effects of US and MB specifically on microvascular thromboembolism, affording opportunities to study various sonothrombolytic regimens in a physiologically and clinically relevant setting. Our preliminary data thus far suggest that an acoustic regimen conferring inertial cavitation on circulating lipid MB has a therapeutic effect on microvascular perfusion, as similarly embolized hindlimbs in rats receiving no treatment US and MB remained persistently hypoperfused. Further studies using this new model are underway to assess other sonothrombolytic regimens as well as microvascular-specific effects of sonothrombolysis on endothelial phenotype.

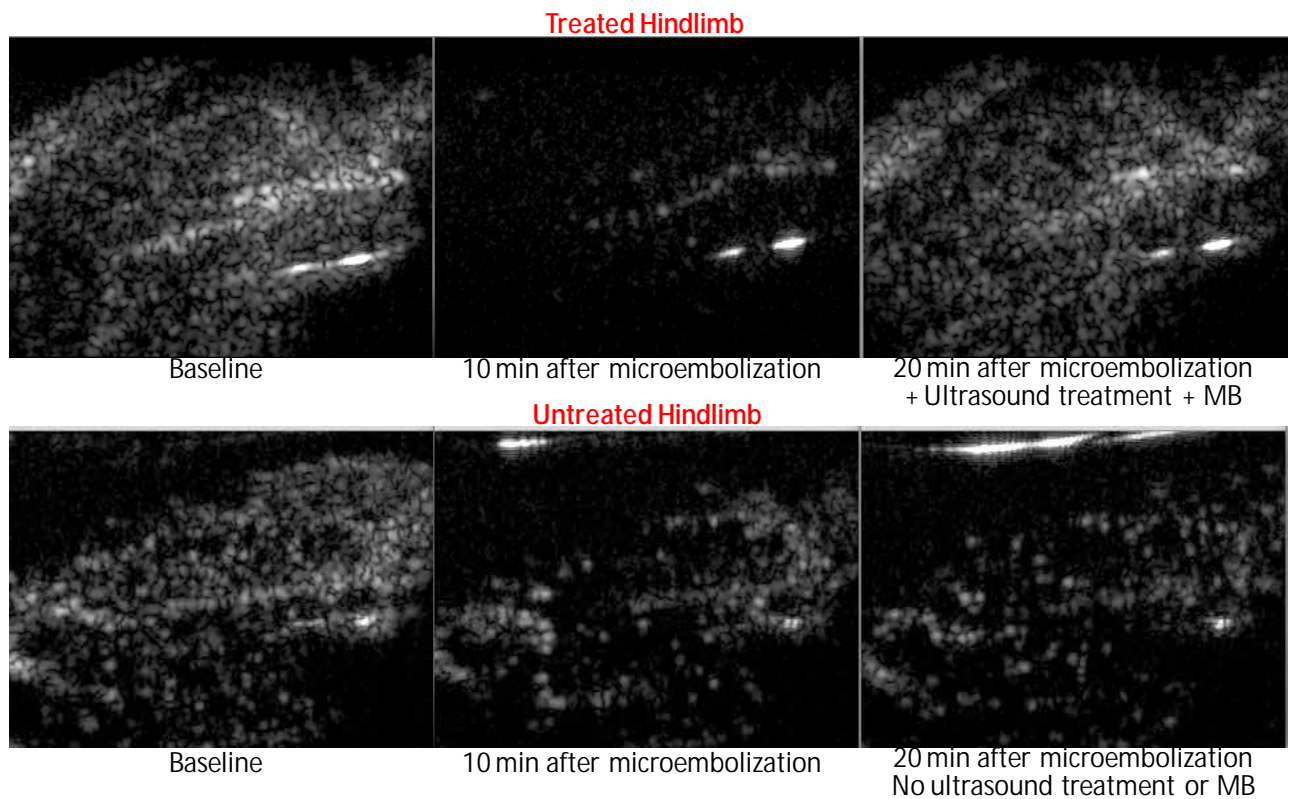


Figure 2. Contrast enhanced ultrasound perfusion images of rat hindlimb at baseline (left panels), 10 min after microembolization (middle panels) and 20 min after microembolization (right panels). In the upper panels, 10 min after microembolization, microbubbles + ultrasound treatment were delivered for another 10 min, resulting in restoration of hindlimb perfusion. In the lower panels, no treatment was administered, and the hindlimb remained hypoperfused. MB = microbubbles

References

1. Ito H, Okamura A, Iwakura K, Masuyama T, Hori M, Takiuchi S, Negoro S, Nakatsuchi Y, Taniyama Y, Higashino Y, Fujii K, Minamino T. Myocardial perfusion patterns related to thrombolysis in myocardial infarction perfusion grades after coronary angioplasty in patients with acute anterior wall myocardial infarction. *Circulation*. 1996; 93: 1993–1999.
2. Xie F, Lof J, Matsnaga T, Zutshi R, Porter TR. Diagnostic ultrasound combined with glycoprotein IIb/IIIa-targeted microbubbles improves microvascular recovery after acute coronary thrombotic occlusions. *Circulation*. 2009; 119: 1378–1385.
3. Leeman JE, Kim JS, Yu F, Chen X, Kim K, Wang J, Chen X, Villanueva FS, Pacella JJ. Effect of Acoustic Conditions on Microbubble-Mediated Microvascular Sonothrombolysis. *Ultrasound Med Biol*. 2012;38: 1589-1598.

Diagnostic performance of contrast-enhanced ultrasound versus computed tomography in detection of liver metastases in patients suspected for pancreatic- or periampullary cancer

P. Taimr, V.L. Jongerius, C.J. Pek, N.C. Krak, B.E. Hansen, H.L.A. Janssen, C.H.J. van Eijck

Aim

The aim of the study was to evaluate diagnostic performance of contrast-enhanced ultrasonography (CEUS) in detection of liver metastases in patients suspected for pancreatic or periampullary cancer. Liver CT alone is often not enough for metastases detection and surgeons frequently encounter unexpected liver lesions during pancreas resection. Surgery will not improve survival prognosis if liver metastases were already present. So far no study has evaluated the performance of liver CEUS in patients suspected for pancreatic cancer.

Methods

Single centre, prospective and comparative study. Total 111 patients were enrolled, but 13 did not fulfill all inclusion criteria. The final group consisted of 98 patients suspected for pancreatic or periampullary cancer. Every patient underwent abdominal CT and CEUS (Hitachi, Japan; Sonovue, Italy) blinded to CT result. Final diagnosis consists of a combination of clinical information, imaging, biopsy if necessary and second CT exam 3 months later.

Results

At least one liver metastasis was found in 15 patients (15/98). From the 17 patients who were suspected having liver metastases on CT scan, there were 11 confirmed. In another 4 patients with finally diagnosed metastasis no malignant focal lesion was suspected on CT. Sensitivity was 73.3% (11/15), the specificity was 92.7% (77/83), PPV 64.7% (11/17) and NPV was 95.1% (77/81). On CEUS 13 patients (13/98) were suggested as having liver metastases and from these 12 were proven. One liver focal non-steatosis was inaccurately suspected as a metastasis. Three patients with metastases were undetected by CEUS. Sensitivity of CEUS in diagnosis of pancreas tumour metastasis was 80% (12/15) and specificity 98.8% (82/83), PPV 92.3% (12/13) and NPV 96.4% (82/85).

Conclusion

Contrast-enhanced ultrasound has a comparable diagnostic performance as CT for the detection of liver metastasis in patients suspected for pancreatic or periampullary cancer and can serve as an additional screening method during preoperative evaluation.

Applications of CEUS for therapy

***Professor Edward Leen, MD, FRCR
Professor of Radiology***

*Clinical Lead for Ablative Therapy Service ICNHT, Imperial College London,
Hammersmith Hospital Campus, London*

The advent of several novel therapies targeting tumour angiogenesis and vascularity used clinically over the last decade has highlighted the need for more accurate and reproducible quantitative techniques to assess more subtle alteration in tumoral vascularity. Imaging modalities such as CT, MRI and positron emission tomography (PET) have been used to assess perfusion changes in monitoring anti-vascular therapies in cancer patients. However all these modalities have disadvantages such as invasiveness, availability and costs which may limit their application into routine clinical practice. With hundreds of oncology therapeutics in current and future development, assessment of early response has invariably proved to be disappointing to date as compared with the pre-clinical animal studies.

Traditional medical imaging techniques, such as dynamic contrast-enhanced computerized tomography (CT), magnetic resonance imaging (MRI), and ultrasound (US), have been used routinely to monitor the therapeutic effects of cancer intervention. Current assessment of response using these conventional methods is purely based on interval evaluation of the tumour sizes using the Response Evaluation Criteria In Solid Tumours (RECIST) (3). However as anti-angiogenic or anti-vascular therapies are predominantly cytostatic, current criteria for monitoring response are clearly inadequate as they reflect only late changes and are unable to identify non-responders at an early time-point (4). In addition, the development of vascular-targeted agents and their clinical usage are also costly; hence accurate, reproducible and non-invasive imaging methods of assessing their effectiveness at an earlier stage are required.

In recent years novel ablative therapies such as Irreversible and reversible electroporation as well as combined with chemotherapy - electrochemotherapy have been under clinical trials. Assessment of their response using imaging are as yet not clearly defined.

In this presentation the use and value of microbubble ultrasound contrast enhanced ultrasound in assessing response and guiding clinical management will be discussed.

Taking advantage of a high spatial resolution contrast mode in the detection of liver metastases: Impact of small liver metastases in different primary malignancies: First results

Weskott HP¹, Höpfner M², Böhm CB¹

¹*Central Ultrasound Dept., Klinikum Siloah, KRH, Hannover, Germany*

²*Dept Gastroenterology, Rotes Kreuz Krankenhaus, Kassel, Germany*

Background

All liver metastases start out small as cellular emboli in arterial or portal venous blood. The chance to detect tiny lesions by using ultrasound depends either on differences in their acoustic properties when compared to the surrounding tissue or when using CEUS in the difference of the tumor vasculature compared to normal liver tissue perfusion. Detection of small metastases will depend on the spatial resolution of the CEUS mode applied.

Objective

Retrospective evaluation of size distribution of liver metastases of different primaries by analyzing digitally stored CEUS loops of the liver in a two center study.

Methods and patients

119 patients with 151 CEUS examinations were included. US basic examination prior and after CA administration of 1.2ml SonoVue[®] (Bracco, Milan, Italy) bolus injection in patients with metastatic liver disease. All patients were examined using the HIREs mode which is a pulse inversion mode at a frame rate about 26fps (LOGIQ E9, GE Healthcare, Milwaukee, IL, USA). All included patients were referred for CEUS examination with the intention to treat, or for staging /restaging purpose after chemotherapy or liver resection. Breast cancer (n=36), GI tract tumors (n=51), melanoma (n=18). Size distribution per patient was defined in four groups: Group 1: <5mm, group 2: 5.1-10mm, group 3: 10.1-20mm and group 4 >20mm. All CEUS examinations were stored digitally starting with the arterial phase, followed by slow sweeps during the PV and late phase in 2-3 scan planes.

Results

In 151 CEUS examinations including the follow up examinations (n=32) 1146 metastases were detected. Their size distribution per patient were: Group 1: 10.9%, 2: 34.3%, 3: 31.0%, 4: 25.2%. Patients with GI tract metastases (n=51 exams, 211 mets) showed the relatively largest metastases: Group 1: 4.8%, 2: 28.0%, 3: 28.5%, 4: 38.9%. Size distribution in breast cancer according to the four groups (n=36 exams, 512 mets): Group 1: 19.8%, 2: 45.9%, 3: 23.6%, 4: 12.9%.

Size distribution in melanoma groups (n=18 exams, 141mets): Group 1: 12.9%, 2: 32.5%, 3: 38.9%, 4: 14.6%. Using high resolution CEUS technique small metastases down to 3mm in size can be detected. The study showed that CEUS is capable to detect also small metastases accounting for 1/3 to 2/3 of all metastases below 10mm. Detection of especially small lesions is most important for planning treatment of metastatic tumor diseases. In patients with a high likelihood of small metastases high resolution CEUS should be performed as the first imaging technique.

Perfusion quantification: The known knowns, the known unknowns, and the unknown unknowns

Michalakis Averkiou

Department of Mechanical and Manufacturing Engineering, University of Cyprus, Nicosia, Cyprus

Imaging is a key factor in the accurate monitoring of response to cancer therapies targeting tumor vascularity to inhibit its growth and dissemination. Dynamic contrast enhanced ultrasound (DCE-US) is a relatively new quantitative method with the advantage of being non-invasive, widely available, portable, cost effective, highly sensitive and reproducible using microbubble contrast agents that are truly intravascular. Advances in nonlinear imaging techniques have enabled ultrasound imaging to visualize the macro- and micro-vasculature in real time. The image intensity of a region of interest (ROI) in the tumor is proportional to the microbubble concentration. Metrics of blood flow and blood volume may be extracted from indicator dilution models.

The present talk will concentrate on the bolus injection method for contrast delivery and the analysis of the wash-in and wash-out of the microbubbles in the ROI. Despite the continued research and excitement in this area, some 10 years after the introduction of real-time perfusion imaging we have still not succeeded in having the required tools and methods to raise perfusion quantification to widespread clinical use. There are many issues in this area that have been resolved, such as low MI imaging modes, extraction of linear/linearized data, and dealing with motion. There are also issues that have been identified and current research approaches are addressing them such the arterial input function, nonlinear imaging artifacts, and standardization and reproducibility. Finally, there are issues that may have not been fully revealed and understood such as tumor angiogenesis hemodynamics, tumor vasculature homogeneity, and the interaction of microbubbles with certain patient population.

A review of current work in this area will be presented and the issues described above will be discussed. Results from clinical trials with liver cancer patients undergoing vascular targeted therapies will be presented in an effort to better describe the above issues.

Prostate cancer imaging by DCE-US

M. Misch¹, M.P.J. Kuenen^{1,2}, T. Saidov¹, C. Heneweer³, H. Wijkstra^{1,2}

¹Eindhoven University of Technology, Electrical Engineering Dept, Eindhoven, the Netherlands

²Academic Medical Center, Urology Dept, University of Amsterdam, the Netherlands

³University Hospital Schleswig-Holstein, Radiology Dept, Kiel, Germany

Introduction

In the United States, prostate cancer (PCa) accounts for 29% and 9% of all cancer diagnoses and deaths in males, respectively [1]. Despite the availability of efficient focal therapies, their use is hampered by a lack of reliable imaging for PCa localization and therapy targeting. Contrast-ultrasound dispersion imaging (CUDI) has been proposed as a new alternative method for PCa localization based on dynamic contrast-enhanced ultrasound (DCE-US) data [2, 3]. Different from other DCE-US methods for cancer localization, invariably based on the assessment of blood perfusion, the intravascular dispersion of ultrasound contrast agents is directly influenced by the angiogenic changes that occur in the microvascular architecture feeding PCa. Angiogenic processes and microvascular changes play a fundamental role in cancer growth [4, 5]; their detection can therefore support with the assessment of cancer aggressiveness and, therefore, with therapy decision making [5].

With the aim of characterizing the microvascular architecture and detecting those changes due to cancer angiogenic processes, the analysis of the fractal dimension (FD) of the microvascular architecture, based on DCE-US data, is also evaluated [6]. Up until now, application of this method was invasive, requiring the analysis of immunohistological data [6]. Validation of CUDI and FD is performed in mice xenograft models by comparison with immunohistological (tomato-lectin FITC binding) [7]. Validation of CUDI is also performed in humans by comparison with histology results following radical prostatectomy.

Methodology

In patients, a 2.4-mL bolus of SonoVue® (Bracco, Milan, Italy) was injected intravenously, and its passage through the prostate was imaged by transrectal DCE-US. To this end, an iU22 scanner (Philips Healthcare, Bothell, WA) was employed. Data acquisition in patients was performed at the Academic Medical Center, University of Amsterdam (the Netherlands). In mice, 0.1-mL MicroMarker® Non-Targeted Contrast Agent Kit (VisualSonics, Toronto, Canada) was injected and imaged by a Vevo 2100 scanner (VisualSonics, Toronto, Canada). Data acquisition in mice was performed at the University Hospital Schleswig-Holstein (Kiel, Germany)

All the analyses proposed in this study require a time-intensity curve (TIC) to be measured at each pixel. For the implementation of CUDI, it can be shown that analysis of the spectral coherence [3] or temporal correlation [8] of TICs measured at neighbor pixels provides an estimate of a dispersion-related parameter. Here dispersion is well represented by the dispersion coefficient in the convective dispersion equation [2, 9]. The intravascular dispersion of the injected agent reflects the effect of multipath trajectories through the microvasculature, and can therefore be employed to characterize the microvascular architecture [10]. The obtained dispersion maps were compared on a pixel basis to the results obtained from histological analysis following radical prostatectomy. Figure 1 shows an example of dispersion maps obtained by CUDI coherence and correlation analysis. The corresponding histology result is also shown.

Validation in the mice xenograft models was performed by comparison with the microvascular density (MVD) estimated by assessment of the gray-scale intensity of 5- μm tumor slices treated with tomato-lectin staining and imaged by fluorescence microscopy (Axiovert, Zeiss, Germany). Two types of PCa cell lines, DU-145 and PC-3, were used for the mice xenograft models. In total, four DU-145 models and three PC-3 models were used.

In order to evaluate the ability of the FD to distinguish between different microvascular architectures, the regions defined by MVD and CUDI in the xenograft models were also investigated for their average FD. The FD was derived from peak intensity maps extracted from the obtained DCE-US data.

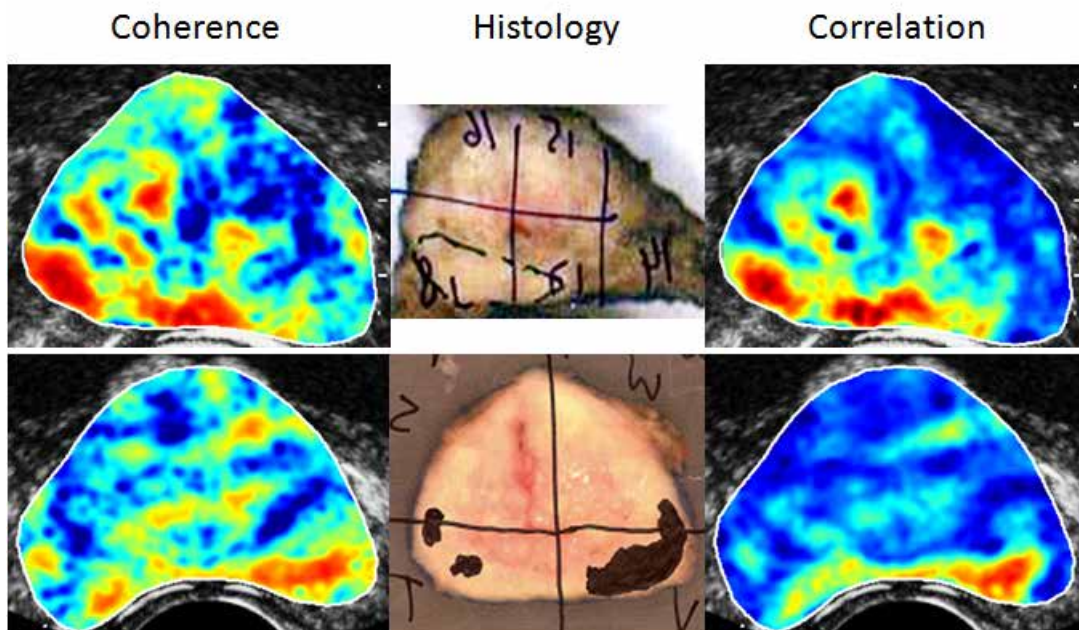


Figure 1. Dispersion maps by CUDI based on coherence (left) and correlation (right) analysis. The corresponding histology results are shown in the middle.

Results

In 10 patient datasets, the dispersion maps obtained by CUDI, both by coherence and by correlation, showed a good agreement at pixel level with the histology. In particular, CUDI outperformed all the other DCE-US maps based on perfusion assessment, such as peak intensity, wash-in rate, time to peak, area under the curve, and mean transit time.

CUDI was also the only imaging method that showed agreement with the immunohistological MVD assessment in the mice models, being able to distinguish between the different spatial distribution of the microvascular architecture in DC-145 and PC-3 ($p < 0.01$). In particular, DC-145 showed a hyper-vascular core as compared to the periphery of the tumor, while PC-3 showed a more homogenous vascularization within the tumor. The same conclusion could be drawn by estimation of the FD within the same regions ($p < 0.05$).

Conclusions

Our results, both in humans as well as in mice, are promising and motivate towards more extensive validation of CUDI for localization of PCa. The agreement between CUDI, MVD, and FD also suggest the ability of CUDI to characterize the microvascular architecture, possibly providing important opportunities for non-invasive cancer grading. In the future, once fully validated, CUDI could support targeting of biopsy and focal therapy.

References

1. *The American Cancer Society, Cancer Facts and Figures, 2012.*
2. M.P.J. Kuenen, M. Mischi, H. Wijkstra, "Contrast-ultrasound diffusion imaging for localization of prostate cancer," *IEEE Trans on Medical Imaging*, vol. 30(8), pp. 1493-1502, 2011.
3. M. Mischi, M.P.J. Kuenen, H. Wijkstra, "Angiogenesis imaging by spatiotemporal analysis of ultrasound-contrast-agent dispersion kinetics," *IEEE Trans on UFFC*, vol. 54(4), pp. 621-629, 2012.
4. N. Weidner, P.R. Carroll, J. Flax, W. Blumenfeld, and J. Folkman, "Tumor angiogenesis correlates with metastasis in invasive prostate carcinoma," *Am J Pathology*, vol. 143(2), pp. 401-409, 1993.
5. G. Russo, M. Mischi, W. Scheepens, J.J. De la Rosette, H. Wijkstra, "Angiogenesis in prostate cancer: onset, progression and imaging," *British J Urology International*, online preview, doi:10.1111/j.1464-410X.2012.11444.x.
6. J.H. van Beek, S.A. Roger, J.B. Bassingthwaite, "Regional myocardial flow heterogeneity explained with fractal networks," *Am J Physiol*, vol. 257, pp. 1670-1750, 1989.
7. T. Saidov, C. Heneweer, M.P.J. Kuenen, T. Liesebach, H. Wijkstra, M. Mischi, "Contrast ultrasound dispersion imaging of different tumor types," *IEEE IUS Proc, Dresden, Oct. 7-10, 2012.*
8. M.P.J. Kuenen, T. Saidov, H. Wijkstra, M. Mischi, "Spatiotemporal methods for prostate cancer detection by contrast ultrasound dispersion imaging," *IEEE IUS Proc, Dresden, Oct. 7-10, 2012.*
9. M. Mischi, "Contrast echocardiography for cardiac quantifications," *Ph.D. dissertation, Dept. of Electrical Engineering, Eindhoven University of Technology, 2004. Available online: <http://www.sps.ele.tue.nl/members/M.Mischi/PhDThesisMassimo.pdf>*
10. G.I. Taylor, "Dispersion of soluble matter in solvent flowing slowly through a tube," *Proc R Soc Lond*, vol. 219(1137), pp. 186-203, 1953.

The future of sonothrombolysis

Thomas R. Porter, MD

University of Nebraska Medical Center

In the presence of a commercially available intravenous microbubble infusion, animal studies have demonstrated that high mechanical index impulses from a modified diagnostic ultrasound transducer can produce thrombus dissolution. In acute myocardial infarction, rapid (within 30 minutes) epicardial recanalization of the infarct vessel has been achieved with this approach, using only low doses of fibrinolytic agents. Other in vivo studies have demonstrated that the guided high mechanical index impulses may be able to recanalize thrombosed vessels and/or mitigate microvascular no reflow, even in the absence of a lytic agent. A commercially available General Electric (GE) system (Vivid 9) is being modified in conjunction with GE Global Research to initiate the first clinical trial exploring the use of image guided sonothrombolysis to restore epicardial and microvascular flow in acute ST segment elevation myocardial infarction (STEMI) patients. Pre-clinical data with this system in atherosclerotic pigs sustaining an acute STEMI indicates that epicardial patency can be achieved within 30 minutes of treatment with a long pulse (20 usec) high mechanical index (1.2) impulse, which is delivered when microbubbles are visualized within the risk area. All pigs in this study received ½ dose tissue plasminogen activator (0.5 mg/kg over 30 minutes), combined with aspirin, Plavix, and heparin. MRI data obtained 48 hours post infarction indicated this approach prevents microvascular obstruction in addition to reducing infarct size. Clinical trials utilizing this modified GE system are expected to begin at the University of Sao Paulo in February 2013, and within the next six months at the VU Medical Center in Amsterdam.

The portability and safety of sonothrombolysis makes it an exciting new approach in the treatment of acute coronary syndromes and ischemic stroke. Beyond this, sonothrombolysis has the potential to be utilized in other clinically relevant pediatric and adult situations, such as treating catheter-related thrombi or graft and shunt thrombosis. In vitro and pre-clinical work is ongoing which will explore (a) the mechanism(s) for sonothrombolysis, and their relation to other ultrasound induced phenomena such as nitric oxide release and sonoporation; b) optimal ultrasound parameters for sonothrombolysis within the microvasculature, and how this may prevent microvascular obstruction; c) the development of optimal transducer design technology for sonothrombolysis (micromachined technology versus piezoelectric crystal); and d) the development of working groups which include the Food and Drug Administration (FDA), that will develop an Investigational Device Exemption exploring the safety, feasibility, complementarity, or potential superiority, of sonothrombolysis over emergent percutaneous catheter based interventions in treating acute coronary syndromes.

References

1. Xie F, Lof J, Matsunaga T, Zutshi R, Porter TR. Diagnostic ultrasound combined with glycoprotein IIb/IIIa – targeted microbubbles improves microvascular recovery after acute coronary thrombotic occlusions. *Circulation* 2009;119:1378-1385 .
2. Xie F, Lof J, Everbach C, He A, Bennett RM, Matsunaga T, Johanning J, Porter TR. Treatment of acute intravascular thrombi with diagnostic ultrasound and intravenous microbubbles. *J Am Coll Cardiol Img* 2009;2:511-518.
3. Leeman JE, Kim JS, Yu FT, Chen X, Kim K, Wang J, Chen X, Villaneuva FS, Pacella JJ. Effect of acoustic conditions on microbubble-mediated microvascular sonothrombolysis. *US Med Biol* 2012; 38:1589-98.
4. Slikkerveer J, Kleijn S, Appelman Y, Porter TR, Veen G, van Rossum AC, Kamp O. Ultrasound enhanced prehospital thrombolysis using microbubbles infusion in patients with acute ST segment elevation myocardial infarction: pilot of the sonolysis study. *US Med Biol* 2012; 38:247-52.

State-of-the-art: Pre-clinical and clinical diagnostic and therapeutic applications of contrast-enhanced ultrasound imaging: Vasa vasorum

*Steven B. Feinstein, MD, FACC, FESC
Professor of Medicine/Cardiology*

Rush University Medical Center, Chicago, Illinois, USA

Summary

2D/3D Contrast-enhanced vascular imaging of the carotid vasa vasorum provides insight and opportunities for diagnostic and therapeutic approaches of systemic inflammatory diseases; primarily atherosclerosis and diabetes. The presence and proliferation of arterial wall angiogenesis (vasa vasorum) are harbingers of localized and systemic inflammatory processes (hypoxia, oxidative stress, etc.). The evidence is recognized through pre-clinical and clinical observations. The results indicate these processes are directly associated with early atherosclerotic plaque development and, importantly, vulnerability. The development of newer imaging technologies (3D volumetric acquisition) permits direct visualization and quantification of adventitial vasa vasorum and intra-plaque neovascularization.

This presentation will review the state-of-the-art pre-clinical and clinical developments in the field of contrast-enhanced ultrasound (CEUS). The application of these novel approaches will impact clinical medicine and permit early identification and treatment of at-risk patients. Once clinically validated, the uses of CEUS may provide a method to non-invasively monitor therapeutic interventions including the therapeutic uses of CEUS for ultrasound-directed, site-specific therapies as vehicles for drug and gene delivery systems into the vulnerable plaque.

Therapeutic ultrasound

Stephen Meairs, M.D., Ph.D.

*Department of Neurology, University Hospital Mannheim,
University of Heidleberg, 68167 Mannheim, Germany*

The last several years have witnessed exciting new developments in the field of therapeutic ultrasound. Particularly promising are emerging applications for treatment of brain diseases. These applications have profited immensely from novel technologies enabling ultrasound to be focused through the skull. First clinical trials for treating essential tremor with therapeutic ultrasound have shown promising results. Microbubbles provide an important foundation for many applications of therapeutic ultrasound, as they enable ultrasound bioeffects to be localized to vessel walls. Targeted opening of the blood-brain barrier, for example, relies upon ultrasound combined with microbubbles.

This new technology will offer many new options for drug delivery to the central nervous system. To optimize this approach, further research into the mechanisms of BBB opening with ultrasound and microbubbles are warranted. A further promising application of therapeutic ultrasound is sonothrombolysis. Studies of both myocardial and cerebral infarction suggest that ultrasound combined with microbubbles can have profound effects upon the microcirculation. Indeed, in the absence of vessel recanalization outcome can be improved by sonothrombolysis of the microcirculation. Little is known regarding the molecular basis of this effect. Recent breakthroughs in the elucidation of stroke pathophysiology may help to explain how ultrasound and microbubbles may contribute to microcirculatory reflow.

Targeted gene therapy using lipoplex loaded microbubbles: Concept, mechanism and application

Ine Lentacker, Heleen Dewitte, Ine De Cock, Stefaan C. De Smedt

Ghent Research Group on Nanomedicine, Laboratory of General Biochemistry and Physical Pharmacy, Department of Pharmaceutical Sciences, Ghent University, Harelbekestraat 72, 9000 Ghent, Belgium

Several research groups have shown that microbubbles and ultrasound are a promising tool for targeted gene therapy. This presentation will give a short introduction on the use of microbubbles and ultrasound to induce gene therapy. More specifically, we will focus on the combined use of nanoparticles and echo contrast agents thereby giving an overview of the recent results we obtained using the concept of “lipoplex loaded microbubbles”. Genetic drugs like pDNA, siRNA or mRNA are pre-complexed in nanoparticles and subsequently attached to the microbubble shell. With live confocal microscopy we are currently studying how lipoplex loaded microbubbles are able to deliver gene complexes to target cells and induce gene expression. Finally, we will provide recent data showing that this concept could be particularly useful for ultrasound guided immunotherapy¹. Dendritic cells treated with mRNA containing lipoplex loaded microbubbles are able to express the encoded antigen and present it to T-cells thereby inducing a tumor specific cytotoxic T-cell response.

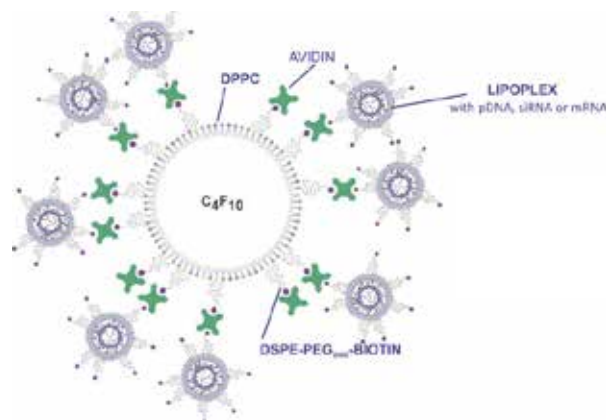


Figure 1: Schematic representation of lipoplex loaded microbubbles. Ultrasound induced microbubble implosion results in the release of intact gene complexes.

Acknowledgements

Heleen Dewitte and Ine De Cock are doctoral fellows of the institute for the Promotion of Innovation through Science and Technology in Flanders, Belgium (IWT-Vlaanderen). Ine Lentacker is a post-doctoral fellow of the Research Foundation Flanders, Belgium (FWO-Vlaanderen).

Reference

Biomaterials 2011, 32, 9128-9135.

High Intensity Focused Ultrasound (HIFU) for pancreas cancer treatment and efficacy evaluation using contrast ultrasound

Fuminori Moriyasu, M.D., Atsushi Sofuni, M.D., Takatomo Sano, M.D.

*Department of Gastroenterology & Hepatology, Tokyo Medical University,
6-7-1 Nishi-Shinjuku, Shinjuku, Tokyo, 160-0023, Japan*

Introduction

HIFU therapy is divided into two categories depending on modalities of image guidance; ultrasound guided HIFU and MRI guided HIFU. The advantage of MRI guidance is temperature monitoring of the ablation area. The advantage of US guidance is capability of real time monitoring and high spatial resolution. At the same time, efficacy evaluation can be performed using the same method as guidance, ultrasound imaging including contrast ultrasound (CEUS).

Severe complications provoked by HIFU therapy for pancreas cancer are perforation of the duodenum/stomach and bleeding from blood vessels, which are located surrounding the pancreas and shifting by respiratory and peristaltic motions. Therefore, accurate targeting and monitoring of HIFU exposure are important in case of HIFU therapy for pancreas cancer.

Aims & methods

We have evaluated the therapeutic effect of HIFU in inoperative pancreas cancer. At the same time the utility of ultrasound guidance and contrast ultrasound studies during and after HIFU treatment were evaluated. We treated pancreas cancer patients using HIFU therapy as combination therapy with systemic chemo / chemo-radiotherapy. This study took approval of the Ethic Committee of Tokyo Medical University Hospital. The HIFU device used was FEP-BY02 (China Medical Technologies Co.LTD., Beijing, China). The subjects were 30 patients, i.e. 16 cases in stage III, 14 cases in stage IV.

HIFU therapy was performed unanesthetized and conscious condition and the treatment was essentially divided into three days during one week. The lesion was targeted using ultrasound transducer installed at the center of the bowl shaped exposure transducer composed of 251 elements of 1 MHz in frequency. Contrast ultrasound (CEUS) was performed just after HIFU on each treatment day and further treatment was planned according to the CEUS findings.

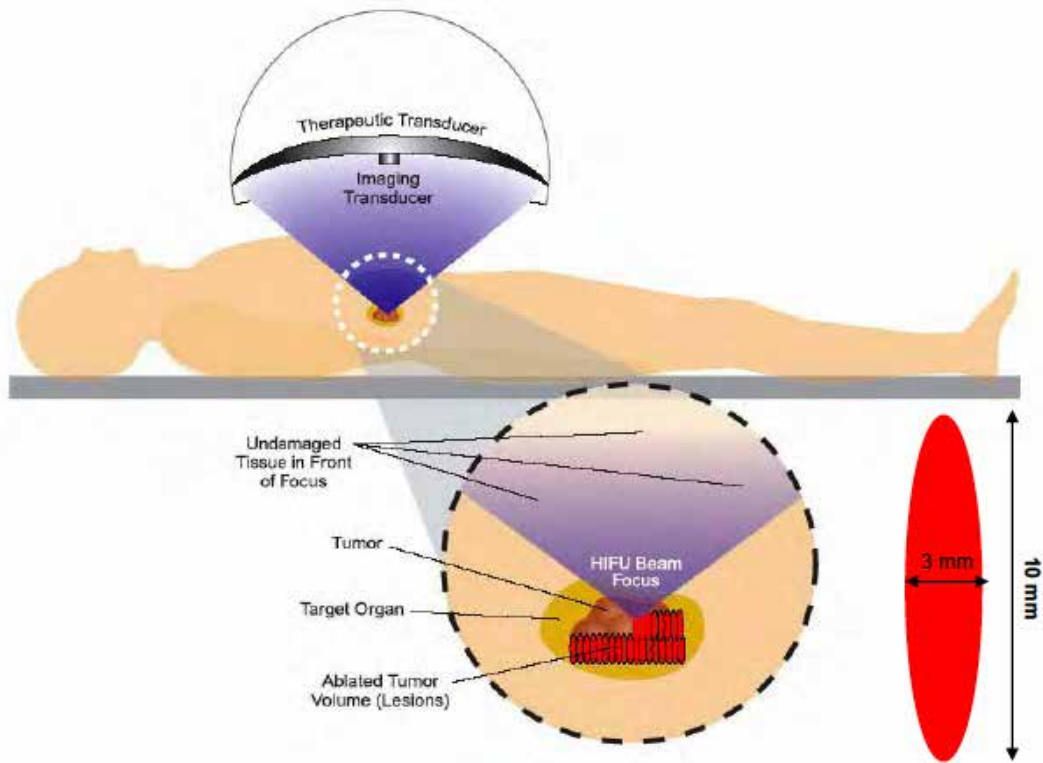


Figure 1: Schema of HIFU therapy. The focus of HIFU exposure is an oval in shape and is approximately 3 mm in diameter and 10 mm in length. Patented multielement array technology ensures an even acoustic field. 80° angle of convergence.

Results

Treatment data in Stage III and IV were as follows; mean tumor size was 31.8 vs 30.1 mm, mean treatment sessions: 2.6 vs 2.7 times, mean total treatment time: 2.7 vs 2.2 hours, mean total number of exposure shot: 2801 vs 1769, respectively. There was no significant difference in treatment data between two groups.

All pancreatic tumors were targeted by HIFU ultrasound monitor system. Echogenic changes of the tumor were observed during HIFU exposure. CEUS revealed the ablated area as hypo vascular or avascular areas after HIFU treatment.

The effects of HIFU therapy in Stage III and IV were as follows; the rate of complete tumor ablation was 87.5 vs 71.4%, the rate of symptom relief effect was 80 vs 56%, the effectiveness of primary lesion was CR:0, PR:2, SD:13, PD:1 vs CR:0, PR:2, SD:10, PD:2, primary disease control rate (DCR) more than SD was 93.8% vs 78.6%. Mean survival time (MST) after HIFU therapy was 14.1 vs 7.2 month, respectively ($p < 0.01$, $p = 0.0009$). Combination therapy of HIFU with chemotherapy in Stage III was

significantly better result than that of the historical control group; chemotherapy/ chemo-radiotherapy without HIFU (MST: 5.7month). There was found no severe adverse events accompanied by HIFU therapy.

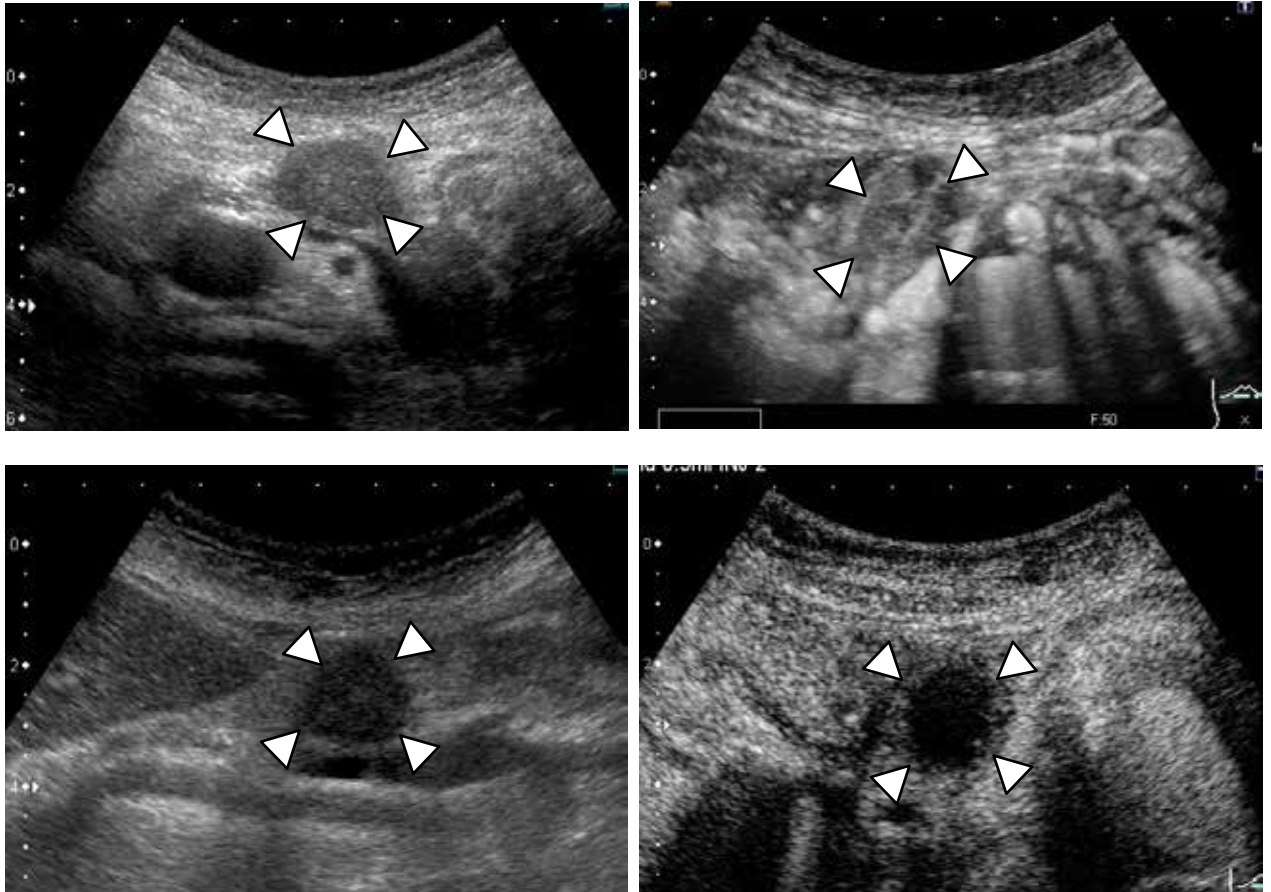


Figure 2: Ultrasound and CEUS of pancreas cancer treated with HIFU (arrow head). a: Fundamental B-mode image before HIFU. b: CEUS image before HIFU. c: B-mode after HIFU. d: CEUS after HIFU. The tumor changed avascular.

Conclusion

This study suggested that ultrasound guided HIFU therapy has the potential of effective therapy for advanced pancreas cancer. Ultrasound including CEUS is useful as an imaging modality assisting HIFU therapy.

Development concept and physicochemical characteristics of a phase shift formulation platform for ultrasound mediated drug delivery

P. Sontum, S. Kvale and A. Healey

Phoenix Solutions AS, Oslo, Norway

Introduction

Two basic dilemmas are often encountered with lipophilic drug molecules: due to their lipophilic nature they are difficult to present in a suitable, injectable formulation; and upon systemic administration they display an unacceptable safety profile at doses relevant for an effective treatment of the indicated pathology. For decades the pharmaceutical industry has tried to solve these problems by incorporating drugs in various kinds of carrier vehicles such as liposomes, nanoparticles and microbubbles, in formulations designed for specific delivery of the drug at the targeted pathology. Such approaches may offer ways to formulate lipophilic molecules and also to minimize systemic exposure/increase the bioavailability, improving the therapeutic index of the drug.

The current paper presents a novel approach to the resolution of these dilemmas: a microbubble-microdroplet formulation designed for ultrasound induced phase-shift.

A Phase-Shift Formulation for Ultrasound Mediated Drug Delivery - Concept

The conceptual idea behind the current approach is ultrasound mediated release of drug from a two component micro-particle system engineered to phase shift in a controlled manner. Drug is incorporated into low boiling point, micron sized oil droplets stabilized with a positively charged phospholipid membrane. Before administration, the drug loaded droplets are mixed with micron sized bubbles consisting of a low solubility perfluorocarbon gas core stabilized with a negatively charged phospholipid membrane. Upon mixing the formulation is designed to allow the formation of small clusters of micro-bubbles and oil droplets. After administration, when exposed to ultrasound (standard medical imaging frequency and intensity) *at the targeted pathology*, the micro-bubble transfers acoustic energy to the attached oil droplets and acts as a 'seed' for the oil to undergo a liquid-to-gas phase shift (vaporization). During this process it is postulated that the drug load will be presented to the surrounding matrix in its free molecular form. The resulting bubble undergoes a rapid expansion to approximately 30 μm and temporarily blocks the local capillary network, transiently stopping blood flow for typically 1 to 3 minutes, keeping the released drug at high concentration and close proximity to the target pathology. Further application of low frequency (0.2 – 2.0 MHz) ultrasound oscillates the bubbles and induces mechanisms that increase the local permeability of the vasculature, allowing for diffusion of the drug

into the tissue space. When the low frequency ultrasound desists the increase in permeability cessates, leaving the drug located (trapped) within the tissue compartment. Compared to the existing state of the art alternative approaches the proposed concept offers a number of unique attributes which may enhance clinical utility significantly;

- Greatly increased loading capacity as the concept utilizes the volume of the micro-particle and not the surface membrane only.
- Deposit properties, transiently trapping the drug within the targeted pathology and avoiding rapid wash out after release.
- Burst release of non-modified drug. No linker technology or chemical modification is necessary – solubility in oil phase is only criterion.

Clearly from a chemical, pharmaceutical, clinical and regulatory point of view this concept is extremely challenging. The ability to control in a reproducible manner the formation of bubble/droplet clusters of the right concentration and size, their stability both in-vivo and in-vitro, their (reproducible) ability to phase shift upon ultrasound activation, potential safety implications with “controlled micro-embolization” etc. are just a few of the potential pit-falls likely to be met with a complex system such as this.

So far the concept has been investigated for medical imaging purposes (i.e. without the incorporation of a drug in the oil phase). During our studies we have focused on understanding the physiochemical system as such; i.e. the formulation platform itself and the physical behaviour of the product in-vivo. Investigations performed under this initial pre-development program have included basic formulation and process studies such as choice of components (type of gas, oil, phospholipids and membrane surfactants), development of a commercial scale aseptic manufacturing process which enables control with droplet/ bubble size, as well as a preliminary optimization of bubble/droplet size and concentration. Primary responses for these studies have been cluster size and concentration measured using in-vitro analytical techniques such as Flow Particle Image Analysis (Sysmex FPIA 2100) and Coulter counting. In addition we have designed and built custom made apparatus for characterization of the activation process (activated bubble size and volume vs time), both in-vitro and in an ex-vivo dog model. When a suitable formulation had been chosen and the process had been proven reproducible, the physical concept was investigated in various models by ultrasound imaging techniques. Also, in order to understand and assess potential safety aspects several pre-clinical safety studies were performed.

Results

A suitable formulation was found in the combination of HEPS-Na stabilized PFB microbubbles (Component A) and phospholipid stabilized microdroplets of a perfluorated oil (Component B) (WO98/17324 and WO99/53963). The bubbles/droplets were formed by high-speed RS homogenization of the gas/oil into a dispersion of lipids followed by various fractionation steps to adjust size. The ability of the system to form bubble/droplet clusters upon mixing (reactivity) was adjusted by addition of various amounts of a cationic surfactant to the lipid membrane of the droplets. In the chosen formulation the volume concentration of microbubbles and microdroplets was set to 10 and 3 $\mu\text{l/ml}$, respectively, with an average size of approximately 1.5 to 2 μm . Typical results from Coulter and FPIA analysis are shown in Figure 1. As can be observed, upon mixing, the bubbles and droplets form a number of clusters in the 4-5 μm range, typically containing 2-8 individual units.

In order to investigate the activation step the total gas volume and bubble size was measured vs time after activation using a custom made sonomtery apparatus. Such analyses confirmed that upon ultrasound activation, a significant fraction of the droplets evaporate with a resulting transient population of bubbles in the size range 20-30 μm . The total volume fraction of gas in the activated system measurement cell increases for approximately 60s before slowly decreasing to pre-activation levels over some 10 minutes. Peak activated bubble volume was typically 300 $\mu\text{l}/\mu\text{l}$ of droplets.

During development more than 20 batches was manufactured aseptically and characterized with these in-vitro techniques. The consistency in selected performance attributes was quite good with cross batch RSDs for cluster and activated bubble size of less than 10% and RSDs for cluster number concentration and activated bubble volume of less than 20%.

In order to understand the clinical significance of the various quality attributes measured in-vitro, a DoE study was performed where the reactivity of the system was varied in a controlled manner through variations in the content of cationic surfactant added to the droplet membrane. 16 batches were produced and characterized and then used assessed for in-vivo performance in a dog model where the response was myocardial enhancement of the ultrasound signal after i.v. injection and activation of the product in the right ventricle. Results from this study are summarized in Figure 2. As can be observed the correlations between in-vitro determined quality attributes and in-vivo performance are reasonably precise, demonstrating their relevance of as predictors of in-vivo behaviour.

The activation process has also been characterized in an ex-vivo dog model where bubble size and concentration was determined in an extracorporeal measurement cell after i.v. injection and activation in the cardiac chamber. The schematics and results for the bubble size distribution are shown in Figure 3. Volume-weighted bubble diameters after *i.v.* injection measured at arterial conditions (normal

arterial blood gas saturation, hydrostatic pressure of 60 mmHg) had a mean diameter of 21.4 μm . The number of activated bubbles in a drug product dose of 10 $\mu\text{l/kg}$ given to an 18 kg dog was about 10 million, and the numerical concentration of bubbles in the myocardium at this dose was calculated to be about 3700/ml tissue.

The chosen formulation was tested in a number of pharmacology and toxicology studies (single and repeat dose in rats, rabbits and dogs at up to 1 ml/kg (100XACD for imaging)). Toxicology responses tested were body weights, histopathology, organ weights, clinical chemistry, haematology, BBB disruption, haemodynamics and CNS. With exception of some caecocolonic lesions in rats (common for USCAs in rats/mice) no significant adverse effects were observed. Blood half-life for the perfluorated oil component was approximately 60 minutes or more, with predominately liver clearance.

Conclusions

A microbubble/microdroplet formulation for controlled and reproducible, ultrasound induced phase shift has been developed. Methodologies for determination of quality attributes have been established and the relevance of these has been proven through correlations to in-vivo performance.

As a general platform for targeted delivery of lipophilic drugs the phase shift concept offers a number of unique attributes which may enhance clinical utility significantly over existing, alternative approaches. Studies to demonstrate this are under way.

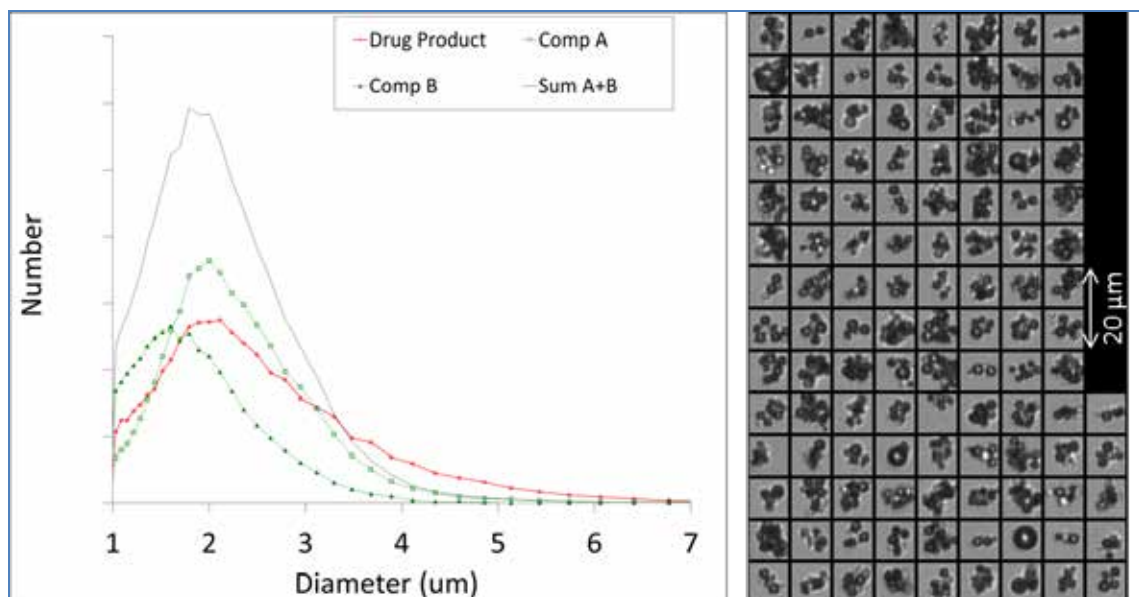


Figure 1: – Results from Coulter analysis (left) on Component A (bubbles), Component B (droplets) and Drug Product (Mix of Component A + Component B) compared to theoretical sum assuming no clustering. Results from FPIA analysis of bubble/droplet clusters in Drug Product (right).

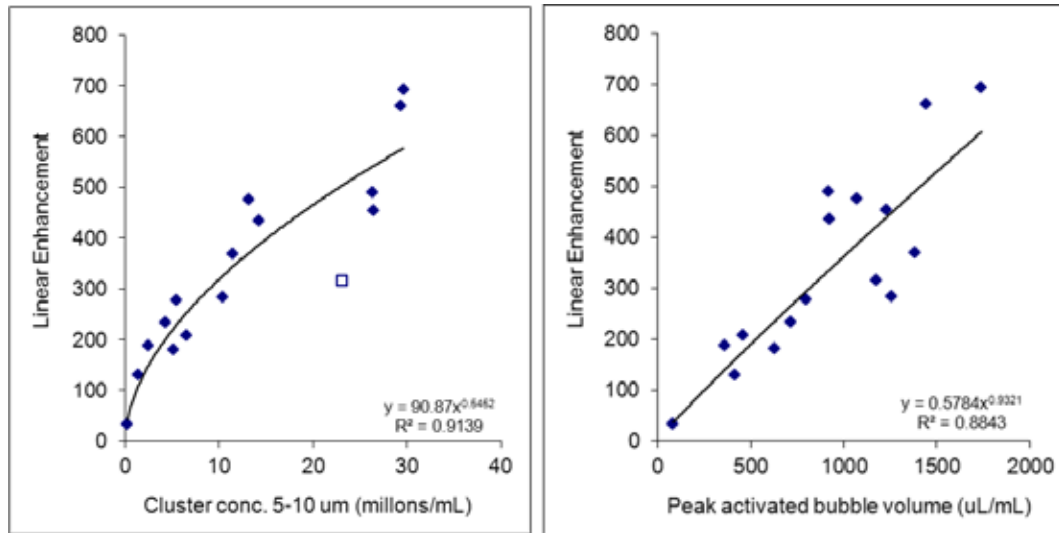


Figure 2 – Correlation between quality attributes determined in-vitro (cluster content between 5 and 10 µm and peak activated bubble volume per ml of drug product) and myocardial enhancement in dogs.

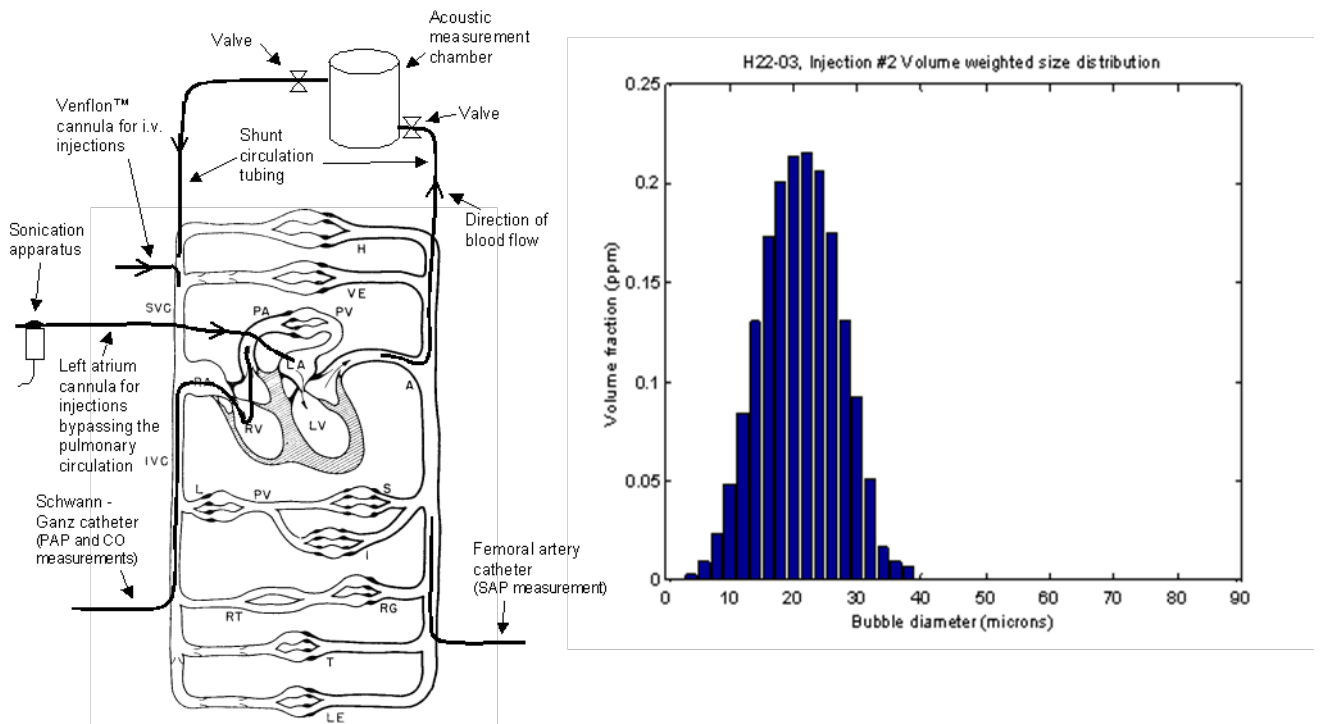


Figure 3 – Schematics for ex-vivo determination of bubble concentration and size after i.v. administration and activation in the heart chamber (left). Histogram of the activated bubble volume weighted size distribution at peak activated volume (right).

Sonoporation, endocytosis and pore formation

Aya Zeghimi, Jean-Michel Escoffre and Ayache Bouakaz

UMR Inserm U930 Imagerie & Cerveau, Université François Rabelais, Tours, France

Introduction

Based on the combination of ultrasound (US) and microbubbles, sonoporation induces a transient plasma membrane permeabilization. The permeabilization mechanisms are still not completely fully elucidated. Among the hypothesized mechanisms are the formation of pores on the plasma membrane [1–5] and/or a further stimulation of endocytosis pathways [6–8]. This study aimed to provide insights on the cell membrane morphological modifications induced by sonoporation using electron microscopy.

Material and Methods

Cell Culture

U-87 MG human glioblastoma cells, provided by ATCC (LGC Promochem, Molsheim, France), were grown in cell culture flasks 100 cm² (Corning Life Science B.V., Amsterdam, The Netherlands) in 13 mL of Dulbecco's Modified Eagle's Medium (DMEM, Gibco-Invitrogen, Carlsbad, CA) supplemented with 10% v/v fetal calf serum (FCS, Gibco-Invitrogen, Carlsbad, CA) and incubated at 37°C under an humidified atmosphere in 5% CO₂ incubator. 48H before ultrasound exposure, the cells were seeded on 18 mm diameter glass cover slips, placed in 24 well-plates, reaching until 80% confluence the day of the experiment.

Ultrasound exposure conditions

Using Vevo SoniGene[®] (VisualSonics Inc., NL), adherent U-87 MG cells were insonated at 1MHz sinusoidal US waves with 1 W/cm² acoustic intensity, 20% duty cycle for 60 s. BR14[®] microbubbles (Bracco Research, Switzerland) were added at a microbubble/cell ratio of 5. These acoustic parameters were obtained as a result of prior optimization experiments.

Membrane Permeabilization

Membrane permeabilization after sonoporation (same ultrasound conditions as described earlier) was assessed using SYTOX[®] Green (Sigma-Aldrich, St. Louis, MO) as a model drug at a final concentration of 1 µM. SYTOX[®] Green is a small impermeant fluorescent molecule and a DNA binding probe that does not diffuse into the cells. Immediately after sonoporation, cells were harvested, resuspended in 500 µL PBS and then analyzed by flow cytometry. Fluorescence histograms were recorded with a flow cytometer (Beckman-Coulter, Fullerton, CA) by collecting 10 000 events, and analyzed using the Kaluza software supplied by the manufacturer. To assess the cell mortality, propidium iodide (Sigma-Aldrich, St. Louis, MO) was added at 0.5 µg/mL concentration to the cell suspension before flow cytometry analysis.

Electron microscopy

The ultrastructural changes of plasma membrane after sonoporation were monitored by scanning electron microscopy (SEM). The cell samples were fixed and prepared using conventional osmium tetroxide staining [9]. The cells were observed either immediately (0 min) or 15 min post-sonoporation. The samples were processed and coated by platinum sputtering (5 nm) and observed using a LEO DSM 982 SEM (Zeiss, Germany).

Genistein treatment

In order to identify whether endocytosis was involved, the cells were incubated before sonoporation with 50 μ M of Genistein (Sigma-Aldrich, St. Louis, MO), an inhibitor of caveolae-mediated endocytosis, during one hour at 37°C. This concentration was identified through a series of cell cytotoxicity assays with various concentrations.

Results and Discussion

A. Cell membrane permeabilization

Flow cytometry analysis was performed to assess the rate of SYTOX[®] Green uptake in the cells. The results (Fig. 1A) show that the cell membrane permeabilization reached 60% after sonoporation in the presence of BR14[®] microbubbles, while the cell mortality remained very low, less than 1.5% (Fig. 1B).

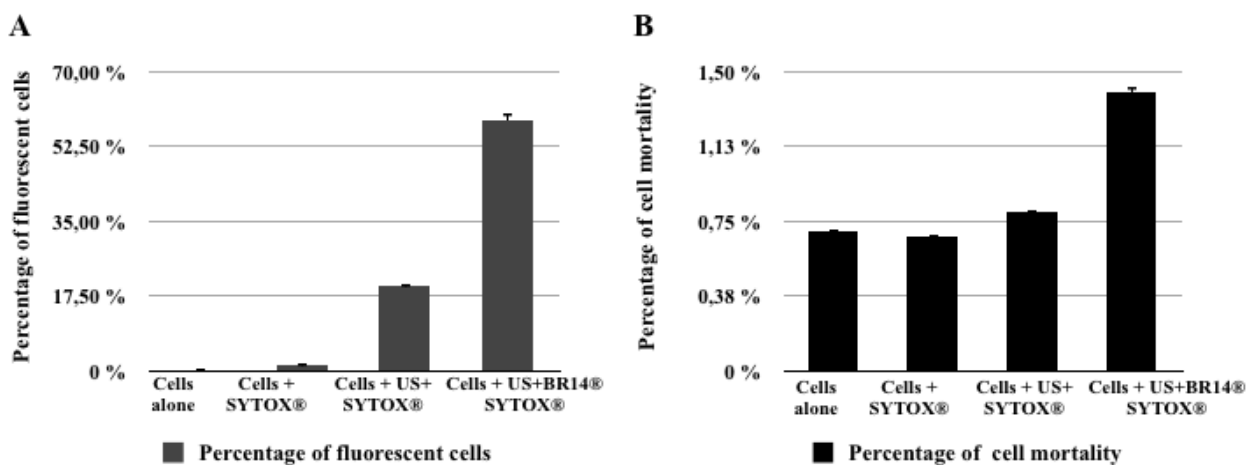


Figure 1: Percentage of SYTOX[®] green positive cells (A) and the cell mortality (B).

B. Scanning electron microscopy

The plasma membrane morphological changes induced by sonoporation using the same US exposure conditions were examined with SEM. The SEM photomicrographs depicted in Fig. 2 show that immediately after US exposure, in the absence of microbubbles (0 min), a small number of dark and tiny structures appear on the plasma membrane, termed here “pore-like structures”, but these structures were not seen in the non-insonified U-87 MG cells (control). Ultrasound exposure in the presence of BR14 microbubbles increased significantly the number of the pore-like structures. Note also that the

size distribution of these structures is heterogeneous. However, cells observed 15 min after sonoporation exhibited less pore-like structures on the plasma membrane indicating that the cells are still metabolically active and tend to resorb these disruptions.

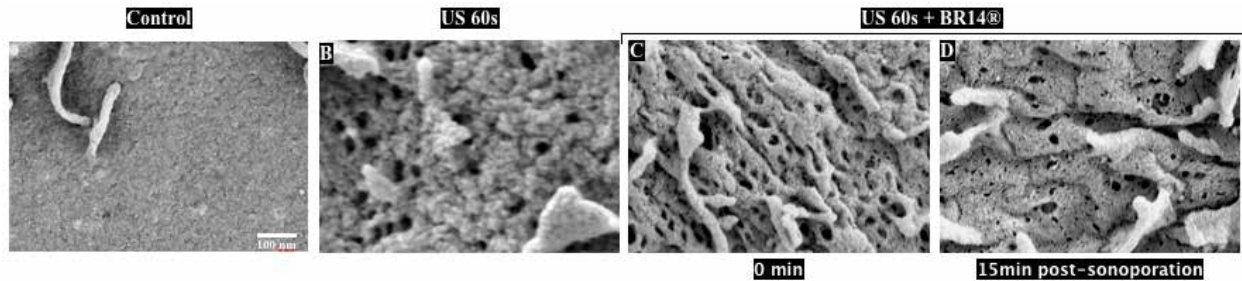


Figure 2: SEM images highlighting the morphology of the U-87 MG plasma membrane. (A) Control cell; (B) ultrasound alone, (C) immediately after sonoporation (US+BR14®) and (D) 15 min post-sonoporation (US+BR14®).

The pore-like structures were counted over the entire surface of the cells and averaged over 10 cells per exposure condition. The results shown in Fig. 3 confirm the decrease of the number of the pore like structures 15 min post-sonoporation (Fig. 3A). More particularly, the analysis shows that the decrease of the number of the pore-like structures is more pronounced for larger ones (60-160 nm) in comparison to small ones (10-60 nm) (Fig. 3B).

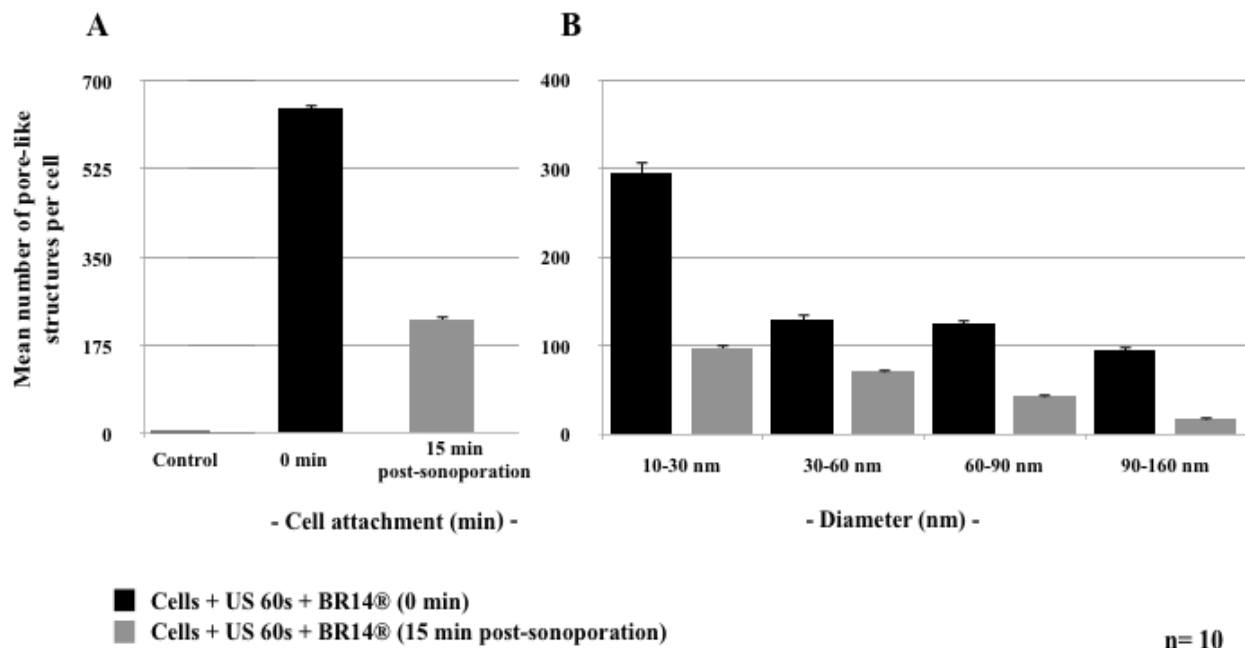


Figure 3: Quantitative analysis of (A) total number of pore-like structures and (B) total number of pore-like structures versus size, immediately after sonoporation (dark) and 15 min post sonoporation (grey).

C. *Genistein treatment*

The cells were treated with Genistein before sonoporation. Genistein is a specific inhibitor of caveolae mediated endocytosis pathways. The results displayed in Fig. 4 point out that Genistein-treated cells have less pore-like structures on their plasma membrane, suggesting that these structures have been inhibited with the Genistein incubation.

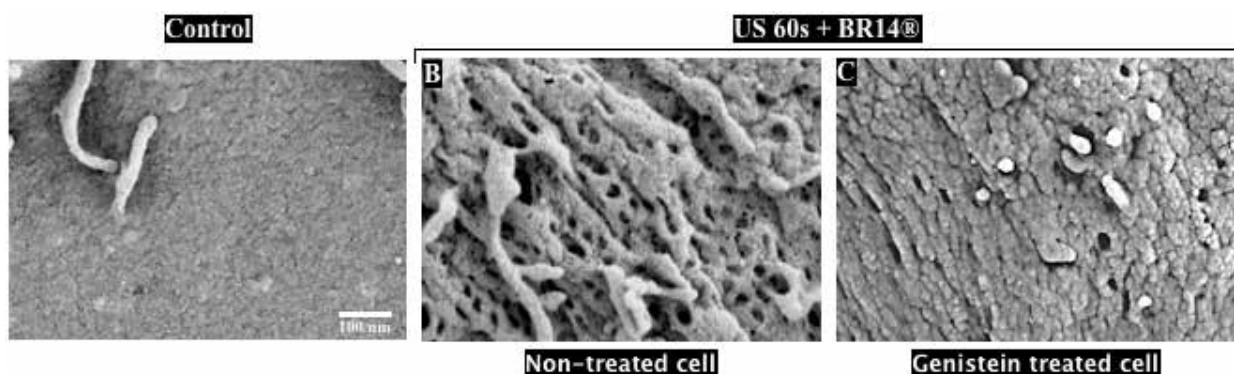


Figure 4: SEM micrographs showing the plasma membrane morphology of control cells (A), sonoporated cells (B) and sonoporated cells after Genistein treatment (C).

This result is also confirmed with the cytometry analysis (Fig. 5), which demonstrates that after Genistein treatment, only 28% of the cells did uptake the SYTOX[®] Green in comparison to sonoporated cells without Genistein incubation (about 60%).

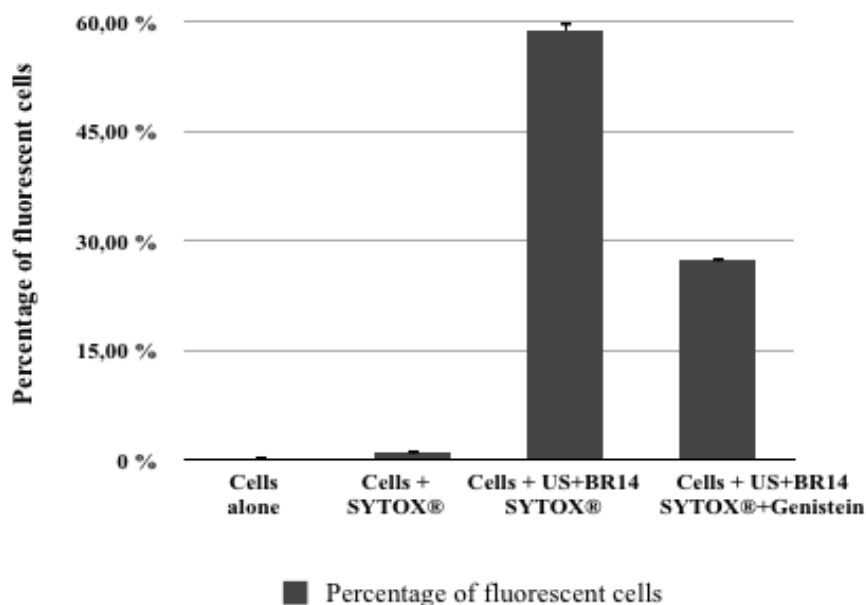


Figure 5: The percentage of fluorescent cells, post-sonoporation, either treated or not with Genistein.

The pore-like structures counting (Fig. 6) confirms further this decrease, estimated at $68 \pm 1.2 \%$, compared to the total number of pore-like structures. Hence, the total number of the pore-like structures decreased from 645 ± 5.09 without Genistein treatment to 206 ± 1.78 when the cells were incubated with Genistein, suggesting that a portion of these structures are caveolae still open. The quantitative study confirms this hypothesis, since the decay of the number of the pore-like structures with a diameter between 50 and 100 nm, reached 80%. Since the caveolae size ranges from 50 to 100 nm [10–11], these results imply that the nature of the remaining pore-like structures (32%) could be attributed to pathway of caveolin-independent endocytosis and/or transient membrane pores.

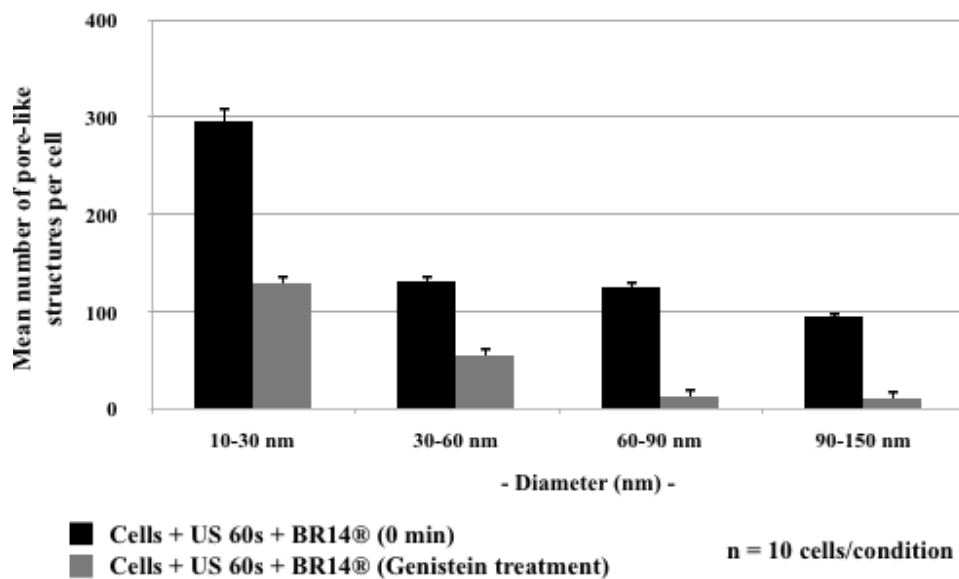


Figure 6: Total number of the pore-like structures versus their diameter, after Genistein treatment.

Discussions and conclusions

We conclude from this study that the sonoporation induces structural changes of the plasma membrane. The electron microscopy observations indicate the creation of pore-like structures on the cell surface, with a size ranging from 10 to 160 nm. Our results demonstrate the reversibility and the transient character of the effects caused by sonoporation, since 15 min later, 68% of pore-like structures disappeared. The results obtained after Genistein treatment showed a pronounced decrease in the number of pore-like structures indicating that caveolae-mediated endocytosis pathway is likely involved in the sonoporation mechanisms. This finding is confirmed since the inhibited pore-like structures showed to be similar in size to the caveolae-mediated pathways. Hence, we presume that for U-87 MG cells, this path remains dominant. However, it does not exclude the involvement of the other endocytic pathways (caveolin-independent), and also the membrane pore formation.

Acknowledgment

This project was funded in part by the EU Project SONODRUGS (NMP4-LA-2008-213706). The authors are grateful to Bracco Research Geneva for supplying the contrast agents and to Dr. Rustem Uzbekov for discussions.

References

1. M. L. Andrew A. Brayman, S. Coppage, and M. W. M. Vaidya, "Transient poration and cell surface receptor removal from human lymphocytes in vitro by 1 MHz ultrasound," *Ultrasound in medicine & biology*, vol. 25, no. 6, pp. 999–1008, 1999.
2. M. J. K. Blomley, J. C. Cooke, E. C. Unger, M. J. Monaghan, and D. O. Cosgrove, "Clinical review Microbubble contrast agents : a new era in ultrasound," *BMJ*, vol. 322, pp. 1222–1225, 2001.
3. P. Prentice, A. Cuschieri, K. Dholakia, M. Prausnitz, and P. Campbell, "Membrane disruption by optically controlled microbubble cavitation," *Nature Physics*, vol. 1, no. 2, pp. 107–110, Oct. 2005.
4. R. . Schlicher, H. Radhakrishna, T. . Tolentino, R. . Apkarian, V. Zarnitsyn, and M. . Prausnitz, "Mechanism Of Intracellular Delivery By Acoustic Cavitation," *Ultrasound in medicine & biology*, vol. 32, no. 6, pp. 915–924, 2006.
5. B. Geers, I. Lentacker, A. Alonso, N. N. Sanders, J. Demeester, S. Meairs, and S. C. De Smedt, "Elucidating the mechanisms behind sonoporation with adeno-associated virus-loaded microbubbles.," *Molecular pharmaceutics*, vol. 8, no. 6, pp. 2244–51, Dec. 2011.
6. L. J. M. Juffermans, A. van Dijk, C. a M. Jongenelen, B. Drukarch, A. Reijerkerk, H. E. de Vries, O. Kamp, and R. J. P. Musters, "Ultrasound and microbubble-induced intra- and intercellular bioeffects in primary endothelial cells.," *Ultrasound in medicine & biology*, vol. 35, no. 11, pp. 1917–27, Nov. 2009.
7. V. Lionetti, A. Fittipaldi, S. Agostini, M. Giacca, F. a. Recchia, and E. Picano, "Enhanced Caveolae-Mediated Endocytosis by Diagnostic Ultrasound In Vitro," *Ultrasound in Medicine & Biology*, vol. 35, no. 1, pp. 136–143, Jan. 2009.
8. B. D. M. Meijering, L. J. M. Juffermans, A. van Wamel, R. H. Henning, I. S. Zuhorn, M. Emmer, A. M. G. Versteilen, W. J. Paulus, W. H. van Gilst, K. Kooiman, N. de Jong, R. J. P. Musters, L. E. Deelman, and O. Kamp, "Ultrasound and microbubble-targeted delivery of macromolecules is regulated by induction of endocytosis and pore formation.," *Circulation research*, vol. 104, no. 5, pp. 679–87, Mar. 2009.
9. A. Zeghimi, R. Uzbekov, B. Arbeille, J.M. Escoffre, A. Bouakaz, "Ultrastructural modifications of cell membranes and organelles induced by sonoporation," in : *proceedings of the 2012 IEEE International Ultrasonics Symposium, Dresden, Germany, Oct. 2012.*
10. G.E. Palade, "Fine structure of blood capillaries," *J. Appl. Phys*, vol. 24, pp. 1424, 1953.
11. E. Yamada, "The fine structures of the cell gall bladder epithelium of the mouse," *J. Biophys. Biochem. Cytol*, vol. 1, pp. 445–458, 1955.

Semi-automated detection of neovascularization

*Avinoam Bar-Zion¹, Shelly Zaffryar-Eilot², Ofra Kessler², Edith Suss-Toby²,
Gera Neufeld², Dan Adam¹*

¹*The Department of Biomedical Engineering, Technion, Israel Institute of Technology, Haifa, Israel*

²*The Bruce Rappaport Faculty of Medicine, Technion, Israel Institute of Technology, Haifa, Israel*

Background

Tumor angiogenesis is recognized as an important mechanism driving tumor development and progression. Estimation of changes of tumor vasculature may help assess and monitor tumor growth, and conversely, the effectiveness of anti-angiogenic treatment. Currently, Contrast Enhanced Ultrasound Imaging (CEUS) is used for evaluation of blood volume and the degree of perfusion within an organ; all available quantitative techniques suffer from low level of repeatability. In this work a semi-automatic method was developed for the enhancement and detection of the spatial structure of the vasculature feeding the tumors, enabling quantification of its proliferation.

Methods

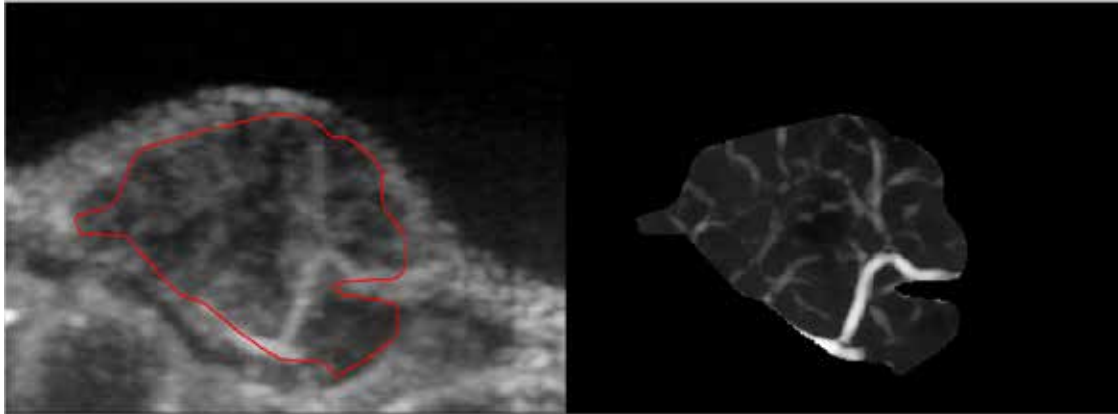
B-mode and CEUS scans of mice bearing Glioblastoma (brain) and Lewis lung carcinoma (LLC) tumors were performed using Vevo 2100 imaging system, then analyzed. Half of the LLC mice were treated by injection of LOXL2 neutralizing antibody AB0023 which inhibits angiogenesis.

Due to the random distribution of micro-bubbles within the vasculature, only partial sections of the blood vessels are detected in each frame and not their full structure. Given cine of grayscale images, the Maximum Intensity Persistence (MIP) algorithm was used to calculate the temporal running maximum for every pixel. The spatially correlated noise characteristic of MIP CEUS was reduced using anisotropic diffusion. A 2D multi-scale vesselness detector was then applied to the each frame, to enhance visibility of small, low contrast vessels.

Results

Scans of Glioblastoma tumors revealed complex dynamic vascular patterns: when contrast agent enters the tumor, initially the major blood vessels are observed. Later, when the contrast material passes through the small blood vessels, perfusion through the capillary bed is dominant. The processed ultrasound scans reveal differences between the scales of blood vessels in the control group and those in treated LCC mice, in good agreement with histological staining.

Alterations of the vascular system may be identified using the proposed methods. Using anisotropic diffusion and vesselness detector most of the MIP artifacts can be removed and the visualization of the main vascular system is improved (see figure: Left – MIP frame, Right - processed).



Quantification of neovascularization in carotid artery plaques

*Johan G. Bosch¹, Zeynettin Akkus¹, Assaf Hoogi³, Guillaume Renaud¹,
Stijn C.H. van den Oord², Arend F.L. Schinkel², Dan Adam³, Nico de Jong¹,
Antonius F.W. van der Steen¹*

¹*Dept. Thoraxcenter Biomedical Engineering, Erasmus MC, Rotterdam, the Netherlands*

²*Dept. Cardiology, Erasmus MC, Rotterdam, the Netherlands*

³*Dept. Biomedical Engineering, Technion, Haifa, Israel*

Background

Neovascularization in atherosclerotic plaques is considered an important marker for plaque vulnerability [1]. In case of plaques in the carotid arteries, the amount of neovascularization could provide a prediction of the risk of stroke or TIA. This neovascularization can be visualized by contrast enhanced ultrasound (CEUS), where it is visible as the intermittent appearance of moving contrast bubbles inside the plaque. The phenomenon has been described extensively but so far has mainly been evaluated qualitatively in patients. Our group is aiming for automated quantification of the extent of intraplaque neovascularization (IPN) from CEUS images of the carotid arteries. This research is performed as part of the CTMM-PARISK project (Plaque At Risk), that is developing an integrated multimodal approach for risk assessment of carotid plaques. In this presentation, an overview will be given of the methods we have developed so far for quantification of carotid artery plaque neovascularization in CEUS.

Methods

Plaques are relatively small, moving structures on the interface of the arterial wall and the blood. We found that current commercially available contrast image analysis tools were not very well suited for quantification of the plaque perfusion, due to motion compensation approaches unfit for small plaques, the proximity of the lumen contrast and artifacts, and the available parameters. These are based on general organ perfusion models, and do not apply to the sporadic passing of bubbles in a small plaque. We developed analysis methods specifically for such plaques in contrast / B-mode paired images of longitudinal views of the carotids. These tools are collected in the integrated analysis program CINQS. We developed a dedicated motion compensation approach, in which a landmark point on or near the plaque is manually indicated and tracked in the B-mode image by Normalized Correlation Block Matching and Multidimensional Dynamic Programming [4].

The plaque region of interest (ROI) is manually drawn in one frame and automatically tracked. Care is taken to exclude lumen contrast and artifacts from the ROI. A host of statistical intensity analyses are performed on the motion-compensated ROI, including parameters derived from a pixel-wise Maximum Intensity Projection (MIP) over time.

Furthermore, to establish the contrast dynamics in the IPN, individual contrast spots are detected by comparison to artificial bubble templates and tracked over time. The contrast channel trajectories and count, the velocity of bubbles and the frequency of occurrence can be assessed [3].

Finally, we devised a special contrast imaging method (counter-propagation contrast imaging) for suppression of the distal wall artifact [2]. This should deliver an artifact-free imaging of the vessel far wall and allow quantitative analysis of the distal wall plaques, which is currently not feasible.

Results

The automated motion compensation method was scored as fully successful in 94% of 67 image sequences. In comparison to manually tracked landmark points in 1650 in-vivo images, the absolute error was $72 \pm 55 \mu\text{m}$ (mean \pm SD) for longitudinal and $34 \pm 23 \mu\text{m}$ for radial displacements [4]. In Fig. 1, an example is shown of the resulting qualitative improvements of MIP images, giving a clear impression of contrast trajectories.

Detection, tracking and classification of the contrast spots in the plaque (Fig. 2) were evaluated in 28 plaques by comparison to manually tracked objects: in 89% of detected objects, the motion was tracked with an average error $< 0.5\text{mm}$. The classification was compared to a four-grade visual scoring of neovascularization by two observers. Agreement within 1 grade was achieved for 91% of plaques, which was comparable to the interobserver variability of visual scoring [3].

Comparison of the different derived IPN quantification parameters to visual scoring was performed in CINQS and is discussed in other presentations at this conference. Best concordance was found so far for the IPN Surface Area parameter.

Compared to standard Amplitude Modulation, the counter-propagation contrast imaging method has been shown to improve the artifact to tissue ratio in-vitro by 12 dB [2]. In-vivo evaluations are pending.

Discussion

Promising results have been obtained so far. However, the methods are limited in several ways and can be extended further. First of all, the 2D imaging limits the assessment to a single slice of the plaque. A true 3D high-framerate imaging of the contrast passage is desired for more integral quantification of the 3D plaque neovasculature. 3D imaging with mechanically scanning probes is not considered adequate for the swiftly moving contrast bubbles and a high-frequency matrix array with suitable contrast mode is needed.

Secondly, its semiautomated character is still a source of analysis variability. Fully automated outlining and tracking will improve reproducibility but will put high demand on classification of artifacts and lumen contrast, to prevent these from contaminating the quantification.

So far, our quantitative methods have been compared to the visual IPN scoring by clinicians (their natural precursor). However, the correlation to anatomical ground truth still needs to be assessed. By comparison of the quantitative CEUS scores to the actual neovascularization extent obtained from histologic analysis of excised plaques in a group of carotid endarterectomy patients, we expect to be able to establish this correlation.

Conclusions

Several methods have been developed that enable quantification of plaque neovascularization. Successful dedicated motion compensation and contrast spot detection and tracking approaches have been realized. An integrated software package for deriving several parameters (CINQS) has been realized. So far, best concordance to visual scoring is found for IPN Surface Area. Further evaluation and comparison to histology is ongoing.

Acknowledgments

This research was performed within the framework of CTMM, the Center for Translational Molecular Medicine (www.ctmm.nl), project PARISk (grant 01C-202), and supported by the Dutch Heart Foundation.

References

1. Hellings WE, Peeters W, Moll FL, Piers SRD, van Setten J, Van der Spek PJ, de Vries JPPM, Seldenrijk KA, De Bruin PC, Vink A, Velema E, de Kleijn DPV, Pasterkamp G. **Composition of carotid atherosclerotic plaque is associated with cardiovascular outcome: a prognostic study.** *Circulation*, 2010;12117:1941–1950.
2. Renaud G, Bosch JG, Ten Kate GL, Shamdasani V, Entekin R, De Jong N, Van der Steen AFW. **Counter-propagating wave interaction for contrast-enhanced ultrasound imaging.** *Phys. Med. Biol.* 57 (2012) L9-L18.
3. Hoogi A, Akkus Z, van den Oord SCH, ten Kate GL, Schinkel AFL, Bosch JG, de Jong N, Adam D, van der Steen AFW. **Quantitative analysis of ultrasound contrast flow behavior in carotid plaque neovasculation.** *Ultrasound in Medicine & Biology* 38(2012);2072-2083.
4. Akkus Z, Hoogi A, Renaud G, ten Kate GL, van den Oord SCH, Schinkel AFL, de Jong N, van der Steen AFW, Bosch JG. **Motion Compensation Method using Dynamic Programming for Quantification of Neovascularization in Carotid Atherosclerotic Plaques with Contrast Enhanced Ultrasound (CEUS).** *Proc. SPIE* 8320, 83200C (2012).

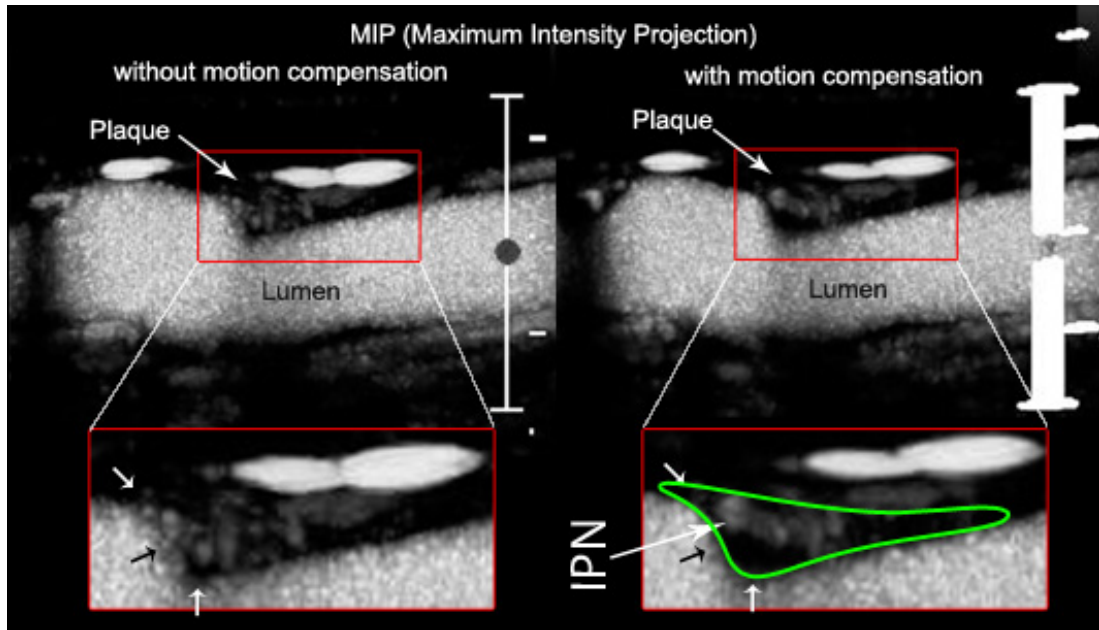


Figure 1: Maximum intensity projection of intraplaque neovascularization without (left) and with motion compensation (right).

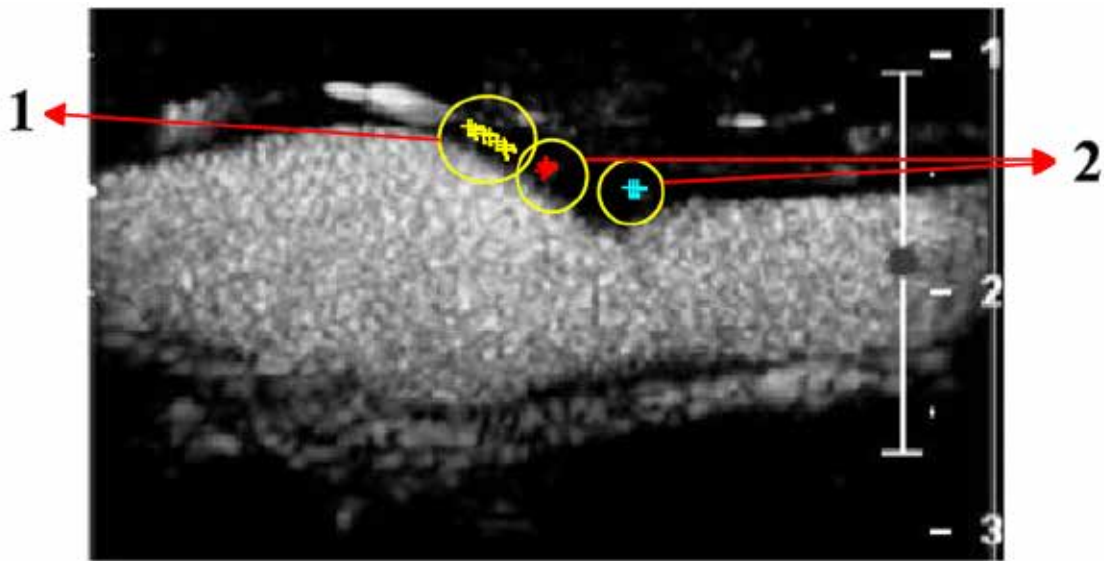


Figure 2: Classification of the detected and tracked objects within the carotid plaque. 1: object classified as neovasculature; 2: objects classified as artifacts. [3]

A systematic comparison of contrast imaging strategies

Jacopo Viti^{1,2}, Riccardo Mori¹, Francesco Guidi¹, Nico de Jong², Piero Tortoli¹

¹*Università di Firenze, Electronics and Telecomm. Dept, Firenze, Italy*

²*Biomedical Engineering Erasmus Medical Center Rotterdam, the Netherlands*

Nowadays a sizeable amount of different contrast imaging (CI) techniques is available, each with its own benefits and disadvantages. Understanding the different performances offered by each is a critical knowledge to possess when choosing which CI technique should be used in a given scenario; however, direct performance comparison between the different CI strategies is confusing and often unfeasible, since the CI methods are most often described and tested each using its own, specific setup. Only a few comparisons made in a controlled environment can be found in the literature, at present time [Eckersley *et al.*; *Ultras. Med. Biol.*, 2004][Renaud *et al.*; *Proceedings of IEEE IUS 2011*]. In this work we present a fair, systematic comparison between various different CI techniques, using a single common *in vitro* setup.

A homogeneous brick of agar-based tissue mimicking material was built in house according to the description provided by Teirlink *et al.* [Teirlink *et al.*; *Ultrasonics*, 1998]; two separate cylindrical cavities 13 mm in diameter were cast in the brick, about 10 mm apart, and were respectively filled with clean water and a continuously-stirred suspension of BR-14 contrast agent (UCA) (Bracco Imaging S.p.A., Milan, Italy). The ultrasound setup consisted of a 5 MHz linear array probe (LA332, Esaote S.p.A., Genova, Italy) connected to the ULA-OP system [Tortoli *et al.*; *IEEE Trans. UFFC*, 2009]. Ten different CI strategies were implemented and compared (see Table 1), as well as standard B-Mode and Chirp B-Mode images. For each CI strategy, an 81-line image is acquired using ULA-OP and displayed in real-time to facilitate any required adjustment to the scanning parameters. Finally, beamformed RF data is downloaded to a PC for quantitative evaluation.

In the processed image three non-overlapping regions of interest (ROI) are selected, respectively centred on UCA, tissue and water. The mean signal intensity is then separately computed for each ROI in order to evaluate the contrast-to-tissue (CTR) and contrast-to-noise (CNR) ratio for each CI strategy. Results using an UCA concentration of 1:200 and an average mechanical index of 0.1 are summarized in Table 2. Results obtained with a lower concentration (1:400 and 1:800) confirmed these results within 3 dB. Every CI strategy shows an improved CTR over the reference B-Mode, except for one case. PM produced the best results amongst the routinely employed CPS techniques (PM, PI, PMPI); excellent performance also came from chirp techniques, with CRAM denoting a most notable CTR improvement of 22 dB over Chirp B-Mode (CB).

The setup was demonstrated as a flexible and extensible instrument for quantitative evaluation of performance of potentially any CI method. Functional parameters (CNR, CTR) are easily obtained for the different CI modalities, allowing for a convenient performance comparison and helping to highlight strengths and weaknesses of the various approaches in a controlled environment. Work is in progress to optimize the performance of the methods already implemented and to further extend the comparison to include novel approaches such as plane wave imaging.

CI Strategy	Transmissions per line	Pulse length [μs]	Frequency [MHz]	Amplitude [Vpp]	Time Windowing	Echo Processing
Power modulation (PM)	<i>PM1</i>	1.14	3.5	6		
	<i>PM2</i>	1.14	3.5	12	Hanning	PM1-PM2+PM3
	<i>PM3</i>	1.14	3.5	6		
Pulse inversion (PI)	<i>PI1</i>	1.14	3.5	12	Hanning	PI1+PI2
	<i>PI2</i>	1.14	3.5	-12		
Power Modulation Pulse Inversion (PMPI)	<i>PMPI1</i>	1.14	3.5	6		
	<i>PMPI2</i>	1.14	3.5	-12	Hanning	PMPI1+PMPI2+PMPI3
	<i>PMPI3</i>	1.14	3.5	6		
Subharmonic (SH)	<i>SH1</i>	3.33	6	12	Rectangular	LPF; fc = 3.5 MHz
Chirp reversal (CR)	<i>CR1</i>	5.00	3-7 (up)	12	Tukey 20%	Chirp compression, then CR1-CR2
	<i>CR2</i>	5.00	7-3 (down)	12		
Chirp amplitude modulation (CAM)	<i>CAM1</i>	5.00	3-7 (up)	6		
	<i>CAM2</i>	5.00	3-7 (up)	12	Tukey 20%	Chirp compression, then CAM1-CAM2+CAM3
	<i>CAM3</i>	5.00	3-7 (up)	6		
Chirp Reversal amplitude modulation (GRAM)	<i>GRAM1</i>	5.00	3-7 (up)	6		
	<i>GRAM2</i>	5.00	7-3 (down)	12	Tukey 20%	Chirp compression, then GRAM1+GRAM3-GRAM2
	<i>GRAM3</i>	5.00	3-7 (up)	6		
Pulse subtraction time delay (PSTD)	<i>PSTD1</i>	1.00	4	12		
	<i>PSTD2</i>	1.00	4	12	Rectangular	PSTD1+PSTD2-PSTD3
	<i>PSTD3</i>	2.00	4	12		
Dual-frequency (DF)	<i>DF1</i>	1.14	3	6	Hanning	
	<i>DF2</i>	1.14	6	6		DF1+DF2-DF3
	<i>DF3</i>			DF1+DF2		
Ring-down (RD)	<i>RD1 (s1 & s2)</i>	<i>s1</i> : 2.5	3	12	Hanning	
		<i>s2</i> : 0.5	6.5	12	Hanning	HPF to suppress <i>s1</i> and <i>s3</i> ; then RD1-RD2
	<i>RD2 (s3 & s4)</i>	<i>s3</i> : 2.5	3	-12	Hanning	
		<i>s4</i> : 0.5	6.5	12	Hanning	

Table 1: Description of TX/RX strategies of contrast imaging modes. Negative amplitudes indicate a 180 degrees phase-shift. Pulses RD1, RD2 each consist of two different excitations, concatenated in time.

Modes	UCA	Tissue	Water	CTR	CNR
B	70.8	51.5	36.7	19.3	34.1
CB	65.9	53.8	20.5	12.1	45.4
PM	63.8	36.3	36.0	27.5	27.7
PI	57.6	37.2	36.9	20.4	20.7
PMPI	64.3	37.8	37.2	26.5	27.1
SH	62.1	40.1	33.2	22.0	28.9
CR	51.9	22.2	19.1	29.7	32.8
CAM	55.0	21.2	19.6	33.8	35.4
GRAM	56.5	22.5	20.0	34.0	36.5
PSTD	62.0	36.7	36.3	25.4	25.7
DF	57.8	36.2	35.8	21.6	22.0
RD	50.4	33.5	33.9	16.9	16.5

Table 2: Mean signal intensities obtained from different scattering regions.

Trade-offs in ultrafast imaging of microbubbles

*Matthew Bruce*¹, *Charles Tremblay-Darveau*², *Ross Williams*³, *Laurent Milot*³,
Peter N. Burns^{2,3}

¹*Supersonic Imagine, Aix en Provence, France*

²*Department of Medical Biophysics, University of Toronto, Toronto, Ontario, Canada*

³*Sunnybrook Health Sciences Centre, Toronto, Ontario, Canada*

Introduction

The imaging of microbubbles with unfocussed ultrasound beams opens new opportunities for visualizing blood flow.[1,2] Unfocussed ultrasound beams enable the imaging of microbubbles hundreds of times faster (kHz) than conventional methods by enabling the reconstruction an entire plane with a single transmit. This approach in previous work has been referred to as ultrafast imaging.[1,2] Traditional focused transmit/receive acquisitions used to image microbubbles have been limited to frame rates of 8 to 30Hz, due to the need of additional pulses to separate nonlinear from linear signals. This approach distributes ultrasound energy to microbubbles in temporally and spatially different manners than focused beams. The increase in temporal acquisitions enables visualization of microbubbles with framerates not possible before as well as ability to tradeoff these framerates for improved SNR by averaging. This work explores the advantages and disadvantages of this approach to traditional focused imaging of ultrasound contrast agents at low mechanical indices (MI).

Methods

Acquisitions from focussed and unfocussed transmits using microbubbles were acquired both *in-vitro* and *in-vivo* using an *Aixplorer* diagnostic ultrasound system (Supersonic Imagine, France). Figure 1 illustrates the differences for focused and unfocused pulse inversion acquisitions. For focused acquisitions, an image is built up by successive transmits covering a limited area, which are translated across the image plane. With the need of additional pulses per line for nonlinear signal separation, framerates for ultrasound contrast are 2 to 3 times slower than conventional b-mode imaging. For unfocussed acquisitions, entire image planes are acquired with alternating polarities. In Figure 1, the red and blue frames denote positive and negative pulses in both acquisitions. Full images were reconstructed per plane-wave transmit from the nonlinear RF obtained after summation of the pre-beamformed data. An ATS 523A flow phantom with a roller pump were were used in the *in-vitro* acquisitions. The animal model used was a New Zealand white rabbit. Definity, a commercial lipid shell microbubble (10 μ L/kg of bolus), was used in all experiments. The *in-vivo* data were acquired with a 7.5Mhz probe. The beam profiles for focused and unfocussed transmits were measured using a Marconi hydrophone.

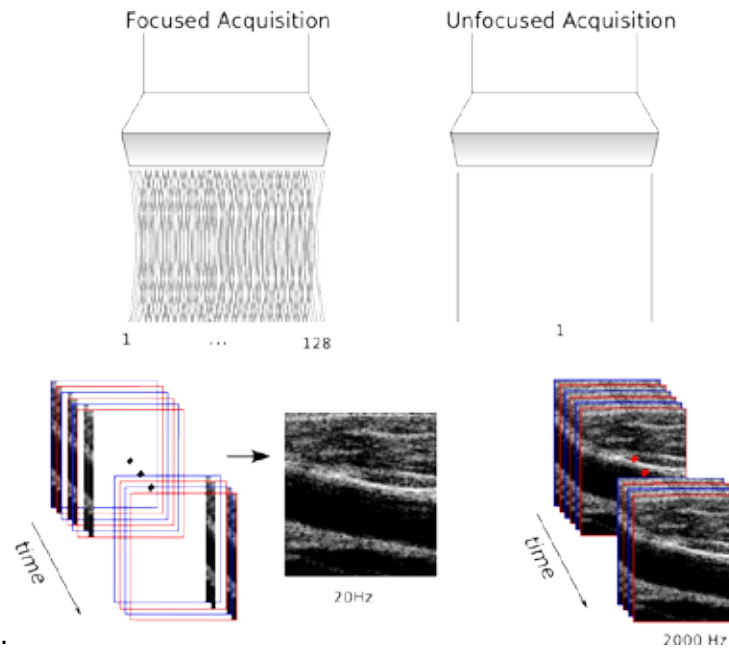


Figure 1: Illustrations of the differences between focused and unfocused pulse inversion acquisitions leading to different magnitudes of framerate. Blue frames denote positive polarity transmits and red denote a negative polarity transmits.

Results

Figure 2 illustrates the differences in the spatial distribution and magnitude of the peak negative pressure for a typical focused beam versus an unfocused beam. For the same voltage, the peak negative pressure is less than half that of the focused beam. The peak of the unfocused beam is driven by the elevational mechanical focus of the probe. Axial control of the acoustic beam is exchanged for broader coverage of the scan plane.

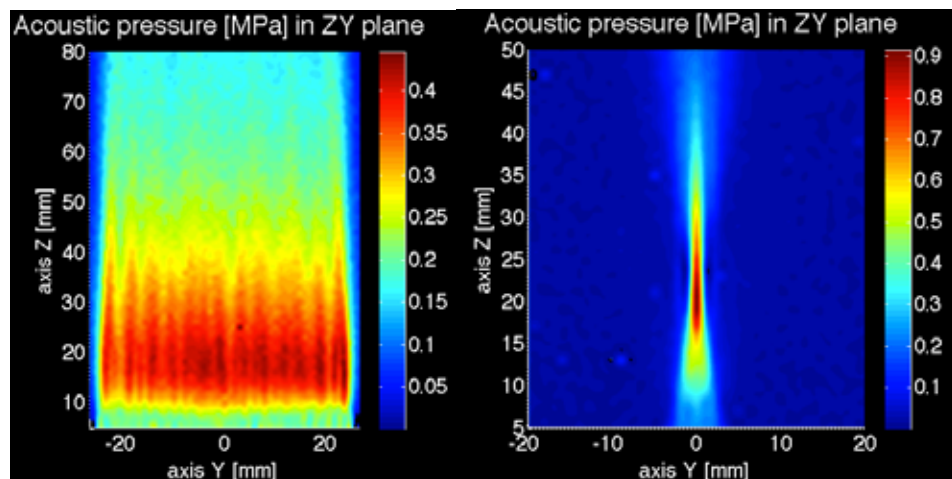


Figure 2: Illustration of the differences in spatial distribution of peak negative pressure between an unfocused beam (Left) and a focused beam (Right) using the same voltage from 7.5Mhz transducer. (Note: the color scale and depths are different)

As the microbubbles are disrupted at higher pressures, a key challenge of imaging microbubbles with unfocused beams is to balance near-field destruction with depth of field. In addition to microbubble disruption, a second challenge for larger depths of field is increased clutter in the near field from nonlinear propagation in tissue. The following example of a rabbit kidney uses a limited depth of field, minimizing the second challenge. Figure 3 shows 3 pulse-inversion images from unfocused acquisitions of the rabbit kidney and the decrease in signal in proximal portion of the cortex.

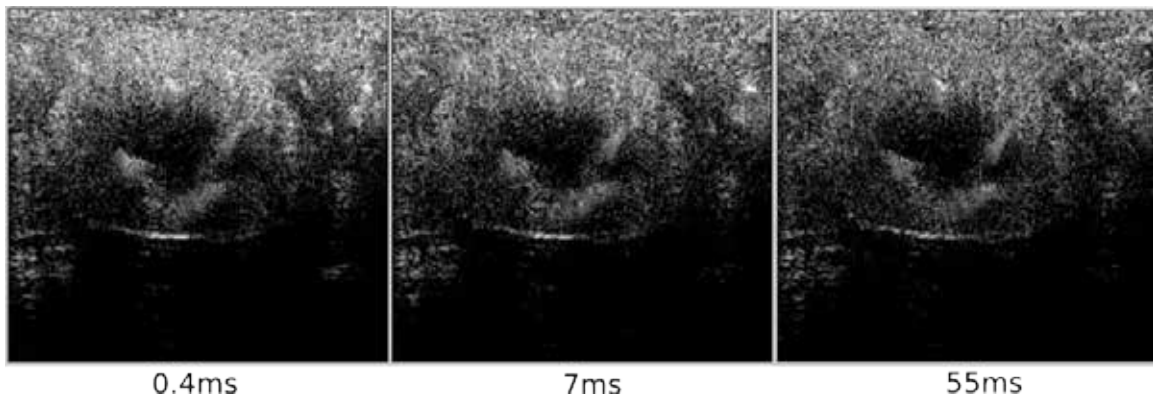


Figure 3: Three pulse-inversion images at different time intervals imaged at 2.5 kHz. The dynamic range of the three images is 30dB.

Figure 4 is an m-mode display of the mean across the image of the pulse-inverted unfocused acquisition and better illustrates the decrease in signal in the proximal portion. A veil effect is also observed in the first hundredths of milliseconds as distal regions increase correspondingly with the decrease in signal of the proximal regions.

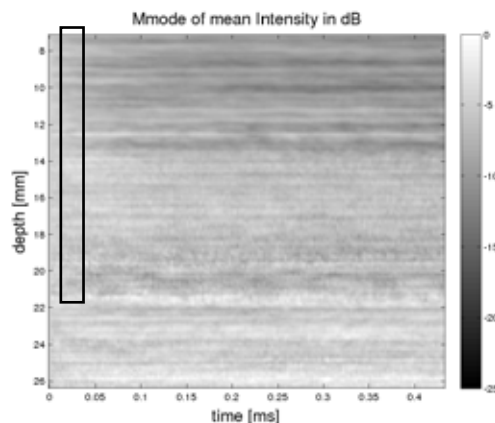


Figure 4: M-mode images of the mean across the image of the pulse-inverted unfocused acquisitions illustrating proximal microbubble disruption. Black box outlines the first 0.02 ms of near field microbubble disruption.

These increased acquisitions rates can be averaged to improve SNR and thus trading off framerate. Figure 5 shows a cross section of a tube filled with Definity from unfocused pulse inversion acquisitions at 2.5kHz with different amounts of averaging. The tube was not visible both from a focused acquisition or a single unfocused acquisition at the same voltage.

However, by averaging successive unfocused pulse-inversion acquisitions the vessel could be extracted from surrounding noise. Figure 5c is the result of 75 images, which still produce a frame rate of 33Hz. Focused microbubble imaging struggles to maintain a clinical usable framerate, limiting the amount of inter-frame averaging.

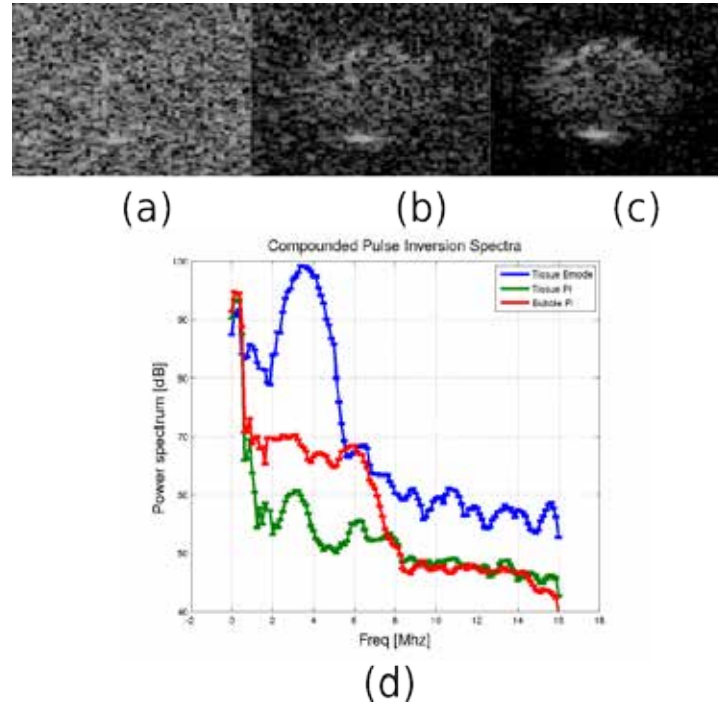


Figure 5: M-mode images of the mean across the image of the pulse-inverted unfocused acquisitions illustrating proximal microbubble disruption. (a-c) Single, 10, and 75 averaged frames of pulse inverted acquisitions respectively. (d) Resulting pulse inversion microbubble spectra after averaging 75 acquisitions in phantom tube.

Figure 5d shows roughly a 9 dB reduction in noise of the pulse inverted spectra after averaging. This could be significant as higher frequency (>5Mhz) imaging of microbubbles have struggled to produce clinically usable results, as the tradeoff in sensitivity and destruction were unfavorable.

Conclusions

The feasibility of imaging of microbubbles using unfocused beams combined with pulse inversion was investigated. It appears the compromise in giving up axial control of the transmit beam might have advantages over focused acquisitions under certain circumstances (e.g. like higher frequency imaging). In addition, the benefits in imaging microbubbles with framerates in the kilohertz might open new avenues of imaging and clinical utility.[1]

References

1. C. Tremblay-Darveau et al. , *Ultrafast Doppler Imaging of Microbubbles*, *Proceedings IEEE-UFFC*, 2012.
2. G. Montaldo et al. , *IEEE transactions on ultrasonics, ferroelectrics, and frequency control*, 56(3), 489–506, 2009.



Thursday, January 17, 2013

S o c i a l E v e n t

Partyship "De Majesteit"
Maasboulevard (near by Tropicana), Rotterdam

Coaches will be leaving from the Hilton at 18:30 and will be back in
Hilton between 22:30 and 23:00

Automated quantification of carotid intraplaque neovascularization using contrast-enhanced ultrasound

Stijn C.H. van den Oord†, MD; Zeynetin Akkus†, MSc; Johan G. Bosch†, PhD;
Assaf Hoogi‡, MSc; Gerrit L. ten Kate§, MD; Guillaume Renaud†, PhD;
Eric J.G. Sijbrands§, MD, PhD; Hence J. Verhagen||, MD, PhD;
Aad van der Lugt¶, MD, PhD; Dan Adam‡, PhD; Nico de Jong†, PhD;
Antonius F.W. van der Steen†, PhD; Arend F.L. Schinkel*, MD, PhD*

**Department of Cardiology, Thoraxcenter, Erasmus Medical Center, Rotterdam, the Netherlands*

†Division of Biomedical Engineering, Thoraxcenter, Erasmus Medical Center, Rotterdam, the Netherlands

*‡Faculty of Biomedical Engineering, Technion, Israel Institute of Technology, Haifa, Israel
§Division of Pharmacology, Vascular and Metabolic Diseases, Department of Internal Medicine, Erasmus Medical Center, Rotterdam, the Netherlands*

*|| Department of Vascular Surgery, Erasmus Medical Center, Rotterdam, the Netherlands
¶ Department of Radiology, Erasmus Medical Center, Rotterdam, the Netherlands*

Purpose

Intraplaque neovascularization (IPN) is associated with future cardiovascular events. Quantification methods for IPN assessed by contrast-enhanced ultrasound (CEUS) are lacking. The purpose of this study was to validate automated IPN quantification methods.

Materials & methods

The study was approved by the local ethical committee. Twenty-five patients with severe carotid stenosis, underwent bilateral carotid CEUS using a Philips iU-22 ultrasound system with a L9-3 transducer. Visual scoring of IPN was performed using a 3 point score. Automated quantification of IPN was performed using custom developed software (figure 1). Regions-of-interest were drawn over the atherosclerotic plaques. After motion-compensation, several IPN parameters were calculated. Spearman's rho and analysis of variance were used to compare visual scoring with the automated IPN parameters. Intraclass correlation coefficients and Bland-Altman plots were used to assess intra-observer and inter-observer variability.

Results

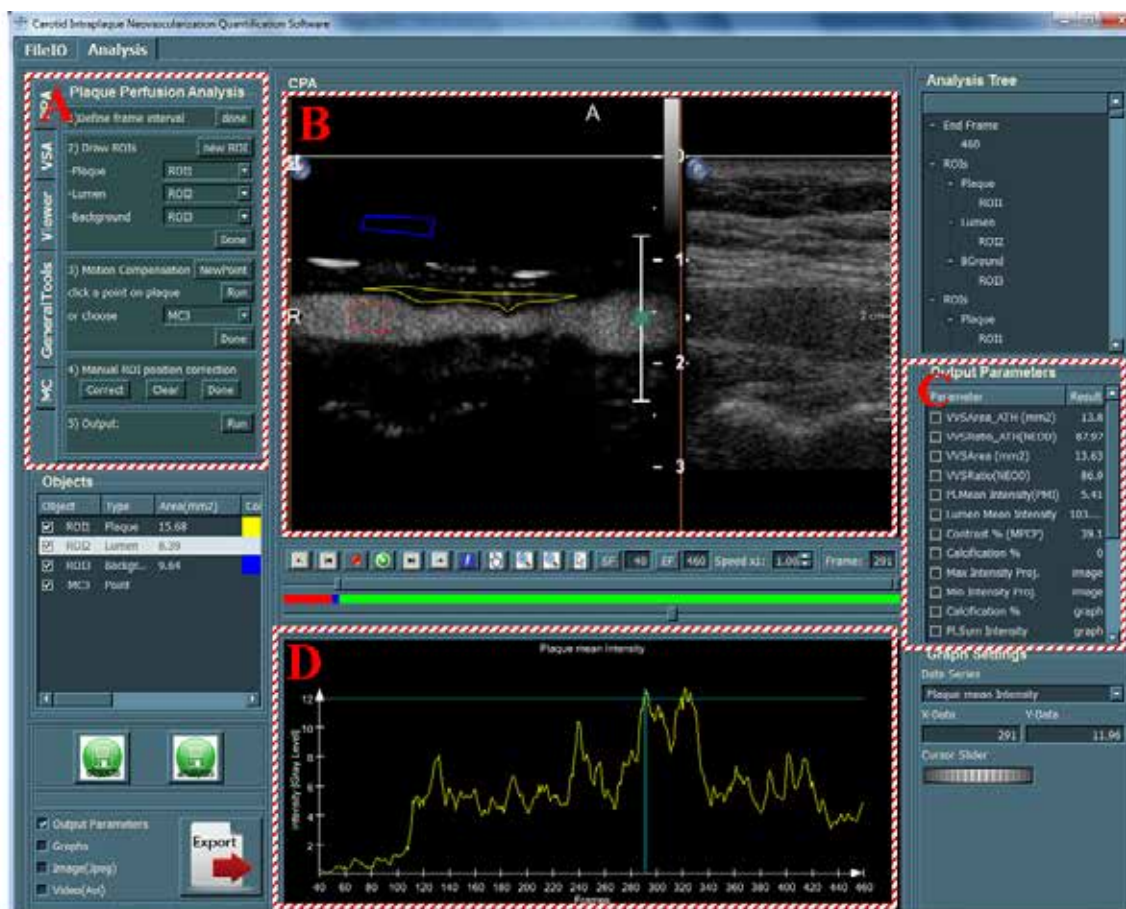
Forty-five carotid arteries were available for validation of the IPN parameters. Automated motion-compensated quantification of IPN was feasible in all 45 carotid plaques. Automated IPN surface area, IPN surface ratio and neovessel count, had a good correlation with visual IPN score (respectively $\rho=0.719$, $\rho=0.538$, $\rho=0.474$ all $p<0.01$) (table 1). The automated IPN surface area score provided the best distinction between the visual IPN scoring groups ($p<0.01$). Exclusion of plaques with severe calcification led to further improvement of automated quantification of IPN ($\rho=0.757$, $p<0.001$). Intra-

observer agreement was excellent (ICC 0.84-0.98 $p < 0.001$), intra-observer variability was low. Inter-observer agreement was good to excellent (ICC 0.68-0.94 $p < 0.01$); inter-observer variability was low.

Conclusion

Automated motion-compensated quantification of carotid IPN on CEUS is feasible and provides multiple parameters on carotid IPN. Automated IPN surface area, IPN surface ratio and neovessel count correlate well with visual scoring of IPN. The automated IPN surface area score provides the best distinction between the visual IPN scoring groups.

Figure 1



Custom developed software. Panel A: In this panel the mandatory settings for analysis are shown. First, the time frame interval needs to be defined. Second, three ROI's are manually drawn for 1. atherosclerotic plaque, 2. lumen and 3. background. Third, the motion compensation is performed. Panel B: The combined CEUS and B-mode clip is loaded. Zoom function allows drawing accurate ROI's. Panel C: Numeric output data of several IPN parameters. Panel D: For several output parameters graphs can be plotted for additional information of atherosclerotic plaque perfusion over time. In this example the plaque intensity is plotted over time.

Table 1. Output and correlation of different IPN parameters assessed using automated quantification software using ultrasound data of all atherosclerotic plaques (n=45).

Parameter	Mean output ± SD	Visual IPN score						Correlation with visual IPN score
		0	1	2	0 vs. 1	0 vs. 2	1 vs. 2	
IPN surface area (mm ²)	1.24 ± 0.73	0.35 ± 0.31	1.08 ± 0.56	2.06 ± 0.47	p<0.01	p<0.001	p<0.001	0.719 (p<0.001)
IPN surface ratio (%)	3.13 ± 1.04	2.20 ± 1.23	2.98 ± 0.96	3.97 ± 0.33	NS	p<0.01	p<0.01	0.538 (p<0.001)
PMI	1.62 ± 1.32	1.43 ± 0.67	1.29 ± 1.20	2.57 ± 1.46	NS	NS	p<0.01	0.277 (p=0.063)
MPCP (%)	15.6 ± 11.8	19.7 ± 11.1	12.8 ± 11.2	20.9 ± 11.2	NS	p<0.05	NS	0.151 (p=0.322)
Neovessel count	3.33 ± 3.12	1.80 ± 1.92	2.66 ± 2.64	5.82 ± 3.54	NS	p<0.05	p<0.01	0.474 (p=0.001)

IPN = Intraplaque neovascularization, MPCP = Mean percentage of the plaque filled with contrast over time, PMI = Plaque mean intensity.

Data are presented as mean ± SD. Difference in mean parameter output was calculated using ANOVA. Correlation coefficients were calculated using Spearman's Rank correlation.

Mechanistic insights of therapeutic potential of long ultrasound tone bursts in microbubble-ultrasound mediated therapies using high speed imaging

Xucui Chen, Jianjun Wang, John J. Pacella and Flordeliza S. Villanueva

Center for Ultrasound Molecular Imaging and Therapeutics, University of Pittsburgh Medical Center, Pittsburgh, PA 15213, USA

Background

Microbubble (MB)-Ultrasound (US) assisted therapy has been shown to restore perfusion in myocardial infarction (sonothrombolysis). Due to a presumption that MBs under high acoustic pressure do not persist after long acoustic cycles, most schemes of US-assisted therapy utilize a very short US pulse (a few acoustic cycles) when a high US pressure is used. However, we have recently observed enhanced sonothrombolytic effect *in vitro* using MBs and long US pulses, at high acoustic pressures. We therefore sought to explore the actual fate of MBs during a long acoustic cycle exposure by visual observation of MB acoustic behaviors at varying pulse lengths in order to gain insights of the mechanistic action.

Methods

MB behaviors were optically observed during long US tone burst excitation using an ultra-high speed imaging system that allows microscopic visualization of MB cavitation. The system is capable of capturing 128 frames at up to 25 million frames per second (Mfps). Long US tone bursts (up to 5,000 acoustic cycles) at 1 MHz and various pressures (0.25, 0.5, 1.0, and 1.5 MPa) were used to study the dynamic behavior of both lipid and polymer MBs in a 200- μ m diameter cellulose tubing. Passive cavitation detection was also performed to study the relationship between MB aggregate formation and therapeutic effect.

Results

High speed movies of the MBs during long tone burst excitation showed that MBs first underwent inertial cavitation then formed gas-filled aggregates that continued to oscillate. The locations of the aggregates were random due to the dynamic nature of MB destruction.

Figure 1 shows still frames of a high speed movie (5 Mpfs) of polymer MBs 1,000 acoustic cycles into a long tone burst at 1.5 MPa. MB aggregates continued to oscillate, break up, and new aggregates were formed. Figure 2 shows the cavitation strength of as a function of time (cycle length) for various bubble concentrations. Similar behaviors were observed for lipid MBs.

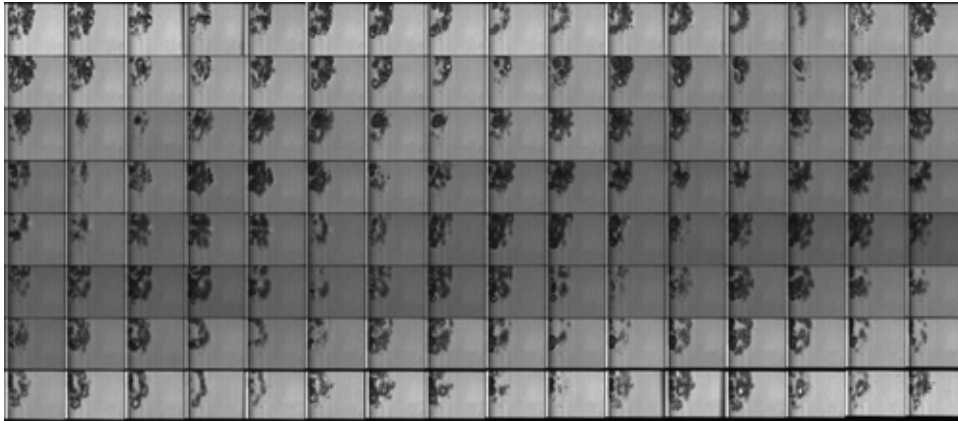


Figure 1: Sequential still frames of high speed movie showing the continued formation of MB aggregates 1,000 acoustic cycles into a long tone burst. For this example, the movie was taken at 5 Mpfs and the movie duration was 25.6 ms (1.5 MPa, 1 MHz).

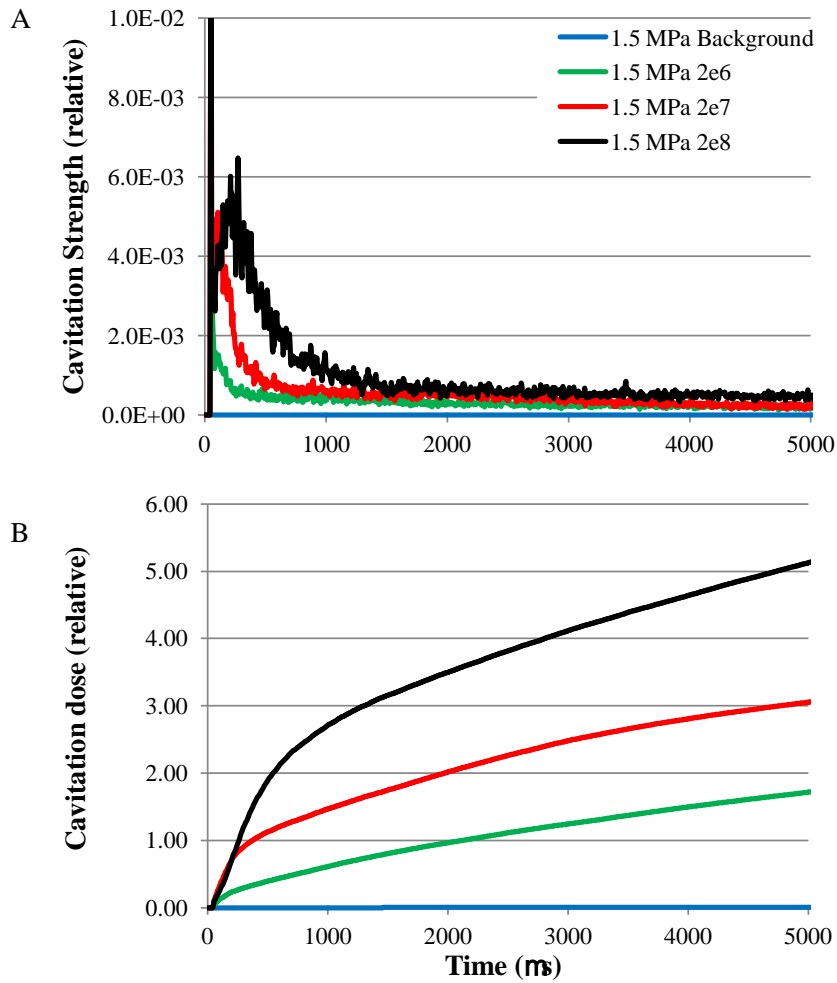


Figure 2: A. Relative cavitation strength (the mean value of power spectra in 4.2-4.8 MHz frequency band) as a function of time (cycle length) for various bubble concentrations. B. Cumulative cavitation doses as a function of time for various bubble concentrations. Ultrasound parameters: 1 MHz, 1.5 MPa, 5000 acoustic cycles. Background is defined as saline only without MBs.

Conclusion

These data indicate that MBs survive as aggregates that continue to oscillate with large amplitude during a long tone burst, demonstrating the therapeutic potential for US-assisted therapy. This discovery suggests that long acoustic cycles have additional therapeutic effect for MB-US assisted therapies such as sonothrombolysis.

Automatic respiratory motion gating for the quantification of liver therapy monitoring

Damianos Christofides¹, Edward Leen², Michalakis Averkiou¹

¹*Department of Mechanical and Manufacturing Engineering, University of Cyprus, Nicosia, Cyprus*

²*Imaging Department, Hammersmith Hospital, London, UK*

Introduction

One of the biggest challenges in the quantitative evaluation of liver lesions with Dynamic Contrast Enhanced Ultrasound (DCEUS) is motion due to respiration, where the lesion being imaged seems to be changing in shape, location, and size, as demonstrated in

Figure 1. Respiratory motion can be addressed by directing patients to hold their breath while an image loop is collected. However it is very difficult, if not impossible, for most patients to hold their breath for over 40 seconds. In addition, hemodynamics is affected during breath hold. Another technique published in the literature[1] is to identify the position of the diaphragm at a reference position and manually reject frames in which the diaphragm deviates from the reference position; this technique can be implemented after the acquisition of the ultrasound loop, but it is time consuming and prone to errors.

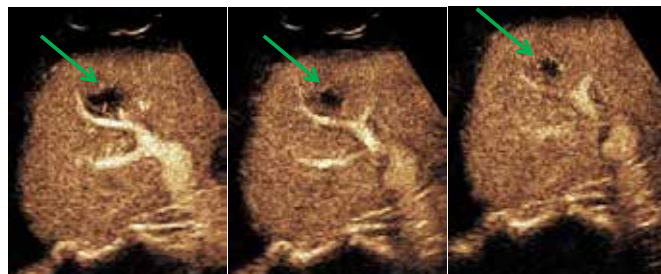


Figure 1: Example of the changes of the size, location, and shape of a liver lesion, in a DCEUS loop, at three different time instances. These changes are mainly attributed to respiratory motion.

Several computational techniques have been proposed that would allow for the automatic gating of respiratory motion[2]–[5]. In the present work a new method is proposed by which a side-by-side DCEUS/B-Mode loop can be gated for respiratory motion automatically. The only intervention needed by the user is to choose a frame, called the “trigger frame”, in which the lesion is clearly seen and can be delineated.

Method

The following are the steps for the automatic respiratory gating algorithm that are applied on B-Mode images of the loop:

- a. The user defines the trigger frame (image). This frame identifies the phase of the breathing cycle to be extracted.
- b. Each frame (2a) is subtracted from the average of all the frames (Figure 2b) [6] and a certain number of structures are extracted as a binary image (2c).
- c. The resulting binary images are added together to form a matrix, see Figure 2d.

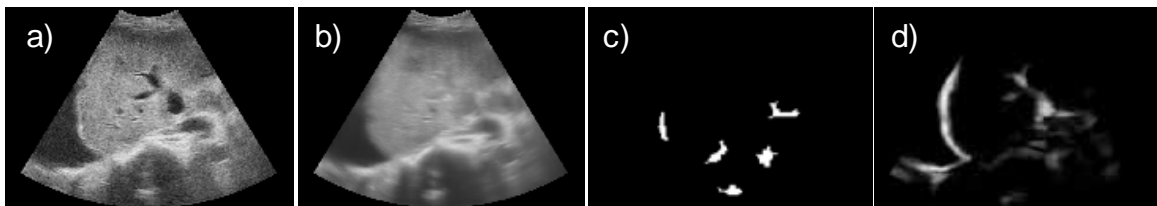


Figure 2: Examples of a) frame from a B-Mode loop, b) average of all the frames, c) structures extracted by subtracting a frame from the average and d) matrix containing the addition of binary images obtained in step (b).

- d. The structures extracted from the trigger frame in step (b) are compared with the information extracted in step (c) in order to be ranked according to the amount of motion associated with them. Also their frequency content is assessed in relation to the frequency range of respiration.
- e. The structure that is ranked first based on the criteria of step (d) is chosen as a binary mask used to extract the respiratory kinetics of the loop.
- f. Respiratory gating is performed by detecting the peaks and troughs of the respiratory kinetics curve. A piecewise cubic Hermite interpolating polynomial (pchip) is fitted on the peaks and troughs. A threshold is then applied on the respiratory kinetics curve in relation to the pchip fit. Frames that are below the chosen threshold are considered not to be at the same breathing cycle phase as the trigger frame and are rejected; an example of this step is shown in Figure 3.

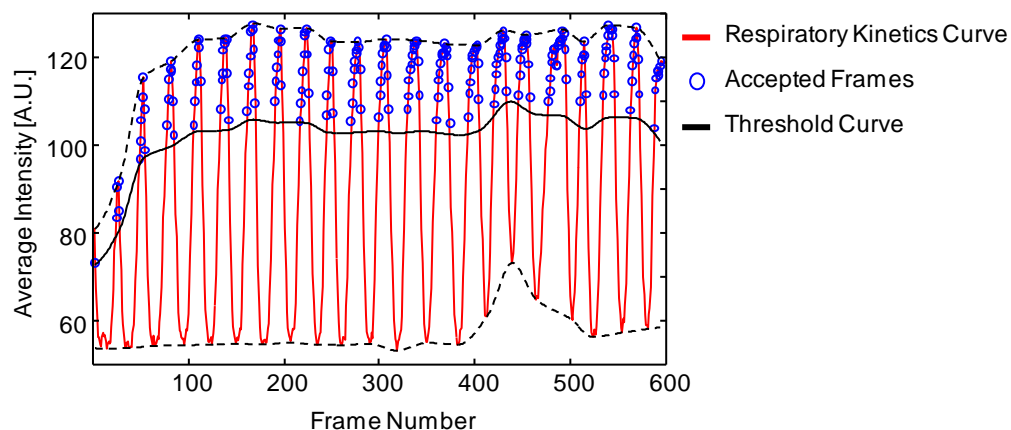


Figure 3: Example of the respiratory gating performed on a respiratory kinetics curve, as it was extracted by the binary mask obtained in step (e).

The algorithm for the automatic respiratory gating was tested on 12 clinical cases of liver cancer patients. Linearized time-intensity curves (TIC) from the lesions were extracted from DCEUS loops with and without gating. The data were fitted to a lognormal function that can characterize the indicator dilution curve of a liver lesion [7]. The goodness of fit of the model to the data was quantified using the R-squared (R^2) value and the root mean squared error (RMSE).

Results

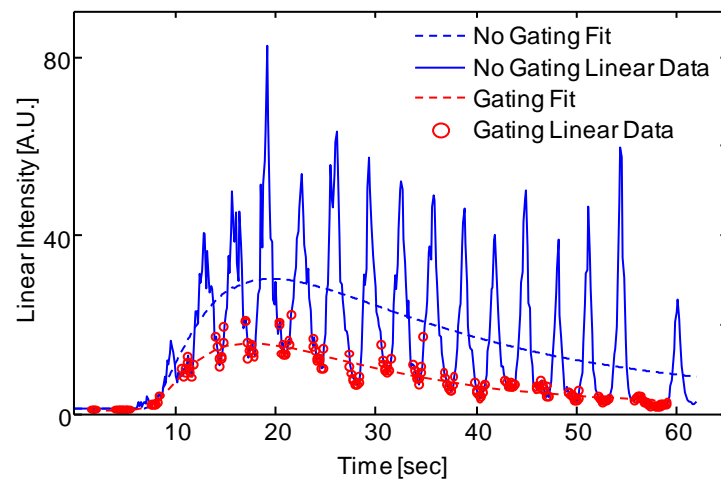


Figure 4: Example of a time intensity curve of a liver metastasis with and without gating performed. The dashed lines are the curve fit to the lognormal model.

A sample TIC obtained with and without automatic respiratory gating is shown in Figure 4. Without respiratory gating the TIC is highly oscillatory and often large spikes appear due to sampling that takes place outside the lesion are seen. With respiratory gating the oscillations almost disappear and the influence from respiratory motion is greatly reduced (see red data points in Figure 4).

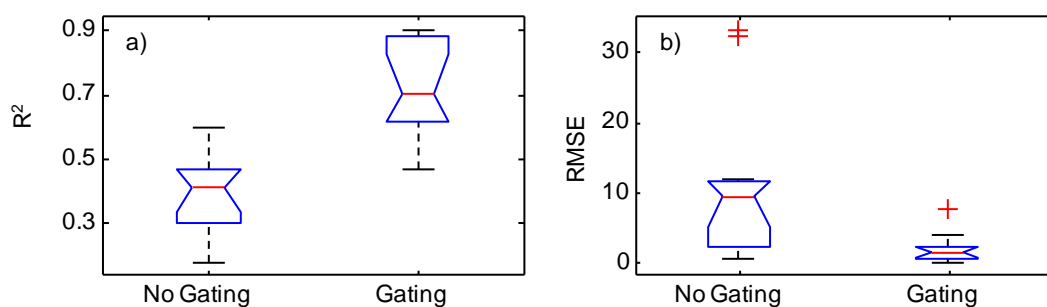


Figure 5: a) Boxplots of the R^2 values and b) Boxplots of the $RMSE$ for the model fit of the clinical cases analyzed with and without gating. The notches on the boxplots are 95% confidence levels.[8]

From the data presented in **Figure 5** it is evident, within a 95% confidence level, that the automatic gating method proposed is beneficial to the fit of the DCEUS linear data onto the lognormal indicator dilution model. Finally our algorithm is faster [1.1 ± 0.06 seconds per 100 frames when it implemented with MATLAB (The MathWorks Inc., Natick, MA, 2000) on an Intel E8400 3GHz PC] than previously published results[2], [4], [5].

Conclusion

An automated and easy to implement and use respiratory gating algorithm has been developed that it is suitable for DCEUS quantification. The algorithm was tested on 12 patient loops (liver metastasis from colorectal cancer) and it effectively removed respiratory motion. Removal of respiratory motion has resulted in improved R^2 and $RSME$ of the curve fits to the lognormal model. In addition, the gated loops were easier to qualitative assess and increased the confidence in clinical evaluation. Overall, this algorithm has the potential to be implemented in the clinical setting and will allow for accurate and fast quantitative analysis of DCEUS loops in the monitoring of liver therapy.

References

1. M. Averkiou, M. Lampaskis, K. Kyriakopoulou, D. Skarlos, G. Klouvas, C. Strouthos, and E. Leen, "Quantification of tumor microvascularity with respiratory gated contrast enhanced ultrasound for monitoring therapy," *Ultrasound Med Biol*, vol. 36, no. 1, pp. 68–77, Jan. 2010.
2. G. Renault, F. Tranquart, V. Perlberg, A. Bleuzen, A. Herment, and F. Frouin, "A posteriori respiratory gating in contrast ultrasound for assessment of hepatic perfusion," *Phys Med Biol*, vol. 50, no. 19, pp. 4465–4480, Oct. 2005.
3. N. Rognin, R. Campos, J. Thiran, T. Messenger, P. Broillet, P. Frinking, M. Mercier, and M. Arditi, "A new approach for automatic motion compensation for improved estimation of perfusion quantification parameters in ultrasound imaging," presented at the 8th French Conference on Acoustics, Tours, France, 2006, pp. 61–65.
4. J. Zhang, M. Ding, F. Meng, M. Yuchi, and X. Zhang, "Respiratory motion correction in free-breathing ultrasound image sequence for quantification of hepatic perfusion," *Med Phys*, vol. 38, no. 8, pp. 4737–4748, Aug. 2011.
5. S. Mulé, N. Kachenoura, O. Lucidarme, A. De Oliveira, C. Pellot-Barakat, A. Herment, and F. Frouin, "An automatic respiratory gating method for the improvement of microcirculation evaluation: application to contrast-enhanced ultrasound studies of focal liver lesions," *Phys Med Biol*, vol. 56, no. 16, pp. 5153–5165, Aug. 2011.
6. A. K. Jain, *Fundamentals of digital image processing*. Englewood Cliffs, NJ: Prentice Hall, 1989.
7. C. Strouthos, M. Lampaskis, V. Sboros, A. McNeilly, and M. Averkiou, "Indicator dilution models for the quantification of microvascular blood flow with bolus administration of ultrasound contrast agents," *IEEE Trans Ultrason Ferroelectr Freq Control*, vol. 57, no. 6, pp. 1296–1310, Jun. 2010.
8. J. M. Chambers, W. S. Cleveland, B. Kleiner, and P. A. Tukey, *Graphical Methods for Data Analysis*. Chapman and Hall, 1983.

Towards quantification of plaque neovascularisation in human carotid arteries – a preliminary study of attenuation correction and segmentation in CEUS images

Jeremy Girard-Desprolet¹, Nikolaos Mavropoulos¹, Wing Keung Cheung¹, Benoy Shah², Navtej Chahal², David Cosgrove³, Roxy Senior², Robert J Eckersley⁴, Meng-Xing Tang¹

¹Department of Bioengineering, Imperial College London, UK

²Department of Cardiology and Echocardiography Laboratory, Royal Brompton Hospital, UK

³Imaging, Hammersmith Campus, Imperial College London, UK

⁴Division of Imaging Sciences, King's College London, UK

Background and aim

Neovascularisation within atherosclerotic plaques is associated with risk of plaque rupture. Contrast enhanced ultrasound (CEUS) has shown potential for imaging and quantifying neovascularisation in such plaques and vasa vasorum [1]. However, current quantification of CEUS images is hampered by attenuation and nonlinear artefacts [2-6]. Furthermore, the analysis of such images is dependent on manual analysis of the regions of interest. Both image artefacts and manual analysis contribute to large variations in quantification of CEUS images. In this study, we aim to develop attenuation correction and computer assisted image segmentation techniques for CEUS images of human carotid arteries.

Methods

Towards attenuation correction, a model was fitted to the image intensity within the lumen, based on which corrections were made for regions within and below the lumen. For image segmentation, a three step algorithm was developed: firstly, two seed points were manually placed in the lumen; secondly, initial estimations of both lumen-intima and media-adventitia interfaces were made through a spatially constrained search of edges across the image; finally these results were refined with temporal constraints with neighbouring frames in the time series of images. Both attenuation and image segmentation were conducted on clinical CEUS images of ten patients.

Results

An example of an attenuation corrected image is shown in Fig 1. Initial analysis show an increase in correlation between contrast enhancement in plaques and adventitia vasa vasorum and patient clinical risk score, although further studies are needed to confirm this finding.

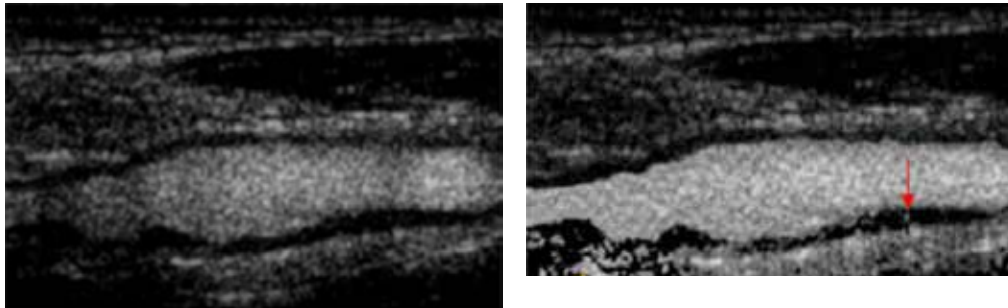


Figure1: an example of CEUS images of carotid before (left) and after (right) attenuation correction. The red arrow points to a bubble that might have been missed due to signal attenuation

An example of the computer assisted image segmentation results is shown in Fig 2. The initial results are found to be consistent with those of manual segmentation.

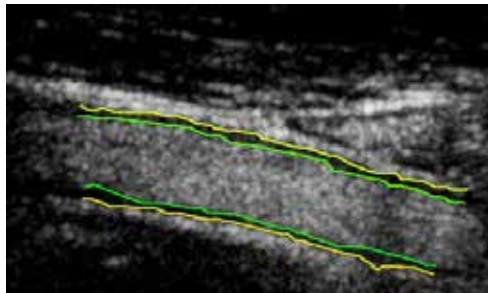


Figure2: an example of image segmentation result. Green lines indicate lumen-intima interface, while yellow lines indicate media-adventitia interface.

Conclusions

To our knowledge this is the first study to develop attenuation correction and computer assisted image segmentation in CEUS carotid images. Our preliminary results suggest that the developed algorithms have promise for improved contrast quantification. This is a first step towards a more reliable and less subjective assessment of neovascularisation and vasa vasorum in CEUS carotid images.

References

1. Feinsein, S.B., *Contrast ultrasound imaging of the carotid artery vasa vasorum and atherosclerotic plaque neovascularization. Journal Of the American College Of Cardiology*, 2006. **48**(2): p. 236-243.
2. Tang, M.X., et al., *Quantitative contrast-enhanced ultrasound imaging: a review of sources of variability. Interface Focus*, 2011. **1**(4): p. 520-539.
3. Tang, M.X., et al., *ATTENUATION CORRECTION IN ULTRASOUND CONTRAST AGENT IMAGING: ELEMENTARY THEORY AND PRELIMINARY EXPERIMENTAL EVALUATION. Ultrasound In Medicine and Biology*, 2008. **34**(12): p. 1998-2008.
4. Tang, M.X., N. Kamiyama, and R.J. Eckersley, *EFFECTS OF NONLINEAR PROPAGATION IN ULTRASOUND CONTRAST AGENT IMAGING. Ultrasound In Medicine and Biology*, 2010. **36**(3): p. 459-466.
5. Thapar, A., et al., *Dose-Dependent Artifact in the Far Wall of the Carotid Artery at Dynamic Contrast-enhanced US. Radiology*, 2012. **262**(2): p. 672-679.
6. ten Kate, G.L., et al., *Far-Wall Pseudoenhancement During Contrast-Enhanced Ultrasound of the Carotid Arteries: Clinical Description and In Vitro Reproduction. Ultrasound in Medicine & Biology*, 2012. **38**(4): p. 593-600.

Ultrasound and microbubble guided delivery of microRNA-based therapeutics *in vitro* and *in vivo*

R.F.J. Kwekkeboom¹, Z. Lei⁴, S.J.P. Bogaards¹, E. Aiazian^{2,3}, O.Kamp³, J.P. Sluijter⁴,
R.J.P. Musters¹

¹Department of Physiology, ICar-VU, VU University Medical Center, Amsterdam,
the Netherlands

²Genus Biotech Corp, United States of America

³Department of Cardiology, ICar-VU, VU University Medical Center, Amsterdam,
the Netherlands

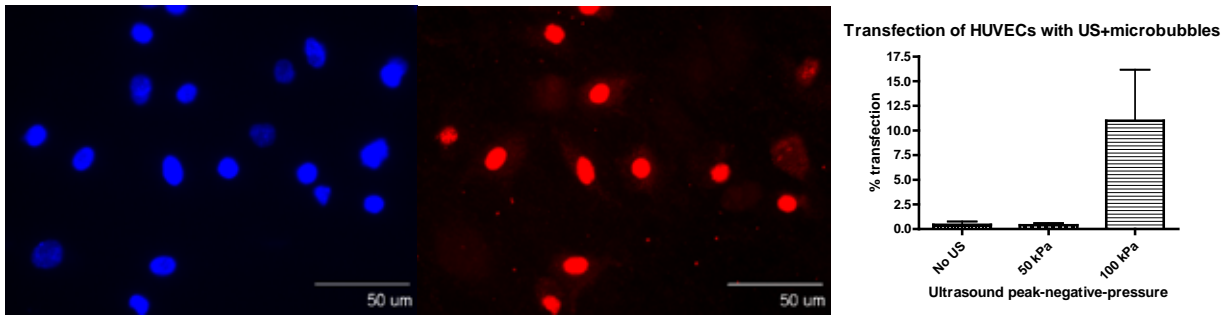
⁴Department of Cardiology, Division Heart and Lungs, University Medical Center Utrecht,
Utrecht, the Netherlands

We aim to locally deliver microRNA-based therapeutics for the treatment of hypoxic disorders like peripheral vascular disease or prevention of heart failure after myocardial infarction (MI). Here we present our progress on miRNA based therapeutics delivery both *in vitro* and *in vivo* in a mouse-model.

We designed and produced cationic lipid microbubbles (MB) that complex with miRNA and miRNA blocking agents (antimiR) through electrostatic interaction. *In vitro*, we treated human umbilical vein endothelial cells (HUVECs) with microbubble-antimiR (fluorescent) complexes and ultrasound (US) intensities below 200 kPa peak negative pressure (PnP) at 1 MHz. Transfection was determined by means of quantitative fluorescence microscopy. For *in vivo* local delivery, we complexed cationic microbubbles with pre-miRNA-159a. These complexes were injected intravenously in mice after which ultrasound was applied to the right hind limb. Skeletal muscles were extracted and miRNA-content was determined by means of qPCR in both the US+MB treated and non-treated hind limbs. The same *in vivo* protocol was applied to locally deliver fluorescent antimiR to the right hind limb of mice. We determined local delivery and antimiR spatial deposition qualitatively using fluorescence microscopy.

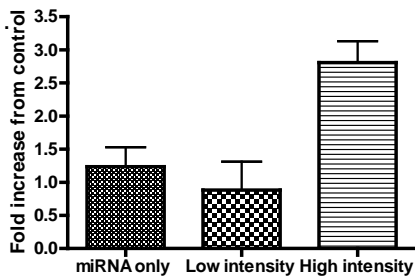
We found that *in vitro*, HUVECs can be transfected with antimiR using ultrasound at 100 kPa PnP but not at 50 kPa or without applying US. Mean transfection% at 100 kPa was 11%. Additionally, we succeeded in increasing *in vivo* delivery of miRNA to the ultrasound microbubble treated area compared to control tissue and visualized the location of the miRNA based therapeutics in the tissue. These results demonstrate the feasibility of ultrasound and cationic microbubbles for both *in vitro* antimiR and *in vivo* microRNA delivery and give us information on the location of our therapeutics. This gives us a clue what cell types and processes might be treated with ultrasound and microbubble guided miRNA based therapy.

Figures:



Fluorescence microscopy picture of HUVECs at 40x magnification. Nuclei are visualized in blue and transfected antagomiR in red. Right panel shows quantification of transfection efficiency as a result of different ultrasound settings.

miR159 delivery in US-treated hind limb



Local delivery of pre-miRNA-159a. Bars represent the fold-increase in miRNA content in the treated muscle compared to non-treated muscle in the same mouse. The miRNA only group received miRNA without bubbles and was treated with the high intensity US protocol.

This research forms part of the Project **P1.05 LUST** of the research program of the **BioMedical Materials** institute, co-funded by the **Dutch Ministry of Economic Affairs, Agriculture and Innovation**. The financial contribution of the **Nederlandse Hartstichting** is gratefully acknowledged.

Studies on agent delivery via ultrasound and microbubbles

*Jason Castle, Matthew Butts, Carl Chalek, David Mills, Jeannette Roberts, Andrew Torres
& Kirk Wallace*

GE Global Research, Niskayuna, NY 12309 USA

Apolipoprotein A-I (apo A-I) is the predominant protein component of high-density lipoprotein (HDL) in plasma, and in animal models, increasing apo A-I in transgenic animals or infusing recombinant HDL (rHDL) promotes prominent regression of atherosclerosis and enhanced macrophage-specific reverse cholesterol transport. Additionally, elevated LDL and low HDL remain independent risk factors for cardiac disease. Furthermore, patients genetic incapable of producing significant levels of HDL (hypoalphalipoproteinemia) demonstrate a debilitating disease prone to early cardiac disease and ultimately death. Although well described, the pharmaceutical intervention of HDL has yet remained allusive.

Here, we report on the efficacy of *in vivo* studies to alter HDL regulation through the targeted delivery of apo A-I DNA. Utilizing ultrasound mediated targeted drug delivery, apo A-I DNA is transported to the liver via intravenous injection of diagnostic microbubble (Optison). Upon perfusion, ultrasound acoustic energy is directed to the liver (GEHC Vivid *i* system) for site-selective cavitation of the microbubbles. This facilitates the delivery of apo A-I DNA to the hepatic intracellular environment. We have demonstrated a study response rate as high as 93%, with rats averaging a 32% increase in HDL level 24 hours post-procedure. Early data in the rabbit model has shown an even more dramatic response to therapy. These results were observed with a lack of significant effects related to liver function and cellular viability.

Additionally we present the delivery of Cyanine labeled PEG (20K) serving as a model drug compound. This data suggests an ultimate utility of this delivery platform to allow therapeutic intervention in challenging diseases by enabling a wider therapeutic index for small molecule drugs as well as improving both the safety and efficacy of gene therapy.

Quantitative evaluation of *ex vivo* livers in machine perfusion with dynamic contrast-enhanced ultrasound

Maria-Louisa Izamis, Andreas Efstathiades, Christina Keravnou and Michalakis Averkiou

Department of Mechanical and Manufacturing Engineering, University of Cyprus, Nicosia, Cyprus

Introduction

Liver transplantation, the only treatment for acute and end-stage liver failure, is severely limited by the global shortage of viable donor organs. In the United States alone, 6,342 transplantations were conducted in 2011 saving the lives of just 28% of the waitlisted patients¹. An estimated 50,000 donor organs could be added to the donor pool if they are recovered to a viable state². However, the current gold standard of organ preservation, static cold storage (SCS), is incapable of delivering and monitoring the necessary treatment these suboptimal organs need. Further, no quantitative metric of organ function exists; utility is based instead on subjective measures of organ history, texture, and appearance. As a consequence, an immensely valuable resource is being lost. Machine perfusion (MP) represents a markedly superior methodology to SCS, since it operates as an artificial body with an artificial blood supply for the isolated organ. Data acquired during perfusion can be analyzed for objective diagnoses and prognoses^{3,4} while administering the necessary treatment to recover the organ to a useful state⁵⁻⁷. Here we introduce dynamic contrast-enhanced ultrasound (DCEUS) as a powerful qualitative and quantitative methodology for non-invasive evaluation of organ recovery during *ex vivo* machine perfusion.

Methods

Animals

Healthy porcine livers were procured from the local abattoir⁸ and randomly divided into 3 groups according to the size of air embolism (AE) introduced to sustain ischemic damage: (1) No AE, (2) Minor AE, (3) Major AE. Livers were flushed with 7L of ice cold Lactated Ringers through both the portal vein (PV) and hepatic artery (HA) followed by an air column sized according to the group (0cc, 5cc, 10cc). The organs were stored on ice and transported to the laboratory where they were connected to the machine perfusion system; warm ischemia time <1hr, cold ischemia (SCS) time ≤2 hrs.

Machine Perfusion

The system comprised of an organ chamber that doubled as a perfusate reservoir. Two peristaltic pumps circulated the perfusate through an oxygenator (95%O₂, 5%CO₂) and a bubble trap prior to perfusing the liver through the portal vein and hepatic artery (Figure 1A). Flow rate was pressure-controlled (PV≤5mmHg, HA=100mmHg). The perfusate comprised 7L of a modified cell culture medium⁵. Bile

samples and vascular resistance were measured every half hour and histology was conducted at the end of perfusion.

DCEUS imaging

To monitor the microcirculation of a specific region, a linear array probe (L9-3) was held in a fixed position on the liver with a mechanical arm (Figure 1B). A bolus of 0.2 mL SonoVue (Bracco S.P.A., Milan, Italy) was injected into the PV followed by an injection into the HA. Image loops of 40sec were captured for each injection with “Contrast side/side” (contrast/tissue) mode. Evaluation of the extent of systemic perfusion by each vessel was conducted after each bolus using a linear array probe (L12-5). High MI imaging was used to eliminate remaining microbubbles between injections. The above procedure was repeated every hour over three hours of perfusion. A region of interest (ROI) was placed at the same site in each of the lobes in all loops, avoiding large vessels, and time intensity curves of the ROIs were processed using commercial quantification software (QLAB version 8.1; Philips Medical System, Bothell, WA, USA). The data were then imported into MATLAB (MathWorks, Inc., Natick, MA, USA) and a custom “Lognormal Model” function was fitted to calculate wash-in time (WIT) and peak intensity (PI).

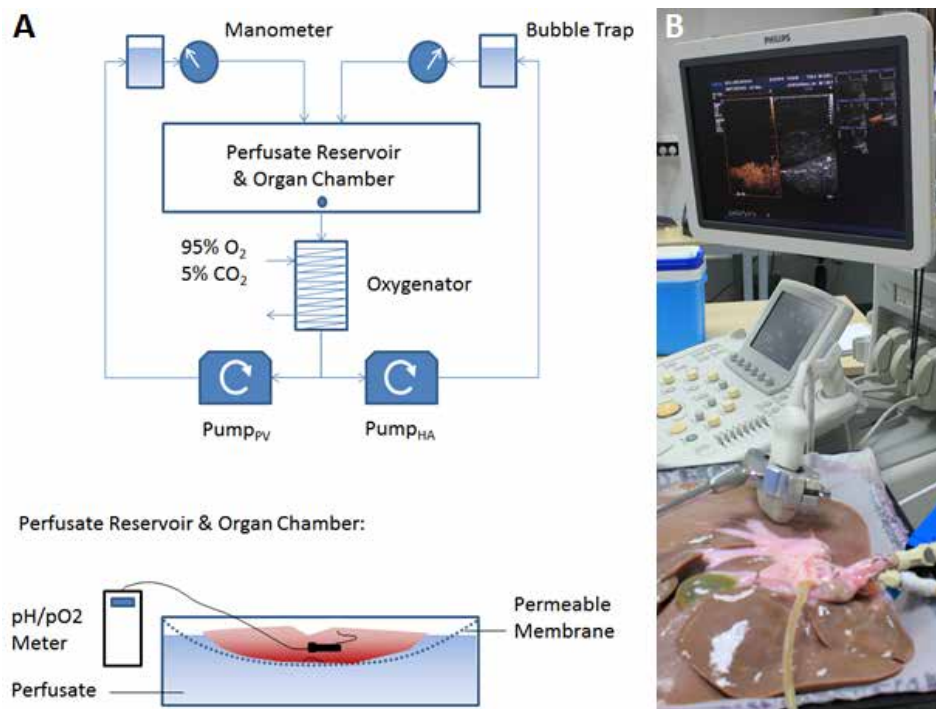


Figure 1: Machine perfusion operated at room temperature is simpler in design than at any other temperature (A) and enables ease of access to the organ for evaluation and treatment (B).

Results

A novel room temperature machine perfusion system has been developed capable of sustaining human-sized porcine livers for at least 3 hours as evidenced by stable WITs, PIs, bile production and hepatic resistances in the “No AE” group. The standard use of organ history, texture and appearance proved completely inadequate in detecting dramatic differences between the experimental groups, while systemic evaluation with DCEUS showed a dose-dependent decline in perfusion with increasing air embolism size (Figure 2). Air embolism size was also negatively correlated with bile production and positively correlated with hepatic resistance. Histology confirmed significantly reduced cell viability in areas of poor- and no-flow. DCEUS confers pathology specificity, accuracy in location, and the ability to intervene (e.g. sonothrombolysis) making it a highly complementary addition to machine perfusion optimization of donor organs.

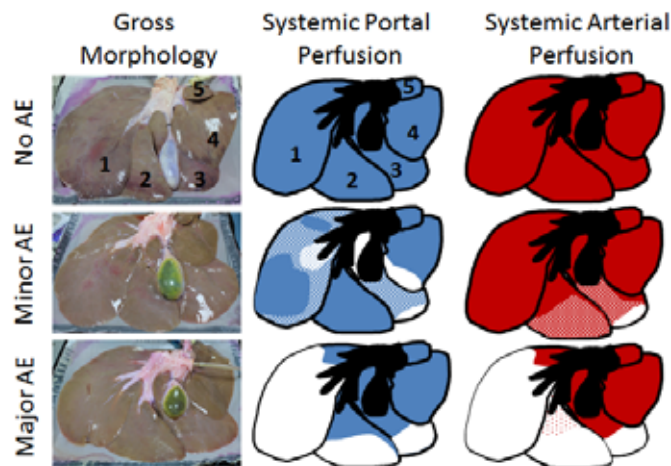


Figure 2: At t=3hrs of perfusion, gross morphology cannot reveal the differences in extent of perfusion between groups that is present in the portal vein and hepatic artery. Shaded areas=optimal perfusion, white areas=no perfusion, spotted areas=marginal perfusion.

Concluding remarks

The novel combination of DCEUS and machine perfusion enables enhanced diagnostic and prognostic capabilities, and can facilitate optimal recovery of disqualified donor organs to a functional state, thereby ultimately increasing the availability of treatment options for patients with end-stage organ failure. The ability to individually control the HA and PV flows will allow for detailed characterization of liver hemodynamics. Future work will concentrate on accurate microcirculation quantification and specifically as applied in therapy monitoring. The machine-perfused human-sized liver will also be useful in the study of ultrasound-enhanced drug delivery.

Acknowledgements

This work was co-funded by the European Regional Development Fund and the Republic of Cyprus through the Research Promotion Foundation (Project: DIDAKTOR/0311/78).

References

1. *Organ Procurement and Transplantation Network* URL: optn.transplant.hrsa.gov (Accessed 1 December, 2012).
2. Deshpande, R.H., N. Can non-heart-beating donors replace cadaveric heart-beating liver donors? *Forum on Liver Transplantation/ Journal of Hepatology* **45**, 499-503 (2006).
3. Perk, S., et al. A metabolic index of ischemic injury for perfusion-recovery of cadaveric rat livers. *PLoS ONE* **6**, e28518 (2011).
4. Perk, S., et al. A fitness index for transplantation of machine-perfused cadaveric rat livers. *BMC Res. Notes* **5**(2012).
5. Izamis, M.L., et al. Simple machine perfusion significantly enhances hepatocyte yields of ischemic and fresh rat livers. *Cell Medicine* **In press**(2012).
6. Tolboom, H., et al. Subnormothermic machine perfusion for recovery and preservation of ischemic rat liver grafts. *J. Surg. Res.* **175**(2011).
7. Uygun, B.E., et al. Organ reengineering through development of a transplantable recellularized liver graft using decellularized liver matrix. *Nat. Med.* **16**, 814-820 (2010).
8. Grosse-Siestrup, C., et al. The isolated perfused liver: a new model using autologous blood and porcine slaughterhouse organs. *J. of Pharmacological and Toxicological Methods* **46**, 163-168 (2002).

Feasibility of standard thrombolysis with the additional therapeutic application of contrast-enhanced ultrasound for acute peripheral arterial occlusions in a porcine model

Johanna H Nederhoed¹, Harm P Ebben¹*, Menno Groeneveld¹, Jeroen Slikkerveer², Otto Kamp², Geert-Jan Tangelder³, Willem Wisselink¹, René JP Musters³, Kak K Yeung^{1,3}*
** Equal contribution*

Departments of ¹surgery, ²cardiology, ³physiology, VU University Medical Center, Amsterdam, the Netherlands

Introduction

Adding local ultrasound to standard intra-arterial thrombolytic therapy has potential to enhance the effect of thrombolysis. Further amplification of thrombolysis can be ensured with the additional use of ultrasound contrast agents, i.e. microbubbles. Therapeutic potential of this technique has been investigated in the settings of stroke and myocardial infarction. In this study we investigated the feasibility of the addition of contrast-enhanced ultrasound (CEUS) to standard intra-arterial thrombolysis in large peripheral arterial occlusions and its potential beneficial effect in a porcine model.

Methods

In ten Yorkshire pigs arterial thrombus was created by mechanical occlusion of 4 cm of the common iliac artery and injection of intraluminal thrombin (Figure 1). Six animals received urokinase therapy via an intra-arterial catheter with concomitant injections of microbubbles (5x 5mL SonoVue vials during the first hour, 15 minutes intervals) intravenously and local intermittent application of ultrasound, 5 seconds off, 1 second on (MI=1.1, 1.6 MHz, focus 3cm). Four pigs exclusively received thrombolytic therapy with continuous urokinase infusion via an intra-arterial catheter. The procedure was stopped and the animals were terminated after three hours of therapy. Parameters measured were iliac blood flow directly distal to the occlusion (by ultrasonic flow probe), microcirculation of the skin (by Laser Doppler), Mean Arterial Pressures (MAP, systemic and in the affected limb), temperature (systemic and in both limbs) and thrombus weight post-mortem. Post-mortem all vital organs were macroscopically investigated on haemorrhagic complications.

Results

Four out of six pigs that received the investigational therapy showed improvement of arterial blood flow during the procedure (Figure 2a). In the standard thrombolysis group, improvement of arterial blood flow was seen in one out of 4 pigs (Figure 2b). Microcirculation and MAP levels fluctuated amongst groups during the procedure, no obvious trends were observed (results not shown).

Thrombus weights may reflect a trend towards lower thrombus weight in the group receiving the interventional therapy (Figure 3a,b). No signs of haemorrhagic complications were observed during the procedures or at the autopsies.

Conclusions

In our porcine model we observed beneficial effects within three hours of therapy with thrombolysis and additional CEUS for large peripheral arterial occlusions in regards to arterial blood flow and thrombus weight. Furthermore, no haemorrhagic complications occurred during these experiments. Therefore, adding CEUS to standard intra-arterial thrombolytic therapy has the potential to improve thrombolytic effect in large peripheral arterial occlusions in a safe manner and should be further investigated in a clinical setting for therapeutic potential.

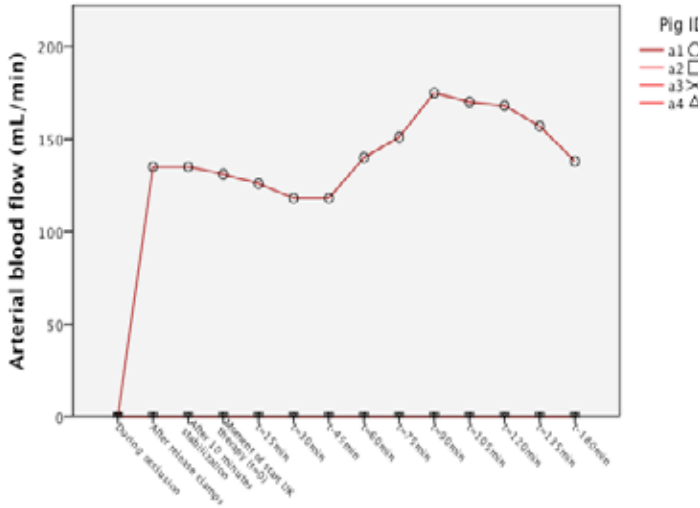
Figures

Figure 1: 4cm thrombus was created in the common iliac artery



Figure 2: Arterial blood flow curves

a. Pigs receiving standard thrombolysis.
Flow of a2, a3 and a4 remained zero.



b. Pigs receiving standard thrombolysis + additional CEUS.
Flow of b4 and b5 remained zero.

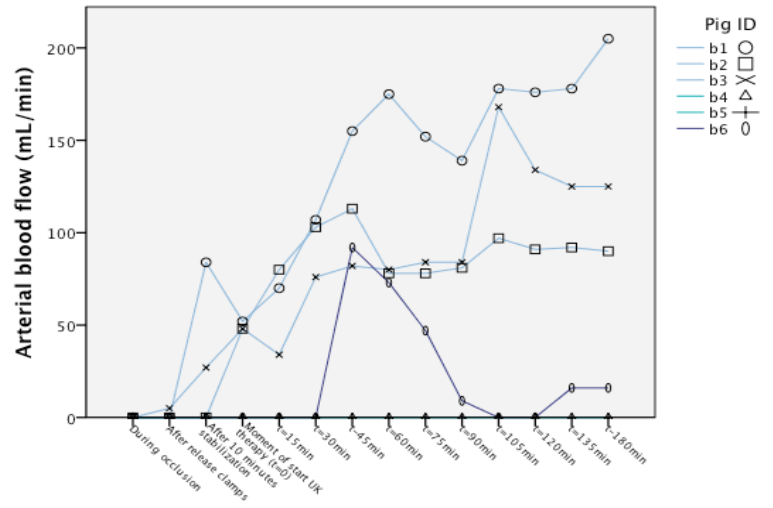
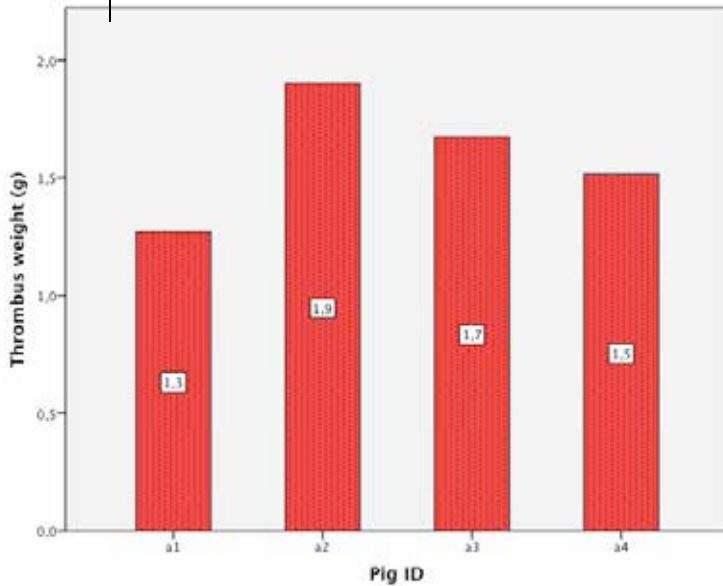
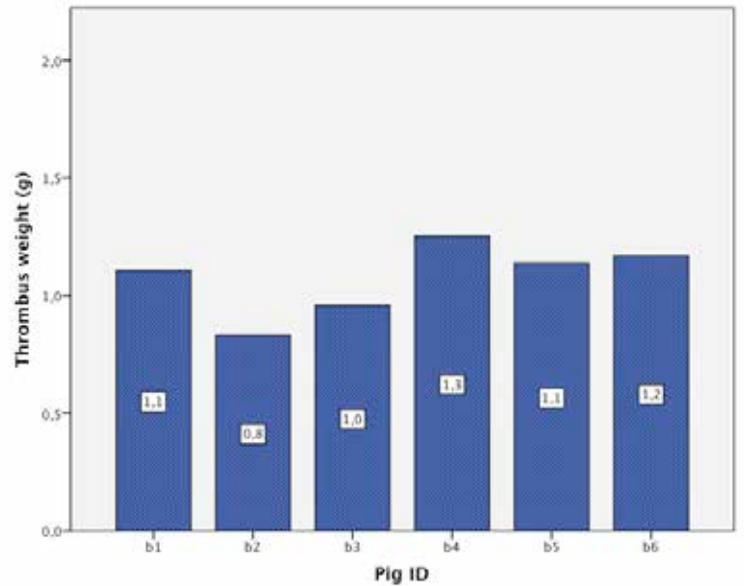


Figure 3: Thrombus weight post-mortem

a. Pigs receiving standard thrombolysis.



b. Pigs receiving standard thrombolysis + additional CEUS.



Numerical and experimental analyses of the translation of microbubbles under short acoustic pulses

Elena Iguualada-Villodre, Indrajit Chakraborty, Ana Medina-Palomo and Javier Rodríguez-Rodríguez

Fluid Mechanics Group. Universidad Carlos III de Madrid, 28911 Leganés, Spain

The present study investigates the translational dynamics of microbubbles under the effect of short acoustic pulses. Nowadays, a very active line of research in ultrasound medical imaging consists of the use of microbubbles as contrast agents. Besides their use as contrast agents, microbubbles can be also employed as drug-carriers to transport drugs inside the blood stream. It is well known that, when excited with an ultrasound pressure wave, bubbles experience a force that pushes them along the axes of propagation of the wave. This force, commonly known as Bjerknes force, is the physical effect that allows us to direct the bubble toward specific targets inside the circulatory system.

Although in principle the idea is simple, in practice the values of the Bjerknes force are too small to significantly affect the trajectory of microbubbles in the blood stream. This makes necessary to optimize the insonation strategies to maximize the transport of bubbles using ultrasound. In particular, an interesting option is to perform numerical simulations of the effect that the ultrasound would have on the bubbles.

In common medical applications, bubbles are excited with short acoustic pulses. Therefore, acoustic fields consisting of short pulses have been considered to perform such simulations. Experiments have been developed in order to corroborate the theoretical computations of primary Bjerknes force on bubbles. For that purpose it is necessary to have an isolated bubble so the secondary Bjerknes force can be neglected. It is experimentally observed that bubbles suffer a translation in the direction of propagation of the acoustic wave while the acoustic pulse is active. Once the pulse has finished, bubble slows down until it reaches the steady state it had before the ultrasound. Interestingly, the deceleration of the bubble after the insonation pulse is much slower than predicted by existing models of the process [1].

Although commonly ignored in most of the scientific literature on microbubbles, as pointed out by Garbin et al. [2], there exist two physical effects that should account for this discrepancy. Namely, the history force and the longer decay time of the bubble radial oscillations compared to the braking time of the bubble [3]. The main goal that has motivated our research is precisely to clarify this point, i.e., to quantify the importance of these physical effects in the deceleration of the bubble after the acoustic pulse.

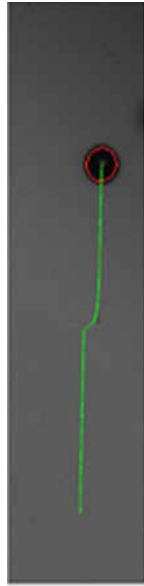
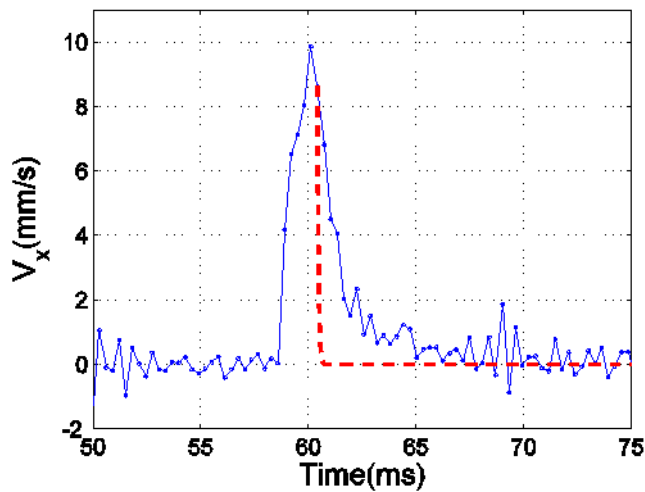


Fig 1: (a) High-speed video sequence which illustrates the trajectory (green points) of a bubble of radius $R_0=30\mu\text{m}$ rising in water due to buoyancy and under the effect of short ultrasound pulses propagating in the horizontal direction.



(b) The dotted blue line represents the bubble experimental velocity in the horizontal direction as obtained using tracking algorithm. The dashed red line represents numerical calculations of the model proposed by Toilliez & Szeri [1], which clearly predicts a much faster braking than that observed.

To this end, a simplified model has been considered. The only external force acting on the bubble in this model is the gravitational one, such that the bubble is rising due to buoyancy effects. After some time gravity is turned off ($g=0$) and the bubble slows down until it reaches its steady state. To study this simplified problem, a full numerical simulation has been carried out, consisting of a coupled level-set and volume-of-fluid (CLSVOF) [4]. The CLSVOF method solves a single set of governing equations (continuity equation for mass conservation and full Navier-Stokes equations for momentum conservation) for gas and liquid phases using variable transportive (density and viscosity) on a fixed

Eulerian two-dimensional (2D) mesh in axisymmetric co-ordinates. In this method, a level-set function (f) is used to track the interface and the volume-of-fluid function (F) is used to ensure mass conservation. The influence of surface tension is incorporated into the momentum equation following the continuum surface force (CSF) model of Brackbill et al. [5]. The numerical method [6] has been extensively validated with the experimental results available in literature.

Results provided by the full numerical simulations are qualitatively good in a sense that they predict a slower deceleration of the bubble than that of the simplified model after the external forcing disappears. It is important to note that these preliminary results do not take into account transient volume oscillations. Thus, the mentioned discrepancy leads us to think that the history force is actually relevant.

This work has been supported by the Spanish government through grant DPI2011-28356-C03-02.

References

1. J.O. Toilliez, A.J. Szeri, *Optimized translation of microbubbles driven by acoustic fields*, *J. Acoust. Soc. Am.* 123 (2008) 1916-1930.
2. V. Garbin et al., *History force on coated microbubbles propelled by ultrasound*, *Phys. Fluids* 21 (2009) 092003.
3. J. Magnaudet and D. Legendre, *The viscous drag force on a spherical bubble with time-dependent radius*, *Phys. Fluids* 10 (1998) 550.
4. M. Sussman, E.G. Puckett, *A coupled level set and volume of fluid method for computing 3D and axisymmetric incompressible two-phase flows*, *J. Comput. Phys.* 162 (2000) 301-337.
5. J.U. Brackbill, D.B. Kothe. C. Zemach, *A continuum method for modeling surface tension*, *J. Comput. Phys.* 100 (1992) 335-354.
6. I. Chakraborty, G. Biswas, P.S. Ghoshdastidar, *Bubble generation in quiescent and co-flowing liquids*, *Int. J. Heat Mass Transfer* 54 (2011).

Transiently stable microbubbles produced by a microfluidic device for therapeutic applications

Adam J. Dixon, Ali H. Dhanaliwala, Johnny L. Chen and John A. Hossack

Department of Biomedical Engineering, University of Virginia, Charlottesville, VA, USA

Introduction

Focal drug delivery to the vessel wall facilitated by intravascular ultrasound and microbubbles holds promise as a therapy for atherosclerosis¹⁻³. Unfortunately, conventional methods of microbubble administration for targeted drug delivery result in rapid clearance of microbubbles and significant drug loss. To address these limitations, we evaluated whether drug delivery could be achieved using microbubbles produced in real-time by a microfluidic device, with the ultimate goal of real-time microbubble production at the tip of an intravascular catheter. By generating microbubbles in close proximity to the therapeutic site, microbubble stability is no longer a concern. As a result, transiently stable microbubbles, which can be produced at rates exceeding those previously demonstrated for the production of stable lipid-shelled microbubbles⁵, can be utilized. We validate that this *in situ* microbubble production strategy enables effective sonoporation and drug uptake *in vitro* across a range of ultrasound, microbubble, and fluid flow parameters.

Methods

Rat aortic smooth muscle cells were grown to confluency on a Thermanox membrane and placed in a flow chamber designed to simulate physiological flow conditions (Fig 1). A flow-focusing microfluidic device (FFMD) producing 8 μm diameter monodisperse microbubbles was then placed within the flow chamber and ultrasound was applied to enhance uptake of a surrogate drug (calcein). Acoustic pressures up to 300 kPa and flow rates up to 18 mL/s were investigated. FFMD produced microbubbles were stabilized with a polyethylene glycol-40 stearate shell and had either a perfluorobutane (PFB) or nitrogen gas core. Calcein delivery efficiency was quantified by counting the fraction of cells that internalized calcein. Cell death was quantified by staining with propidium iodide. Cells that detached from the Thermanox membrane were considered to be dead.

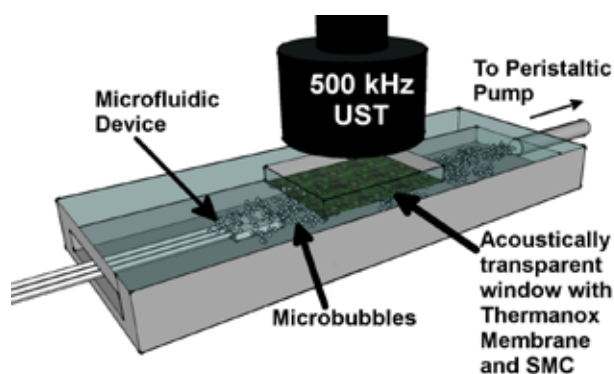


Figure 2: *In vitro* flow chamber

Microbubbles were stabilized with a polyethylene glycol-40 stearate shell and had either a perfluorobutane (PFB) or nitrogen gas core. Calcein delivery efficiency was quantified by counting the fraction of cells that internalized calcein. Cell death was quantified by staining with propidium iodide. Cells that detached from the Thermanox membrane were considered to be dead.

Results

(a) Microbubble Properties: Transiently stable microbubbles with diameters between 8 – 17 μm were produced at rates between $0.1 - 0.5 \times 10^6$ per second by adjusting the operating parameters of the microfluidic device. All microbubbles were monodisperse at the device nozzle with a polydispersity index less than 6 %. Microbubble size distribution and stability upon ejection from the FFMD into an air saturated medium (simulating the partial gas pressures found in blood) was observed to be dependent on the composition of the gas core. PFB microbubbles initially grew and then shrank over time (half-life = 40.7 s) (Fig 2A). Nitrogen microbubbles did not significantly expand when introduced to the air-saturated saline and exhibited a shorter half-life of 18.2 s (Fig 2B).

(b) Calcein Delivery: Fluid flow by itself did not cause calcein delivery or cell death. Calcein delivery was observed at all flow rates, with maximal delivery at 9 ml/s and maximal cell death at 2 ml/s. Results in Table 1 are for 8 μm diameter PFB-gas microbubbles and 300 kPa peak ultrasound pressure. Minimal calcein delivery or cell death was observed below 200 kPa. Results in Table 2 are for 8 μm diameter PFB-gas microbubbles at a 9 ml/s flow rate. Nitrogen-core microbubbles required higher acoustic pressures than PFB-core microbubbles to achieve calcein delivery. Results shown are at a 9 ml/s flow rate (Table 3).

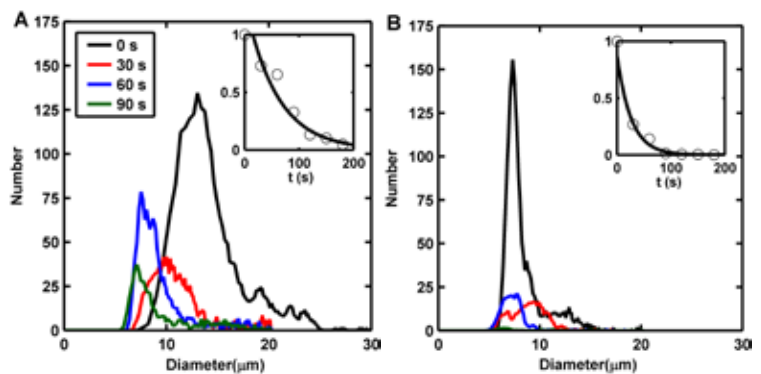


Figure 3: (A) PFB and (B) N₂ microbubble size distributions over time in air-saturated saline. Inset: Calculated half-life.

Table 1: Effect of fluid flow rate on delivery

	<i>Fluid Flow Rate</i>		
	2 ml/s	9 ml/s	18 ml/s
% Delivery	32%	78%	64%
% Death	57%	18%	16%

Table 2: Effect of ultrasound pressure on delivery

	<i>Ultrasound Pressure (kPa)</i>			
	0	100	200	300
% Delivery	2%	2%	59%	78%
% Death	3%	5%	9%	19%

Table 3: MB gas core effect on delivery

	<i>Ultrasound Pressure (kPa)</i>			
	0	100	200	300
PFB-MB	2%	2%	59%	78%
N ₂ -MB	3%	5%	9%	19%

Conclusions

This is the first demonstration of *in vitro* ultrasound-mediated drug delivery using microbubbles produced by a microfluidic device *in situ*. We observed that ultrasound pressure, flow rate, and microbubble composition all affected drug delivery efficiency. In addition, we show that microbubbles with short half-lives are still effective as drug delivery agents. This unique behavior could enable the use of larger microbubbles *in vivo* by reducing embolic risk.

References

1. Phillips, L. C. et al. Focused *in vivo* delivery of plasmid DNA to the porcine vascular wall via intravascular ultrasound destruction of microbubbles. *Journal of Vascular Research* **47**, 270–4 (2010).
2. Kilroy, J., Klibanov, A., Wamhoff, B. & Hossack, J. Intravascular ultrasound catheter to enhance microbubble-based drug delivery via acoustic radiation force. *IEEE Transactions on Ultrasonics, Ferroelectrics and Frequency Control* **59**, 2156–2166 (2012).
3. Phillips, L. C., Dhanaliwala, A. H., Klibanov, A. L., Hossack, J. A. & Wamhoff, B. R. Focused ultrasound-mediated drug delivery from microbubbles reduces drug dose necessary for therapeutic effect on neointima formation--brief report. *Arteriosclerosis, thrombosis, and vascular biology* **31**, 2853–5 (2011).
4. Dhanaliwala, A. H., Chen, J. L., Wang, S. & Hossack, J. A. Liquid flooded flow-focusing microfluidic device for *in situ* generation of monodisperse microbubbles. *Microfluidics and Nanofluidics* 1–11 (2012).doi:10.1007/s10404-012-1064-x
5. Hettiarachchi, K., Talu, E., Longo, M. L., Dayton, P. A. & Lee, A. P. On-chip generation of microbubbles as a practical technology for manufacturing contrast agents for ultrasonic imaging. *Lab on a Chip* **7**, 463 (2007).
6. Dixon, A. J., Dhanaliwala, A. H., Chen, J. L., & Hossack, J. A. Enhanced intracellular delivery of a model drug using microbubbles produced *in situ* via a microfluidic device. *Ultrasound in Medicine and Biology*. Submitted 24 Oct 2012.

Acoustic bubble sorting of ultrasound contrast agents

Tim Segers and Michel Versluis

*Physics of Fluids Group and MESA+ Institute of Nanotechnology, University of Twente,
the Netherlands*

Ultrasound contrast agents resonate to the driving pressure pulse transmitted by the clinical ultrasound system. These systems operate at a narrow bandwidth optimized for the ultrasound transducer. Due to the large size distribution of commercially available UCA only a small selection of bubbles contribute to the echo signal. Thus the sensitivity in diagnostic imaging can be improved by narrowing down the size distribution.

We present a novel lab-on-a-chip bubble-sorting method based on the acoustic forcing of microbubbles. A bubble in a traveling pressure wave experiences a net acoustic radiation force that pushes the bubble in the direction of wave propagation. The magnitude of the radiation force is bubble size-dependent through resonance; bubbles close to resonance experience the largest force. We use this acoustic radiation force to sort bubbles in a microfluidic channel made in polydimethylsiloxane (PDMS) with an embedded piezo transducer (Fig. 1).

We quantify the physical parameter space of the bubble-sorting device first by scaling up the problem by one order of magnitude to minimize the effects of diffraction and Mie scattering typically experienced in contrast bubble sizing. Secondly, the bubbles are produced in a flow focusing geometry and are characterized in the unbounded fluid to provide physical input parameters for a model consisting of a Rayleigh-Plesset-type model for the radial dynamics coupled to a translation equation. The translation equation consists of the instantaneous radiation force, the drag force and the added mass force. We find good agreement for the modeled displacement as a function of the bubble radius for a range of sizes in the unbounded fluid. Within the confinement of the sorting chip we find good agreement for the resonance behavior and overall with a smaller displacement than predicted as a result of bubble-wall interactions (Fig. 3A).

Next, we design a sorting device with a smaller flow focusing geometry and show that sorting of bubbles with a size similar to those of UCA is feasible, see Fig. 3B. Finally, we show that UCA bubbles can be sorted with this novel sorting strategy. We focus them hydrodynamically between two co-flows to produce a bubble train with large enough spacing between the bubbles to minimize bubble-bubble interactions (Fig. 1B). We find good agreement for the resonance behavior predicted by the Marmottant model using typical shell parameters adapted from literature.

Parallelization of this novel sorting method may lead to an overall improvement of the sensitivity of contrast-enhanced medical ultrasound by at least an order of magnitude.

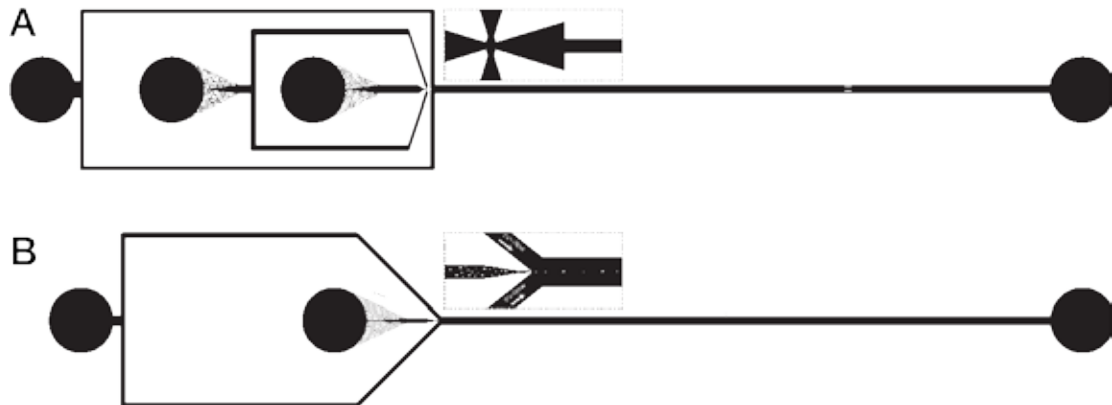


Figure 1: Channel geometry of the microfluidic bubble sorting devices. Figure A shows a flow focusing geometry (see inset) connected to the main channel in which the bubbles are sorted in a traveling ultrasound wave produced by an embedded piezo transducer. This sorting chip was used with flow focusing geometries with orifice sizes of 20 μm and 3 μm . Figure B shows the channel geometry that was used for UCA bubble sorting. The UCA bubbles are focused between two co-flows to produce a bubble train in the center of the channel.

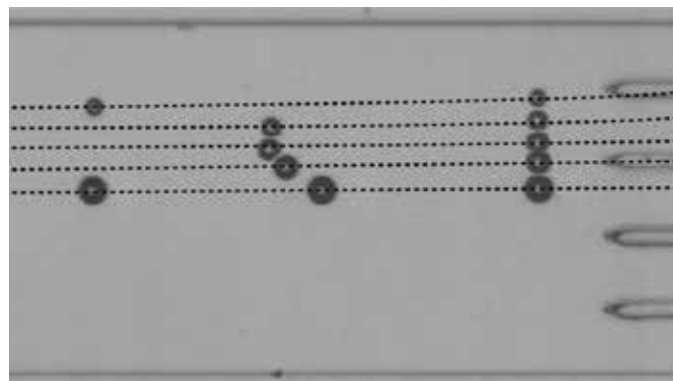


Figure 2: The image shows 5 superimposed frames of a high speed recording at 30,000 fps. The dashed lines show the translation paths of bubbles of different sizes. The channel in which the 15 μm bubbles were sorted has a width of 500 μm and a height of 110 μm , the channel in which the 3 μm bubbles and the UCA bubbles were sorted has a width of 200 μm and a height of 13 μm .

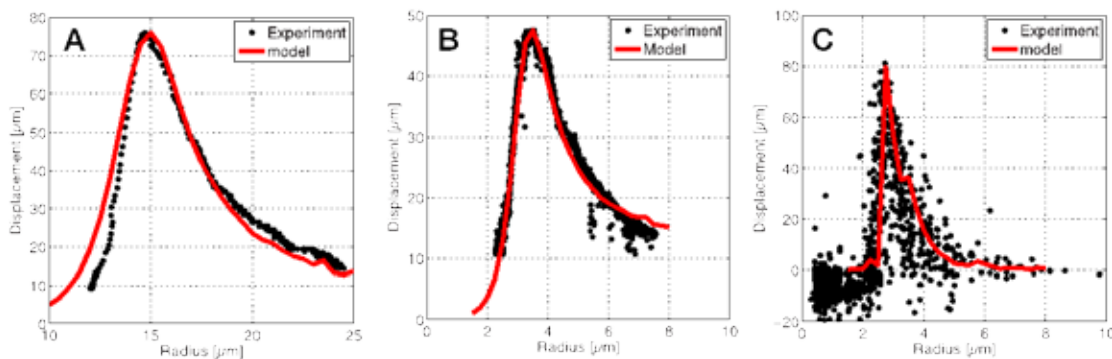


Figure 3: Figures A, B, and C show the resonance curves as where measured during the sorting experiments with the different bubbles. The red lines show the (scaled) resonance curves from a translational model coupled to the radial dynamics.

Sub- to ultra-harmonic imaging of contrast agent at high frequency: In vitro characterization

V. Daeichin, J.G. Bosch, A.F.W. van der Steen and N. de Jong

Biomedical Engineering, Thorax Center, Erasmus MC, Rotterdam, the Netherlands

Despite of the technological evolution of high-frequency micro-ultrasound and the virtue of its high temporal and spatial resolution, and a nonlinear contrast imaging mode with high sensitivity and specificity still remains a challenge. Higher harmonic imaging modes (main focus of the conventional contrast detection techniques at lower frequencies) are hampered by strong nonlinear propagation of the ultrasound wave in tissue at such high frequencies. Distortion of the propagating wave through populations of microbubbles causes nonlinear artifacts from the tissue; this is another challenge for contrast imaging. Also, excitation far from the resonance frequency of the ultrasound contrast agent (UCA) reduces the nonlinear behavior of these agents dramatically. Therefore, most of the studies are still relying on linear contrast detection techniques (subtracting pre- from post-injection), although most of the micro-ultrasound systems offer high bandwidth probes suitable for nonlinear contrast detection pulse sequences. Subtraction methods are not successful under many imaging conditions, such as for tissue perfusion in small capillaries or in the presence of breathing and cardiac-induced motions. Also in applications such as molecular imaging with targeted microbubbles, where the amount of signals from the attached bubbles is significantly lower than in perfusion applications, the subtraction techniques do not provide reliable measurements because of the tissue and motion artifacts.

In this study we used a VisualSonics micro-ultrasound system (Vevo 2100) with a high frequency linear probe (MS 250) in an in vitro study to characterize the advantages and limitations of subharmonic (SH), nonlinear fundamental (NF) and ultraharmonic (UH) imaging as the possible candidates for an optimized nonlinear contrast detection technique at high frequencies (>15 MHz). The MS 250 probe has a -6 dB bandwidth of 15 MHz to 30 MHz with the center frequency around 22 MHz. Therefore, following transmission frequencies were chosen: 15 MHz for UH imaging, placing the UH component at 22.5 MHz; 22 MHz for NF imaging; and 30 MHz for SH imaging, placing the SH component at 15 MHz. A tissue mimicking phantom (TMP) with contrast-filled wall-less cylinders in two depths (center of the cylinders at 6 mm and 12 mm) was scanned. For better axial resolution, short bursts and for better enhancement and separation of the SH and UH nonlinear components, longer bursts are desired. Bursts with rectangular envelopes with different lengths (4, 6 and 10 cycles) and different pressures (4%, 10% and 50% power) were transmitted with the following pulse sequences: B-mode, pulse inversion (PI), amplitude modulation (AM), and combination of PI and AM (PIAM). The received

echoes for each of the combinations (pulse length, pressure, target depth, concentration of microbubbles, and pulse sequences) were analyzed off-line using MATLAB. Identical rectangular regions of interest at the same depths, in the TMP and UCA (MicroMarker), were selected for contrast to tissue ratio calculations for each of the two depths and each combination. Signal to noise ratio (SNR), contrast to tissue ratio (CTR), contrast to artifact ratio (CAR), and the limitations of SH, NF and UH imaging as well as the effect of pulse length, transmit pressure and target depth will be presented. Figure 1 shows an example of the analysis for CTR, transmitting 10 cycle bursts with 10 % power for the target at lower depth and contrast concentration of 1:500. These results show that the SH imaging for such a situation (low depth, high concentration and moderate transmit pressure) always gives the best CTR regardless of the applied pulse sequences. The highest CTR (24 dB), in the presented dataset, is achieved with PI and AM pulse sequences for SH imaging. However, taking into account parameters such as target depths, axial resolution, and artifact might completely change the selected settings for the optimal contrast imaging at these frequency range.

In this work in vivo validation of these different contrast-imaging modalities with chick embryo and mouse models will also be demonstrated. Figure 2 depicts an in vivo example of a 6-day chicken embryo with SH imaging using the PI pulse sequence after a bolus injection of 5 μ l of MicroMarker contrast agent. Figure 2 shows the images of the embryo in B-mode and SH mode before injecting the UCA (Fig. 2a and 2b), and after administering the UCA and performing a maximum intensity projection over 480 frames (Fig. 2c and 2d).

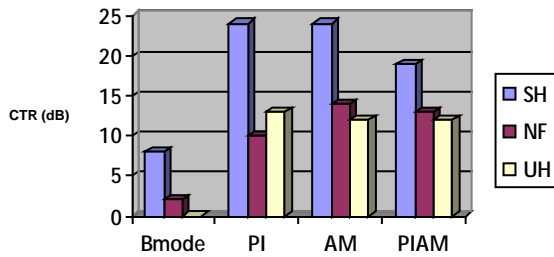


Fig. 1: Summary of contrast to tissue ratio measurements for subharmonic (SH), nonlinear fundamental (NF), and ultraharmonic (UH) imaging with four pulse sequences: B-mode, PI, AM and PIAM.

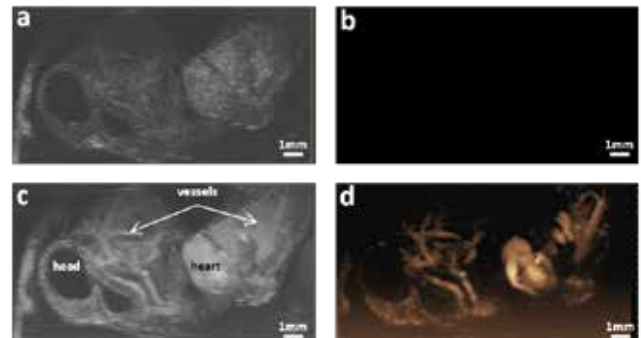


Fig. 2: In vivo validation of SH imaging with PI in a 6-day chicken embryo. 6-cycles, 10% transmit power pulses with rectangular envelopes were transmitted at 30 MHz and 5 μ l of MicroMarker was administered as the UCA. a: B-mode image before injecting the UCA, b: contrast mode image before injecting the UCA, c: B-mode image after injecting the UCA and applying a maximum intensity projection, d: contrast mode image after injecting the UCA and applying a maximum intensity projection

Fractal dimension of tumor microvasculature by CEUS: preliminary study in mice

Tamerlan Saidov¹, Carola Heneweer³, Thorsten Liesebach³, Maarten Kuenen^{1,2}, Hessel Wijkstra^{1,2}, Massimo Mischì¹

¹*Dept. of Electrical Engineering, Eindhoven University of Technology, the Netherlands*

²*Dept. of Urology, AMC University Hospital, Amsterdam, the Netherlands*

³*Clinic of Diagnostic Radiology, University Hospital Schleswig-Holstein, Kiel, Germany*

Introduction

Angiogenesis, the formation of a dense microvascular network [1,2], plays an important role in cancer growth and development. Thereby, angiogenesis is a relevant imaging marker for cancer localization and a promising prognostic indicator of cancer aggressiveness. Currently, the characterization of an angiogenic network requires an invasive procedure, being performed by analysis of the microvascular density (MVD) from histological sections of resected tumors [3,4]. Methods allowing non-invasive characterization of angiogenic structures can therefore provide an important contribution to cancer diagnostics.

Recently, contrast ultrasound dispersion imaging (CUDI) has been proposed for non-invasive cancer localization by assessment of ultrasound-contrast-agent (UCA) dispersion [8,9]. Several key properties of the microvascular architecture, such as microvascular density, vessel tortuosity, and multipath trajectories, influence the dispersion kinetics of contrast agents. On the other hand, the regional blood flow distribution, defined by the geometry of vascular network, is also affected by the presence of angiogenesis. The well-known concept of Mandelbrot suggests fractal bifurcating networks to mimic the vascular tree [5], permitting characterization of angiogenic networks in terms of fractal mathematics. In recent work [5-8], the concept of Mandelbrot was applied for characterization of regional blood flow distribution and cancer grading in immunohistological samples. By studying resected tissue samples, it was shown that a vascular network can be represented by a specific parameter, i.e., by the fractal dimension (FD). The FD is related to regional blood flow [6,7], and is given as

$$\frac{RD(m)}{RD(m_{ref})} = \left(\frac{m}{m_{ref}}\right)^{1-D}, \quad (1)$$

where D is the FD, RD is the relative dispersion (standard deviation divided by mean) of the normalized regional blood flow distribution for a given tissue sample size m (mass, surface area, etc.) with respect to a reference (subscripted as “ref”) RD_{ref} and a reference sample m_{ref} .

In this work, we evaluate the potential of FD for characterizing microvascular networks by non-invasive contrast enhanced ultrasound (CEUS) imaging. The method was tested on two type mice xenograft models of human prostate cancer, namely, DU-145 and PC-3. These models are characterized by a marked difference in MVD distribution [4]. For validation purpose, the method was compared with immunohistology-based MVD, immunohistology-based FD, and the recently proposed CEUS-based CUDI (coherence) analysis [9,13].

Materials and methods

The animal experiments were performed at the University Hospital Schleswig-Holstein (Kiel, Germany), in compliance with the Institutional Animal Care and Use Committee guidelines. The method for CEUS-based FD parameterization was developed and tested at the Eindhoven University of Technology (Eindhoven, the Netherlands).

Two types of prostate cancer (PCa) cell lines, DU-145 and PC-3, were implemented on xenograft mice models [4]. Seven mice were injected with cancer cells (four with DU-145 and three with PC-3). Once the tumors had developed, all the mice were administrated with a 0.1 mL MicroMarker Non-Targeted Contrast Agent Kit (VisualSonics Inc., Toronto, Canada) using a tail vein catheter, and time intensity curves (TICs) of the UCA passage through the tumors were measured. Necrosis was observed in one xenograft mouse model (DU-145). This mouse was therefore excluded from further analysis.

CEUS imaging was performed with a Vevo 2100 imaging system (VisualSonics Inc.) equipped with a MS-250 probe, using contrast-specific imaging (power modulation) at 18 MHz. A low mechanical index was adopted to prevent microbubble disruption [10,11]. Separate in-vitro measurements were performed to establish the relation between UCA concentration and image intensity; a logarithmic relation between contrast-agent concentration and image intensity was observed ($R^2 = 0.985$).

To assess the regional blood flow distribution, a parameter must be chosen that represents a measure of blood flow. For CEUS imaging, parameters such as peak intensity (PI), time-to-peak (TP), and wash-in-rate (WiR), reflect properties of blood flow. Therefore, these are employed as the measure of flow to assess the regional blood flow distribution. For that purpose, CEUS data maps, e.g., PI, TP and WiR, were obtained for all mice from calibrated TICs.

CEUS-based FD assessment of the data maps was performed in several steps:

1. From (CEUS) CUDI and (immunohistological) MVD maps, two zones with different MVD were defined in each tumor: a central and a peripheral zone [13]. For DU-145, the central zone showed higher vascularization than the periphery by both CUDI and MVD [13]. The same techniques revealed a higher degree of homogeneity in the vascularization of PC-3 tumors [13].
2. For each tumor, the function RD(m) was obtained from both zones separately. To this end, the zones were divided in 2 equal pieces (m=1/2) and the relative dispersion function RD(1/2) of the pieces was calculated. This process was repeated for m=1/4, 1/8, ..., and the relative dispersion function RD(m) was calculated for each scale.
3. The FD was estimated by curve-fitting of eq. (1) to the obtained RD(m) values.
4. To investigate whether CEUS-based FD detects a difference in the vascularization of the two zones, the relative difference in FD between the two defined zones was evaluated as

$$\frac{\Delta FD}{FD} = \frac{FD_{center} - FD_{periphery}}{FD_{center}} . \quad (2)$$

To validate the proposed method for CEUS-based FD assessment, two types of immunohistological studies were performed aimed at the determination of MVD and FD from the obtained MVD maps. For that purpose, 50 μ L of tomato-lectin-FITC (Vector Labs) were injected via the tail vein catheter. The animals were sacrificed after 8 min circulation. The tumors were resected, embedded within OCT (Tissue Tek) in cryomolds, and stored at -80°C. Tissue sections of 5- μ m thickness were cut from the tumor and imaged with a fluorescence microscope (Axiovert, Zeiss). Normalized gray-scale intensity was taken as a measure for bound tomato-lectin-FITC and converted into parametric maps, allowing quantification of MVD and FD.

Results

The results are presented in Table 1 and Figure 1. As presented in [13], for DU-145 tumors both MVD and CUDI shows two zones with a lower (periphery) and a higher (center) microvessel density, while no significant difference between the two zones is appreciated for PC-3. In order to compare the obtained FD results, relative differences between FDs in the central and peripheral zones are schematically shown in Figure 1. Among the chosen CEUS data maps, PI-based FD shows a better capability to discriminate between the central and peripheral zone in case of DU-145. The same method shows higher similarity between these zones in case of PC-3. The difference in the microvasculature distribution across the tumor permits discriminating between DU-145 and PC-3 cancer lines (p<0.05). These results are in agreement with those obtained by immunohistology and CUDI.

Conclusions

The presented results indicate CEUS PI-based assessment of FD to correlate well with immunohistology and CUDI, showing a capability to distinguish the areas with different vascular densities. This seems a promising result towards the discrimination between different tumor types by means of FD. The results show that DU-145 type of cancer develops two spatial regions with different FDs: a core with increased FD and outer part with lower FD. PC-3 has no spatially different FD zones, indicating a more homogeneous vascularization. These results are validated with immunohistological analysis and agree with our previous analysis of DU-145 and PC-3 cancer lines by CUDI [13].

The ability to detect different degrees of vascularization by the presented methods can possibly lead to new options for noninvasive tumor grading, supporting with critical therapeutic decision making. To this end, an extensive clinical validation in humans is required.

Table 1. Overall results (mean \pm SD) of different imaging methods in DU-145 and PC-3 mice xenograft models. The results for the chosen parameters are presented as relative difference between the central and peripheral zones (with p-values: * p<0.05, ** p<0.01).

	DU-145	PC-3
Δ FD/FD (immunohistology)*	0.11 \pm 0.05	0.002 \pm 0.02
Δ FD/FD (CEUS, TP-based)*	-0.13 \pm 0.05	0.01 \pm 0.08
Δ FD/FD (CEUS, WiR-based)*	0.17 \pm 0.12	0.05 \pm 0.20
Δ FD/FD (CEUS, PI-based)*	0.18 \pm 0.12	-0.08 \pm 0.07
Δ CUDI [a.u.]**	0.23 \pm 0.06	0.03 \pm 0.03
Δ MVD [a.u.]**	0.11 \pm 0.03	0.02 \pm 0.03

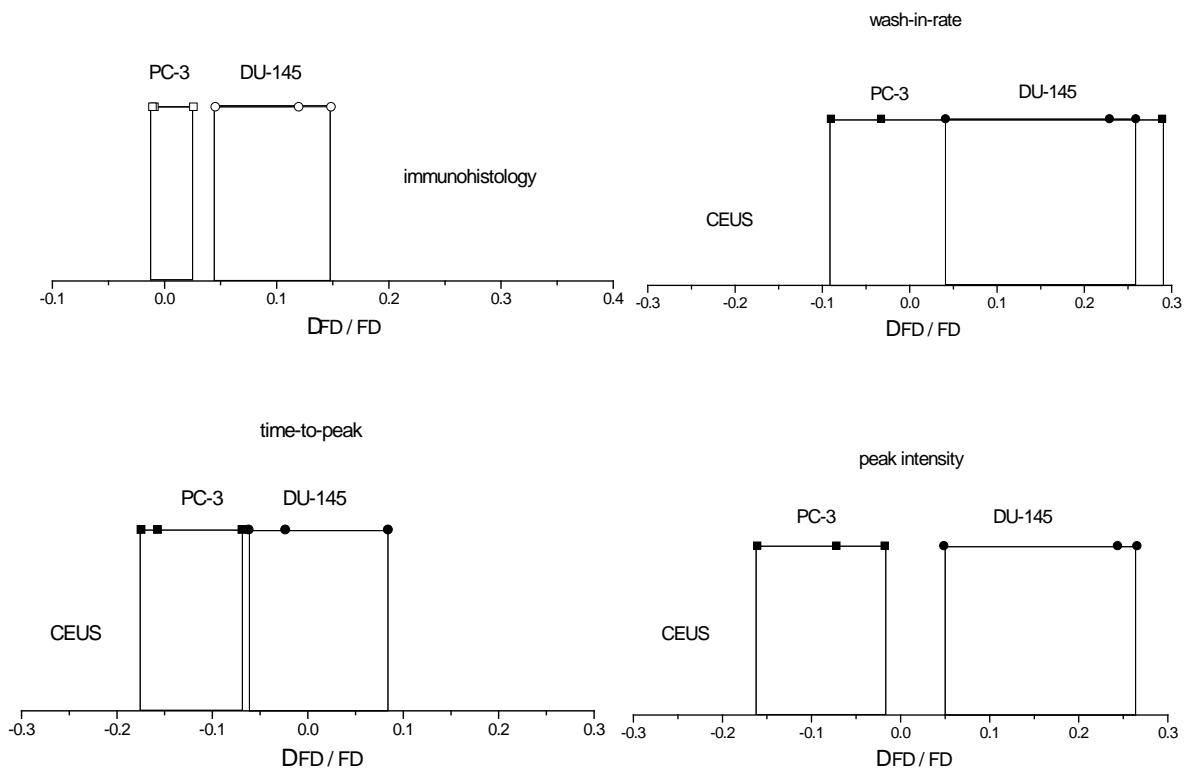


Figure 1. Relative difference in FDs as determined for DU-145 and PC-3 cancer from immunohistology maps and CEUS maps based on wash-in-rate, time-to-peak and peak intensity.

References

1. Folkman, J., et al., *Induction of angiogenesis during transition from hyperplasia to neoplasia*, *Nature*, 339, pp. 58-61, 1989.
2. Braver, M. K., *Quantitative microvessel density. A staging and prognostic marker for human carcinoma*, *Cancer*, 78(2), pp. 345-349, 1996.
3. Russo G, Mischi M., Scheepens W., De la Rosette J.J., Wijkstra H., *Angiogenesis in prostate cancer: onset, progression and imaging*, *BJU International*, DOI: 10.1111/j.1464-410X.2012.11444.x, accepted for publication 31 May 2012.
4. Heneweer C., Holland J.P., Divilov V., Carlin S., Lwis J.S., *Magnitude of enhanced permeability and retention effect in tumors with different phenotypes: 89Zr-Albumin as a model system*, *J. Nucl. Med.*, 52(4), pp. 625-633, 2011.
5. Mandelbrot B.B., *The fractal geometry of nature*, san Francisco: WH Freeman & Co, 1983.
6. Qian H., Bassingthwaighe J.B., *A class of flow bifurcation models with lognormal distribution and fractal dispersion.*, *J. Theor. Biol.*, 205(2), pp. 261-269, 2000.
7. Van Beek J.H., Roger S.A., Bassingthwaighe J.B., *Regional myocardial flow heterogeneity explained with fractal networks*, *Am. J. Physiol.*, 257, pp. 1670-1750, 1989.
8. Kuenen, M.P.J., et al., *Contrast-ultrasound diffusion imaging for localization of prostate cancer*, *IEEE Trans. Med. Im.*, 30(8), pp. 1493-1502, 2011.
9. Mischi M., Kuenen M.P.J., Wijkstra H., *Angiogenesis imaging by spatiotemporal analysis of ultrasound-contrast-agent dispersion kinetics*, *IEEE Transactions on Ultrasonics, Ferroelectrics and Frequency Control*, 59(4), pp. 621-629, 2012.
10. Baish J.W., Jain R.K., *Fractals and cancer*, *Cancer. Res.*, 60(14), pp. 3683-3691, 2000.
11. Smeenge, M. et al., *Novel contrast-enhanced ultrasound imaging in prostate cancer*, *World J. Urology*, 29(5), pp. 581-587, 2011.
12. Delorme, S. and M. V. Knopp, *Non-invasive vascular imaging: assessing tumour vascularity*, *Eur. Radiol.*, 8, 517-527, 1998.
13. Saidov T., Heneweer C., Kuenen M., Liesebach T., Wijkstra H., Mischi M., *Contr ultrasound dispersion imaging of different tumor types*, *Proceedings on the IEEE IUS, Dresden, Oct. 7-10, 2012*, 4 pages.

Ultrafast Doppler imaging of microbubbles

Charles Tremblay-Darveau¹, Ross Williams², Laurent Milot², Matthew Bruce³ and Peter N. Burns^{1,2}

¹*Department of Medical Biophysics, University of Toronto, Toronto, Ontario, Canada*

²*Sunnybrook Health Sciences Centre, Toronto, Ontario, Canada*

³*Supersonic Imagine, Aix en Provence, France*

Introduction

Ultrasound synthetic plane wave images acquired with a single plane wave can achieve higher frame rates (~5kHz) than conventional scanners (~60-100 Hz). Higher frame rates are beneficial for Power Doppler since independent signals can be compounded to increase the signal to noise ratio [1]. The Doppler ensembles can also be extended which in turn increases velocity sensitivity [2], but the detection of very slow flows is ultimately limited by low-velocity tissue motion (also known as clutter) [3]. Meanwhile, microbubble contrast-enhanced imaging has a better signal to noise ratio and specificity in detecting blood from tissue signal, but lacks the ability to segment fast from slow moving blood on conventional ultrasound scanners. Long Doppler ensembles are required to minimize the spectral broadening of clutter on slower flows, but aliasing constrains each A-line of the power Doppler image to be taken in series on conventional scanners. This greatly limits the duration of the ensemble length that can be acquired (see figure 1), which becomes problematic if contrast sequences such as pulse inversion are considered. The Doppler pulse sequence scheme for plane wave imaging is remarkably simpler since each image is acquired with a single pulse-echo (or two for pulse inversion). This allows very long Doppler ensembles to be obtained even if multi-pulse contrast sequences such as pulse inversion are used. With the advent of ultrafast imaging, we investigate the idea of using contrast enhanced Doppler. It will be shown in particular that conventional wall filtering, combined with plane wave imaging, can be used to segment fast from slow flows.

Method

Ultrafast ultrasound contrast cine loops at low MI were acquired at up to 2.5 kHz *in vivo* using an *Aixplorer* scanner (Supersonic Imagine, France). Successive plane waves of inverse polarities are emitted at a pulse repetition frequency of 5kHz. A full image is reconstructed per transmit from the nonlinear RF obtained by summation of pairs of acquisitions with inverted polarities [4]. The animal model used was a New Zealand white rabbit. *Definity*, a commercial lipid shell microbubble (10 µL/kg of bolus), was used in all experiments.

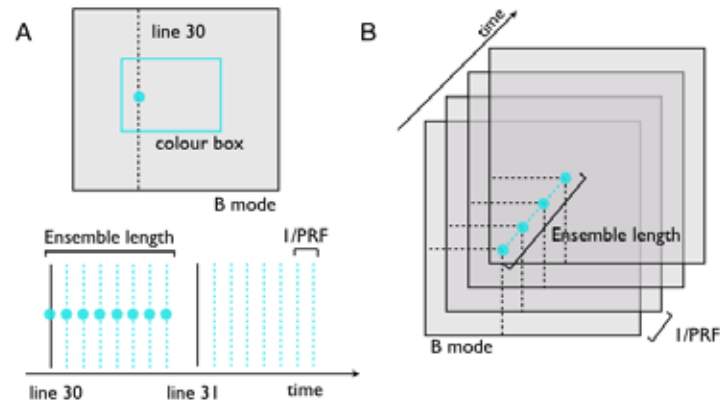


Figure 1: Pulse sequence scheme used to create a Doppler image. (A) Conventional scanners acquire the same A-line many times in a row. (B) Ultrafast plane-wave ultrasound generates B-mode at a frame rate equal to the PRF. Therefore stacks of B-mode can be used directly to estimate the Doppler signal.

Results

Improving conventional Power Doppler imaging using microbubbles and wall-filters

Tissue acceleration limits the smallest blood vessel that can be detected using linear Doppler (without microbubbles) even if long ensembles are used [3]. Ultrafast imaging allows to combine contrast imaging with Doppler wall filters processing (using a lower cut-of frequency) [5]. The wall filter is used to remove the stationary cloud of bubbles filling the region of interest as well as the weak harmonic clutter from tissue. The perfusion of a rabbit kidney with and without microbubbles was imaged at a frame rate of 2.5kHz with an 8MHz linear array transducer using a plane-wave pulse inversion sequence. Higher order branching (typically masked by the perfusion cloud of bubbles) can be observed in Figure 2 when microbubbles are used.

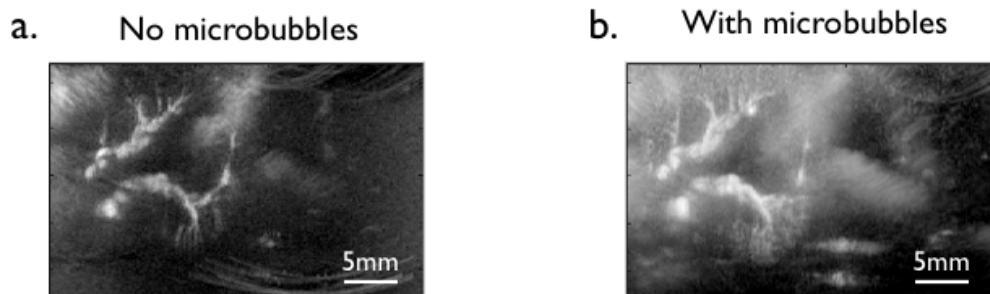


Figure 2: Power Doppler of a rabbit kidney with (b) and without (a) microbubbles (pulse inversion) using long Doppler ensembles.

In vivo flow segmentation using non-linear Doppler

The Power Doppler higher velocity flow was overlaid on the contrast B-mode. This allows to identify faster moving blood vessels from the slow perfusion background in the contrast image. As a proof of principle, the Power Doppler of a rabbit kidney perfused by microbubbles was produced using both the linear (subtraction of successive pulses) and non-linear (addition of successive pulses) Doppler signals.

These Power Doppler maps were then overlaid on the contrast B-mode (grayscale). The resulting images are shown in Figure 3b) illustrating the vascular tree structure of the kidney. Regions with low or null Doppler signal, mostly within the kidney cortex, are dominated by perfusion. Both the linear and non-linear Doppler yield the same structures, but using non-linear Doppler images further reduce the flashing from very echoic structures such as the skin. It is also possible to selectively image the slow moving blood to create a perfusion-only Power Doppler by applying a low-pass filter (instead of the usual high-pass filter) on the non-linear Doppler signal. This removes most of the signal from the major arteries and veins, which have a significant velocity component in the axial direction. A perfusion-only contrast Power Doppler of a rabbit kidney is shown in figure 3c).

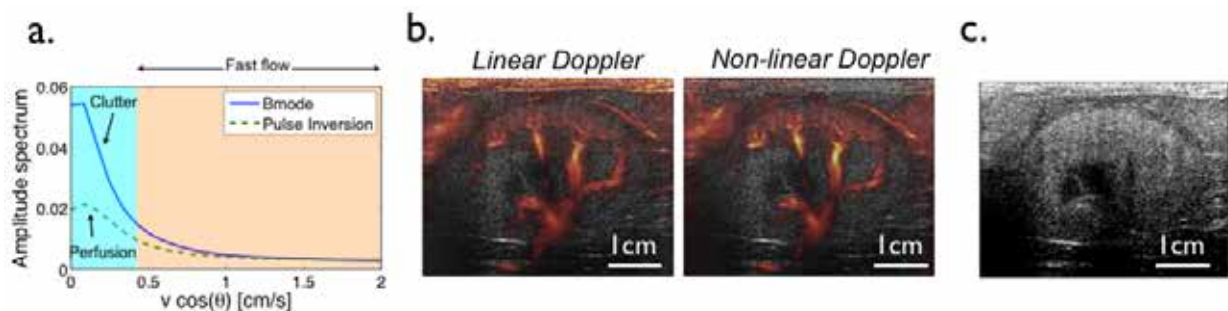


Figure 3: Segmenting fast from slow flows using non-linear contrast-enhanced Doppler. a) The Doppler spectrum (linear and non-linear) is integrated over the full image. The bandwidth of the clutter, evaluated using the linear Doppler spectrum, is used to optimize the wall-filter for fast flow detection. b) Contrast enhanced Bmode (grayscale) overlaid with Power Doppler (hot colormap) mapping the fast flows. c) The Perfusion-only Power Doppler is produced by integrating the non-linear Doppler over the clutter bandwidth only, effectively removing the signal from fast flows.

Conclusions

Microbubble contrast-enhanced Doppler was implemented on a plane-wave synthetic ultrasound scanner. Long Doppler ensembles can be acquired which reduce the spectral leakage associated with tissue motion. Contrast Power Doppler was compared with conventional non contrast-enhanced Doppler showing improved visualization of smaller vasculature in the kidney, while concurrently enabling the visualization of blood flow in the microcirculation. Fast flow was segmented from slow flows by applying an high-pass digital filters to the Power Doppler signal. Moreover, using low-pass filters instead of the conventional high-pass filter can also produce a perfusion-only image, free of large blood vessels.

References

1. J. Bercoff et al. ,*IEEE transactions on ultrasonics, ferroelectrics, and frequency control*, 58(1), 134–147, (2011).
2. G. Montaldo et al. *IEEE international symposium on biomedical imaging*, 324–327, (2010).
3. A. Heimdahl et al. *IEEE transactions on ultrasonics, ferroelectrics, and frequency control*, 44(4), 873–881 (1997).
4. D. Hope Simpson et al. *IEEE transactions on ultrasonics, ferroelectrics, and frequency control*, 48(6), 1483-1494 (2001).
5. S. Bjaerum et al., *IEEE transactions on UFFC*, 49(2), 204-216 (2002).

Investigation of acoustic properties of vaporized submicron perfluorocarbon droplets

Nikita Reznik¹, Guillaume Lajoinie², Oleksandr Shpak², Erik Gelderblom², Ross Williams³, Nico de Jong^{2,4}, Michel Versluis², Peter N. Burns^{1,3}

¹*Department of Medical Biophysics, University of Toronto, Toronto, ON, Canada*

²*Physics of Fluids Group and MIRA Institute of Biomedical Technology and Technical Medicine, University of Twente, Enschede, the Netherlands*

³*Sunnybrook Research Institute, Toronto, ON, Canada*

⁴*Biomedical Engineering Thoraxcenter, Erasmus Medical Center, Rotterdam, the Netherlands*

Submicron droplets of liquid perfluorocarbon (PFC) are studied as a new generation of extravascular contrast agents for ultrasound. With a size of a few hundreds of nanometers, these droplets have the ability to extravasate selectively in regions of tumour growth and stay intravascular in healthy tissues, due to the enhanced permeability and retention effect [1], allowing for their passive targeting to tumour growth regions. The liquid droplets are acoustically inert, until exposed to a sufficiently high intensity ultrasound pulse, at which point they vaporize to produce echogenic microbubbles [2].

Previous studies have established a number of conditions necessary for droplet vaporization (e.g. [2]-[5]). Furthermore, it was shown acoustically that vaporized droplets can scatter ultrasound non-linearly [2], and preliminary *in-vivo* results [4] suggested that droplets are selectively retained by tumours prior to vaporization. However, only limited information is available in regards to the acoustic properties of vaporized droplets. For their successful application as ultrasound contrast agents (UCAs), upon vaporization, the droplets should produce bubbles that respond to ultrasound in a manner similar to the currently used microbubbles at clinically relevant timescales (at least hundreds of milliseconds, for typical ultrasound imaging rates of tens of frames per second).

Here we conduct an initial study on the acoustic properties of vaporized PFC droplets. Using ultra high frame rate optical imaging, we examine the acoustic response of individual vaporized droplets to a low intensity 2.5 MHz ultrasound pulse at timescales of hundreds of milliseconds following vaporization. We examined the bubble oscillation amplitude and non-linearity, and model the bubble behaviour using the de Jong bubble oscillation model [6], in order to characterize the effects of shell retention by the bubbles [7] on their acoustic behaviour. We compare the nonlinearity in the acoustic response of these bubbles to that of commercially available SonoVue microbubbles, in order to assess how adequate the acoustic properties of the bubbles are for their potential use as UCAs.

Methods

PFC droplet emulsions were prepared by a combination of water, 5% v/v perfluoropentane, 0.8% v/v negatively charged fluorinated surfactant Zonyl FSP. The mixtures were emulsified with a tip-sonicator to produce polydispersed droplet emulsions with mean diameter of 400 nm.

Both the high-intensity vaporization pulse and the low-intensity characterization pulses were sent from a 5 MHz center frequency Olympus transducer (1.9 cm diameter, $f/\#$ 2.0), driven by a Tabor Electronics Arbitrary Waveform Generator, amplified by an E&I 350L power amplifier. The transducer was focused on an Opticell containing highly diluted droplet sample. The Opticell was placed under a 60X water immersion objective (N.A. = 1.00) of an Olympus BX-FM microscope, coupled to the Brandaris 128 ultra-high-speed imaging facility [8]. The microscope objective was co-aligned with the transducer focus. The setup was placed in a tank of deionized water, kept at a temperature of 37 ± 1 °C.

Droplet samples were vaporized with single ultrasound pulses, 10 cycles in length, and peak negative pressure (PNP) of 3.5 MPa, producing bubbles with radii in the range from 0.5 to 5 μm . Within 80 to 500 ms following vaporization, low-intensity acoustic characterization pulses at 2.5 MHz, 10 cycles in length at 116 kPa PNP (corresponding to mechanical index (MI) of 0.07) were sent. The camera recorded sets of 128 images at 15 million frames per second depicting individual bubble oscillations in response to incident ultrasound. Bubble contours from the recorded optical images were traced and bubble Radius-Time (RT) curves were obtained. The traces were examined in both the time and frequency domains, and compared to response expected for an uncoated bubble and the fit of de Jong coated bubble oscillation model [6] with best fit parameters of $S_p = 0.3 \text{ N/m}$ and $S_f = 3.17 \cdot 10^{-7} \text{ kg/s}$, as shown in Fig. 1.

Results and Discussion

The relative amplitude of bubble oscillation as a function of bubble resting radius is shown in Fig 2. Presence of shell material on the bubble induced increased elasticity and viscosity on bubble oscillation. As a result, the experimentally observed oscillation amplitude was significantly lower than the simulated response of an uncoated bubble. Furthermore, there was an apparent shift in the size of maximum oscillation. The best fit of de Jong model appeared to follow the experimental data and describe the effects of shell presence.

The acoustic signal emitted due to bubble oscillation has been calculated from the measured RT curves, and analyzed in the frequency domain. It was observed that the ratio of the power in the 2nd harmonic band to the power in the fundamental band was on the order of -5 to -15 dB, depending on the bubble size. These values are similar to the value of approximately -12 dB observed for SonoVue microbubbles

[9] at the same MI for 2.25 MHz excitation frequency, suggesting that the bubbles under investigation have similar nonlinear scattering properties to these of SonoVue.

Conclusions

This work investigated the acoustic characteristics of the product of submicron droplet vaporization on clinically relevant time scales. It was shown that the presence of coating material on the surface of the bubble induces a shift in the bubble resonance size due to increased elasticity and substantial amount of damping due to shell viscosity as compared to a response predicted for an uncoated bubble. Furthermore, it was shown that vaporized PFC droplets exhibit nonlinear scattering properties, comparable to these of currently commercially available UCAs. Combined with previous acoustic measurements of scattering from populations of vaporized droplets and the preliminary *in-vivo* results, these findings suggest that stable vaporized PFC droplets possess the adequate acoustic characteristics necessary for their potential application as UCAs in the clinical setting.

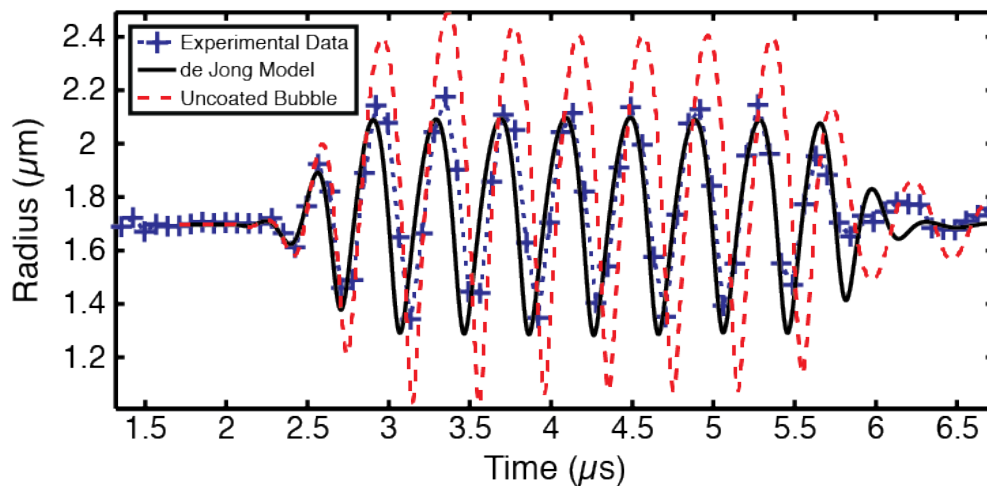


Fig 1: Radius-time trace of a bubble with initial radius of $R_0 = 1.7 \mu\text{m}$, with the fit by de Jong model and the trace simulated for an uncoated bubble of the same size.

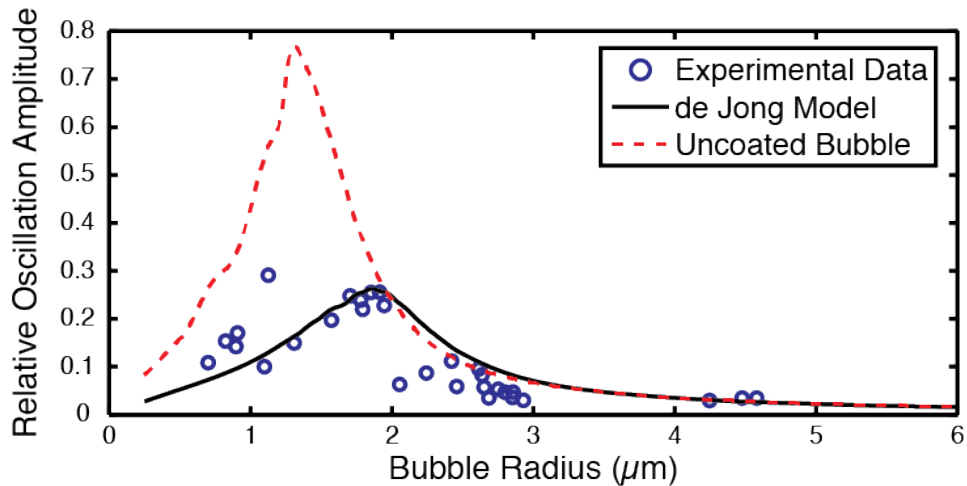


Fig. 2: Amplitude of bubble oscillation, normalized to the initial bubble size, as a function of bubble resting radius. Shown are the experimental data, the fit by de Jong model and the simulated response from an uncoated bubble. A decrease in amplitude of oscillation and increase in resonant bubble size of the experimental result from the uncoated bubble simulation is apparent.

References

1. H. Maeda, J. Wu, T. Sawa, Y. Matsumura, and K. Hori, "Tumor vascular permeability and the EPR effect in macromolecular therapeutics: a review," *J Control Release*, vol. 65, no. 1, pp. 271–284, Mar. 2000.
2. N. Reznik, R. Williams, and P. N. Burns, "Investigation of vaporized submicron perfluorocarbon droplets as an ultrasound contrast agent.," *Ultrasound Med Biol*, vol. 37, no. 8, pp. 1271–1279, Aug. 2011.
3. O. D. Kripfgans, J. B. Fowlkes, D. L. Miller, O. P. Eldevik, and P. L. Carson, "Acoustic droplet vaporization for therapeutic and diagnostic applications," *Ultrasound Med Biol*, vol. 26, no. 7, pp. 1177–1189, Sep. 2000.
4. R. Williams, C. Wright, E. Cherin, N. Reznik, M. Lee, I. Gorelikov, F. S. Foster, N. Matsuura, and P. N. Burns, "Characterization of submicron phase-change perfluorocarbon droplets for extravascular ultrasound imaging of cancer," *Ultrasound Med Biol*, In Press, 2012.
5. P. S. Sheeran, V. P. Wong, S. Luois, R. J. McFarland, W. D. Ross, S. Feingold, T. O. Matsunaga, and P. A. Dayton, "Decafluorobutane as a phase-change contrast agent for low-energy extravascular ultrasonic imaging," *Ultrasound Med Biol*, vol. 37, no. 9, pp. 1518–1530, Sep. 2011.
6. N. de Jong, R. Cornet, and C. Lancee, "Higher harmonics of vibrating gas-filled microspheres. Part one: simulations," *Ultrasonics*, vol. 32, no. 6, pp. 447–453, 1994.
7. N. Reznik, M. Seo, R. Williams, E. Bolewska-Pedyczak, M. Lee, N. Matsuura, J. Garipey, F. S. Foster, and P. N. Burns, "Optical Studies of Vaporization and Stability of Fluorescently Labelled Perfluorocarbon Droplets," *Phys Med Biol*, vol. 57, no. 21, pp. 7205–7217, 2012.
8. C. T. Chin, C. Lancée, J. M. G. Borsboom, F. Mastik, M. E. Frijlink, N. de Jong, M. Versluis, and D. Lohse, "Brandaris 128: A digital 25 million frames per second camera with 128 highly sensitive frames," *Rev Sci Instrum*, vol. 74, no. 12, p. 5026, 2003.
9. M. Schneider, "Characteristics of SonoVue (TM)," *Echocardiogr-J Card*, vol. 16, no. 7, pp. 743–746, 1999.

Molecular dynamics study on inclination change of molecules forming the surface membrane of an insonified coated microbubble

F.Ueki, N.Sugita, S.Ito, K.Z.Takahashi, K.Yasuoka and T.Sugiura

Mechanical Engineering, Faculty of Science and Technology, Keio University, Japan

Introduction

Shell-coated microbubbles are used as ultrasound contrast agents. They show complicated nonlinear oscillation under ultrasound radiation. Marmottant et al. proposed the effective surface tension model on the basis of experimental facts that the surface tension changes with the bubble radius. This model has been widely used in recent years. However its physical background is still unclear. Focusing on the molecular level state of the membrane of a coated microbubble, we have performed Molecular Dynamics (MD) simulations taking account of interactions between respective molecules. In this research, inclination change of the membrane molecules is investigated in addition to structural change of the membrane with the bubble radius.

Method

In our MD simulation, molecules are arranged in a water-membrane-gas interfacial system, as shown in Fig. 1. We applied Shinoda's coarse-grained (CG) models[1], in which several atoms were simplified as one group. They have been developed recently as a potential technique for efficient calculations. Membrane molecules are amphipathic ones composed of some particles, as shown in Fig. 2. The surface density of the membrane molecules can be given depending on the bubble radius. Therefore simulations were run for different surface densities. Stable alignments of the membrane molecules can be obtained first as results of MD simulations. The inclination of the membrane molecules to the axis normal to the surface as shown in Fig. 2 can then be calculated from those results.

Results

Fig. 3 shows alignments of the membrane molecules for their three surface densities. In Fig. 3(b), all the membrane molecules align neatly, turning the hydrophilic part to the water side and the hydrophobic part to the gas side and forming a monolayer membrane. If the bubble is larger, the membrane is thinner, as in Fig. 3(c). If the bubble is smaller, the membrane molecules, not in order, are moved up or down, as in Fig. 3(a), and thus the membrane is thicker. This is what is called a buckling.

Fig. 4 shows dependence of the inclination of the molecules on their surface density. It can be found that if the bubble is larger, the membrane molecules incline more in various directions, crossing with each other as shown in Fig. 2(c). This result successfully shows qualitative change in the alignment of the membrane molecules, which can be a kind of phase transition.

Conclusion

In this study we carried out MD simulations and calculated the inclination of molecules forming the membrane of a coated microbubble. Obtained results show that the inclination of the molecules changes with the bubble radius. The present MD study can further evaluate the effective surface tension as a function of the bubble radius and can thus be a useful approach for clarifying the dynamics of a coated microbubble.

Reference

W. Shinoda, et al, *Molecular Simulation*, 33, (2007).

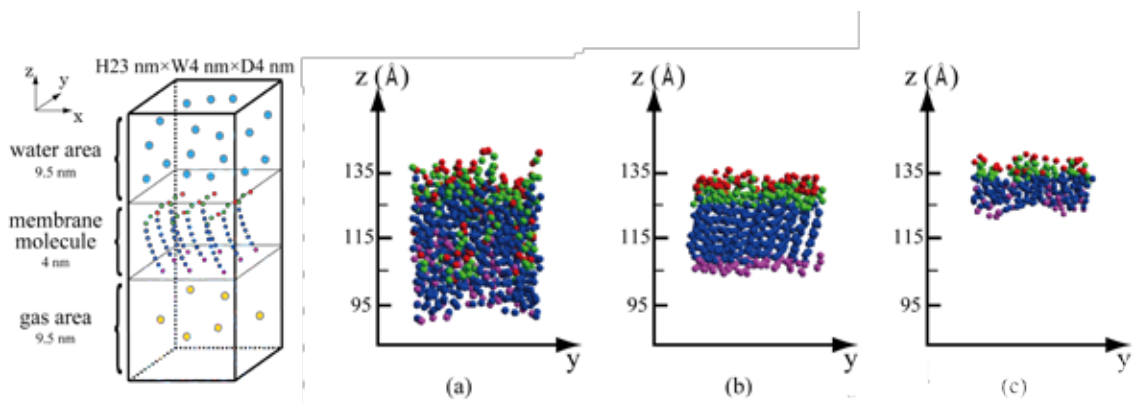


Fig.1: MD calculation model

Fig.3: The alignments of the membrane molecules for three surface densities: (a)16.67, (b)23.53, and (c)50.00Å²/molec

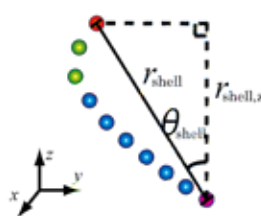


Fig.2: Membrane molecule model (red and green grains: hydrophilic, blue and purple grains: hydrophobic)

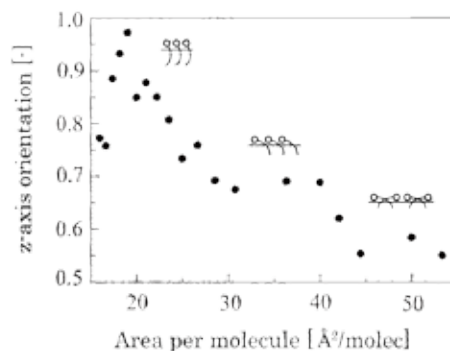


Fig.4: The inclination of the membrane molecules

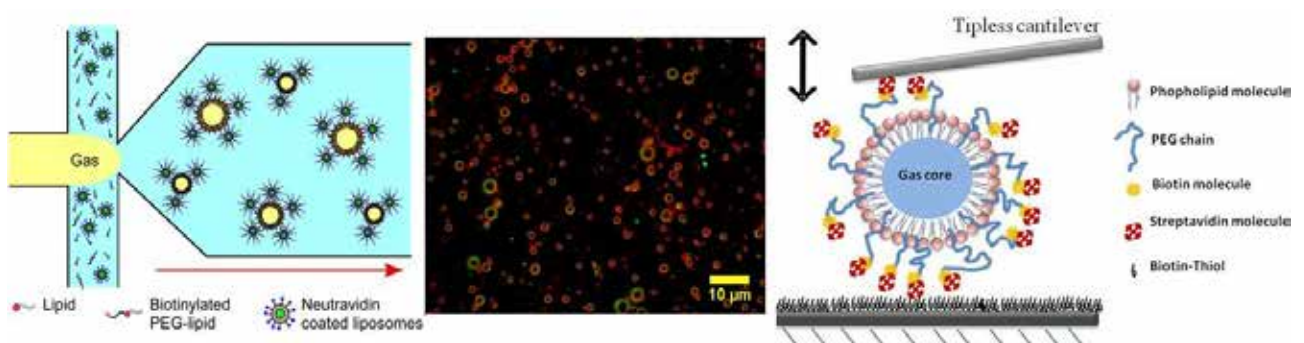
Microfluidic production and nanomechanics of therapeutic microbubbles for targeted drug delivery

Radwa H. Abou-Saleh, Sally A. Peyman and Stephen D. Evans

School of Physics and Astronomy, University of Leeds, LS2 9JT, UK

Microfluidics provides a reproducible means for microbubble production and surface functionalisation using a flow-focussing microfluidic geometry that combines streams of gas and liquid through a nozzle a few microns wide and then subjecting the two phases to a downstream pressure drop. Here, we introduce a new micro-spray flow regime that generates consistently high bubble concentrations, in the order of 10^9 bubbles mL^{-1} . We also demonstrate that it is possible to attach liposomes encapsulating quantum dots or fluorescein in a single step during the MB formation procedure.

The addition of different components to the shell architecture can change the mechanical properties of the bubbles and therefore its ultrasound response. The mechanical properties of $3\mu\text{m}$ diameter bubbles were tested with a tipless atomic force microscope (AFM) cantilever for small and larger deformations up to $\sim 50\%$ to obtain a full bubble response. The apparent stiffness increased as a function of deformation for all MBs. Addition of a coating layer increased the initial deformation stiffness ~ 2 -fold for a streptavidin layer and ~ 3 -fold for Q-dots layer. The presence of a polyethylene glycol (PEG) linker in between the lipid and functional coating led to enhanced stiffening at high deformations



New production method for nanoscale phase change contrast microbubbles

Guillaume Lajoinie, Tim Segers and Michel Versluis

Physics of Fluids Group, University of Twente, Enschede, the Netherlands

Phospholipid coated microbubbles have been studied extensively in the context of contrast enhanced ultrasound imaging. Their unique echogenicity is up to nine orders of magnitude larger than that of solid particles of the same size and the non-linear bubble dynamics and the non linear coating properties results in a subharmonic response offering a greatly improved signal to noise ratio for tissue imaging. The dynamics of coated microbubbles is now well understood, described by numerous models and they are in regular clinical practice for over a decade now. In order to be efficient, microbubbles need to be resonant with the frequency of commercial ultrasound scanners, which limits their size to a few micrometers in diameter. This practical requirement renders them unsuitable for extravasation into interstitial tissues thus making impossible the enhanced imaging of inner tissues.

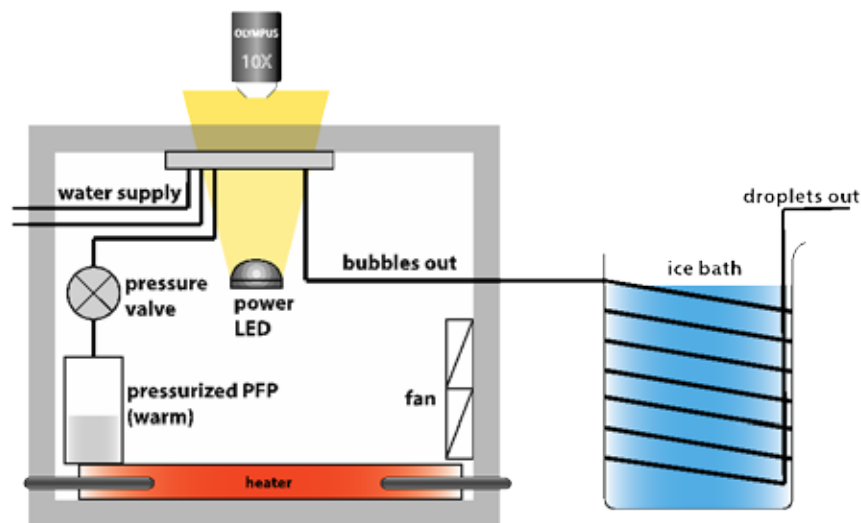


Fig. 1: schematic of the setup. The perfluoropentane solution is thermally pressurized, monodispersed droplets are produced by flow focusing and condensed in an ice bath

Therefore a special interest recently arose for phase change ultrasound contrast agents. These agents are injected as nanosized superheated droplets that remain stable due to the absence of nucleation sites. Perfluoropentane (PFP) is typically used for this purpose as it is inert and biocompatible. PFP has a boiling point around 29°C making it a stable liquid at room temperature and superheated once injected. Once extravasated through the leaky tumor endothelial barriers, they can be acoustically or thermally vaporized. The resulting bubbles can then be imaged using a commercial scanner.

There is a strong demand of producing highly stable monodispersed nanoemulsions of droplets, due to the expected limited efficiency of the transport and phase change processes. The controlled formation of nanodroplets is non-trivial, although recent success was reported using stable tip-streaming mode or flow-focusing nano/microfluidic chips for such purposes.

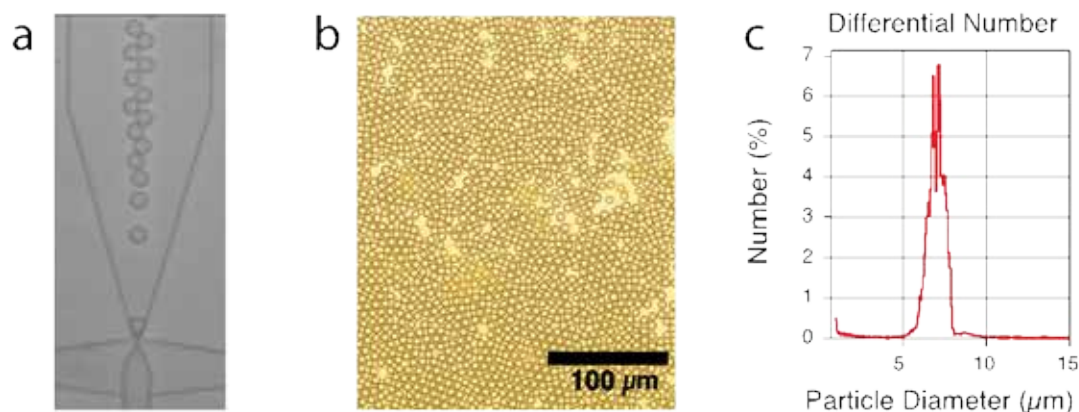


Fig. 2: a. Flow focusing geometry: a gas thread is focused in between to liquid flows resulting in 10 μm monodispersed bubbles. b. The produced PFP droplets are monodispersed and stable over time. c. Example of size distribution of an emulsion centered on 3.5 μm. radius

Here we propose a novel method based on the existing microfluidic technology to produce highly concentrated and highly monodispersed PFP nanoemulsions. In this method, the PFP is heated above its boiling point in a sealed container and the resulting vapor pressure is used to drive and supply in gas a flow focusing chip made of PDMS (figure 1). The bubble production process occurs in the a closed heated box to ensure the good functioning of the chip. The produced droplets are then cooled by circulation in an ice bath inducing their condensation before being collected. Next, the samples are sized using a Coulter counter (figure 2). The technique presents the advantage of making nanoemulsions while actually producing micron sized bubbles using traditional chips. The manipulation is considerably eased considering the clogging and stability issues of nanofluidic devices. The small size variation reached in the production of microbubbles can be directly translated in the nanometer scale and the production of any satellite droplets as a typical byproduct with the usual production method of emulsions is avoided.

Assessment of carotid plaque perfusion and ulceration with dynamic contrast enhanced ultrasound

Thapar A¹, Zheng Y², Dharmarajah B^{1,2}, Averkiou M³, Shalhoub J¹, Davies AH¹,
Leen ELS²

¹Academic Section of Vascular Surgery, Imperial College London, UK

²Department of Experimental Medicine, Imperial College London, UK

³Department of Mechanical and Manufacturing Engineering, University of Cyprus, Cyprus

Introduction

To identify if dynamic contrast enhanced ultrasound (DCE-US) could identify differences in intraplaque perfusion and ulceration between symptomatic and asymptomatic patients with carotid atherosclerosis.

Method

Ethical approval was obtained for this cross-sectional study. Twenty-two patients were required to give a 90% power and 5% false positive rate to detect a difference of 50% v 5% in generalised plaque perfusion.

Fifty-six patients with 50-99% internal carotid stenosis were scanned by a vascular scientist using colour Doppler. Stenosis and ulceration (>1.5mm surface defect) were recorded. They were rescanned using a non-linear pulse sequence, a 2ml bolus of SonoVue™, L9-3 transducer at MI 0.06. DICOM loops were analysed offline by a blinded vascular radiologist. Intraplaque perfusion was graded as generalised (>50% of plaque area) or localised (<50%) and ulceration as earlier specified.

Results

Generalised plaque perfusion was seen in 9/26 (35%) of symptomatic and 12/30 (40%) of asymptomatic patients. There was no significant difference between the groups (p=0.78). Intra-reader Kappa was 0.43 and inter-reader Kappa=0.49.

Ulceration was seen in 4/56 (7%) of patients with colour Doppler and 9/56 (16%) with DCE-US (p=0.24). With colour Doppler there was no significant difference in ulceration between symptomatic or asymptomatic patients (1/26 vs 3/30, p=0.62). With DCE-US there was a trend towards more ulceration in symptomatic patients (7/26 v 2/30, p=0.07). Intra-reader Kappa was 0.87 and inter-reader Kappa=0.64.

Conclusion

Semi-quantitative binary plaque perfusion grading was subjective and did not discriminate between symptomatic and asymptomatic carotid plaques. Imaging of plaque ulceration using DCE-US appears more promising for risk assessment.

Figure 1

DCE-US image a carotid plaque in longitudinal view of a patient with ipsilateral stroke demonstrating a 2.4mm deep ulcer (red line) and generalized (>50% plaque area) plaque perfusion (yellow arrow).

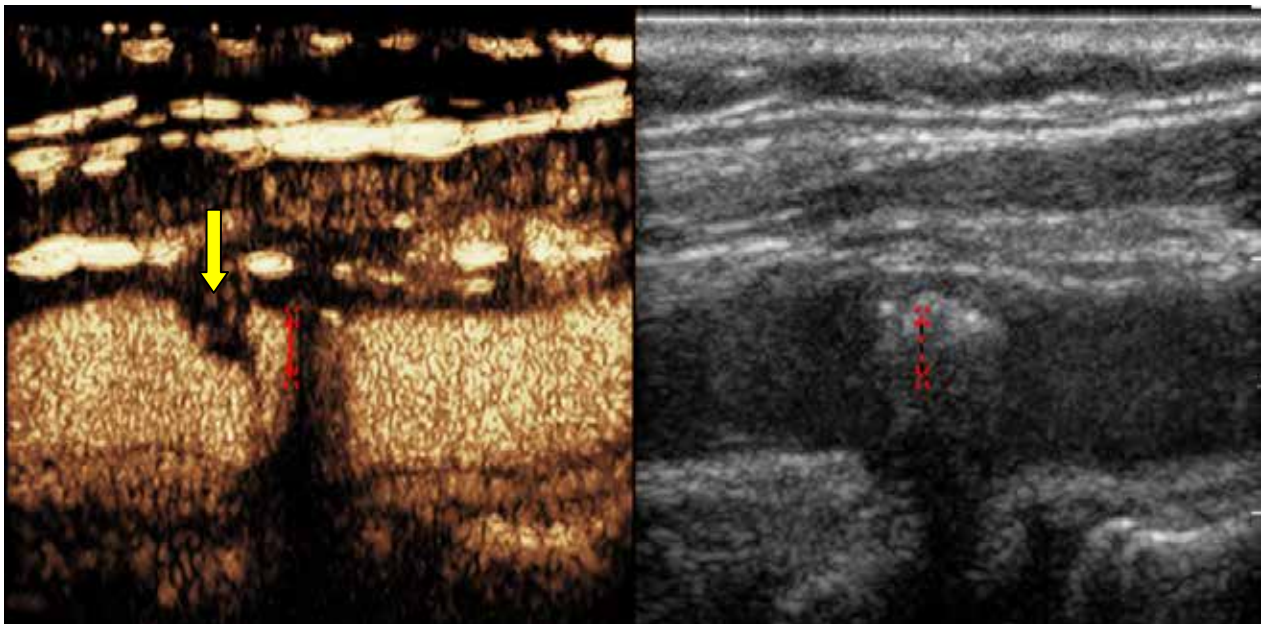
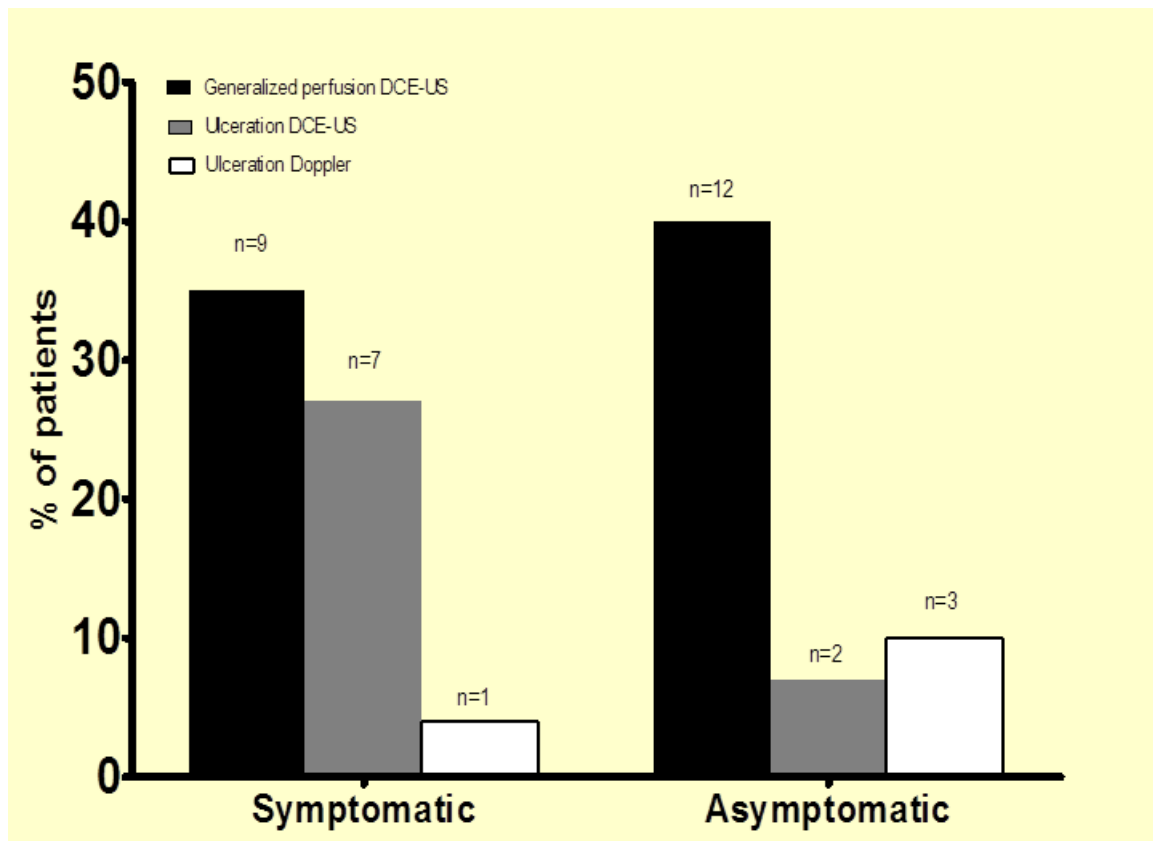


Figure 2

Proportion (n=absolute number) of symptomatic and asymptomatic patients with generalized plaque perfusion and ulceration on DCE-US and colour Doppler. There was no significant difference in either generalized plaque perfusion (p=0.78) on DCE-US or ulceration detected by colour Doppler (p=0.24) between the groups. There was a trend toward more ulceration on DCE-US in symptomatic patients (p=0.07).



Three modality contrast imaging using multi-functionalized microbubbles

-Achievements so far in the FP7-NMP project 3MiCRON (245575)-

*Anna Bjällmark^{1,2}, Malin Larsson¹, Matilda Larsson^{1,2}, Dmitry Grishenkov^{1,6},
Gaio Paradossi³, Melanie Poehlmann⁴, Lars Dähne⁵, Björn Gustafsson², Torkel Brismar⁶,
Kenneth Caidahl², Lars-Åke Brodin¹*

¹*Department of Medical Engineering, KTH Royal Institute of Technology, Sweden*

²*Department of Molecular Medicine and Surgery, Karolinska Institutet, Sweden*

³*Physical Chemistry of Macromolecules, Università di Roma Tor Vergata, Italy*

⁴*Department of Physical Chemistry II, University of Bayreuth, Germany*

⁵*Surflay Nanotec GmbH, Germany*

⁶*Department of Clinical Science, Intervention and Technology (CLINTEC), Division of Medical Imaging and Technology, Karolinska Institutet, Sweden*

Background

In-vivo multimodality and targeted imaging is a fast growing field in medical research. Hybrid systems, where two imaging methods are combined, are increasingly used in the healthcare sector. The combination of two imaging techniques can overcome the limitation of a single imaging system by displaying functional and anatomical information in one image, and thereby adding incremental diagnostic value. A multimodal contrast agent is needed to support these hybrid imaging systems. Targeting inflammation is another important application for contrast agents, both for identification of vulnerable atherosclerotic plaques in the blood vessel wall but also for diagnosis and therapeutic deposition of drugs towards other inflammatory diseases such as cancer and rheumatoid arthritis.

3MiCRON is a 3-year project which gathers medical and technical institutions together to address the design of new strategies in diagnostics in multimodality and targeted imaging. The specific aims of the project are:

- Ø Synthesis of polyvinyl alcohol (PVA) microbubbles (MBs) for multimodal imaging and inflammatory tissue targeting
- Ø Characterization of mechanical and acoustic properties of the different types of MBs
- Ø Optimization of imaging systems including phantom studies
- Ø In-vivo distribution studies and to study biocompatibility
- Ø In-vitro and in-vivo detection of inflamed tissue using MBs

Methods and Results

The PVA-based MBs used in this project have high mechanical and chemical stability, facilitating the use of the MBs as a carrier for different substances that can be incorporated into the shell or attached to the shell surface. The air-filled and polymer-shelled ultrasound MBs originate from a cross-linking reaction of PVA at the air/water interface. Within the 3MiCRON project, superparamagnetic iron oxide nanoparticles (SPIONs) were integrated to the MBs for combined ultrasound and magnetic resonance imaging (MRI). This was done in two ways, either by covalently linking the SPIONs to the shell surface through chitosan molecules (Type A) or by embedding the SPIONs in the shell (Type B). Single-photon emission computed tomography (SPECT) imaging was enabled by attaching ^{99m}Tc to the shell surface by the use of a potent metal chelator (NOTA). MBs for inflammation targeting were generated by the conjugation of antibodies against various cellular inflammation markers, e.g. ICAM-1, VCAM-1, E-selectin.

The plain ultrasound MB and the two types of magnetic MBs were extensively tested for their structural properties and their low and high frequency mechanics. The geometrical dimensions do not change with the introduction of SPIONs, and size distribution measurements ($n=209$) obtained by atomic force microscopy (AFM) resulted in a mean diameter of $35\pm 0.8\ \mu\text{m}$ and a mean shell thickness of $150 \pm 60\ \text{nm}$ for dried MBs (hydrated shell thickness is $250\text{nm} \pm 130\ \text{nm}$, 45% increase in aqueous medium). The elastic modulus of the shell material obtained by quasi-static force measurements in the low frequency regime using AFM was 1.3 MPa for plain ultrasound MB, 0.2 MPa for type A MB and 3.2 MPa for type B MB. The resonance frequency of the MBs ranged from 14-20 MHz and was determined in high frequency experiments with MBs exposed to an acoustic field. MBs type B showed the highest resonance frequency, which is in accordance with the observed increase of the shell's elastic modulus in the low frequency experiments.

Multimodality phantoms consisting of 3 % Agarose (for matrix stiffness) and 2.5 % Sephadex (gives tissue like absorption and scattering) were created in order to optimize the image generation of the different types of MBs. Due to the relatively thick and hard shell, the visualization of MBs using ultrasound is more challenging and high mechanical index contrast schemes was shown to be superior in the detection of the MBs. In-vivo testing in mice, rats, rabbits and pigs showed that it was feasible to detect MBs with ultrasound, MRI and SPECT/CT imaging systems. Different pharmacokinetic properties were obtained for various types of surface-modified MBs. However, a common feature for the tested MBs was a high distribution of MBs into the lungs, which might be due to their size, lipophilicity or the building of aggregates.

In-vitro testing showed an increased adhesion (up to 185 % higher than for control cells) of targeted MBs to inflamed cells. In-vivo testing using MBs conjugated with anti-ICAM-1 and cRGD has been initiated using different inflammation models.

Conclusions

A multimodal MB with targeting potential has been developed and characterized. We have demonstrated that it is feasible to detect the MB in-vitro and in-vivo by three modalities, ultrasound, MRI and SPECT. Further studies on in-vivo distribution, elimination and targeting are ongoing.

Polyplex-microbubble hybrids for ultrasound-guided plasmid DNA delivery to solid tumors

Shashank Sirsi,¹ Sonia Hernandez,² Henning Blomback¹, Lukasz Zielinski¹, Adel Koubaa¹, Milo Synder¹, Jessica Kandel,² Darrell Yamashiro², Mark Borden¹

¹University of Colorado, Boulder, CO 80309

²Columbia University, New York, NY 10027

Introduction

Over the last decade, microbubble contrast agents (MCA's) have frequently been cited as promising vehicles for targeted gene delivery applications. By tailoring the surface properties of MCA's, therapeutic genes or nanoparticle carriers can be loaded onto the microbubble surface to improve nucleic acid payload and systemic circulation of nucleic acid vectors. This technique can be utilized to improve circulation and targeting of highly potent *in vitro* transfection agents that typically demonstrate poor circulation *in vivo*, such as the non-viral vector polyethyleimine (PEI).

In this study, we present a simple method of combining PEI, with lipid-microbubbles to create polyplex-microbubble hybrids for ultrasound-guided gene therapy applications. Novel polyplex-microbubbles were synthesized, characterized and evaluated for systemic circulation and tumor transfection. Branched PEI (25 kDa) was modified with polyethylene glycol (PEG; 5 kDa), thiolated and covalently attached to maleimide groups present on lipid-coated microbubbles. The PEI-microbubbles demonstrated increasingly positive surface charge and DNA loading capacity with increasing maleimide content, achieving DNA loading capacities up to 0.005 ± 0.001 pg/ μm^2 , which is ~2.5 fold higher than the commonly used cationic lipid microbubbles used for DNA loading. The circulation persistence of the polyplex-loaded microbubbles was monitored *in vivo* following bolus injections of microbubbles into the tail vein of CD-1 mice using a high-frequency ultrasound imaging probe (30 MHz) placed over the mouse kidney. The ultrasound contrast time-intensity curves were fit to a novel two-compartment pharmacokinetic model designed to distinguish freely circulating microbubbles from non-circulating adherent ones. The model suggested that PEI loading (without DNA) dramatically reduced free circulation and increased nonspecific adhesion to the vasculature. However, DNA loading to form polyplex-microbubbles increased circulation in the bloodstream and decreased nonspecific adhesion. PEI-microbubbles coupled to a luciferase bioluminescence reporter plasmid DNA were shown to transfect tumors implanted in the mouse kidney. Site-specific delivery was achieved using ultrasound applied over the tumor area following bolus injection of the DNA/PEI-microbubbles. *In vivo* imaging showed over 10-fold higher bioluminescence from the tumor region compared to untreated tissue. *Ex vivo* analysis of excised tumors showed greater than 40-fold higher expression in tumor tissue than non-sonicated control (heart) tissue.

These results suggest that the polyplex-microbubble platform offers improved control of DNA loading and packaging suitable for ultrasound-guided tissue transfection.

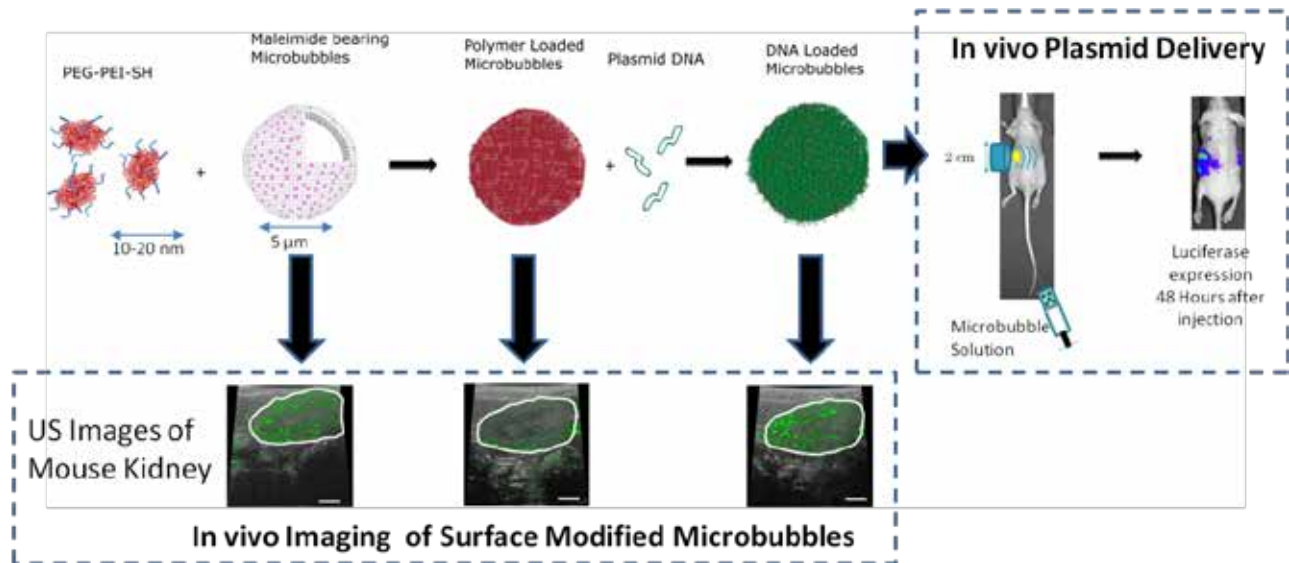


Figure 4. Schematic of polyplex-microbubble formulation, circulation, and ultrasound-mediated plasmid DNA transfection. Polymer only loaded microbubbles display reduced circulation profiles compared to unloaded control microbubbles. DNA loading onto polymer microbubbles recovers the ability to circulate. Microbubble suspensions containing DNA-loaded polymer bubbles was delivered to tumor bearing mice during ultrasound exposure to the tumor. The mice are imaged for luciferase expression 48 hours post treatment.

Investigating the potential of microbubble contrast agents as biosensors

Caroline Harfield^{1, 3}, Chris Fury^{2, 3}, Phil Jones², Gianluca Memoli³, Nick Ovenden⁴, Eleanor Stride¹

¹*Institute of Biomedical Engineering, Department of Engineering Science, University of Oxford*

²*Department of Physics and Astronomy, University College London*

³*Acoustics Group, National Physical Laboratory*

⁴*Department of Mathematics, University College London*

Microbubbles have become well established as effective contrast agents for diagnostic ultrasound imaging due to their high scattering efficiency and non-linear response to ultrasound excitation. For a given ultrasound field, the signal scattered by a microbubble may be different for different sizes of bubble, different coating materials and for different environments, for example it may be sensitive to changes in local viscosity, temperature or pressure. This dependence can potentially be exploited to detect changes in these quantities or the presence of particular chemical species *in vitro* for bio-sensing applications and to obtain quantitative information relating to the surrounding tissue *in vivo*.

To facilitate this, firstly the sensitivity of the microbubble acoustic response to changes in its environment must be analysed. Secondly, it is essential in the interpretation of experimental results, that the solution to the theoretical model describing the bubble dynamics must be unique for a given set of parameters describing the bubble coating material and/or surroundings. A modified Rayleigh-Plesset equation was derived that includes the effects of gas diffusion and adsorption/desorption of a surfactant coating, and coupled to an equation describing the translation of the microbubble. The model was then extended to include the presence of a rigid boundary, via an image bubble method.

A sensitivity analysis was performed for the effect of each of the physical variables in the model upon the bubble response. This indicated high sensitivity to species altering the dynamic surface tension of the bubble and also proximity to a boundary (Fig.1). A mathematical proof has been developed to investigate analytically the conditions under which a unique set of parameters describing the response of the bubble might be derived from experimental measurements. The results have been applied to the design of a microfluidic system for microbubble characterisation (Fig.2).

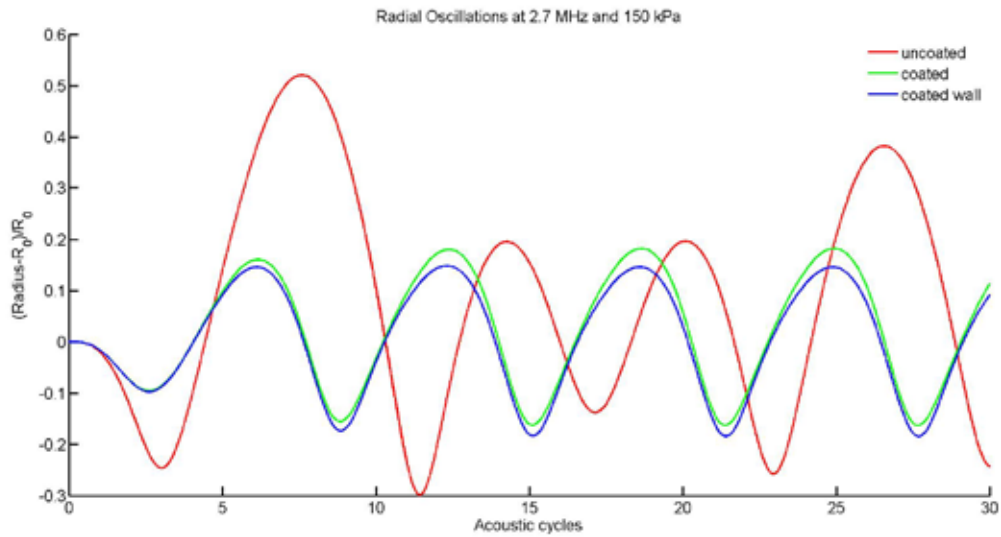


Figure 1: Radial oscillations of an uncoated and lipid coated bubble the latter also shown for a bubble close to a rigid wall. The microbubble radius was $2\mu\text{m}$ and the pulse centre frequency 2.7 MHz and peak negative pressure 150kPa.

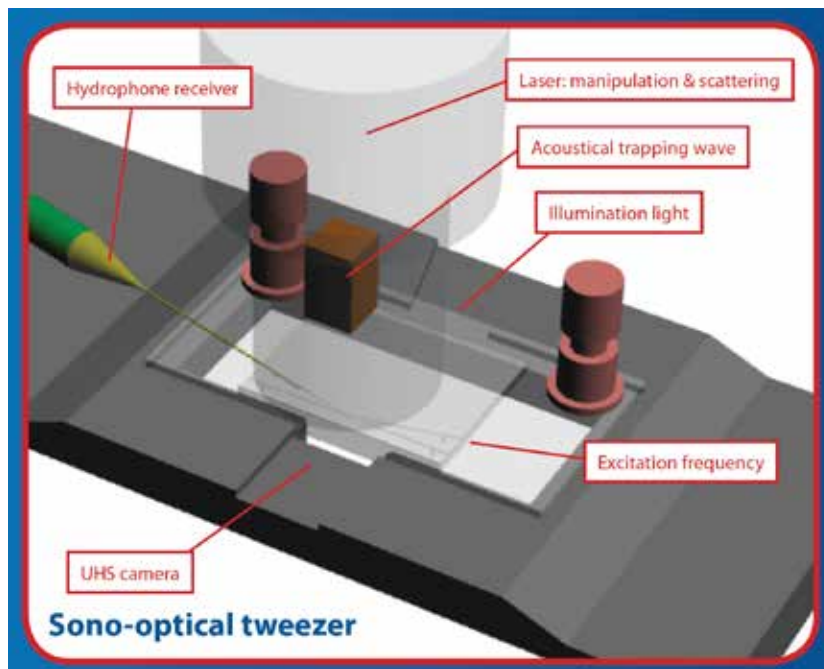


Figure 2: Schematic of a microfluidic device for characterising microbubbles.

Magnetic targeting of microbubbles at physiologically relevant flow rates

Joshua Owen¹, Paul Rademeyer¹, Quentin Pankhurst², Eleanor Stride¹

¹*Institute of Biomedical Engineering, University of Oxford, Oxford, UK*

²*Davy-Faraday Research Laboratory, The Royal Institution of Great Britain, London, UK*

The localisation of microbubbles to a target site has been shown to be essential to their effectiveness in therapeutic applications such as targeted drug delivery and gene therapy [1]. A variety of different strategies for achieving localisation have been investigated, including antibody and other forms of biochemical targeting, acoustic radiation force and the incorporation of super paramagnetic nanoparticles into the microbubble coating to enable them to be manipulated using an externally applied magnetic field. The last of these strategies has the advantage of concentrating microbubbles at a target site without exposing them to ultrasound which may lead to their degradation and can be used in complement with biochemical targeting methods to achieve greater specificity.

Magnetic microbubbles have been shown to be effective in therapeutic delivery both *in vitro* and *in vivo* in a mouse model [2-4]. Whether this technique can be successfully applied in humans, however, remains an open question given the much greater tissue depths and consequently magnetic field strengths and gradients at which microbubbles must be retained. The aim of this study was to determine the range of vessel diameters, flow rates and consequently shear rates under which retention could be achieved with clinically relevant magnetic field parameters.

A flow phantom was designed and constructed consisting of latex tubes of varying internal diameter (1.6 – 6 mm) embedding in a tissue mimicking gel and immersed in a water bath. Pulsatile flow with rates ranging from (0.05 ml/s to 3 ml/s) was created using a peristaltic pump and magnetic microbubbles (consisting of an air core surrounded by a layer of ferrofluid stabilised by a phospholipid coating.) were injected into the flow. A magnetic field was applied by positioning a Halbach array of permanent magnets at different distances from the vessel.

The bubbles were imaged using the ULAOP platform at 2.5 MHz using a standard imaging probe simultaneously acquiring B-mode and RF data (Figure 1). The images were then analysed to quantify the concentration of bubbles on the vessel wall closest to the magnet relative to that at the top of the vessel before and after the application of the magnetic field (Figure 2).

The results indicate that magnetic microbubbles can be retained at physiologically relevant flow rates in arterial conditions (~ 200 ml/min) or at a shear rates found within the capillary network (>500 s $^{-1}$). This study provides further evidence for the potential of magnetic microbubbles for targeted therapeutic delivery.

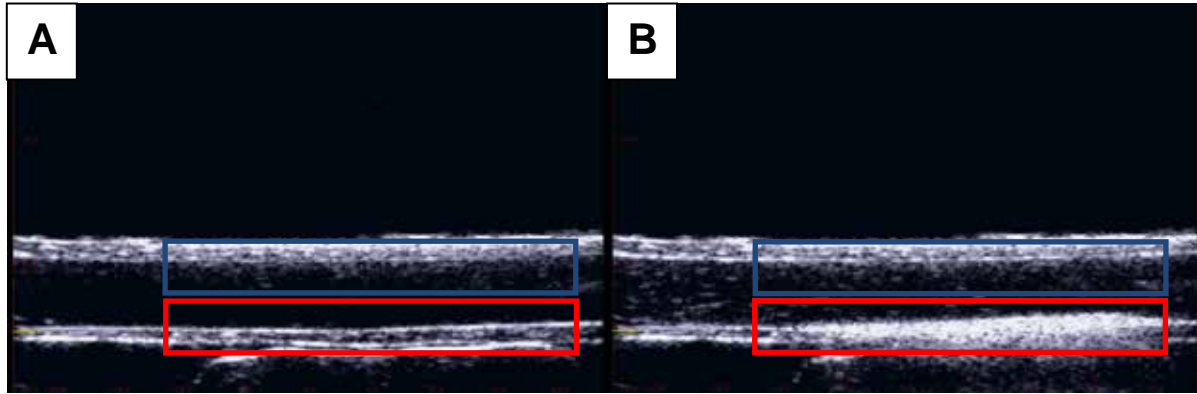


Figure 5: B-mode ultrasound imaging of vessel phantom (6 mm inner diameter) with magnetic array located beneath it A) image with water flowing through vessel at a rate of 0.75 ml/s before injection of magnetic microbubbles B) image after injection of magnetic microbubbles showing retention along the bottom of the tube directly above the magnet.

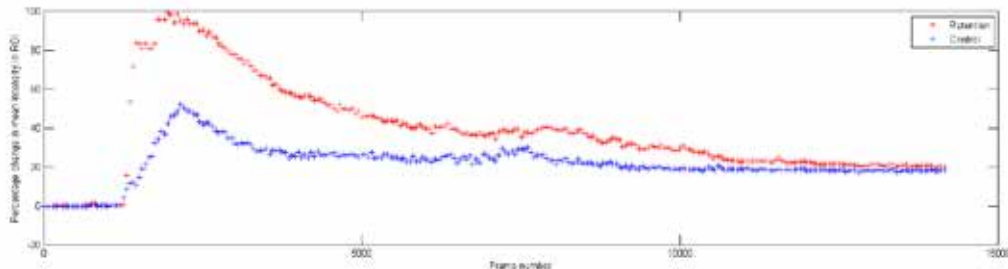


Figure 6: Signal intensity profile for lower (red) and upper (blue) regions of the vessel phantom indicating a much higher concentration of microbubbles along the bottom of the tube than the top owing to retention by the magnetic field.

References

1. Hernot, S. and A.L. Klibanov, *Microbubbles in ultrasound-triggered drug and gene delivery*. *Advanced Drug Delivery Reviews*, 2008. **60**(10): p. 1153-1166.
2. Mulvana, H., et al. *Enhanced gene transfection in vivo using magnetic localisation of ultrasound contrast agents: Preliminary results*. 2010. San Diego, CA.
3. Stride, E., et al., *Enhancement of Microbubble Mediated Gene Delivery by Simultaneous Exposure to Ultrasonic and Magnetic Fields*. *Ultrasound in Medicine & Biology*, 2009. **35**(5): p. 861-868.
4. Vlaskou, D., et al., *Magnetic and Acoustically Active Lipospheres for Magnetically Targeted Nucleic Acid Delivery*. *Advanced Functional Materials*, 2010. **20**(22): p. 3881-3894.

Ultrasound Super-Localization (USL)

Yann Desailly, Olivier Couture, Mathias Fink, Mickael Tanter

As in other medical imaging methods based on waves, the resolution of ultrasound imaging is limited by the wavelength. In optics, this limitation was overcome by super-localizing single events induced by fluorescent excitation (F-PALM). In recent years, our laboratory developed plane-wave ultrasound allowing frame rates up to 20 000 fps. Ultrafast processes such as rapid movement or disruption of ultrasound contrast agents (UCA) can thus be monitored. These rapid events provide us with distinct punctual sources that could be localized above the diffraction limit. The aim of this study is to determine the experimental and theoretical limitations of ultrasound super-localization.

The experimental resolution was determined by observing UCA flowing through microchannels. Ultrafast imaging was performed with a 1.75 MHz transducer matrix (64 x 8 elements) driven by a SuperSonic Imaging scanner at a frame rate of 1000 kHz. These microchannels were smaller than the wavelength used to observe them ($\lambda = 860\mu\text{m}$, width of the channels = $500\mu\text{m}$, height = $100\mu\text{m}$). Events lasting less than a thousandth of a second were observed with 3D ultrafast imaging. The punctual echo was backpropagated to find the exact location of the source. The super-localized position of 693 bubbles was used to construct an image of the channel. The same conditions were used to determine, in simulation, the maximal resolution limit. The timing error of the echo was propagated to find the variation in the super-localization of each bubble.

The acquired ultrafast images were differentiated in order to enhance the contrast of the single events. Single ultrasonic echo from microbubbles were observable by ultrafast imaging. As shown on figure 1, all the echo sources were super-localized within the boundaries of the real location of the channel. This channel was $\lambda/3$ wide and $\lambda/8$ thick. Standard focused imaging formed a spot $2000\mu\text{m}$ wide and $600\mu\text{m}$ thick. Super-localization thus improved resolution by a factor 10. The resolution-limit calculated in simulation was around $20\mu\text{m}$. The limiting factor is thus the size of the channel through which we manage to let the UCA flow.

Our first results prove that localization above the diffraction limit can be achieved with 3D ultrafast imaging of ultrasound contrast agent. This method being highly sensitive to motion, a compensation algorithm will be needed. Applying this technique in-vivo could lead to a super-resolve mapping of the vascular network, down to the smallest capillary.

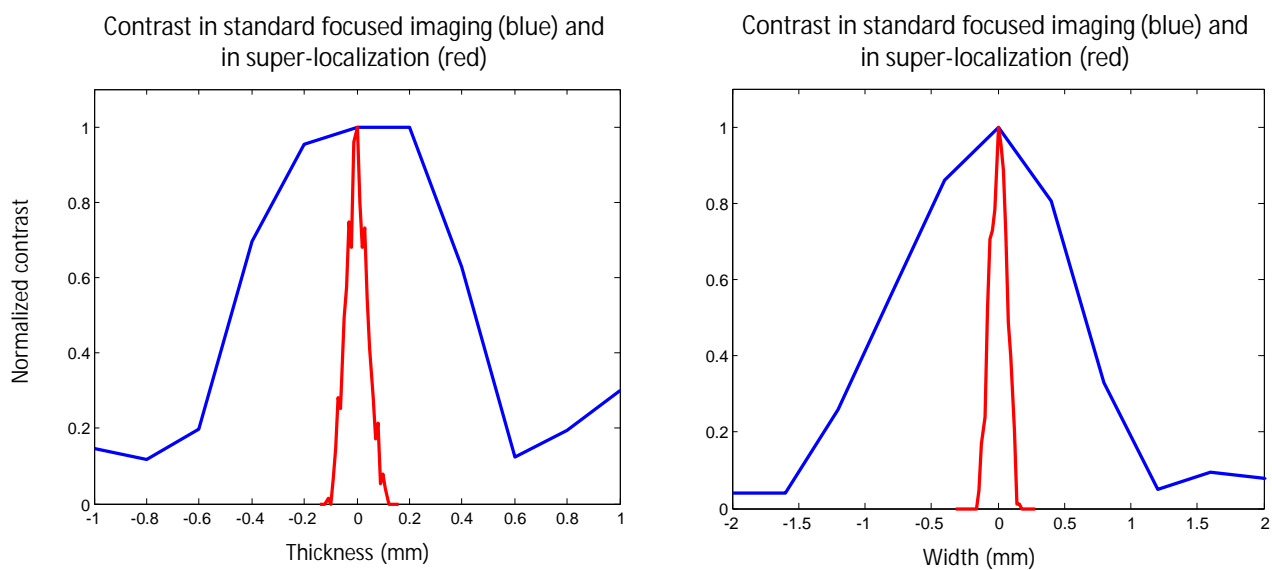


Figure 1: Comparisons between axial (left) and lateral (right) resolutions in conventional focused imaging and in USL (693 microbubbles localized)

The acoustic properties of different size-populations of microbubbles from 12 - 43 MHz

Chao Sun¹, Vassilis Sboros^{1,2}, Mairead Butler^{1,2}, Carmel M Moran¹

¹Medical Physics, Centre for Cardiovascular Science, University of Edinburgh, Edinburgh, UK

²Institute of Biochemistry, Biophysics and Bioengineering, Heriot-Watt University, Edinburgh, UK

Introduction

High frequency ultrasound (>20MHz) is utilized to obtain high spatial resolution images for intravascular, superficial tissue and preclinical ultrasound imaging applications. This study investigated the contrast to tissue ratio (CTR) measured by two high frequency ultrasound transducers with 3dB bandwidth ranging from 12 to 43MHz. In addition the subharmonic to fundamental ratio (SFR) at 25MHz of sized sub-populations of microbubbles (MBs) from two clinical ultrasound contrast agent (UCAs): Definity (Lantheus Medical Imaging, USA), SonoVue (Bracco Group, Italy) and a preclinical UCA: MicroMarker (untargeted) (Visualsonics, Canada) was measured at $20^{\circ}\text{C} \pm 1^{\circ}\text{C}$.

Method

Experiments were performed based on a broadband substitution technique using the Vevo770 preclinical ultrasound scanner (VisualSonics Inc., Canada) and two transducers (bracketed 3dB bandwidth, power, measured peak negative pressure by polyvinylidene fluoride membrane hydrophone with an active element of 0.2-mm and focal length): 710B (12-25MHz, 3%, 0.56MPa, 15mm), 711 (24-43MHz, 50%, 0.58MPa, 6mm). UCAs were reconstituted as per the manufacturer's instructions and diluted in air saturated distilled water to a concentration of 0.8×10^6 MBs·ml⁻¹. Definity and SonoVue were divided into three size groups: native size, small (diameter <2 μm) and large size MBs. *The small MBs* were acquired from the solution after 1-hour decantation for 0.5ml Definity and 2-hour decantation for 2ml SonoVue. *The large MBs* were obtained from the native population after decantation of the small MBs. MicroMarker was measured only at native population. The volume-based size distribution of three UCAs was measured by a Mastersizer 2000 Hydro MU (Malvern Instruments Ltd, Malvern, UK).

The CTR (dB) of the UCA solutions were calculated over the 3dB bandwidth of the transducers and normalised to the mean squared acoustic power of the backscattered signal from a tissue mimicking material (TMM). SFR (dB) was measured using transducer 710B, centre frequency 25MHz, using 25-cycle pulse at 3% output power, and was calculated by subtraction of the power spectra of backscattered signal integrated over the 2 MHz bandwidth of the transmitting frequency (25MHz) and subharmonic frequency (12.5MHz).

Each experiment was repeated three times and 900 independent samples (300 consecutive frames on 3 lines of radio-frequency (RF) data (digitised at 420 MHz)) in a region-of-interest were collected per experiment.

Result and discussion

Figure 1 shows that the size distribution of the three UCAs. The small MBs were found to be successfully removed via decantation, but a certain number of small MBs still existed in the large MB population. In Figure 2.a the CTR of three native UCAs are comparable over the frequency range 12-25MHz measured by transducer 710B, though their size distributions and encapsulated gases and shells are significantly different. However, in comparison to native Definity and SonoVue, MicroMarker shows a higher CTR over the frequency 24-43MHz measured by transducer 711 and higher SFR when insonated at 25MHz. For Definity and SonoVue, the largest CTR (closest to zero) is from the large MB population (Figure 2.a), while the largest SFR (closest to zero) is from the small MB population (Figure 2.b).

Conclusion

Altering the size distribution and concentration of microbubbles through decantation enables further enhancement of specific acoustic properties of the contrast microbubbles and may take full advantage of the imaging capabilities of the scanner.

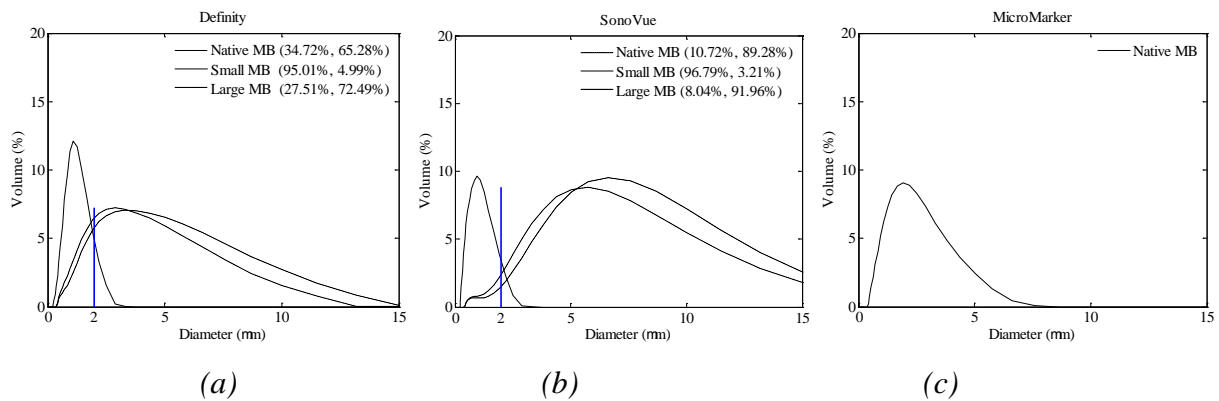
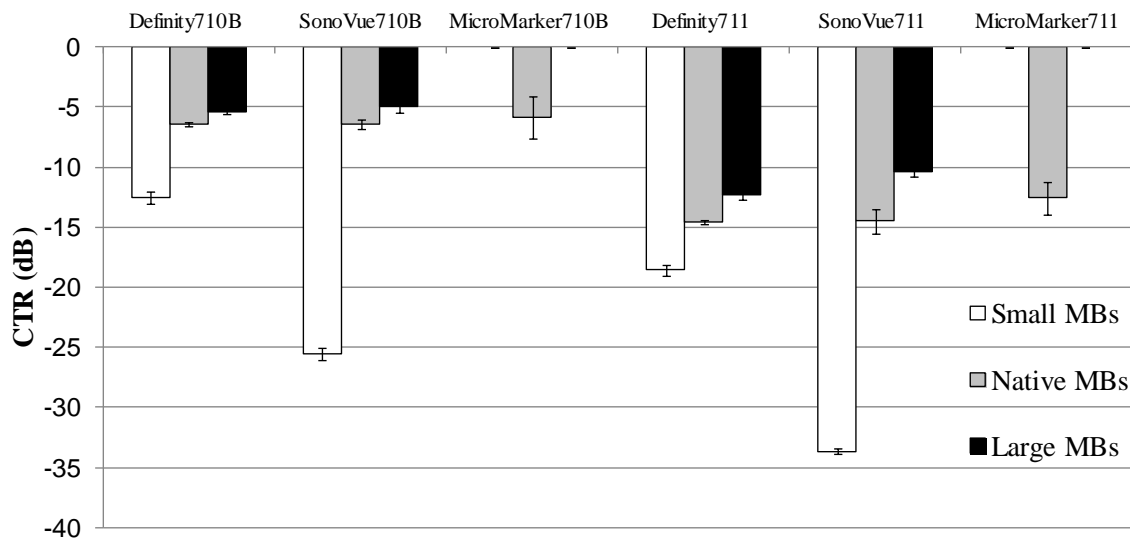
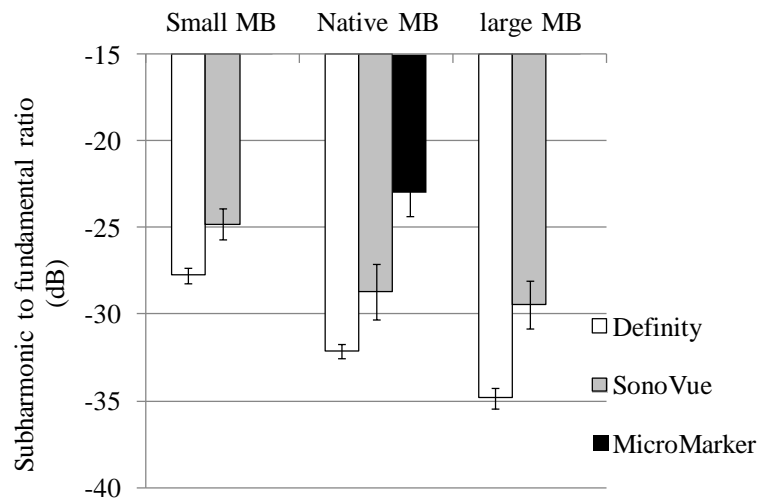


Figure 1: The volume based size distribution of 3 populations of (a) Definity, (b) SonoVue and 1 population of (c) MicroMarker. The 2 percentages in the legend of Definity and SonoVue are the percentages below and above 2 μm .



(a)



(b)

Figure 2: (a) CTR measured by transducer 710B (12-25MHz) and 711 (24-43MHz) and (b) SFR of three UCAs at three populations measured by transducer 710B (25MHz, 25-cycle signal)

Improving drug uptake by sonoporation using chirp excitation of polydispersed microbubbles

Nicola Ingram^{*1}, James McLaughlan^{*2}, Peter Smith², Stephen Evans³, Louise Coletta¹,
Steven Freear²

**these authors contributed equally to this work*

¹Leeds Institute of Molecular Medicine, University of Leeds, Leeds, UK

²School of Electronic and Electrical Engineering, University of Leeds, Leeds, UK

³School of Physics and Astronomy, University of Leeds, Leeds, UK

Drug delivery to solid tumours and metastatic lesions remains a major problem in the treatment of cancer. Ultrasound (US) contrast agents or microbubbles (MBs) are currently being developed for their theragnostic capabilities, potentially linking US diagnosis with drug delivery and monitoring of therapeutic response. To this end, the Leeds Microbubble Consortium is examining methods to improve sonoporation efficiency using phospholipid encapsulated microbubbles. The generation of shear stress on the cell membrane by microbubble oscillations is one mechanism that results in pore formation in the cell membrane. A microbubble oscillating at its resonant frequency would generate maximum shear stress on a membrane. However, due to the polydispersed nature of phospholipid microbubbles, a range of resonant frequencies would exist in a single population. Thus, the use of a linear frequency modulated ultrasound pulse, or “chirp”, to excite a microbubble population was examined to improve sonoporation efficiency.

Colorectal cancer cells were plated in 24 well plates and the membrane-impermeable drug, propidium iodide was added to the wells. DPPC, DSPE biotin-PEG2000 microbubbles were generated in C₃F₈ gas using a mechanical shaker. This produced a microbubble population with a mean diameter of 1.7±0.7µm and a concentration of 1×10¹⁰ microbubbles/ml. α_vβ₆-targeted or isotype control-targeted microbubbles were added to the wells and the wells were subjected to a tone or chirp exposure as shown in Figure 1. Tone exposures were performed at 2 and 5 MHz with chirp exposures performed over the 1.32-3.08 and 3.12-7.28 MHz ranges. CellTracker Green was then added to the cells where it enters viable cells and forms a cell-impermeant product. Under fluorescence microscopy, cells were counted that were positive for both PI and CellTracker Green, indicating viable cells that had been sonoporated (Figure 2).

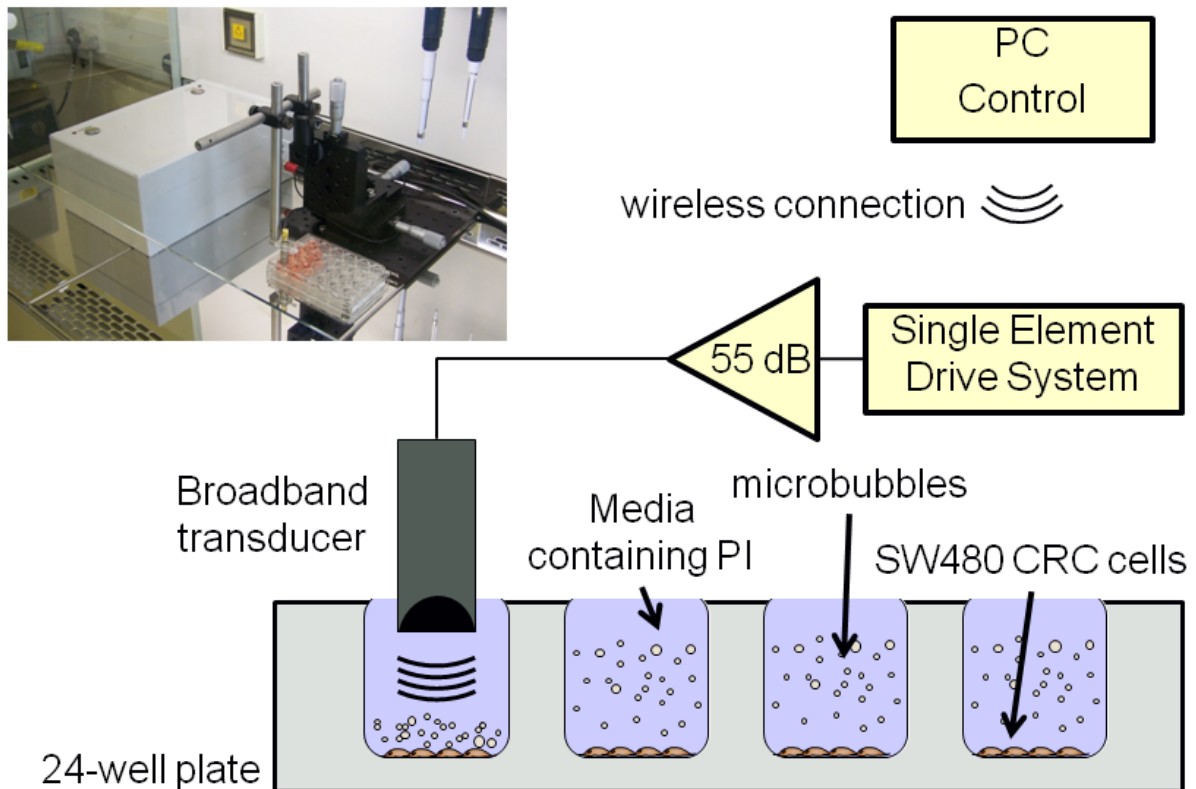


Figure 1: A schematic view of the experimental apparatus used for the sonoporation study, with an inset photograph showing the apparatus located within a biosafety cabinet.

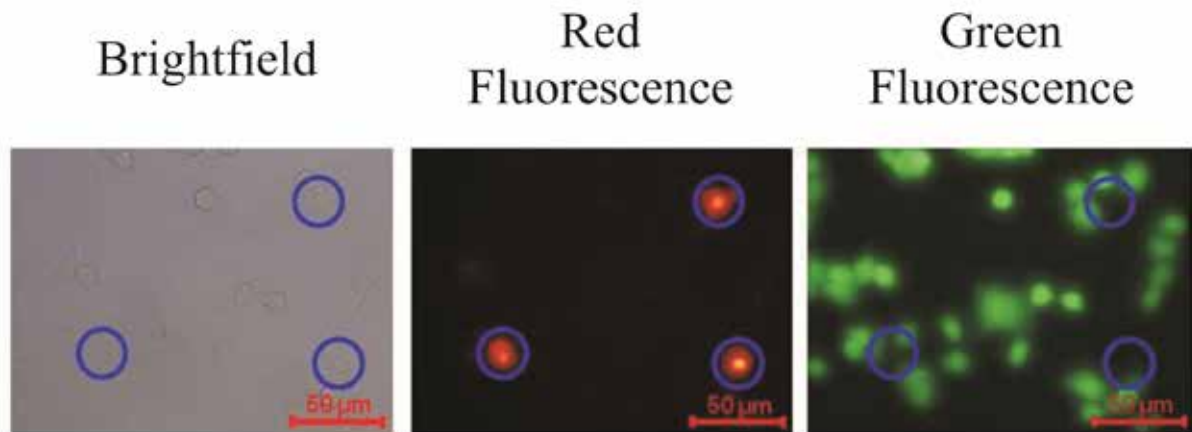


Figure 2: A sequence of images highlighting (blue circle) cells that were positive for PI but were not viable.

This study showed that using chirp excitations for polydispersed microbubble populations resulted in an increase in the sonoporation efficiency of cell culture mono-layers over the use of equivalent duration and acoustic pressure tone bursts. The chirp centred at 5 MHz showed the highest level of sonoporation efficiency at $27\pm 5\%$. Use of chirp excitation will therefore facilitate pre-clinical evaluation of MB vehicles for US-triggered targeted drug delivery and may prove useful in the development of clinical sonoporation strategies.

Ultrasound contrast agents mediated cell labeling for MRI tracking

*Ilya Skachkov¹, Ying Luan¹, Sandra van Tiel², Ton van der Steen^{1,3}, Klazina Kooiman¹,
Monique Bernsen², Nico de Jong^{1,3}*

*¹Department of Biomedical Engineering, Thoraxcenter, Erasmus MC, P.O. Box 2040,
3000 CA Rotterdam, the Netherlands*

²Department of Radiology, Erasmus MC, P.O. Box 2040, 3000 CA Rotterdam, the Netherlands

³Interuniversity Cardiology Institute of the Netherlands (ICIN), Utrecht, the Netherlands

Background

Live time cell tracking in vivo is an emerging field and a promising technique for tracking stem cells, metastasis and inflammation. Specific labeling of endothelial cells is important for molecular imaging of inflammation, atherosclerosis and tumor progression [1]. Cells labeled with super paramagnetic iron oxide (SPIO) can be detected by MRI. In vitro labeling is usually done by lipofectamine but cannot be used in vivo [2]. Recently we showed that ultrasound (US) activated targeted microbubbles (tMB) induced drug uptake in endothelial cells [3], which could be used in vivo. The aim of this study was to find optimal US parameters for tMB-mediated SPIO-labeling of endothelial cells.

Methods

Human umbilical vein endothelial cells (HUVECs) were cultured until confluence in OptiCells [3]. Biotinilated lipid coated microbubbles were made by sonication as described by Klivanov et al [4]. Biotinylated anti-human CD31-antibody was conjugated to the microbubbles via avidin-biotin bridging as described by Lindner et al [5]. tMB (10^7) were added to an OptiCell, which was turned upside down to let microbubbles adhere to the cells by flotation and incubated at 37°C for 5 min. SPIO was added 5 min before, immediately before (0 min), 5 and 15 min after insonification (Fig. 1) at a final concentration of 22.4 µg Fe/ml. Then the OptiCell was placed into the experimental setup and insonified with a 1.0 MHz single element focused transducer for 30 sec (10-160 kPa, 1MHz, 1,000-10,000 cycles, 20 Hz pulse repetition frequency, 6.5 mm -6dB beamwidth). No US was used as control. After insonification the OptiCells were incubated for one hour since SPIO addition at 37°C. The experiments were done in triplicate. After treatment, cells were fixed with 4% formaldehyde and stained with Prussian Blue [6] to detect the SPIO. After drying, the microscopic examination was done. SPIO uptake was assessed by manually counting Prussian Blue positive cells for ~500 cells within a 6 mm spot around the center of each insonified area. Cell viability was evaluated by changes in cell morphology and normalized by amount of cells per field of view.

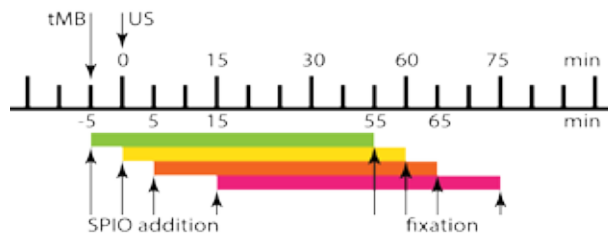


Figure 1: Experimental scheme.

Results

In fig. 2, the percentages of SPIO positive cells are plotted for four different moments of SPIO addition in relation to the moment of insonification for different acoustic pressures (no US, 10, 20, 40, 80 and 160 kPa). The number of SPIO positive cells increased for increasing acoustic pressure up to a value of 13-15 % for both the addition of SPIO 5 min prior to as well as just before US application. SPIO addition after US application resulted in lower SPIO uptake. No US gave less than 2 % of SPIO positive cells.

Normalized cell viability for all studied ultrasound settings is plotted in fig. 3. Cell death became significant for pressures above 40 kPa for all conditions.

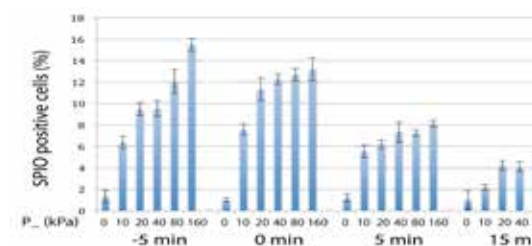


Figure 2: SPIO uptake by HUVECs assessed by Prussian Blue.

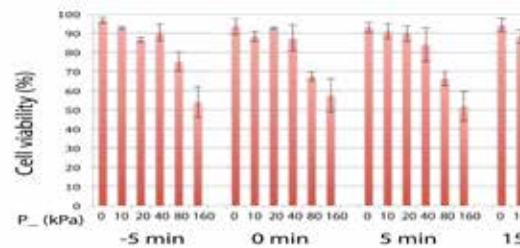


Figure 3: Cell viability normalized to cell density

Conclusion

The optimal US parameters for SPIO delivery to HUVECs were 40 kPa at 1 MHz, 10000 cycles, 20 Hz pulse repetition frequency, applied 5 minutes after SPIO addition. This setting gives an up to 7 times increase of SPIO uptake compared to the control with 90% cell viability. A ~10% labeling should be sufficient for in vivo MRI tracking. This technique could therefore safely be used for in vivo labeling of endothelial cells with SPIO, where other cell labeling techniques may not be applicable.

Acknowledgement

Authors would like to thank, Michiel Manten, Robert Beurskens and Geert Springeling from the department of Biomedical Engineering, Erasmus MC and Gabriela Doeswijk from the Department of Radiology for their assistance.

References

1. E. M. Shapiro, et al., "In vivo detection of single cells by MRI," *Magn Reson Med*, vol. 55, pp. 242-9, Feb 2006.
2. S. T. van Tiel, et al., "Variations in labeling protocol influence incorporation, distribution and retention of iron oxide nanoparticles into human umbilical vein endothelial cells," *Contrast Media & Molecular Imaging*, pp. n/a-n/a, 2010.
3. K. Kooiman, et al., "Sonoporation of endothelial cells by vibrating targeted microbubbles," *Journal of controlled release : official journal of the Controlled Release Society*, vol. 154, pp. 35-41, Aug 25 2011.
4. A. L. Klibanov, et al., "Detection of individual microbubbles of ultrasound contrast agents: imaging of free-floating and targeted bubbles," *Invest Radiol*, vol. 39, pp. 187-95, Mar 2004.
5. J. R. Lindner, et al., "Ultrasound assessment of inflammation and renal tissue injury with microbubbles targeted to P-selectin," *Circulation*, vol. 104, pp. 2107-12, Oct 23 2001.
6. G. Clark, *Staining Procedures*, 3 ed. Baltimore: Willams and Wilkins Co, 1973.

Modeling contrast microbubbles: From echocardiography to noninvasive blood pressure monitoring and targeted drug delivery

Kausik Sarkar

*Department of Mechanical and Aerospace Engineering,
George Washington University*

For the past decade, we have been performing experimental and analytical research on contrast microbubbles. We proposed and subsequently developed an interface model of the encapsulation which has an intrinsic interfacial rheology with surface viscosities and elasticities and therefore addresses the wide disparity of scales between the overall bubble size and that of the encapsulation.

In this talk, I will discuss material characterization of these contrast agents where progressively more sophisticated models have been developed guided by experimental observations. The characterization process includes independent estimation and validation components—attenuation is used to estimate the model material parameters, and then the estimated model is validated against independently measured subharmonic response. A model for the dissolution of microbubbles that accounts for the effects of encapsulation is developed to show that the encapsulation hinders the permeability of the gas-liquid surface, and its elasticity balances the surface tension-induced dissolution stress. The subharmonic aided noninvasive pressure estimation that depends on experimentally observed decrease of subharmonic response of many commercial contrast agents with local hydrostatic pressure will also be critically examined. I will show and explain unusual behaviors of subharmonic response in sharp contrast to “plausible expectations” and classical results from free bubble dynamics. It will be shown that the basic bubble dynamics predicts either a decrease or an increase of subharmonic response with pressure increase depending on the excitation frequency and the bubble size. The minimum threshold excitation for subharmonic generation from an encapsulated microbubble will be revisited to show that in contrast to the classical perturbative result, it is not always obtained at twice the resonance frequency; instead it can occur over a range of frequency from resonance to twice the resonance frequency. The quantitative variation of the threshold with different models of encapsulation will be discussed. I will also briefly discuss specifically targeted and cytosolic delivery of cancer drugs from “echogenic liposomes”. [support: NSF, NIH, DOD]

Brandaris 128 ultra-high-speed imaging facility: 10 years of operation, updates, and enhanced features

Michel Versluis

Physics of Fluids Group, University of Twente, Enschede, the Netherlands

The Brandaris 128 ultra-high-speed imaging facility has been updated over the last 10 years through modifications made to the camera's hardware and software. At its introduction the camera was able to record 6 sequences of 128 images (500×292 pixels) at a maximum frame rate of 25 Mfps. The segmented mode of the camera was revised to allow for subdivision of the 128 image sensors into arbitrary segments (1–128) with an inter-segment time of 17 ns. Furthermore, a region of interest can be selected to increase the number of recordings within a single run of the camera from 6 up to 125. By extending the imaging system with a laser-induced fluorescence setup, time-resolved ultra-high-speed fluorescence imaging of microscopic objects has been enabled. Minor updates to the system are also reported here.

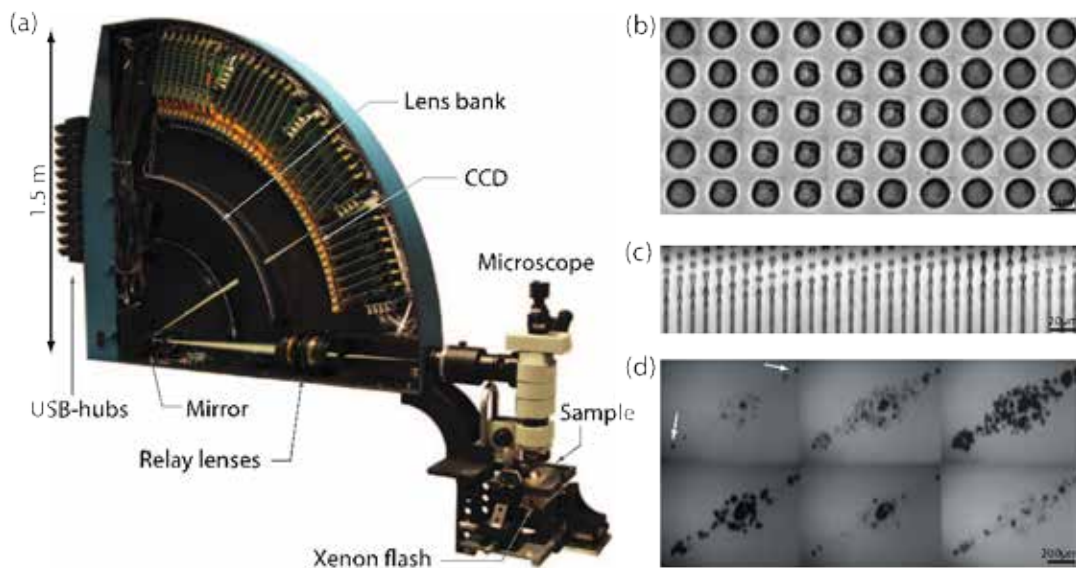


Fig. 1: (a) The Brandaris 128 ultra high-speed imaging facility. (b) Ultrasound contrast agent showing buckling behavior recorded at 14.5 Mfps. (c) Breakup of a $1.25 \mu\text{m}$ radius liquid jet into microdroplets, visualized with an interframe time of 73 ns. (d) Cleaning of a silicon wafer by the growth and collapse of a cloud of cavitation bubbles located in between two micro-pits (white arrows), recorded at 5.4 Mfps.

Sensing subharmonic volume variations of single contrast agent microbubbles in response to ultrasound with an “acoustical camera”

Guillaume Renaud¹, Johan G. Bosch¹, Antonius F.W. van der Steen^{1,2} and Nico de Jong^{1,2}

¹Biomedical Engineering, Thorax Center, Erasmus MC, Rotterdam, the Netherlands

²Interuniversity Cardiology Institute of the Netherlands, Utrecht, the Netherlands

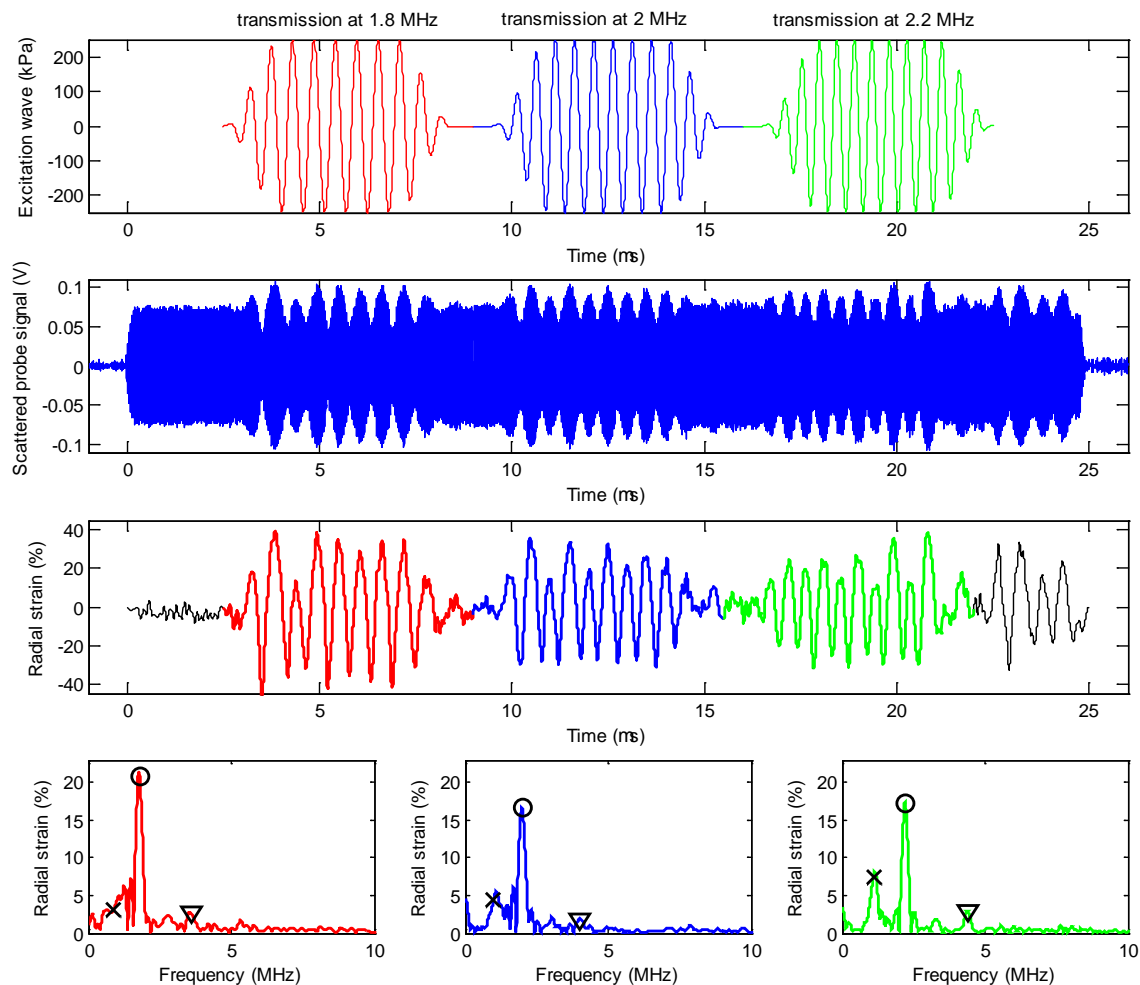
Measuring and understanding the nonlinear vibrations of contrast agent microbubbles in response to an ultrasound wave is essential to optimize the technique employed by an ultrasound scanner to distinguish microbubbles from tissue.

In this context, an acoustical method was developed to retrieve the radial response of single microbubbles to a pressure wave by means of a low-amplitude probing wave [1,2]. If the frequency of the latter is much higher than the spherical resonance frequency of the microbubble (typically between 1 and 10 MHz), the relative amplitude modulation (induced by a pressure wave) in the signal scattered in response to the probing wave is quasi-equal to the radial strain (i.e. relative variation in radius) induced by the pressure wave. A reference response to the probing wave acquired before and after the transmission of the pressure wave allows us to reveal asymmetry in microbubble oscillations. Although efficient nonlinear wave interaction is well known in bubbly liquids, we demonstrated [1,2] that such an “acoustical camera” can extract quantitative information on single bubble vibrations by analyzing the nonlinear coupling between two ultrasound waves.

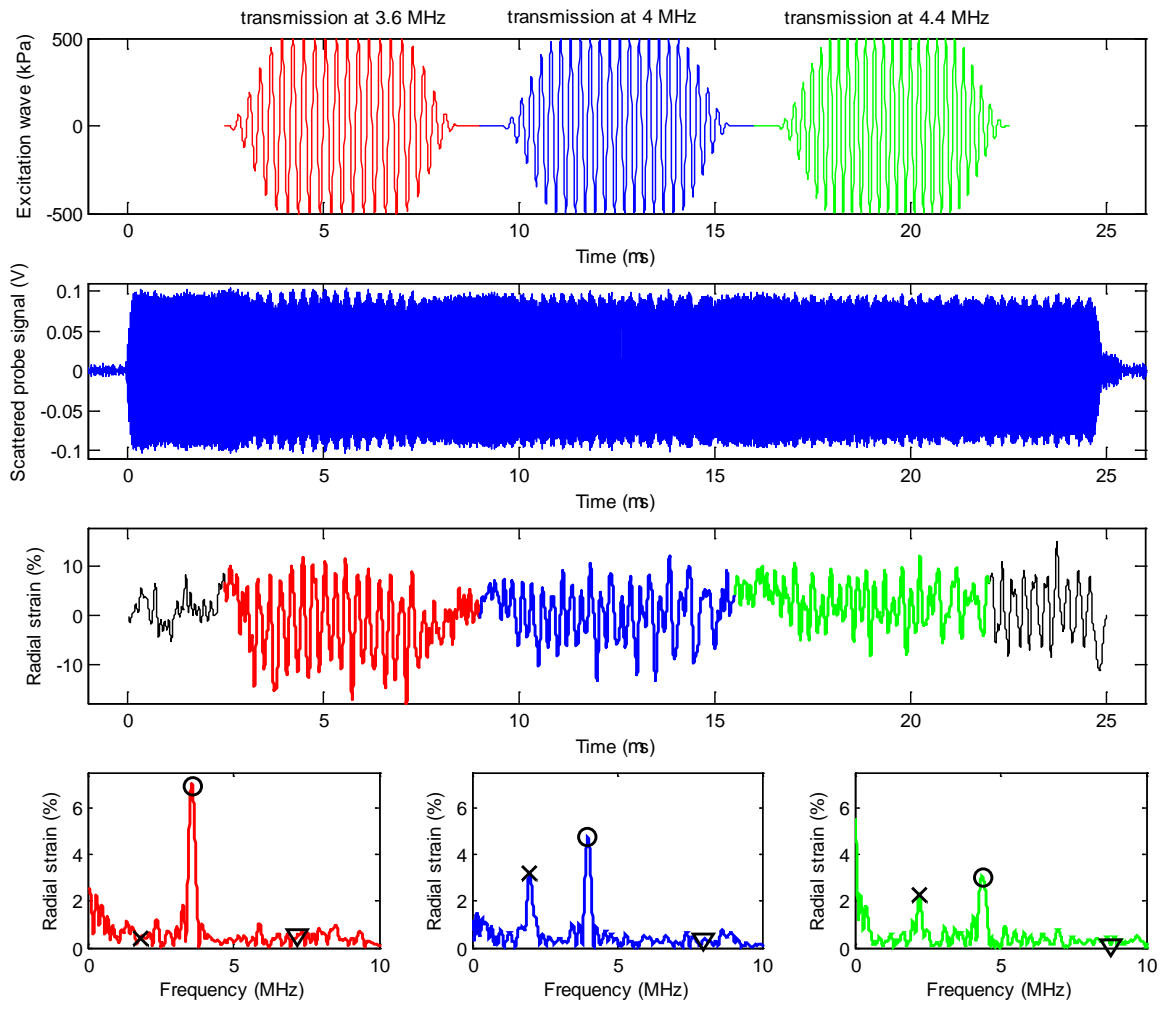
In this work, the subharmonic response of BR14 contrast agent (Bracco Research SA, Geneva, Switzerland) is investigated. Unlike high-speed optical measurements [3], the “acoustical camera” has the advantage to measure only volume subharmonic vibrations (and no isochoric surface modes [4]). These vibrations are of interest for contrast imaging since they produce the most efficient radiation of subharmonic echoes to be received by the probe of the ultrasound scanner. An experimental setup allows us to insonify single microbubbles simultaneously with two focused ultrasound beams, a probing wave at 30 MHz and a pressure wave having a frequency between 1 and 9 MHz [1,2]. The average resonance frequency of BR14 is close to 2 MHz. Therefore a sequence of three 6 microsecond sine bursts at 1.8-2.2 MHz is transmitted in order to excite the so-called TR (transmit at the resonance frequency) subharmonic response [5]. In order to produce the so-called T2R (transmit at twice the resonance frequency) subharmonic response, another set of measurements is performed by transmitting a sequence of three 6 microsecond sine bursts at 3.6-4.4 MHz. The figures show exemplary subharmonic responses of two single microbubbles.

References

1. G. Renaud, J.G. Bosch, A.F.W. van der Steen, N. de Jong. An "acoustical camera" for in vitro characterization of contrast agent microbubble vibrations. *Appl Phys Lett.*, 100 (10), 101911, 2012.
2. G. Renaud, J.G. Bosch, A. F. W. van der Steen, N. de Jong. Chirp resonance spectroscopy of single lipid-coated microbubbles using an "acoustical camera". *J Acoust Soc Am.*, 132 (6), EL470-EL475, 2012.
3. J. Sijl, B. Dollet, M. Overvelde, V. Garbin, T. Rozendal, N. de Jong, D. Lohse, M. Versluis. Subharmonic behavior of phospholipid-coated ultrasound contrast agent microbubbles. *J Acoust Soc Am.* 128 (5), 2010.
4. H.J. Vos, B. Dollet, M. Versluis, N. de Jong. Nonspherical shape oscillations of coated microbubbles in contact with a wall. *Ultrasound Med Biol.*, 37 (6), 935-948, 2011.
5. J. Chomas, P. Dayton, D. May, and K. Ferrara. Nondestructive subharmonic imaging. *IEEE Trans Ultrason Ferroelectr Freq Control.*, 49 (7), 883-92, 2002.



Example of TR subharmonic response of a single BR14 microbubble (circle: fundamental, triangle: 2nd harmonic, cross: subharmonic)



Example of T2R subharmonic response of a single BR14 microbubble (circle: fundamental, triangle: 2nd harmonic, cross: subharmonic)

Dynamics of StemBells in an ultrasound field

*T.J.A. Kokhuis^{1,2}, B.A. Naaijens^{2,3}, L.J.M. Juffermans^{2,4}, O. Kamp^{2,5},
A.F.W. van der Steen^{1,2}, M. Versluis⁶, N. de Jong^{1,2}*

¹*Biomedical Engineering, Thorax Center, Erasmus MC, Rotterdam, the Netherlands*

²*Interuniversity Cardiology Institute of the Netherlands, Utrecht, the Netherlands*

³*Department of Pathology, VU University Medical Center, Amsterdam, the Netherlands*

⁴*Department of Physiology, VU University Medical Center, Amsterdam, the Netherlands*

⁵*Department of Cardiology, VU University Medical Center, Amsterdam, the Netherlands*

⁶*Physics of Fluids, University of Twente, Enschede, the Netherlands*

Introduction

Cardiovascular diseases are the major cause of mortality worldwide [1]. Ischaemic heart diseases account for more than 40% to the total number of cardiovascular-related causes of death. Due to continuous developments in medical healthcare, the survival rate after a myocardial ischaemic event increases, introducing a new group of patients who are prone to develop heart failure. For these patients, restoration of the contractile function after such an event is important. Stem cell therapy is a promising tool to regenerate and repair damaged myocardium [2,3]. However, a common finding in experimental and clinical studies is that only a small fraction of the transplanted cells engraft and survive in the ischaemic area of the heart [4]. To improve the engraftment of stem cells we have proposed a new technique, in which microbubbles are conjugated to stem cells [5]. These complexes, dubbed StemBells, can then be targeted to specific inflammatory markers present in the ischaemic area of the heart, directing the stem cells to the desired location. Furthermore, the conjugation of bubbles to the stem cells facilitates ultrasound-mediated stem cell tracking and makes the complexes susceptible for acoustic radiation force in order to increase the lodging efficiency. For these applications, the interplay between an incident ultrasound field and StemBell needs to be known. The aim of the current study was therefore to investigate the dynamics of StemBells during ultrasound insonification using high-speed optical imaging.

Materials and methods

Preparation of targeted microbubbles

Fluorescent (DiI) biotinylated microbubbles with a perfluorobutane (C₄F₁₀) were made by sonication as described by Klivanov et al. [6]. The monoclonal anti-human CD90 antibody was conjugated to the microbubbles using biotin-avidin chemistry, as described by Lindner et al. [7].

Construction of StemBells

Cells from the stromal vascular fraction of adipose tissue were cultured in low glucose Dulbecco's modified Eagle's medium (DMEM) containing 5% human platelet lysate according to Naaijens et al. [8]. Prior to trypsination, cells were fluorescently labeled with CellTracker Green. Subsequently, cells

were trypsinized and mixed with the CD90-targeted microbubbles under continuous rotation for 30 min at room temperature.

Experimental protocol

StemBells dynamics were studied at driving frequencies in between 0.4 - 3 MHz at pressures P_{-} = 50–200 kPa. A broadband PVDF transducer (PA275, Precision Acoustics) was used in between 1-3 MHz. A 500 kHz PZT transducer (V318, Panametrics) was used for frequencies below 1 MHz. The dynamics were imaged with the Brandaris128 camera [9]. The contour of the StemBells in each frame was determined using custom software. The discrete Fourier transform was then calculated to determine the radial excursion of the StemBell in response to each driving frequency. The data was fitted with a Lorentzian function, resulting from a linearized Rayleigh-Plesset equation [10,11].

Results

The constructed StemBells were found to be very stable during repetitive ultrasound insonifications. Detachment and/or deflation of targeted bubbles was observed in a few occasions only. Interestingly, StemBells appeared to be pulsating as one big entity (i.e. resembling one big bubble). Figure 1A shows the response of a StemBell (with an equivalent initial radius of 12.6 μm) as a function of the driving frequency in between 1-3 MHz. The StemBell was most responsive at the lowest applied frequency of 1 MHz. Figure 1B shows the response of a StemBell (with an equivalent initial radius of 10 μm) as a function of the driving frequency in between 0.4-0.8 MHz. A peak of maximum response can be observed at 0.6 MHz.

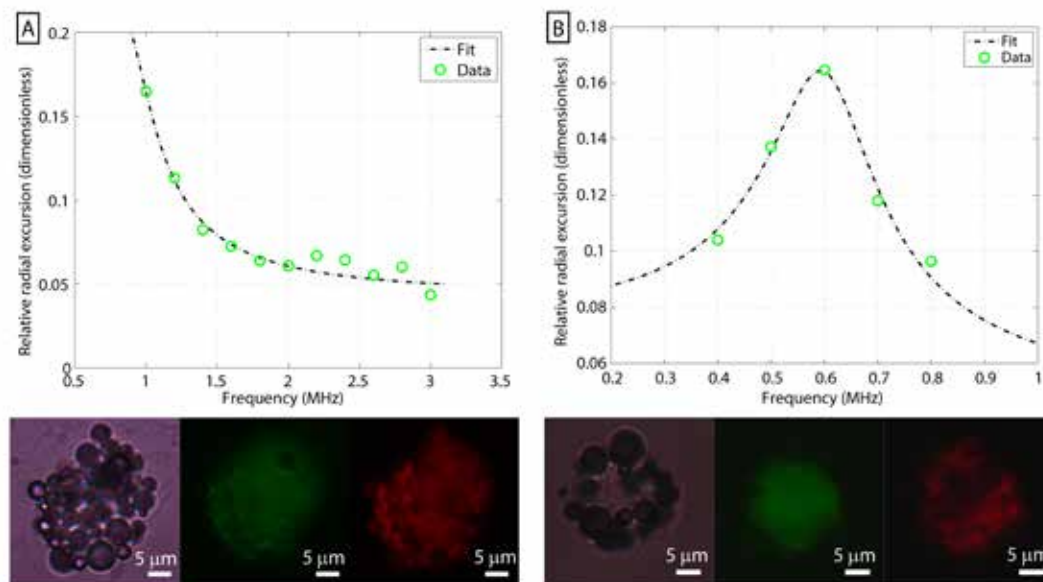


Fig 1. Amplitude of response (non-dimensionalized) of StemBells to driving frequencies from 1-3 MHz (A) and 0.4 – 0.8 MHz (B). The corresponding brightfield, CellTracker fluorescence (green) and DiI fluorescence (red) images are also shown.

Discussion, conclusions and outlook

StemBells were found to be most responsive at frequencies < 1 MHz. Our results suggest that the acoustical properties of a StemBell cannot be simply interpreted as the collective result of the independent contributions of the constituent microbubbles. The presence of neighboring bubbles was observed to change the acoustical properties of individual targeted bubbles, causing an apparent shift in the resonance frequency of the complex towards lower frequencies. A model capturing the StemBell dynamics in an ultrasound field is currently in development.

Acknowledgments

This project was funded by the Dutch Technology Foundation (STW). The authors thank Frits Mastik for developing the contour-tracking software and Robert Beurskens, Geert Springeling and Michiel Manten for their technical assistance.

References

1. World Health Organization, *Global Health Observatory Data Repository: Cause specific mortality 2008*, URL: <http://apps.who.int/gho/data/?vid=10012#>.
2. Houtgraaf, J.H. et al. *First experience in humans using adipose tissue-derived regenerative cells in the treatment of patients with ST-segment elevation myocardial infarction. J. Am. Coll. Cardiol.* **59**, 539-540 (2012).
3. van Dijk, A. et al. *Reduction of infarct size by intravenous injection of uncultured adipose derived stromal cells in a rat model is dependent on the time point of application Stem Cell Res.* **7**, 219-229 (2011).
4. Wang, Q. et al. *Myocardial regeneration with stem cells: Pharmacological possibilities for efficacy enhancement Pharmacol. Res.* **53**, 331-340, (2006).
5. Juffermans, L.J.M et al. *Directing adipose derived stem cells to the area at risk in the heart after myocardial infarction using targeted microbubbles – Development of a new molecular therapeutic technique Abstract book of the 15th European symposium on Ultrasound Contrast Imaging, 21-22 January 2010, Rotterdam, The Netherlands.*
6. Klibanov, A. L. et al. *Detection of individual microbubbles of ultrasound contrast agents: imaging of free-floating and targeted bubbles. Invest Radiol* **39**, 187-195 (2004).
7. Lindner, J.R. et al. *Ultrasound assessment of inflammation and renal tissue injury with microbubbles targeted to P-Selectin Circulation* **104**, 2107-2112 (2001).
8. Naaijken, B.A. et al. *Human platelet lysate as a fetal bovine serum substitute improves human adipose-derived stromal cell culture for future cardiac repair applications Cell Tissue Res* **348**, 119-130 (2012).
9. Chin, C. T. et al. *Brandaris 128: A digital 25 million frames per second camera with 128 highly sensitive frames. Rev Sci Instrum* **74**, 5026-5034, (2003).
10. Hilgenfeldt et al, *Response of bubble to diagnostic ultrasound: A unifying theoretical approach Eur Phys J B* **4**, 247-255 (1998).
11. van der Meer, S.M. et al. *Microbubble spectroscopy of ultrasound contrast agents J Acoust Soc Am* **121**, 648-656 (2007).

The effect of boundary proximity on the frequency of maximum response and nonlinear emissions of individual microbubbles in the 4 to 13.5 MHz range

Brandon Helfield^{1,2}, Ben Leung², David Goertz^{1,2}

¹*Department of Medical Biophysics, University of Toronto, Toronto, Ontario, Canada*

²*Sunnybrook Research Institute, Toronto, Ontario, Canada*

Contrast imaging in the 5-15 MHz range is of interest in applications such as the assessment of carotid atherosclerosis and superficial tumor detection/diagnosis (e.g. breast). The proximity of microbubbles to a boundary may affect their emissions in the context of targeting or microbubbles present within microvessels. To date, there have been only limited experimental investigations of these effects, conducted at lower frequencies (< 5 MHz) where the influence of proximity to polystyrene membranes (Opticell) on microbubble resonant frequencies was examined. In this study, both resonant frequencies and subharmonic emissions from individual microbubbles were examined as a function of boundary proximity at higher frequencies. Two types of boundaries were employed; an Opticell due to its use in previous studies, and a compliant agarose layer in order to represent a more biologically relevant boundary.

Both MicroMarker and Target-Ready MicroMarker (Bracco, Geneva) were employed in this study. Individual microbubbles were optically sized while situated adjacent to either an Opticell or an agarose boundary. An optical tweezer system was then used to manipulate microbubble position, and the acoustic response from the individual microbubble was recorded as a function of distance from the boundary (0-150 μm). For a subset of experiments ($n=30$), an “acoustic spectroscopy” approach was employed, whereby microbubbles were insonicated with 8-cycle Gaussian tapered tone bursts (4 to 13.5 MHz in 0.5 MHz increments) at peak negative pressures ranging from 20-50 kPa. Echoes were detected, corrected for the transducer and receive circuit response, and used to estimate radial excursions in order to assess the low-pressure frequency of maximum fundamental response (f_{MR}) and maximum amplitude of oscillation (A_{MR}). In a second set of experiments ($n=56$), microbubbles were insonicated with an 11 MHz, 15-cycle Gaussian tapered pulse at 69 kPa. Both the fundamental and subharmonic scattered pressure emissions were recorded and compared to simulations that utilize a “method of images” approach.

For the Opticell boundary ($n=11$), f_{MR} and A_{MR} for a given bubble were shown to shift with boundary proximity in an oscillatory manner – first increasing then decreasing. The magnitudes of the deviations of f_{MR} and A_{MR} were up to 30% and 110% of their value at the boundary (i.e. at 0 μm), respectively. For the agarose boundary ($n=19$), no appreciable shift in f_{MR} with increasing boundary distance was observed, with only slight differences in A_{MR} apparent ($\approx 10\%$). For both boundary types, a shift in f_{MR} to lower frequencies and A_{MR} to larger amplitudes with increasing acoustic pressures was observed. At 69 kPa, both fundamental and subharmonic pressure emissions from microbubbles were also shown to exhibit oscillatory behavior with increasing distance from the Opticell boundary ($n=15$), while for the agarose boundary case ($n=41$) fundamental emissions were shown to decrease by up to 10% and subharmonic emissions were shown to substantially increase by up to 200% with increasing distance. When oscillatory behavior was observed (Opticell case), the locations of the peaks and troughs were broadly consistent with simplified analytical simulations incorporating the “method of images”, and suggests that this effect is more prominent at higher frequencies (shorter wavelengths) and in smaller vessels. For the agarose boundary case, analytical simulations modeling an encapsulated bubble-planar boundary system underestimate the magnitude of fundamental and subharmonic response with increasing boundary distance. These results suggest that microbubble response exhibits a complex transmit pressure dependence on boundary proximity and the boundary properties themselves.

Ultrasound contrast and molecular imaging in small animals

F. Stuart Foster, Melissa Yin, Eva Chan, Robert S. Kerbel, Daniela S. Ardelean and Michelle Letarte

Sunnybrook Health Sciences Centre and Hospital for Sick Children, Department of Medical Biophysics, University of Toronto

The use of microbubble contrast imaging in clinical applications is finally gaining some acceptance in the non-invasive diagnosis of cardiac diseases and commonly encountered liver and kidney masses. Other applications such as prostate cancer, breast cancer and Crohn's disease offer intriguing potential for future successes. Current microbubble (MB) contrast formulations such as lipid encapsulated perflutren and sulphur hexafluoride have been optimised with respect to size and shell elastic parameters to resonate effectively in the 3 – 5 MHz range. The implementation of effective contrast imaging on specialized platforms operating at frequencies above 10 MHz also have potential applications in ocular disease, coronary atherosclerosis, endoscopic imaging ,and small animal imaging. The development of high frequency contrast imaging has largely been tied to previous contrast developments at low frequencies. However the introduction of dedicated high frequency systems for preclinical imaging has led to the development of specific microbubble agents designed for small animal imaging. The results achieved with these agents have been mixed: Whereas low frequency contrast studies routinely achieve 30 – 40 dB contrast to tissue ratios high frequency agents are challenged to achieve 20dB and performance drops significantly above 30MHz. This situation has led investigators to pursue creative variations such as subharmonic imaging, self-demodulation imaging, and dual frequency imaging to improve performance. The current state of the art in these areas will be briefly reviewed.

A wide range of applications for high frequency preclinical contrast imaging are being pursued. Two areas of application will be describe here: High frequency MB contrast imaging of inflammatory bowel disease and MB contrast imaging in experimental cancer models designed to parallel human clinical trials of targeted receptor tyrosine kinase inhibitors (RTKIs) and antibodies. Inflammatory bowel diseases are the most common chronic intestinal conditions. Their incidence and prevalence have shown a significant increase in the last decades. IBD is often refractory to anti-inflammatory agents, and novel therapeutic strategies are much needed. Approaches for preclinical MB contrast imaging of IBD will be described with preliminary results for an experimental therapy based on anti VEGF treatment. The development of new therapeutics for cancer therapy have been complicated by acquired resistance and “rebound” effects that appear to reduce the expected clinical gains. Recent high profile papers have even suggested that targeted antiangiogenic mono therapies may increase the aggressiveness of disease by accelerating metastasis and angiogenesis independent growth patterns.

In this presentation, tumor growth in the mouse is studied using MB contrast to investigate the differences between mono and combination therapy with an emphasis on the issues of rebound and resistance.

The use of targeted microbubbles (MBs) for the detection of specific molecular signals has been established for many years. Interest from the radiological community has recently been kindled by the development of the first clinically translatable microbubble contrast agent (BR55, Bracco). Yet the use of this remarkable capability has not found widespread application due, in part, to the fact that the quantitative relationship between detected signals and the actual target density has not been well established. Efforts to define the relationship between an important receptor (VEGFR-2) and signals obtained in molecular imaging experiments with targeted microbubbles will be described over a range of concentrations and tumour types. The objective of this work was to derive a quantitative means to evaluate molecular expression patterns. Although VEGFR-2 targeted MBs showed significant injection-to-injection coefficients of variation that ranged from 10 to 46% in individual mice a linear dependence between bound MB power was observed in three tumour types: Hep3B human hepatocellular carcinoma (HCC), Lewis lung carcinoma (LLC) and 231/LM2-4 breast cancer. Normalization of these data to peak contrast wash-in power levels significantly reduced variability resulting in an injection concentration independent measurement of the molecular signal. These studies illustrate the need for improved contrast delivery as well as better means to suppress concentration dependent artifacts in molecular imaging. The proposed normalization strategy investigated here represents a preliminary step towards accurate quantification of molecular markers such as VEGFR-2 in mouse tumours.

Molecular imaging in humans: Ultrasound in comparison with other imaging modalities

A.L. Klibanov

*Cardiovascular Division, Department of Medicine, University of Virginia, Charlottesville VA 22908,
USA*

Molecular imaging is defined as “visualization, characterization, and measurement of biological processes at the molecular and cellular levels in humans and other living systems” [1]. The actual term came into existence at the very beginning of this century [2], however, practical applications, including human clinical use, were relatively widespread significantly earlier, and called “targeted imaging” [3].

Traditionally, radioisotopes were first to find clinical use as cancer imaging contrast agents, or in the cardiovascular applications. A substance that possesses specific ability to accumulate in the tissue of interest (e.g., cancer-specific ligand, or viable myocardium) such as an antibody carries a radioactive isotope label (or is a radiolabel itself, such as thallium isotope used in myocardial perfusion imaging). It is injected in the patient, circulates in the bloodstream and accumulates in the tissue of interest; residual material is cleared from the bloodstream so that targeted imaging can be performed, using gamma camera radiation detectors. Because radioisotope is selected as a rapidly decaying gamma ray emitter with little to no beta radiation, resulting bioeffects for the patients are considered acceptable.

Initially, planar gamma cameras were applied, obtaining a flat “snapshot” projection of the isotope biodistribution pattern – but it was already practically feasible for the delineation of cardiac perfusion defect following myocardial infarction, or finding tumor metastasis nodes. Later, a 3D technique, single-photon emission computer tomography (SPECT), which implied rotation of the gamma camera detector head around the patient, found its way into widespread clinical use, and followed by a more precise and sensitive positron emission tomography. PET is based on the synchronous emission (and therefore improved detection) of two oppositely directed photons from the positron annihilation event. PET is now widely used in the clinic with F-18-labeled contrast materials, most popular being fluorodeoxyglucose, for visualization of the areas of enhanced metabolism. Novel PET contrast agents enter the field currently, and may get widespread clinical use in the near future. To obtain the reference of the anatomical position of the label, most SPECT and PET scanners are now combined with CT. Combined PET-MRI units will become available in near future.

Magnetic resonance imaging by itself did not yet find widespread use in molecular and cellular imaging in the clinic. Most popular MRI contrast agents are limited to blood pool imaging with rapid clearance via kidneys, although there is significant history and interest in preclinical research for targeted MRI contrast for receptor imaging and cell labeling. One significant lesson that ultrasound imaging equipment manufacturers may want to learn from their MRI colleagues is widespread availability and flexibility of MR imaging pulse sequences.

Molecular imaging with optical detection is widespread in preclinical studies, but its move into the human clinical setting is restricted by the shallow penetration of light in the patient body, so catheter-based approaches, surface (skin) monitoring, and fluorescence-guided surgery will be first to move to the clinic, with simple contrast agents such as fluorescence dye-labeled folate that accumulates in tumor nodes, to facilitate their surgical removal in ovarian cancer [4].

Gas-filled targeted microbubble contrast agents useful in ultrasound molecular imaging have been formulated more than 15 years ago [5,6,7]. Contrast particle design is optimized to assure excellent detection sensitivity, rapid clearance, maximize targeting and minimize potential side effects. Microbubbles are purely intravascular agents (mean size ~1-2 μm). Microbubbles are typically coated with a lipid monolayer shell, with ~2nm thickness. This assures ability to compress and expand in the ultrasound field to provide efficient ultrasound scattering. Lipid shell is decorated with a PEG brush, which improves microbubble stability and circulation time, yet minimizes nonspecific adhesion of microbubbles in normal tissues or the chances of complement activation. Targeting ligands are often located on the distal tip of the grafted PEG polymer chain: this extended spacer arm improves ability of ligand-decorated bubbles to adhere to the target receptor surface. Targeted microbubbles can delineate receptor surfaces that carry as little as several dozens of target molecules per μm^2 area, so this is indeed a molecular imaging approach. Microbubble contrast agents are quite competitive as molecular imaging agents for intravascular markers monitoring, and are already at the clinical trials stage, e.g., as BR55 microbubble targeted towards VEGF Receptor 2 on the tumor vascular endothelium [8,9]. Other possible targets include the endothelial markers of inflammation, ischemia-reperfusion injury, ischemic memory or active clot markers, such as activated platelets – the latter could be useful for active atherosclerotic plaque detection.

Patient safety is the most important factor that regulatory agencies will take into account, in relation to the benefits of the required diagnostic accuracy when considering clinical use of the contrast imaging. Microbubble agents do not require ionizing radiation; the injected dose of contrast and targeting ligands is so small that Phase 0 “exploratory” IND trials should be possible, which will aid with the clinical introduction of ultrasound contrast molecular imaging.

Overall, the use of molecular ultrasound imaging has good prospects to become as widespread in the clinic as other molecular imaging modalities, and may become especially helpful for real-time image guidance of biopsies or image-guided therapy applications.

References

1. Mankoff DA. A definition of molecular imaging (a task force report). *J Nucl Med.* 2007;48(6):18N, 21N.
2. Weissleder R, Mahmood U. Molecular imaging. *Radiology.* 2001;219:316-33.
3. Torchilin V.P. *Handbook of Targeted Delivery of Imaging Agents*, CRC Press, 1995.
4. van Dam GM, Themelis G, Crane LM, Harlaar NJ, Pleijhuis RG, Kelder W, Sarantopoulos A, de Jong JS, Arts HJ, van der Zee AG, Bart J, Low PS, Ntziachristos V. Intraoperative tumor-specific fluorescence imaging in ovarian cancer by folate receptor- α targeting: first in-human results. *Nat Med.* 2011;17:1315-9.
5. Klibanov AL, Hughes MS, Marsh JN, Hall CS, Miller JG, Wible JH, Brandenburger GH. Targeting of ultrasound contrast material. An in vitro feasibility study. *Acta Radiol Suppl.* 1997;412:113-20.
6. Targeting and ultrasound imaging of microbubble-based contrast agents. Klibanov AL, Hughes MS, Villanueva FS, Jankowski RJ, Wagner WR, Wojdyla JK, Wible JH, Brandenburger GH. *MAGMA.* 1999;8:177-84.
7. Unger EC, McCreery TP, Sweitzer RH, Shen D, Wu G. In vitro studies of a new thrombus-specific ultrasound contrast agent. *Am J Cardiol.* 1998;81:58G-61G.
8. Pochon S, Tardy I, Bussat P, Bettinger T, Brochot J, von Wronski M, Passantino L, Schneider M. BR55: a lipopeptide-based VEGFR2-targeted ultrasound contrast agent for molecular imaging of angiogenesis. *Invest Radiol.* 2010;45:89-95.
9. Tardy I, Pochon S, Theraulaz M, Emmel P, Passantino L, Tranquart F, Schneider M. Ultrasound molecular imaging of VEGFR2 in a rat prostate tumor model using BR55. *Invest Radiol.* 2010;45:573-8.

Ultrasound-targeted microbubble destruction to deliver siRNA cancer therapy

Andrew Carson, Charles McTiernan, Jianjun Wang, Xucai Chen and Flordeliza Villanueva

Center for Ultrasound Molecular Imaging and Therapeutics, University of Pittsburgh, Pittsburgh, PA, USA

Strategies targeting Epidermal Growth Factor Receptor (EGFR), including the use of RNA interference, have shown great promise to treat carcinoma, but would benefit from improved delivery techniques. Microbubble contrast agents have the ability to specifically deliver nucleic acids to target tissues when treated with ultrasound parameters that mediate ultrasound-targeted microbubble destruction (UTMD). We hypothesized that microbubbles and UTMD could be used to enhance delivery of EGFR-directed small inhibitory RNA (siRNA) and limit growth of squamous cell carcinoma tumors *in vivo*. Custom designed microbubbles were shown to efficiently bind high levels of siRNA (~7 µg per 10⁹ microbubbles) and mediate protection from RNase. UTMD mediated delivery of microbubbles loaded with EGFR-siRNA to murine squamous cell carcinoma cells (SCC-VII) *in vitro* slowed EGF-dependent cell replication in the subsequent 48 hrs, resulting in significantly fewer viable cells than following UTMD-mediated delivery of control-siRNA ($3.3 \pm 0.4 \times 10^5$ vs. $8.3 \pm 2.4 \times 10^5$, $p < 0.001$). Serial UTMD mediated delivery of EGFR-siRNA *in vivo* significantly and markedly increased the tumor doubling time in a murine model of squamous cell carcinoma (EGFR-siRNA treated tumors 10 ± 6 days; control-siRNA treated tumors 2 ± 0 days; no siRNA treated tumors 2 ± 0 days; $p = 0.002$). UTMD of microbubbles loaded with EGFR-siRNA also significantly decreased EGFR expression as assayed by immunofluorescent analysis ($p = 0.005$) and RT PCR analysis ($p = 0.035$) of tumor samples. These data indicate that custom designed microbubbles and UTMD can deliver gene-targeted siRNA to tumors and blunt tumor growth.

DNA loaded albumin microbubbles for ultrasound & microbubble mediated gene transfection in vivo

Richard J Browning^{1,3}, Meng-Xing Tang², Robert J Eckersley³

¹Imaging Sciences Department, Imperial College London, UK

²Bioengineering Department, Imperial College London, UK

³Biomedical Engineering Department, King's College London, London, UK

Introduction

Ultrasound (US) and microbubble (MB) mediated gene transfection is a rapidly advancing field with great potential for the targeted treatment of many diseases, however transfection efficiencies are still low. As such, modifications to the MB have been undertaken to improve their functionality and potential transfection ability, for instance, DNA loading. Lipid based MBs made with cationic lipids have been shown to be capable of loading naked DNA and protecting it from nucleases, leading to an improvement in transfection compared to neutral MBs (Wang *et al.*, 2012).

Previous studies have shown that albumin based MBs cause a greater level of transfection than lipid shelled formulations (Alter *et al.*, 2009), however the potential of DNA-loaded albumin based MBs has not fully been explored for transfection *in vivo*.

In this work, a DNA-loading albumin MB was created by the addition of glucosamine (GlcA), a sugar with a cationic amine group, to the formulation. We present detailed acoustic characterisation of the GlcA MB by bulk acoustics, optical and fluorescence microscopy. Preliminary investigations into the transfection ability of the MB have also been conducted.

Methods

GlcA MBs were manufactured from a 1:3 mix of a 2% albumin solution and a 40% dextrose/15% GlcA solution, heated to 50°C. Octafluoropropane gas was bubbled through the solution before sonication (20 kHz, 33-45 W, 1 min). The resulting suspension was centrifuged twice and the supernatant aspirated by syringe after each spin. A Control MB was made by replacing GlcA with dextrose, e.g. 55% dextrose. Counting and sizing was performed by optical microscopy (Sennoga *et al.*, 2010).

For qualitative demonstration of DNA-loading, MBs were incubated with plasmid DNA and the fluorescent DNA-binding dye DAPI for 10 minutes at room temperature. MBs were then washed and examined under fluorescence microscopy. To quantify DNA-loading, MBs were incubated with plasmid DNA for 5 minutes and then washed. DNA was isolated from MBs using a Qiagen miniprep kit and the purified DNA quantified by UV absorbance at 260 nm (Nanodrop 2000).

Acoustic attenuation measurements of bulk MB suspensions were performed in gas saturated, 34°C water as previously described (Mulvana *et al.* 2010). MBs were added to a 300 ml acoustically

transparent vessel at the focus of a single element transducer. The transducer was driven with a single cycle, 3.5 MHz centre frequency pulse at 125 and 200 kPa peak negative pressure. Pulse repetition frequency was 1 Hz and signals were acquired in the far field using a needle hydrophone for 5 minutes. Measurements were normalised against the actual volume of contrast agent added to generate each measurement and mean attenuation was calculated against a no bubble sample.

Preliminary *in vivo* transfection experiments were performed on the myocardium of 6-8 week old, female, CD1 mice. 7.5×10^7 MBs and 200 μg of a luciferase plasmid, were tail vein administered by a 27G needle prior to 2 minutes of diagnostic US (6.1 MHz, 1.6 MI). After 72 hours, IP injection of luciferin and *in vivo* bioluminescence imaging (IVIS 100) were used to identify areas of transfection.

Results

Bubble manufacture produced suspensions with similar size distribution and concentration (Table 1).

Microbubble	Mean Diameter (μm)	Concentration (MBs/ml)	Gas Concentration ($\mu\text{l/ml}$)
GlcA	1.58 ± 0.13	$1.44 \pm 0.13 \times 10^9$	5.82 ± 2.56
Control	1.46 ± 0.08	$1.56 \pm 0.23 \times 10^9$	5.06 ± 1.52

Table 1. MB population statistics (Mean \pm S.D.).

Under fluorescence microscopy, DNA-loaded GlcA MB (Fig. 1d) showed greater fluorescence than Control (Fig. 1h) suggesting greater DNA-loading. No fluorescence was seen in unloaded MBs. UV absorbance quantification revealed GlcA MB could load 0.33 ± 0.19 pg of DNA per MB, whereas the amount of DNA loaded by Control MB was below the limit of UV detection.

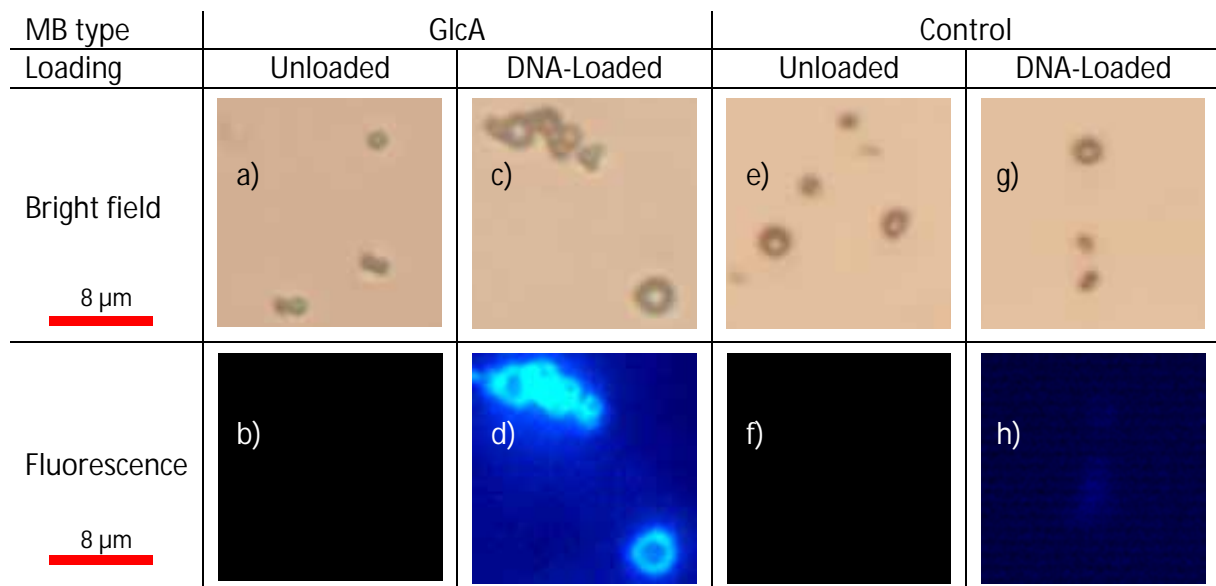


Figure 1: Microscopy images of DNA-loaded (c,d,g,h) or unloaded (a,b,e,f) GlcA (a-d) and Control MB (e-h).

Attenuation measurements of bulk suspensions showed that GlcA MB caused significantly greater attenuation at lower pressures than Control MB, but similar attenuation at higher pressures in both the time and frequency domain (Fig. 2).

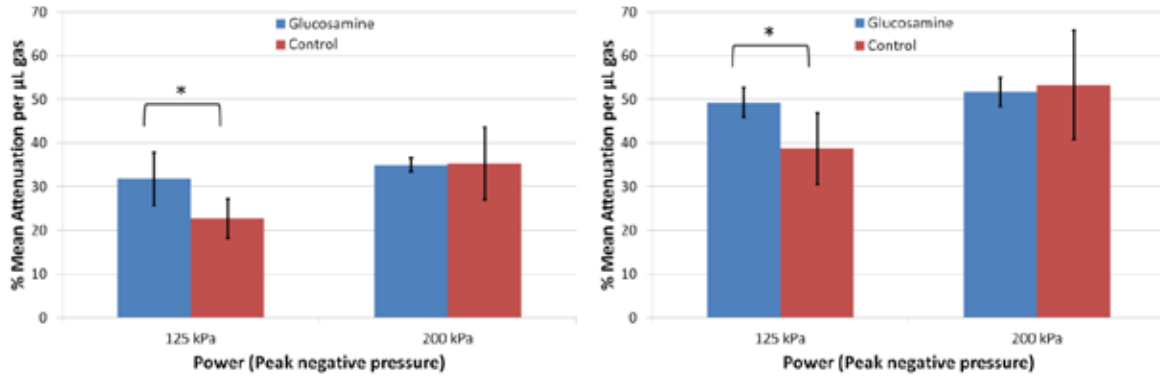


Figure 2: Mean attenuation normalised to MB gas volume of GlcA and Control MBs at 125 and 200 kPa. Error bars in S.D., * = $p < 0.05$

Preliminary *in vivo* work demonstrated no difference in the level of bioluminescence from the cardiac regions of mice transfected using either GlcA or Control MBs (Fig. 3).

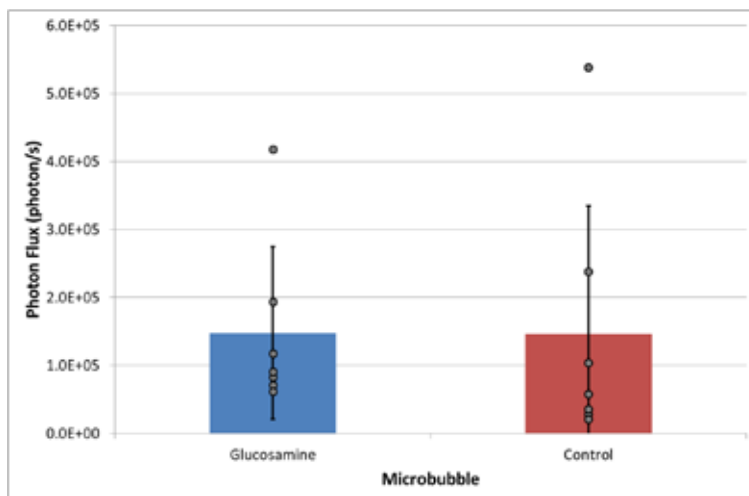


Figure 3: *In vivo* bioluminescence from the heart regions of CD1 female mice transfected using 6.1MHz, 1.6 MI US and either GlcA or Control MBs. Error bars in S.D., individual results shown as filled dots.

Summary/Discussion

Our findings indicate that DNA-loading MBs can be simply manufactured by adding GlcA to the initial ingredients. Additionally, MB produced in this manner have similar population statistics and acoustic behaviour at higher acoustic powers, as used in transfection, to control MB produced with dextrose only. As such, any difference in transfection levels should be linked to DNA-loading only. However, preliminary work suggests that DNA loading of albumin MBs does not improve transfection ability.

In this work, this is possibly due to the high amount of DNA used (200 µg), which would have oversaturated the GlcA MBs carrying capacity, causing most DNA to be unloaded (~88%). Considering the variability of US transfection experiments, any transfection due to the loaded 12% would likely be masked. Secondly, it has not been established that DNA loading is maintained once MB are introduced to the blood environment. Indeed, preliminary quantification work showed a reduction in the DNA-loading capacity of GlcA MB when washed with 0.9% saline. If loading is eliminated when introduced to the blood, GlcA MB transfection ability would potentially be similar to Control MBs due to similar acoustic behaviour. Thirdly, it may also be possible that DNA-loading of albumin MB has no effect on *in vivo* transfection. Nomikou *et al.* (2012) found that whilst DNA-loaded cationic lipid MBs were more effective at transfection *in vitro* compared to neutral lipid MBs, the difference was not significant *in vivo*. At this stage, further transfection work is underway to determine the effect of DNA-loading of albumin based MB *in vivo*.

Conclusions

DNA-loading albumin MB can be simply manufactured by the addition of GlcA to the pre-sonication mix with no effect on other important MB characteristics, such as size or high power, acoustic behaviour. However, the investigation into the effect on transfection *in vivo* is still on-going but may reveal DNA-loading to be an unimportant factor for effective transfection.

References

1. Alter, J., *et al.* (2009), *Ultrasound Med. Biol.*, 35 (6), pp. 976-84.
2. Nomikou, N., *et al.* (2012), *Acta Biomater.*, 8, pp. 1273-80.
3. Mulvana, H., *et al.* (2010), *Ultrasound Med. Biol.*, 36 (6), pp. 925-34.
4. Sennoga, C., *et al.* (2010) *Ultrasound Med. Biol.*, 36 (12) pp. 2093-6.
5. Wang, D. *et al.*, (2012), *Radiology*, 264 (3), pp. 721-32.

The optimal lipid coating for therapeutic bubbles

*Klazina Kooiman¹, Tom J.A. Kokhuis^{1,2}, Tom van Rooij¹, Ying Luan¹, Ilya Skachkov¹,
Johannes G. Bosch¹, Antonius F.W. van der Steen^{1,2}, Wiggert A. van Cappellen³,
Nico de Jong^{1,2}*

¹*Dept. of Biomedical Engineering, Thoraxcenter, Erasmus MC, Rotterdam, the Netherlands*

²*Interuniversity Cardiology Institute of the Netherlands, Utrecht, the Netherlands*

³*Dept. of Reproduction and Development, Erasmus MC, Rotterdam, the Netherlands*

Background

Ultrasound contrast agents consist of gas-filled coated microbubbles with diameters between 1 and 10 μm . For more than a decade, they are used to improve diagnostic imaging in cardiology and radiology. Nowadays, microbubbles also show potential for therapeutic applications in both drug delivery and molecular imaging. Lipid-coated microbubbles can be used for all therapeutic applications [1]. However, the coating properties may need to be fine-tuned for each specific application. This research aims to in more detail study the coating of lipid-coated microbubbles for the therapeutic applications: 1) co-administration; 2) the bubble as drug carrier; and 3) molecular imaging. The type of lipid coating, the lipid distribution, acoustic behaviour, and the surface contact area of targeted microbubbles were evaluated.

Method

Biotinylated lipid-coated microbubbles (composition in mol %: DSPC or DPPC 59.4; PEG-40 stearate 35.7; DSPE-PEG(2000) 4.1, DSPE-PEG(2000)-biotin 0.8) with a C_4F_{10} gas core were made by sonication using the method described by Klibanov et al [2].

To study the lipid distribution, fluorescent streptavidin Oregon Green 488 was conjugated to the biotinylated microbubbles via avidin-biotin bridging as described by Lindner et al [3]. High-resolution images were recorded with 4Pi microscopy [4]. Acoustic behaviour was studied using the Brandaris-128 high-speed camera [5]. Bubble spectroscopy [6] was performed with transmitting frequencies from 1-4 MHz at an acoustic pressure of 50 kPa.

Surface contact area of targeted microbubbles was studied by adding the lipid dye DiD to the microbubbles before sonication and coating an Opticell membrane with fluorescent streptavidin Oregon Green 488 (5 $\mu\text{g}/\text{ml}$) by physisorption. From 4Pi high-resolution recordings [4], the surface contact was determined by calculating the cross-section of the streptavidin plane with the bubble surface.

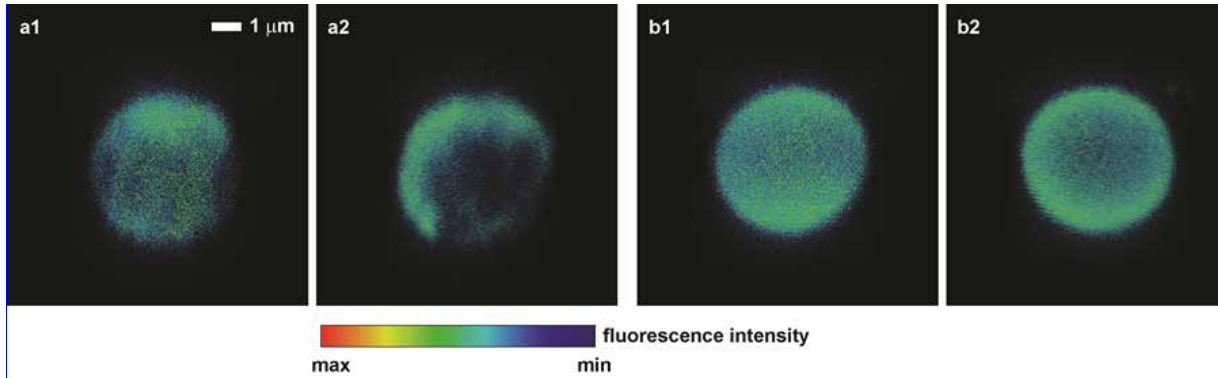


Fig. 1: Lipid distribution within coating of DSPC microbubbles (a) and DPPC microbubbles (b) recorded with 4Pi microscopy. Per microbubble, two views extracted from a full 3D acquisition (1 and 2) are shown. DSPE-PEG(2000)-biotin was fluorescently labelled whereas the other components DSPC, DPPC and PEG-40 stearate were not.

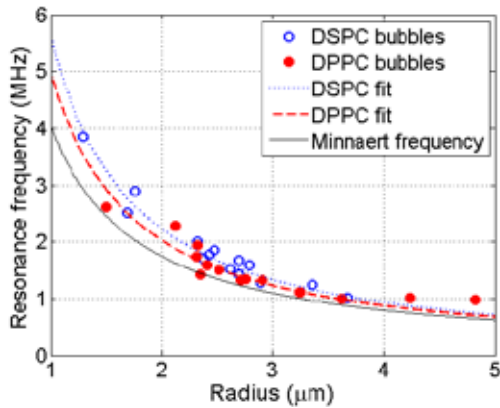


Fig. 2: Resonance frequency of DSPC microbubbles (open blue circles) and DPPC microbubbles (closed red circles).

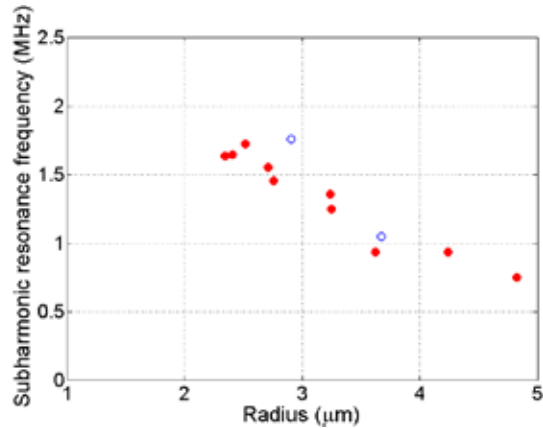


Fig. 3: Subharmonic resonance frequency of DSPC microbubbles (open blue circles) and DPPC microbubbles (closed red circles).

Results

For all studied microbubbles (2-10 μm in size), we observed an inhomogeneous streptavidin distribution when DSPC was the main coating lipid, indicating a non-uniform DSPE-PEG(2000) distribution in the coating (see Fig. 1a). When the lipid DSPC was replaced by DPPC, a homogeneous DSPE-PEG(2000) lipid distribution was observed, as shown in Fig. 1b. This can be explained by the miscibility of the lipids [7].

During insonification, both the DSPC and the DPPC microbubbles did not significantly shrink, indicating a good stability of the microbubbles. The resonance frequency is shown in Fig. 2. The DSPC microbubbles (blue open circles) had a marginally higher resonance frequency than the DPPC microbubbles (red closed circles). The shell elasticity for both microbubble types was not significantly different at ~ 0.10 N/m. Subharmonic behaviour was observed in 10 out of 14 DPPC microbubbles (71%) while this was only 2 out of 15 (13%) for the DSPC microbubbles (see Fig. 3), suggesting that the DPPC microbubbles will be better suited for non-linear ultrasound imaging.

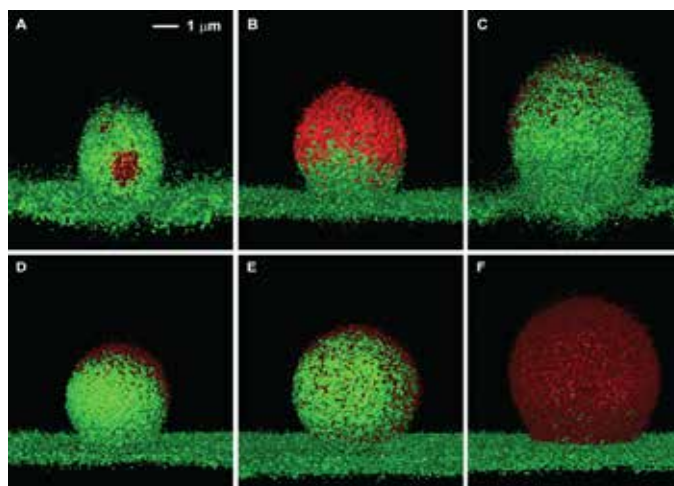


Fig. 4: Biotinylated targeted microbubbles (red fluorescent) bound to a streptavidin-coated surface (green fluorescent) for DSPC microbubbles (A-C) and DPPC microbubbles (D-F).

An example of DPSC microbubbles targeted to the streptavidin-coated surface is shown in Fig. 4A-C. Fig. 4D-F shows examples of targeted DPPC microbubbles. The bubbles are shown in red, and the streptavidin is shown in green. Streptavidin was also observed on the microbubbles, which is likely due to resorption of streptavidin from the surface. This is supported by preliminary data in which we did not observe any streptavidin on the microbubbles when the streptavidin was covalently linked to the surface. When the surface contact of the targeted microbubbles was calculated, this was found to be $6 \pm 4\%$ of the total microbubble surface for microbubbles with DSPC as the main lipid ($n=22$) and $11 \pm 4\%$ for microbubbles with DPPC as the main lipid ($n=24$).

Conclusion

This study reveals that lipid-coated microbubbles differ in lipid distribution, acoustic behaviour and surface contact area on the basis of their lipid composition. Which lipid composition is optimal for therapy, is best discussed per therapeutic application. For co-administration, the mechanism is not known [8] and therefore it is speculative what coating composition would be optimal. As we have reported that the vibration amplitude of microbubbles needs to exceed a threshold [9], it would be optimal if equally sized microbubbles have the same amplitude of vibration. However, this was not observed for both composition types.

When the microbubble is used as drug carrier by for example conjugating drug-filled liposomes to it [10], a homogeneous distribution of the liposomes would be optimal as we observed for the DPPC microbubbles. In these microbubbles, the lipids to which the liposomes are conjugated are homogeneously distributed and therefore there is hardly any competition during the conjugation. A maximum amount of drug can therefore be loaded onto these microbubbles.

For molecular imaging, it is important that the microbubbles are distinguished from tissue using the microbubble's non-linear behaviour. The DPPC microbubbles show more non-linear behaviour and may therefore be optimal. The binding also has to be considered for molecular imaging microbubbles. Within small microvessels, a difference in binding is not expected between both composition types as the microbubbles will be in close proximity to the vessel wall on all sides. However, for larger vessels, where the blood flow is also significantly higher [11], the probability of a successful binding event is likely to be higher for a microbubble with a homogeneous ligand distribution which is the DPPC microbubble. Although the average surface contact for the DPPC targeted microbubbles was higher, this does not imply that the binding force is also higher. For DSPC microbubbles, the ligand distribution is heterogeneous throughout the coating and areas with high concentrations of the ligand are also frequently observed. A higher amount of ligand molecules within a smaller area could therefore equal a lower amount of ligand molecules in a larger area which would still result in the same binding force.

Acknowledgements

This research is supported by the Center for Translational Molecular Medicine and the Dutch Heart Foundation (PARISK), and by NanoNextNL, a micro and nanotechnology programme of the Dutch Government and 130 partners. The authors would like to thank Michiel Manten and Frits Mastik from the Dept. of Biomedical Engineering, Erasmus MC for technical assistance, and A.L. Klibanov from the University of Virginia, Cardiovascular Division, Charlottesville, Virginia, USA for discussions about the microbubble preparation.

References

1. *Klibanov et al, Invest Radiol 2006; 41: p. 354.*
2. *Klibanov et al, Invest Radiol 2004; 39: p. 187.*
3. *Lindner et al, Circulation 2001; 104, p. 2107.*
4. *Hell et al, J Microsc-Oxf 1997; 187, p.;1*
5. *Chin et al, Rev Sci Instru 2003, 74: 5026.*
6. *van der Meer et al, J Acoust Soc Am 2007; 121, p. 648.*
7. *Lozano et al, Soft Matter 2007; 5, p. 1822.*
8. *Pua et al, IEEE Eng Med Biol 2009; 28, p.64.*
9. *Kooiman et al, J Control Release 2011; 154, p. 35.*
10. *Lentacker et al, Mol Ther 2010; 18, p. 101.*
11. *Kornmann et al, Ultrasound Med Biol 2010; 36, p. 181.*

Cardio perfusion imaging

Sharon L. Mulvagh MD FASE FACC FAHA FRCP(C)

Mayo Clinic, Rochester MN USA

Myocardial perfusion abnormalities occur as a result of limited coronary flow reserve, with a consequent decrease in myocardial contractility, often referred to as “the ischemic cascade”. Ultrasound contrast agents enhance the backscattered ultrasound signal, permitting their detection not only in the LV cavity, while improving endocardial visualization and alterations in contractility by regional wall motion assessment, but also in the myocardium, through visualization of microbubbles within the microcirculation, ie. perfusion. Indeed, improved multipulse ultrasound imaging strategies for microbubble detection have resulted in routine visualization of contrast within the myocardium, and stimulated a proliferation of investigative work into the non-invasive ultrasound assessment of myocardial perfusion. Image acquisition techniques using reduced acoustic power (mechanical index 0.1–0.2), while maintaining realtime imaging frame rates (20–30Hz), have allowed realtime myocardial contrast echocardiography (MCE) and simultaneous assessment of both function and perfusion.

Stress myocardial contrast perfusion echocardiography (MCE): diagnostic value

The use of contrast significantly enhances image quality in stress echocardiography (SE), thereby increasing the feasibility of test performance, decreasing the number of non-diagnostic exams, reducing the need for alternative testing, influencing clinical management decision-making, and ultimately improving cost-effectiveness. Myocardial perfusion imaging in conjunction with contrast SE provides yet further incremental benefits and is emerging in its clinical application. Destruction (depletion) of microbubbles and observation (qualitative and/or quantitative) of gradual refill (replenishment) into the myocardial microvasculature are the keys to accurately evaluating perfusion using realtime MCE.(1) A meta-analysis of eight studies comparing the sensitivity and specificity of qualitative MCE with those of SPECT/dobutamine SE for the detection of CAD showed at least equivalent (non-inferior) results.(2) SE studies have employed coronary angiography as the gold standard for CAD diagnosis, with reported sensitivities of 64–97% and specificities of 51–100%; MCE perfusion consistently improved sensitivity for detection of CAD over wall motion analysis alone. Vasodilator stress has also been utilized to demonstrate both perfusion and wall motion abnormalities during MCE with overall sensitivity, specificity, and accuracy for MCE perfusion detection of a >50% diameter stenosis of 81%, 73%, 78%, while for wall motion analysis it was 61%, 75%, 65% (p=0.038 for differences in sensitivity) (3). Examples of perfusion defects during realtime perfusion MCE are shown with dobutamine (Figure 1), and with regadenoson (Figure 2) stress testing.

Stress MCE: prognostic value

Stress MCE also provides prognostic value in patients with stable CAD. Tsutsui and colleagues studied 788 patients with realtime MCE during dobutamine SE during a median follow-up of 20 months. The authors reported that patients with normal perfusion have a better outcome than patients with normal wall motion. Furthermore, abnormal myocardial perfusion had significant incremental value over clinical factors, resting ejection fraction, and WM responses in prediction of cardiac events. Indeed, abnormal myocardial perfusion was an independent predictor of cardiac events (HR 5.2, 95% CI, 3.0–9.0; $p < 0.001$).⁽⁴⁾ Similarly, Dawson and colleagues ⁽⁵⁾ demonstrated that abnormal MCE in 261 patients with known or suspected CAD undergoing simultaneous dipyridamole stress MCE and ^{99m}Tc-sestamibi SPECT (mean follow-up 14 months) was an independent predictor of an adverse outcome (OR 23, 95% CI 6–201; $p < 0.001$) and provided incremental prognostic value over the clinical variables: LV systolic function, inducible wall thickening abnormalities, and SPECT results.

MCE: quantification of myocardial blood flow

MCE is a readily available, portable (bedside) noninvasive technique to accurately quantify myocardial blood flow (MBF) by visualization and measurement of the rate and volume of microbubble movement through the coronary microcirculation. During continuous microbubble infusion, steady-state microbubble concentration is achieved in the blood pool. After a brief high-mechanical-index impulse to deplete the myocardium of microbubbles, replenishment is characterized by a time–intensity curve, which is subsequently fitted to the mono-exponential function $Y = A(1 - e^{-\beta t})$, where β represents the rate of rise in signal intensity (microbubble velocity) and A is the peak plateau of video intensity (myocardial blood volume). The product of $A \times \beta$ represents an index of MBF.⁽⁶⁾ A meta-analysis of 627 patients undergoing quantitative stress (vasodilator or dobutamine) MCE for detection of CAD with comparative coronary angiography and/or SPECT demonstrated a significantly lower weighted mean difference (95% CI) for each of the measured parameters— A , β , and $A\beta$ reserve parameters in those patients with CAD versus those without: 0.12 (0.06–0.18), 1.38 (1.28–1.52), and 1.47 (1.18–1.76), respectively (all with $p < 0.001$). Pooled sensitivity and specificity for β reserve was 81% (76–85) and 77% (73–80), respectively, while pooled sensitivity and specificity for $A\beta$ reserve was 80% (75–84) and 81% (77–84), respectively.⁽⁷⁾ The assessment of quantitative myocardial perfusion during SE was shown to further improve the accuracy of SE over qualitative MCE alone.⁽⁸⁾

MCE: additional clinical applications

Assessment of myocardial perfusion using MCE may also be useful in the following clinical situations: determination of ischemic burden and infarct size in acute coronary syndromes; evaluation of success of reperfusion after percutaneous intervention; prediction and diagnosis of secondary complications (myocardial rupture, pseudoaneurysm); of acute coronary syndromes and assessment of effectiveness of reperfusion (viability) by PCI or thrombolytics; assessment of myocardial perfusion in suspected stress-induced cardiomyopathy; and differentiation of myocardial and intracardiac masses (tumor vs. thrombi).

References

1. Wei K, Skyba DM, Firschke C, et al., *Interactions between microbubbles and ultrasound: in vitro and in vivo observations*, *J Am Coll Cardiol*, 1997;29(5):1081–8.
2. Dijkmans PA, Senior R, Becher H, et al., *Myocardial contrast echocardiography evolving as a clinically feasible technique for accurate, rapid, and safe assessment of myocardial perfusion: the evidence so far*, *J Am Coll Cardiol*, 2006;48(11):2168–77.
3. Porter TR, Adolphson M, High RR, Smith LM, Olson J, Erdkamp M, Xie F, O'Leary E, Wong BF, Eifert-Rain S, Hagen ME, Abdelmoneim SS, Mulvagh SL. *Rapid detection of coronary artery stenoses with real-time perfusion echocardiography during regadenoson stress*. *Circ Cardiovasc Imaging*. 2011; 4(6):628-35.
4. Tsutsui JM, Elhendy A, Anderson JR, et al., *Prognostic value of dobutamine stress myocardial contrast perfusion echocardiography*, *Circulation*, 2005;112(10):1444–50.
5. Dawson D, Kaul S, Peters D, et al., *Prognostic value of dipyridamole stress myocardial contrast echocardiography: comparison with single photon emission computed tomography*, *J Am Soc Echocardiogr*, 2009;22(8):954–60.
6. Wei K, Jayaweera AR, Firoozan S, et al., *Quantification of myocardial blood flow with ultrasound-induced destruction of microbubbles administered as a constant venous infusion*, *Circulation*, 1998;97(5):473–83.
7. Abdelmoneim SS, Dhoble A, Bernier M, Erwin PJ, Korosoglou G, Senior R, Moir S, Kowatsch I, Xian-Hong S, Muro T, Dawson D, Vogel R, Wei K, West CP, Montori VM, Pellikka PA, Abdel-Kader SS, Mulvagh SL. *Quantitative myocardial contrast echocardiography during pharmacological stress for diagnosis of coronary artery disease: a systematic review and meta-analysis of diagnostic accuracy studies*. *Eur J Echocardiogr*. 2009; 10(7):813-25.
8. Kowatsch I, Tsutsui JM, Osorio AF, et al., *Head-to-head comparison of dobutamine and adenosine stress realtime myocardial perfusion echocardiography for the detection of coronary artery disease*, *J Am Soc Echocardiogr*, 2007;20(9):1109–17.

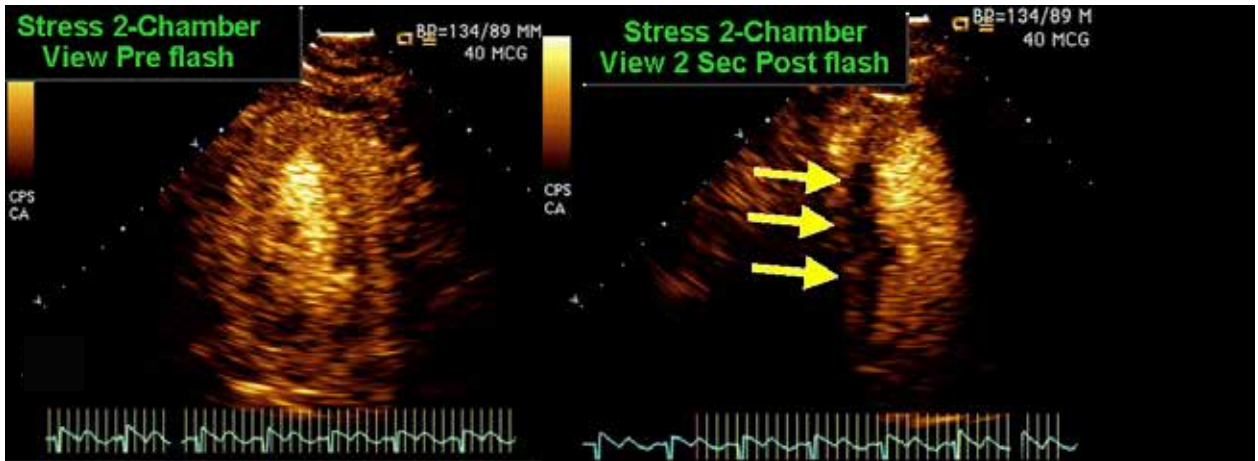


Figure 1: Dobutamine Stress Echocardiogram during realtime MCE at peak dobutamine stress (Apical 2-chamber view): Left Panel: Before high MI impulse (microbubble destruction “flash”). Right Panel: 2 heart beats after high MI impulse showing inferior wall perfusion defect (arrows). Acoustic shadowing prevents visualization of normal perfusion in the anterior wall in this view. No regional wall motion abnormalities were detected at peak dobutamine stress. Coronary angiography (not shown) demonstrated a normal left anterior descending artery (LAD), and proximal right coronary artery (RCA) 60% stenosis.



Figure 2: Regadenoson Stress Echocardiogram during realtime MCE immediately (30 sec to 3 min) after regadenoson IV bolus: An example of multiple inducible perfusion defects in the lateral, inferior, and inferolateral segments with realtime perfusion MCE during vasodilator (regadenoson) stress in a patient with multi-vessel CAD at quantitative angiography. Arrows depict the segments with inducible defects. (as published in ref #3 above)

***In-vivo* Irinotecan delivery using microbubble-mediated ultrasound into subcutaneous glioblastoma tumors**

Jean-Michel Escoffre, Anthony Novell and Ayache Bouakaz

UMR Inserm U930 Imagerie et Cerveau - Université François Rabelais de Tours, France

Rationale and aim

Irinotecan is a powerful anticancer drug used for the treatment of colorectal cancer and glioblastoma. The Irinotecan metabolism leads to the production of the pharmacologic active metabolite SN-38, a potent topoisomerase I inhibitor. However, the therapeutic effectiveness of Irinotecan is strongly limited by the development of drug resistance and its adverse side effects. The development of an efficient, safe and targeted delivery is required to overcome these problems. Recently, microbubble-assisted ultrasound has become a promising strategy for non-invasive local drug delivery to increase the drug concentration locally and to reduce systemic side effects. Escoffre *et al.* demonstrated the synergetic effect of microbubble-assisted ultrasound on *in-vitro* delivery of anticancer drug¹. The aim of this study is to evaluate the *in-vivo* effectiveness of this strategy for the Irinotecan delivery into subcutaneous glioblastoma tumors.

Material & Methods

Under gaseous anesthesia (Aerrane®), tumors were implanted subcutaneously in both flanks of the mice using 100 µL of U-87 MG cell suspension prepared from *in-vitro* cell culture (3×10^6 cells/mouse). A total of 15 mice were divided into three experimental groups (1) control group (*i.e.* w/o treatment), (2) Irinotecan group (*i.e.* injection of Irinotecan alone) and (3) Irinotecan + sonoporation group (*i.e.* Irinotecan injection followed by sonoporation). Tumor treatment was initiated under gaseous anesthesia when the tumors reached a volume of 100 mm³. It consisted in a direct i.v. administration of Irinotecan via penile vein (20 mg/kg; Camptosar®, Pfizer) followed by an i.v. bolus injection of MM1 microbubbles (70 µL) 1 hour after Irinotecan administration. This delay is required to reach the pharmacological peak of SN-38 distribution in the blood². The tumor was covered with ultrasound conducting gel and exposed to 1 MHz sinusoidal ultrasound waves with a pulse repetition period of 100 µs, 40 cycles per pulse (40% duty cycle), at peak-negative pressure of 400 kPa during 3 min. The treatment with Irinotecan and sonoporation was performed at 28th, 32nd and 36th day of tumor growth. The tumor growth and perfusion were measured before and after treatment using anatomical and nonlinear contrast ultrasound imaging, respectively (Vevo®2100 system). The tumor volume was calculated using:

$$Volume = \frac{Length \times Width^2}{2}$$

At the 39th day, tumors were removed and fixed in the formol-acetic acid solution. Then, histological samples were embedded in paraffin and prepared using conventional haematoxylin/eosin staining protocol. An expert clinical pathologist reviewed the stained tissue sections.

Results

The treatment of the subcutaneous glioblastoma tumors was applied three times, either using Irinotecan on its own or in combination with sonoporation. The therapeutic effectiveness of Irinotecan delivery was evaluated by anatomic ultrasound imaging every four days. As shown in the Fig. 1A, Irinotecan treatment on its own induced approximately 2-fold decrease in tumor volume compared to the control group. However, Irinotecan in combination with sonoporation led to an additional 2-fold decrease in tumor volume in comparison to Irinotecan alone. No side effect was observed with the treatment.

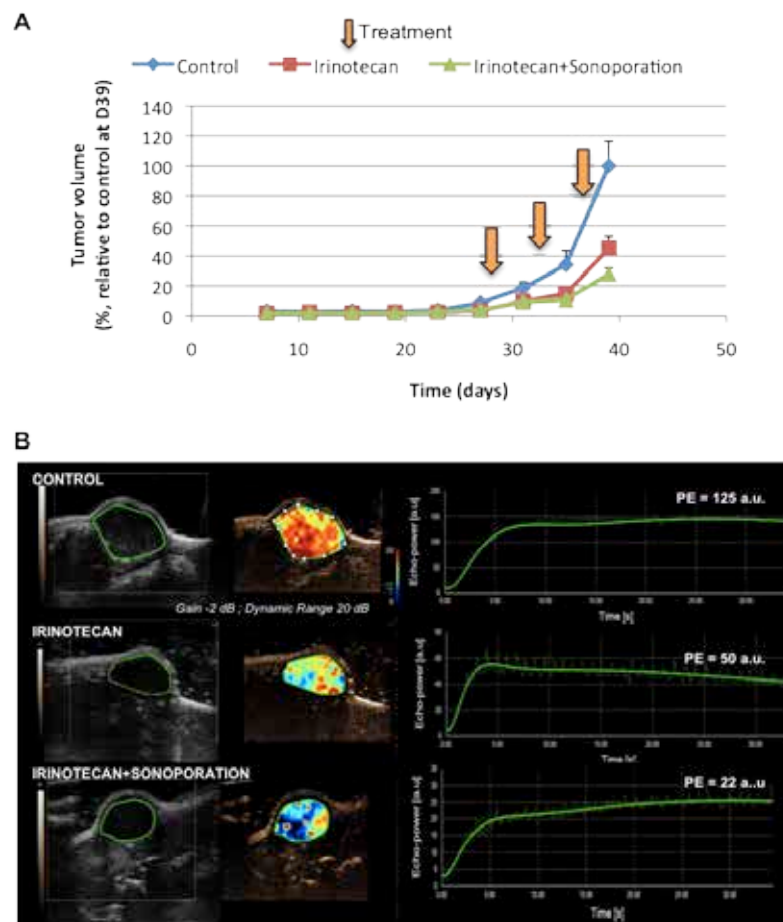


Figure 1. Tumor growth (A) and perfusion quantification as a function of time (B).

The therapeutic efficiency is also estimated through the measurement of the tumor-doubling time. The tumor doubling time was 6.7 days in the control group whereas this value increased after Irinotecan treatment alone (*i.e.* 8 days) or Irinotecan delivery with sonoporation (*i.e.* 8.7 days).

Tumor perfusion was estimated using VevoCQ software (Fig. 1B). The perfusion enhancement index (PE) revealed that Irinotecan treatment on its own induced a 2.5 fold decrease in tumor perfusion compared to the control group. However, Irinotecan in combination with sonoporation caused around 5.5-fold decrease in tumor perfusion in comparison to the control tumors.

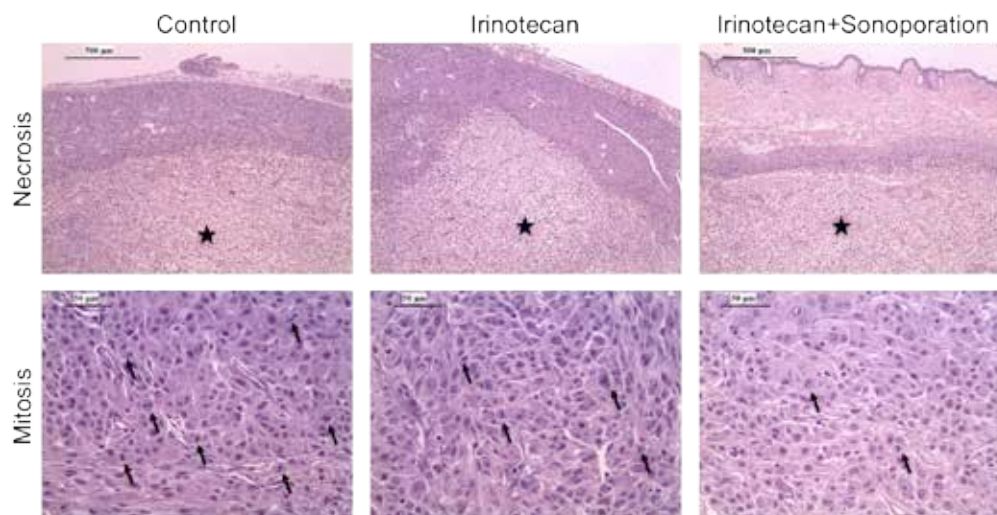


Figure 2. Histopathological analysis of tumors

At 39th day, a histopathological analysis was performed on the tumors after haematoxylin/eosin staining. Our data showed that the tissue necrosis significantly increased after Irinotecan delivery by sonoporation whereas the mitotic rate decreased (Fig. 2).

Conclusions

In conclusions, this pilot study demonstrated the synergetic effect of sonoporation and Irinotecan delivery for tumor treatment of subcutaneous glioblastoma tumors. Hence sonoporation increases further the therapeutic efficacy of Irinotecan. We assume that this effect is attributed to the ultrasonic activation of the microbubbles, which enhances the permeability of the tumor microvasculature and increases by that the Irinotecan bioavailability inside the tumor.

Acknowledgement

Project funded in part by the EU FP7 Project SONODRUGS (NMP4-LA-2008-213706).

References

1. Escoffre JM, Piron J, Novell A, Bouakaz A (2011) *Mol. Pharm.*, 8:799-806.
2. Kaneda N, Nagata H, Furuta T, Yokokura T (1990) *Cancer Res.*, 50:1715-1720.

Real-time imaging of sonoporation in ultrasound mediated drug delivery

De Cock I., De Smedt S. and Lentacker I.

Laboratory for General Biochemistry and Physical Pharmacy, Ghent University, Ghent, Belgium

Introduction

Ultrasound mediated drug delivery is gaining increasing interest as an alternative drug delivery technique, since it allows time and space controlled delivery. Although there is consensus that ultrasound in combination with microbubbles can enhance drug delivery, a lot of contradictory results were reported on the biophysical mechanisms involved in this process. However, it is imperative to remark that often different ultrasound settings were used, leading to different bubble behavior. In general, two mechanisms are suggested: enhanced delivery by increased endocytosis and permeabilization of cell membranes through pore formation [1]. Frequently used approaches to study sonoporation, such as flow cytometry, fluorescence microscopy [1] and atomic force or electron microscopy [2], typically study cell populations before and after ultrasound treatment. By voltage clamp techniques [3] the influx of calcium by sonoporation can be monitored real-time, but it leaves the biophysical processes unraveled. Although the above mentioned techniques have provided some insights in the sonoporation mechanisms, both real-time information during ultrasound insonation and visualization of cells and microbubbles is required to really understand the interactions between ultrasound driven microbubble oscillations and cells. Therefore we developed the ultrasound and microscopy setup depicted in figure 1.

Methods

The cell membrane was labeled red by CellMask Deep Red Plasma membrane Stain[®]. Microbubbles were labeled green by incorporating cholesterylBODIPY FL C₁₂ in the lipid shell. Propidium iodide, a cell impermeable dye, was used as a small molecule model drug and emits fluorescence when bound to nucleic acids. The sonoporation process was studied in real-time by swept field confocal microscopy at a frame rate of 15.61 fps.

Results

The effects of microbubbles on the cell membrane can be categorized in two main phenomena. The first is bubbles propelled towards the cell membrane causing pore formation, i.e. influx of propidium iodide (figure 2); the second is bubbles deforming the cell membrane without sonoporation. By increasing the acoustic pressure, a higher sonoporation rate is achieved.

Our observations show that pore formation is caused by the impact of the propelled bubbles on the cell membrane rather than fluid streamings created by microbubble oscillation. It also appears that the microbubbles are able to break through the cell membrane ending up inside the cell. This implies that loading of the microbubbles with the drugs may be necessary to achieve high delivery rates, since this would bring the drug exactly at the site of pore formation or even directly in the cytoplasm. Nevertheless, deformation of the cell membrane by bubbles might also induce upregulation of other pathways.

Conclusion

Pore formation is caused by bubbles propelled towards the cell membrane, which is important in optimizing microbubble and drug design. If deformation of the cell membrane induces upregulation of other pathways, e.g. endocytosis, is a topic for future experiments. Which mechanism is involved in ultrasound enhanced delivery is undoubtedly not only dependent on ultrasound parameters, e.g. pressure, but will probably also differ with molecule size.

References

1. *Meijering et al., Circ. Res., 2009, 104, 679-687.*
2. *Mehier-Humbert et al., J. Control. Release, 2005, 104, 213-222.*
3. *Deng et al., Ultrasound in Med.&Biol., 2004, 30, 519-526.*

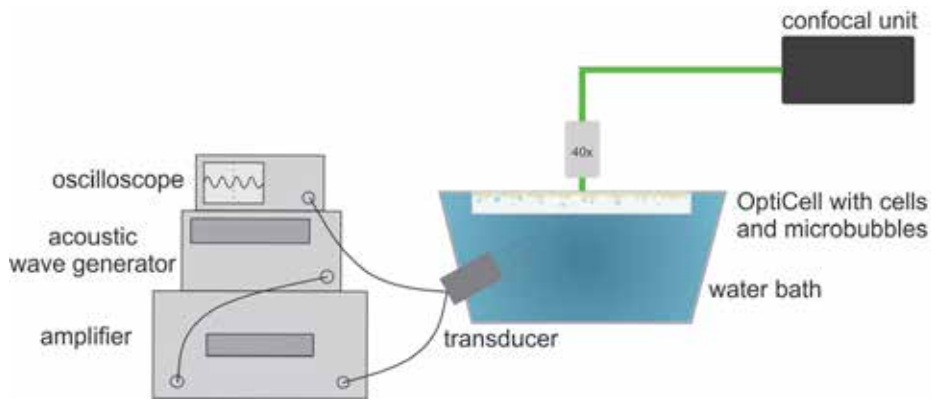


Fig 1: Ultrasound and swept field confocal microscopy setup.

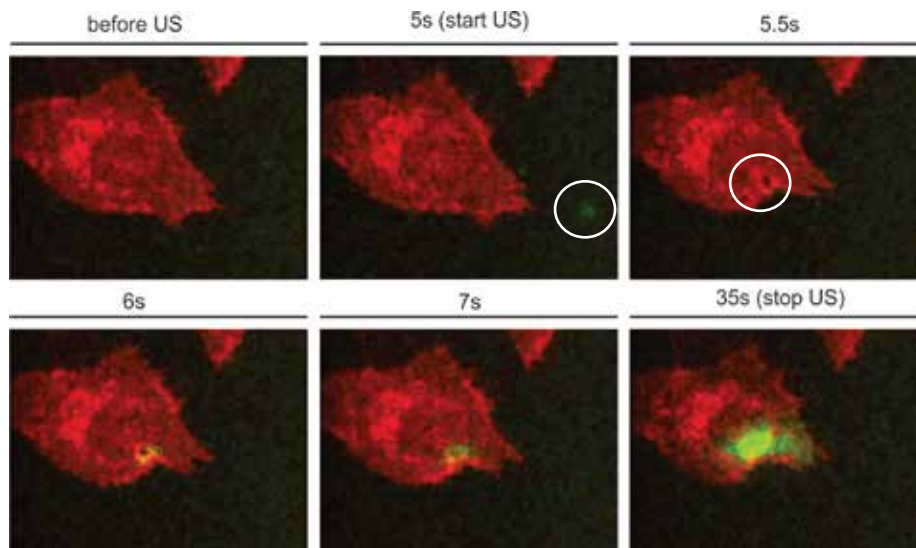


Fig 2: Microbubble propelled towards the cell causing pore formation: frames of different time points during ultrasound insonation. The cell and microbubble are fluorescently labeled red and green, respectively. Influx of propidium iodide is indicated by the appearance of green fluorescence, by binding of propidium iodide to nucleic acids inside the cell.

Contrast enhanced ultrasound image-guided cisplatin delivery

-an *in vivo* feasibility study-

Noboru Sasaki[†], Nobuki Kudo[§], Clemens Bos[†], Chrit Moonen[†], Mitsuyoshi Takiguchi**

**Graduate school of Veterinary Medicine, Hokkaido University, Japan*

§Graduate School of Information Science and Technology, Hokkaido University, Japan

†Division Imaging, University Medical Center Utrecht, the Netherlands

Background

Contrast enhanced ultrasound (CEUS) contributes to non-invasiveness cancer diagnosis in human and veterinary medicine. Moreover, the combination of ultrasound (US) and microbubbles (MBs) is useful for drug and gene delivery. Therefore, CEUS image-guided US-mediated drug delivery is a candidate theranostic approach. In this study, the feasibility of CEUS image-guided cisplatin delivery was assessed.

Methods

Sonazoid® (GE Healthcare) microbubbles, a second generation ultrasound contrast agent, were injected with cisplatin directly into a canine thyroid tumor in nude mice. CEUS imaging and MB activation were conducted concurrently using a linear array probe of a diagnostic US machine (TOSHIBA APLIO-XG). The US settings were as follows: the pulse subtraction imaging mode, transmitting frequency 4 MHz; 78 frames/sec; mechanical index 1.6. This mechanical index is not used for CEUS imaging, but was specifically aimed at MB destruction. The tumor was exposed to US for 15 sec in each treatment, and treatment was repeated four times with a two-day interval.

Results

After the intratumor injection of MBs, hyperechoic speckles spread into the whole tumor, and echogenicity of the tumor became higher (Fig.1A-C). Interestingly, the echogenicity of the tumor remained high after US exposure (Fig.1D). No petechiae were observed at the US exposed region. Cisplatin + MBs + US significantly delayed the tumor growth, while Cisplatin + US did not delay the tumor growth (Fig.2). Body weight of mice did not decrease in any treatment of the treatment groups.

Conclusion

CEUS image-guided anticancer drug delivery is promising as minimum invasive anticancer therapy. Additional modification, such as the MB administration method and optimization of treatment, may improve the efficacy of CEUS image-guided drug delivery.

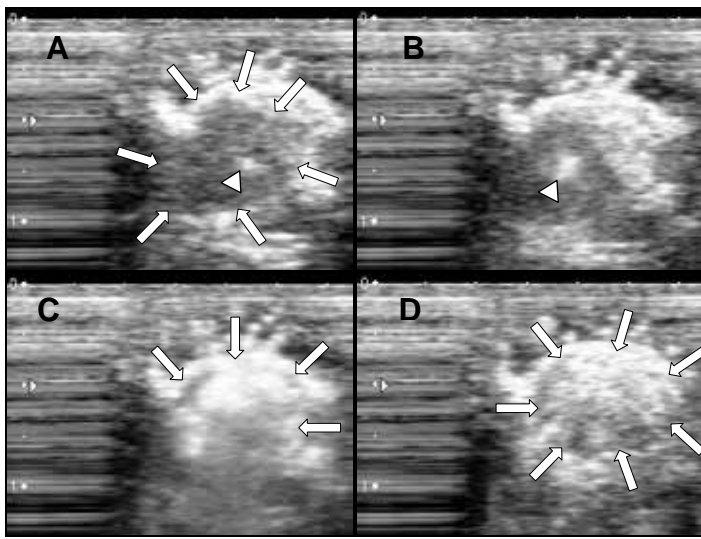


Figure 1: CEUS images of the treatment. (A) Before exposure. The echogenicity of tumor is low (*arrows*). The needle tip was observed (*arrow head*). (B) Starting MB injection. Hyperechoic speckles were observed around the needle tip (*arrow head*). (C) Spreading MBs. Hyperechoic speckles spread into the whole tumor. (D) After exposure. The echogenicity of tumor was still high.

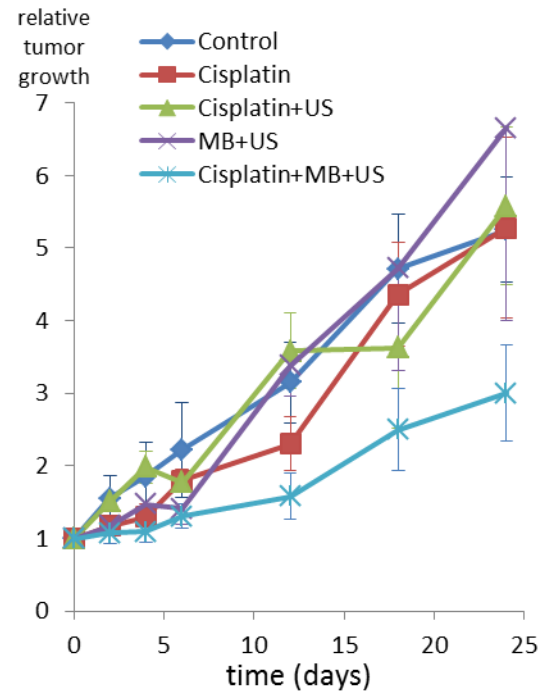


Figure 2: Relative tumor growth. Only Cisplatin + MB + US delayed the tumor growth compared with Control.

The bubble breakthrough in cancer immunotherapy

Heleen Dewitte^a, Sandra van Lint^b, Stefaan C. de Smedt^a, Karine Breckpot^{b,},
Ine Lentacker^{a,*}*

**both senior authors contributed equally to this work*

^aLab for General Biochemistry and Physical Pharmacy, Faculty of Pharmacy, Ghent University, Ghent, 9000, Belgium

^bLaboratory of Molecular and Cellular Therapy, Department Immunology-Physiology, Medical School of the Free University of Brussels (VUB), 1090, Jette, Belgium

Introduction & aim

Microbubbles are versatile agents with applications in contrast enhanced ultrasound imaging as well as in ultrasound-triggered drug and gene delivery. On the pursuit of new applications, we investigated the potential of microbubbles and ultrasound in dendritic cell-based cancer immunotherapy.

Ever since dendritic cells (DCs) first emerged as the most potent antigen presenting cells (APCs) and key initiators of immune responses, they have sparked interest in DC-based immunotherapy^{1,2}. DCs are specialized in taking up antigens and presenting them to naïve T cells. If these recognize the antigen as non-self, the T cells become activated, proliferate, and differentiate into effector T cells. Once active, the effector T cells will selectively target and destroy cells that express the antigen.

This capacity of DCs to trigger antigen-specific immune responses can be used to our benefit: when DCs are modified to present tumor associated antigens (TAAs), specific anti-tumor immune responses can be evoked. As an alternative to the currently used strategies for antigen-loading of DCs, we propose mRNA-sonoporation (i.e. ultrasound-triggered implosion of mRNA-loaded microbubbles), as schematically represented in **figure 1**.

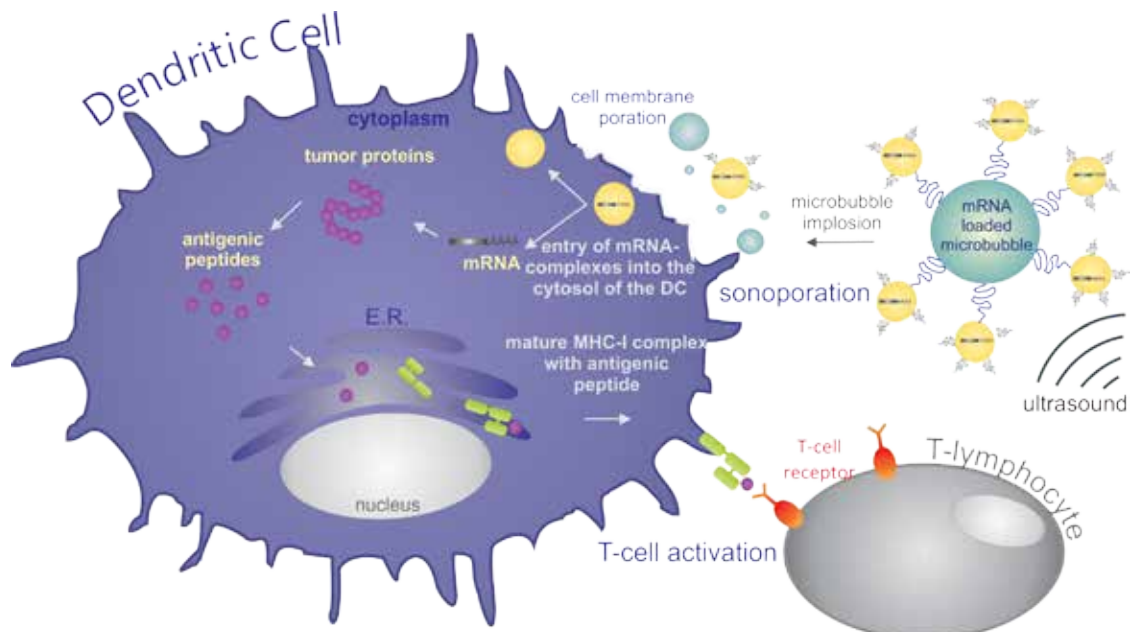


Figure 1: Using mRNA-sonoporation, DCs can be modified to present tumor-associated antigens to T cells. Upon T cell activation, an antigen-specific immune response is generated.

***In vitro* DC transfections by mRNA-sonoporation**

To ensure mRNA stability, we first complexed the mRNA to cationic lipids. The resulting mRNA-lipoplexes could then be attached to the surface of lipid microbubbles via avidin-biotin linkages. These mRNA-lipoplex loaded microbubbles were used for *in vitro* transfection of murine primary DCs in OptiCells™, using a Sonitron 2000 device for ultrasound application (1 MHz, 2 W/cm², 20% Duty Cycle). Using reporter mRNAs, we were able to reach transfection efficiencies up to 27%, without important cytotoxic effects on the DCs³ (see **figure 2**).

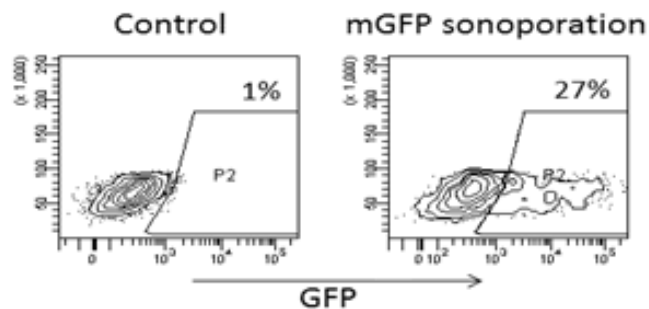


Figure 2: Transfection efficiency using mRNA encoding the green fluorescent protein (mGFP).

***In vivo* vaccinations with mRNA-sonoporated DCs**

An important feature of DCs is their capacity to respond to “danger signals”. Upon encounter of such stimuli the DCs will mature, which means that a number of phenotypic changes occur in the cells, resulting in a shift in function from antigen-uptake (immature DCs) to antigen-presentation (mature DCs). It is of crucial importance to use mature DCs for vaccination purposes, as these cells are associated with induction of immunity, whereas immature DCs are rather linked to tolerance and suppression of antitumor immune responses.

We were able to demonstrate that mRNA-sonoporation has an – albeit partial – effect on the maturation status of the DCs. In order to induce a more complete phenotypic switch, we included TriMix in the sonoporation. TriMix is a mixture of 3 mRNAs that encode proteins that modulate the DC’s functionality, resulting in more mature, and hence more immunogenic cells⁴. To evaluate the effect of TriMix inclusion on immune induction, *in vivo* T cell proliferation assays were performed in mice. For this, DCs were either untreated (control), sonoporated with antigen-mRNA or sonoporated with a combination of antigen-mRNA and TriMix. When these cells were injected s.c. as a vaccine, we could observe significant antigen-specific T cell proliferation in both sonoporated groups, compared to the control group. Importantly, sonoporation with a combination of antigen-mRNA and TriMix resulted in a more extensive T cell response compared to sonoporation with antigen mRNA alone.

To test if this increased T cell proliferation also resulted in a superior anti-tumor effect, we performed therapeutic vaccinations in mice that were inoculated with ovalbumin (OVA)-expressing melanoma cells (MO4). Two vaccinations were performed at day 10 and 13 after tumor inoculation, with either mGFP sonoporated DCs (as a control), DCs sonoporated with mOVA, or DCs sonoporated with both mOVA and TriMix. In line with the T cell proliferation results, we observed a significant slowdown of tumor outgrowth in the mOVA, but especially in the mOVA-TriMix combination group, also resulting in a prolonged overall survival (**figure 3**).

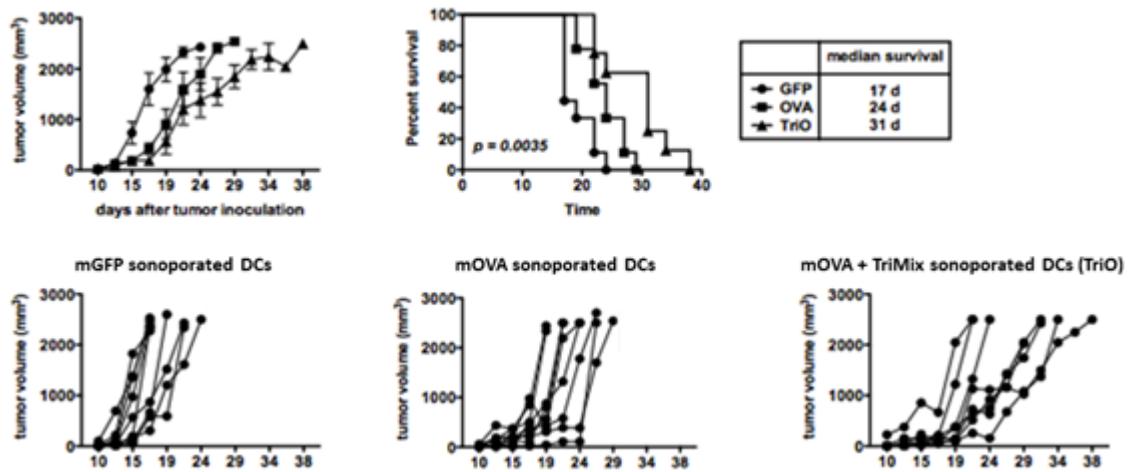


Figure 3: tumor outgrowth and overall survival of MO4-bearing mice after 2 vaccinations with either DCs sonoporated with mGFP, mOVA or a combination of mOVA and TriMix.

Conclusions & future perspectives

In conclusion, mRNA sonoporation is a promising tool in DC-based cancer immunotherapy. The major advantage of this approach is its *in vivo* potential: we aim to use mRNA-loaded microbubbles for immediate *in vivo* transfection of DCs in the lymph nodes, in this way circumventing current expensive and labor-intensive *ex vivo* transfection procedures. With our ongoing ultrasound imaging experiments that show intranodal contrast enhancement upon intradermal injection of mRNA-lipoplex loaded microbubbles, we hope to make a first step in this new and exciting direction.

Acknowledgements

Heleen Dewitte is a doctoral fellow of the Institute for the Promotion of Innovation through Science and Technology in Flanders, Belgium (IWT-Vlaanderen). Ine Lentacker is a postdoctoral fellow of the Research Foundation Flanders, Belgium (FWO-Vlaanderen).

References

1. Steinman, R.M. & Cohn, Z.A. Identification of a novel cell type in peripheral lymphoid organs of mice. *Journal of Experimental Medicine* **137**, 1142-1162 (1973).
2. Steinman, R.M. & Dhodapkar, M. Active immunization against cancer with dendritic cells: the near future. *International Journal of Cancer* **94**, 459-473 (2001).
3. De Temmerman, M.-L. & Dewitte, H. et al. mRNA-Lipoplex loaded microbubble contrast agents for ultrasound-assisted transfection of dendritic cells. *Biomaterials* **32**, 9128-9135 (2011).
4. Van Lint, S. et al. Preclinical Evaluation of TriMix and Antigen mRNA-Based Antitumor Therapy. *Cancer Research* (2012).

Time-resolved ultrasound-triggered release from a liposome-loaded microbubble

Ying Luan¹, Erik Gelderblom², Guillaume Lajoinie², Ilya Skachkov¹, Heleen Dewitte³, Bart Geers³, Ine Lentacker³, Ton van der Steen¹, Michel Versluis², Nico de Jong¹

¹*Erasmus Medical Center, Rotterdam, the Netherlands*

²*University of Twente, Enschede, the Netherlands*

³*University of Ghent, Ghent, Belgium*

Background

Microbubble-mediated drug delivery is under extensive investigations for enhancing drug delivery efficiency and controllability at desired region. Various designs of drug-loaded microbubbles have been developed. Earlier, we have reported preparation of a self-assembly liposome-loaded (loaded) microbubble by conjugating liposomes to microbubble surface through covalent thiol-maleimide linkages [1]. This loaded microbubble ensures a high drug payload, a high compatibility with drugs, and transportation of drugs in a stable fashion.

In the process of ultrasound-triggered drug delivery, an essential step is the release of the drug from the microbubble surface. In case of a loaded microbubble, two possible therapeutic agents can be released from a loaded microbubble under insonification: Intact drug-encapsulated liposomes detached from bubble surface [2], and/or free drug molecules released from disrupted liposomes. Understanding the release dynamics and the release process are crucial for further application using loaded microbubbles.

Here we present a parametric study into the controlled release from loaded microbubbles. The phospholipid-shelled (unloaded) microbubble was applied as a reference. We used fluorescence lipid probe to label liposomes or lipids on the bubble shell, and applied high-speed fluorescence imaging to capture time-resolved release triggered by ultrasound.

Materials and Methods

Microbubble samples of three configurations were prepared. Figure 1 shows a schematic view of the sample system. Sample A is unloaded microbubbles with fluorescence DiI incorporated in the phospholipid monolayer of the bubble shell. Sample B is loaded microbubbles with DiI-labeled liposome shell. Sample C is loaded bubbles with encapsulated fluorescent dextran or Doxorubicin inside liposomes. 157 bubbles of sample A and 132 bubbles of sample B was used to observe and quantify the release dynamics, while 161 bubbles of sample C was applied for investigation of the release process.

The Opticell™ containing the microbubbles was placed in a water bath, located underneath an upright fluorescence microscope setup. A continuous wave laser (5 W@532 nm; Cohlibri; Lightline, Germany) was employed for fluorescence excitation of the fluorescent label. Bright field illumination was combined to track the microbubble size and location during high-speed recordings, which was performed by a CMOS-based high-speed camera (SA-1.1; Photron Ltd,UK), operating at 100 kfps (320×160 pixels). Microbubbles were insonified by single ultrasound pulses containing 10 to 1000 cycles at 1 MHz and a peak-negative pressure ranging from 20 to 500 kPa.

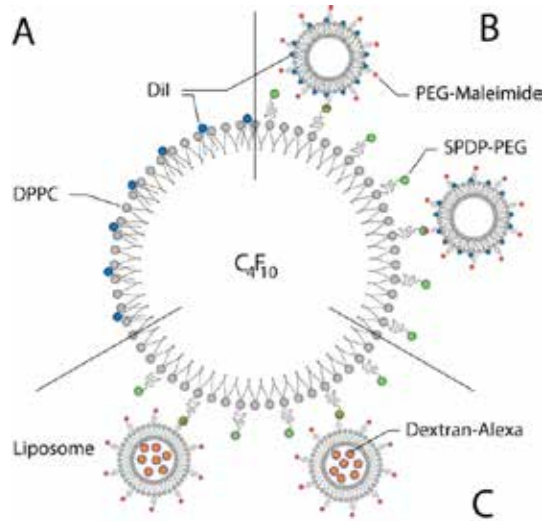


Figure 1: Schematic representation of the three configurations of microbubble samples.

Results

Various release dynamics were observed and quantified. At low pressures (20 kPa to 40 kPa), mainly rearrangement and budding of shell materials was observed. Shape mode oscillations of microbubbles generate release in a microstreaming pattern [3]. In addition, release can take place in forms of a cloud of small particles (cloud release) or larger clusters (vesicle release), depending on ultrasound parameters and microbubble categories. Under the applied acoustic settings, the release from a loaded microbubble is on a length scale of tens of microns, with an initial speed up to 0.1 m/s. In general, higher pressures and longer pulses can transport the released materials further away from the microbubble surface.

Figure 2 shows an example of budding and release of liposomes from a loaded bubble.

Acoustic dissolution of loaded microbubbles show a clear trend of the dependence on the ultrasound pressures, indicating a similar release process compared with unloaded bubbles, as reported by Borden *et al.* [4]. On the other hand, based on imaging technique, no apparent release of Doxorubicin (Dox) was found for Dox-encapsulated liposomes upon insonation. This implies that intact liposomes were released from loaded bubbles under ultrasound settings applied in this study.

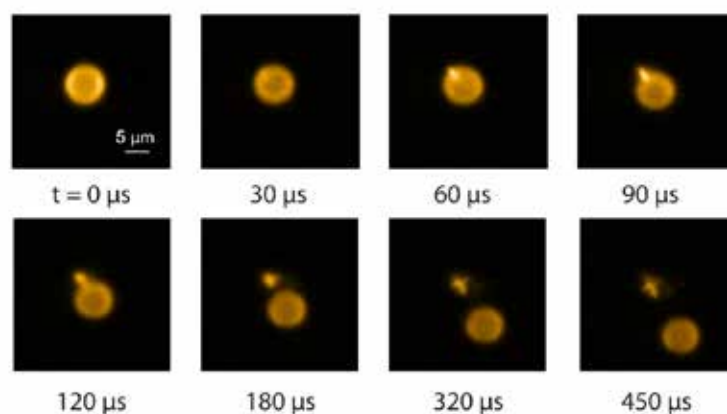


Figure 2: Budding and subsequent release of shell materials of a loaded bubble applied with ultrasound of 40 kPa, 1000 cycles.

Conclusions

High-speed fluorescence imaging provides detailed, time-resolved information about the ultrasound-triggered release of lipids or liposomes from microbubbles. The results provide ultrasound parameters for a controlled release of loaded microbubbles. It also gives valuable insights into the potential of using liposome-loaded microbubbles for a safe and efficient drug delivery.

References

1. B. Geers, I. Lentacker, N. N. Sanders, J. Demeester, S. Meairs, and S. C. De Smedt, "Self-assembled liposome-loaded microbubbles: The missing link for safe and efficient ultrasound triggered drug-delivery," *J Control Release*, vol. 152, pp. 249-56, 2011.
2. I. Lentacker, N. Wang, R. E. Vandenbroucke, J. Demeester, S. C. De Smedt, and N. N. Sanders, "Ultrasound exposure of lipoplex loaded microbubbles facilitates direct cytoplasmic entry of the lipoplexes," *Mol Pharm*, vol. 6, pp. 457-67, 2009.
3. A. Ooi, P. Tho, and R. Manasseh, "Cavitation microstreaming patterns in single and multiple bubble systems," *J Acoust Soc Am*, vol. 122, pp. 3051-3051, 2007.
4. M. A. Borden, D. E. Kruse, C. F. Caskey, S. K. Zhao, P. A. Dayton, and K. W. Ferrara, "Influence of lipid shell physicochemical properties on ultrasound-induced microbubble destruction," *Ieee Transactions on Ultrasonics Ferroelectrics and Frequency Control*, vol. 52, pp. 1992-2002, 2005.

Ultrafast dynamics of the acoustic vaporization of phase-change droplets

*Oleksandr Shpak¹, Tom Kokhuis², Ying Luan², Detlef Lohse¹, Nico de Jong²,
Brian Fowlkes³, Mario Fabiilli³, Michel Versluis¹*

¹*Physics of Fluids group, MIRA Institute of Biomedical Technology and Technical Medicine,
MESA+ Institute of Nanotechnology, University of Twente, Enschede, the Netherlands*

²*Biomedical Engineering, Erasmus MC, Rotterdam, the Netherlands*

³*Department of Radiology, University of Michigan, Ann Arbor, USA*

Background, motivation and objective

Ultrasound can be used to phase-transition liquid droplets into gas bubbles – a process known as acoustic droplet vaporization (ADV) [1]. These droplets are composed of a volatile perfluorocarbon, such as perfluoropentane (PFP, 29°C boiling point), and stabilized by a surfactant shell. A PFP emulsion does not spontaneously vaporize when injected in vivo at 37°C [2, 3]. However, upon exposure to ultrasound above certain acoustic pressure amplitude, the PFC within the emulsion is vaporized [4]. The resulting bubbles become acoustically active ultrasound contrast agents, which are detectable for at least one second after nucleation [5]. Precursor phase-change droplets are about five times smaller in diameter with respect to the resulting bubbles. Such a small size allows them to extravasate through the leaky tumor vessels prior to activation. This opens up the possibilities in a wide variety of diagnostic and therapeutic applications, such as tumor imaging, localized drug delivery, and embolotherapy [6]. However, the physical mechanisms underlying the ultrasound-triggered nucleation and subsequent vaporization of these phase-change emulsions are largely unexplored. Here, we study both theoretically and experimentally the acoustic vaporization of individual micron-sized PFP droplets at a nanosecond time scale.

Methods

Single perfluoropentane emulsions were prepared with bovine serum albumin following ref [7]. Droplet samples were vaporized with a single ultrasound pulse, consisting of a burst of 4 to 10 cycles in length and at a peak negative pressure of 4.5 MPa. They were imaged under a microscope equipped with a 40× water-immersion objective coupled to the Brandaris 128 ultra-high speed imaging facility providing a spatial resolution of 0.269 μm per pixel. The camera recorded sets of 128 images at a frame rate of up to 20 million frames per second (fps), thus providing an interframe time as low as 50 nanoseconds. Within the available parameter space, we also varied the ambient temperature of the liquid bath and as such the degree of superheat.

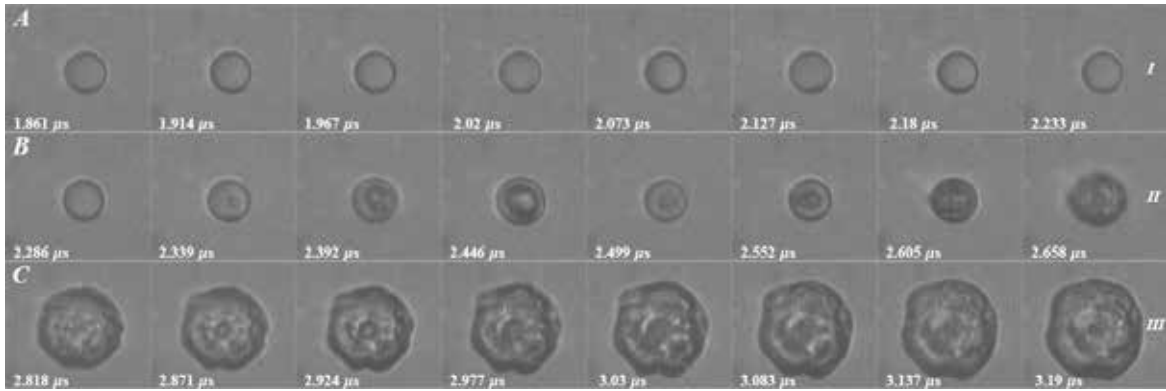


Fig. 1: A set of consecutive images showing acoustic droplet vaporization of a size of 5 μm taken at 18.5 Mfps at an ambient temperature of 50 $^{\circ}\text{C}$. The recordings can be categorized in three distinct regimes: I - oscillatory translations of a droplet prior to nucleation, II - vapor bubble expansion during which ultrasound is ON, and III - continued growth of the vapor bubble with ultrasound turned OFF.

Results and discussion

The droplet vaporization dynamics (see Fig. 1) was observed to have three distinct regimes:

- I. Prior to nucleation, a regime of droplet deformation and oscillatory translations within the surrounding fluid along the propagation direction of the applied ultrasound with an amplitude of 150 nm.
- II. A regime characterized by the rapid growth of a vapor bubble with a speed of 5-10 m/s enhanced by ultrasound-driven rectified heat transfer (see Fig 2).
- III. A final phase characterized by a relatively slow expansion, after ultrasound stops and that is fully dominated by heat transfer.

We propose a method to measure the moment of inception of the nucleation event with respect to the phase of the ultrasound wave. Furthermore, a simple physical model captures quantitatively all of the features of the subsequent vapor bubble growth. These new physical insights give valuable input in the design of new acoustic imaging and drug delivery agents. In addition, we study the role of gas through a model for a vapor-gas bubble, including thermal diffusion and gas diffusion inside the liquid and we find good agreement with the experimental data. We underline the fundamental role of gas diffusion to prevent total recondensation of the bubble at collapse.

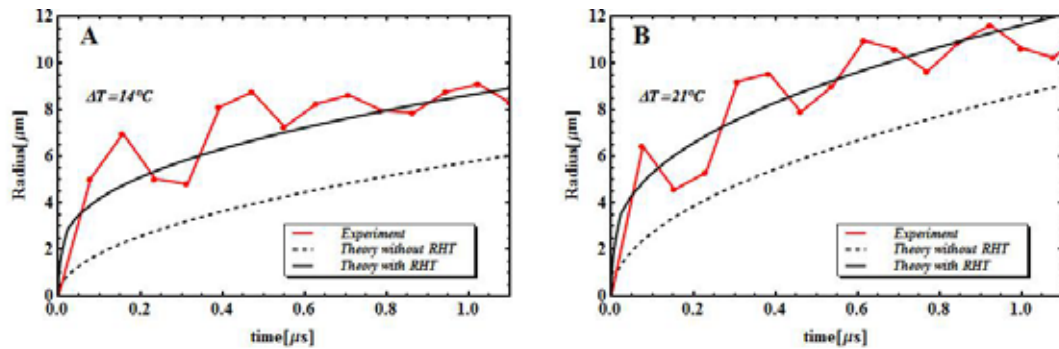


Fig. 2: Radial expansion of the vapor bubble at various settings of superheat, while forced by ultrasound. The red line represents the experimental data. The black dashed line is a fit to the heat transfer limited growth without applying the rectified heat transfer (RHT) correction, while the black solid line is with the rectified heat transfer correction applied.

Conclusion

Acoustic microdroplets vaporization was imaged for the first time at nanoseconds time scale with a sampling rate of 3-5 per cycle. With the developed pressure restoration method it was shown that the inception of nucleation occurs during the peak negative half cycle of ultrasound and slightly shifted towards the end of it. During regime III the physics of the vapor bubble expansion is shown to be heat transfer limited. The vapor bubble expansion was observed to have two components, one monotonic with a typical velocity of expansion of 5-10 m/s and a second, oscillatory, component with a typical amplitude of 1.2 μm associated with the applied ultrasound. The vapor bubble growth rate is enhanced by acoustic driving and through a simple physical model it was shown to be the result of rectified heat transfer.

References

1. O. D. Kripfgans et al. *Ultrasound Med Biol.* 2000;26:1177-89.
2. O. D. Kripfgans et al. *IEEE Trans Ultrason Ferroelectr Freq Control.* 2005;52:1101-10.
3. M. Zhang et al. *Acad Radiol.* 2011;18:1123-32.
4. P. S. Sheeran et al. *Ultrasound Med Biol.* 2011;37:1518-30.
5. N. Reznik et al. *Ultrasound Med Biol.* 2011;37: 1271-79.
6. P. S. Sheeran et al. *Curr Pharm Des.* 2012;18:2152-65.
7. M. L. Fabiilli et al. *IEEE Trans Ultrason Ferroelectr Freq Control.* 2009;56:1006-17.

The 18th European Symposium on Ultrasound Contrast Imaging Rotterdam is sponsored by:

SIEMENS AG - Ultrasound Division

Mr. Richard Medley, Product Manager
H WS ES US CRM Operations
Sir William Siemens Square
Newton House
Frimley, Camberley, SY GU16 8QD – UK

BRACCO International BV

Mr. Marco Graf, Congress Manager
GCO Global Strategic Marketing
Centro Galleria 2
Via Cantonale
CH-6928 Manno - Switzerland

GE Healthcare - Medical Diagnostics

Mr B. B. Newton
Global Product Leader - Ultrasound
The Grove Centre
White Lion Road
Buckinghamshire, HP7 9LL – UK

Philips Europe

[Medizin Systeme Böblingen GmbH](#)
Mr. James Walchenbach
Hewlett-Packard-Str. 2
71034 Böblingen
Germany

Philips Healthcare

Mr. Jim R. Brown
Global GI Luminary Management
Ultrasound Business Unit
22100 Bothell-Everett Highway
Mail Stop 501
Bothell, WA 98021-8431 - USA

Visualsonics

Mr. Anil K K Amlani
Acting President and CEO
3080 Yonge Street
Toronto, Ontario
M4N 3N1 – Canada

Oldelft BV

Mr. R. 't Hoen
Elektronicaweg 10
2628 XG Delft
The Netherlands

Hitachi Medical Systems

Ellison Bibby
European Marketing
Sumpfstrasse 24
6300 Zug – Switzerland

Nederlandse Hartstichting

Mw. Dr.ir. K. Eizema
Manager Research Department
P.O. Box 300
2501 CH Den Haag
The Netherlands

Coeur

Mr. H. Boersma
Erasmus MC - Thoraxcenter
Dr. Molewaterplein 50
3015 GE Rotterdam
The Netherlands

FIRST ANNOUNCEMENT 2014

19th EUROPEAN SYMPOSIUM ON ULTRASOUND CONTRAST IMAGING

23-24 JANUARY 2014

ROTTERDAM, THE NETHERLANDS

Course Directors: Folkert ten Cate

Nico de Jong

Arend Schinkel

Edward Leen

**Information on the 19th EUROPEAN SYMPOSIUM ON ULTRASOUND CONTRAST
IMAGING: Mieke Pruijsten, m.pruijsten@erasmusmc.nl**



GE Healthcare



SIEMENS

PHILIPS

HITACHI
Inspire the Next

 **Oldelft
Ultrasound**



The 18th European Symposium of Ultrasound Contrast Imaging, Rotterdam is sponsored by:



PHILIPS

GE Healthcare



SIEMENS



HITACHI
Inspire the Next